Computational aeroacoustics of rotor noise in novel aircraft configurations
A lattice-boltzmann method-based study

Romani, G.

DOI
10.4233/uuid:5d36b4de-8593-4f7e-bc92-a7ae175a0900

Publication date
2022

Document Version
Final published version

Citation (APA)
Romani, G. (2022). *Computational aeroacoustics of rotor noise in novel aircraft configurations: A lattice-boltzmann method-based study*. [Dissertation (TU Delft), Delft University of Technology]. https://doi.org/10.4233/uuid:5d36b4de-8593-4f7e-bc92-a7ae175a0900

COMPUTATIONAL AEROACOUSTICS OF ROTOR NOISE IN NOVEL AIRCRAFT CONFIGURATIONS

A LATTICE-BOLTZMANN METHOD-BASED STUDY

COMPUTATIONAL AEROACOUSTICS OF ROTOR NOISE IN NOVEL AIRCRAFT CONFIGURATIONS

A LATTICE-BOLTZMANN METHOD-BASED STUDY

Dissertation

for the purpose of obtaining the degree of doctor
at Delft University of Technology,
by the authority of the Rector Magnificus Prof.dr.ir. T.H.J.J. van der Hagen;
Chair of the Board for Doctorates
to be defended publicly on Monday 7 February 2022 at 15:00 hours

by

Gianluca ROMANI

Master of Science in Aeronautical Engineering,
Roma Tre University, Italy,
born in Aprilia, Italy.

This dissertation has been approved by the promotor

Promotor: Prof.dr. D. Casalino

Composition of the doctoral committee:

Rector Magnificus,	chairperson
Prof.dr. D. Casalino,	Delft University of Technology & Dassault Systemes Deutschland GmbH, promotor
Independent members:	
Prof.dr. K.S. Brentner,	Penn State University, USA
Prof.dr. M. Roger,	École Centrale de Lyon, France
Prof.dr. M. Gennaretti,	Roma Tre University, Italy
Prof.dr. F. Scarano,	Delft University of Technology
Dr. E. Manoha,	ONERA, France
Prof.dr.ir. L.L.M. Veldhuis,	Delft University of Technology, reserve member
Other members:	
Dr. W.C.P. van der Velden,	Dassault Systèmes BV, the Netherlands

Keywords: Trailing-edge noise, propeller noise, blade-vortex interaction noise, fan boundary-layer ingestion noise, LBM, CFD, FW-H, CAA

Printed by: Ridderprint BV

Front & Back: Renderized image from a PowerFLOW simulation of an eVTOL aircraft showing multiple blade-vortex interactions and the resulting noise radiation. Picture created by Gianluca Romani.

ISBN 978-94-6366-498-1

An electronic version of this dissertation is available at
http://repository.tudelft.nl/.

to Maria, my amazing partner in life

SUMMARY

THE accurate and reliable prediction of the aerodynamic noise sources of open rotors and ducted-fans in electric Vertical Take-Off and Landing (eVTOL) and non-conventional aircraft configurations is a challenging task from a computational perspective. Indeed, such propulsive systems can often operate in highly distorted and non-homogeneous flows, with the rotating blades interacting with strongly non-uniform and turbulent flows; and/or experience phenomena related to low Reynolds numbers and boundary-layer transition, due to the relatively small diameters and blade tip speeds. While analytical, semi-empirical and low-fidelity numerical models can provide quick and computationally inexpensive predictions, their results are often not fully reliable and their state-of-the-art requires a further development step to properly address the problem of rotor noise prediction in non-conventional aircraft and rotorcraft. On the other hand, Navier-Stokes based scale-resolving approaches such as Large Eddy Simulation (LES) have the capability to capture most of the aforementioned phenomena, but at a prohibitive computational cost for a routine employment in the design stages of such innovative vehicles. In view of this, high-fidelity scale-resolving lattice-Boltzmann numerical simulations, coupled with the Ffowcs Williams & Hawkings' acoustic analogy, are extensively performed and validated in this thesis with the aim of identifying, characterizing and predicting the primary sources of aerodynamic noise associated to open rotors/propellers and ducted-fans in eVTOL and novel aircraft configurations.

First, the problem of broadband rotor trailing-edge and its reduction is addressed at airfoil level for a cambered profile operating at moderate Reynolds numbers and undergoing natural boundary-layer transition, by considering both a straight trailing-edge and serrated trailing-edges at different flap angles. For the straight trailing-edge cases, the numerical results compare favorably against the experimental data. The numerical results reveal that the serration flap angle primarily affects the trailing-edge noise reduction through a modification of: the effective angle at which the turbulent structures are convected over the serrated edge; the convection velocity and spanwise coherence length along the serration; the intensity of the hydrodynamic wall-pressure fluctuations that are scattered along the serrated edge; with the first and last phenomena playing the most significant role on the far-field noise reduction. The best-suited orientation of the add-on in terms of turbulent boundary-layer trailing-edge noise reduction turns out to be that for which the serration is oriented as the mean streamlines deviation angle with respect to the tangent to the mean camber line. Finally, the destructive interference mechanism among noise sources along the serrated edge is found to be largely reduced when a serration is at incidence, compared to zero incidence cases.

Then, the prediction of broadband trailing-edge noise, along with that of tonal noise and performances, is extended to a complete propeller geometry operating at low-Reynolds numbers. Specifically, a computational approach based on the use of a zig-zag transition trip applied on the propeller blades is adopted in the numerical simulations to drive the numerical scheme from modeled to scale-resolving turbulence mode, and trigger the formation of vortical structures with scales able to emulate the complexity of a low-Reynolds number boundary-layer on the blade. Two different tripping strategies are attempted by placing the trip along the blade quarter-chord and expected turbulent boundary-layer transition lines, respectively. It is observed that the trip chordwise position marginally affects the thrust prediction and to a slightly larger extent the torque one. Moreover, tonal noise at the blade-passing frequencies results to be insensitive to the trip position, while broadband noise is found to be slightly more influenced by it, especially at high advance ratios at which the boundary-layer transition is expected to occur closer to the blade trailing-edge. Finally, the low sensitivity of the numerical results to the trip location, as well as their good agreement with loads and noise experimental data, demonstrates the robustness of the proposed approach for industrial applications.

The same approach is then used to address the impact of angular inflows, due to non-zero propeller angles of attack or yaw angles, on the tonal and broadband noise radiated by a low blade-tip speed propeller. The numerical noise predictions are found to be in a very good agreement with the experimental measurements, with the zig-zag based approach being able to reproduce the strong tonal noise directivity change, as well as the minor variation of the broadband noise levels observed in the experimental data. The numerical results confirmed that the presence of an angular inflow is responsible for a radiation of tonal loading noise along the propeller axis; and for an increment/reduction of the sound pressure level in the region from/to which the propeller is tilted away/towards. However, in contrast to propellers operating at high blade-tip Mach numbers, the noise directivity change is found to be governed only by the rise of periodic unsteady loadings, with the modulation of the strength of the noise sources on the blade - due to the periodic variation of the observer-source relative Mach number (in the rotating frame) - being negligible. Finally, both thickness noise and turbulent boundary-layer trailing-edge noise are not significantly altered when the propeller is yawed with respect to the free-stream.

Next, the problem of tonal noise generated by a rotorcraft experiencing strong blade-vortex interaction conditions is considered. The numerical simulations are performed by considering a rigid blade motion, but a computational approach is employed to account for the steady and unsteady aerodynamic effects associated to the blade elastic deformations, through the application of a transpiration velocity boundary condition, a fluid body-force field and the steady deformed blade shape. The predictions of both unsteady loading and far-field noise result to be in a satisfactory agreement with the experimental data, although some intrinsic inaccuracies in the numerical results are observed, primarily due to the lack of a proper simulation of the rotor blade elastic deformations. However, it is shown that the modeling of the aerodynamic effects associated to the elastic deformation of the rotor blade leads to more accurate predictions of trim settings, unsteady airloads and noise footprint.

Finally, the lattice-Boltzmann method is applied to the analysis of the noise generation mechanisms and to the quantification of the related tonal and broadband noise emissions of a boundary-layer ingesting ducted-fan/OGV (outlet guide vane) embedded propulsion system. The analysis is performed by considering a modified version of the Low-Noise NASA SDT fan-stage integrated into the ONERA NOVA fuselage. Installation effects due to the boundary-layer ingestion are quantified by comparison with an isolated configuration of the modified Low-Noise SDT fan-stage at the same operating condition, namely a take-off with power cut-back. It is found that the boundary-layer ingesting fan/OGV stage is characterized by strong azimuthal fan blade loading unsteadiness, less axisymmetric and coherent rotor wake tangential velocity variations and higher levels of in-plane velocity fluctuations compared to the isolated engine. This results in no distinct tonal components and higher broadband levels up to 20 dB in the far-field noise spectra, as well as in an increment of the cumulative noise levels up to 18 EPNdB.

SAMENVATTING

De nauwkeurige en betrouwbare voorspelling van de aerodynamische geluidsbronnen van open en geïsoleerde rotoren voor elektrisch gemotoriseerde verticale start en landing (eVTOL) configuraties alsmede niet-conventionele vliegtuigconfiguraties is een uitdagende taak. Dit vanwege het feit dat deze voortstuwingssystemen vaak in sterk vervormde en niet-homogene stromingen aanwezig zijn, waar de rotorbladen in wisselwerking staan met sterke en vaak niet-uniforme en turbulente stromingen, en in combinatie met verschijnselen die verband houden met lage Reynoldsgetallen en grenslaagovergangen door de relatief kleine diameters en bladpuntsnelheden van de rotoren. Hoewel analytische, semi-empirische en versimpelde numerieke modellen vaak snelle en rekenkundig goedkope voorspellingen kunnen bieden, zijn de resultaten niet altijd volledig betrouwbaar en zijn er nieuwe technieken vereist voor een verdere ontwikkeling om het probleem van de voorspelling van rotor geluid goed aan te pakken. Aan de andere kant hebben Navier-Stokes gebaseerde benaderingen zoals een Large Eddy Simulation (LES) de mogelijkheid om het meeste van bovengenoemde fysica vast te leggen, maar vaak tegen een onbetaalbare rekenkracht voor routinematig gebruik, wat natuurlijk nodig is in de ontwerpfasen van dergelijke innovatieve voertuigen. Vandaar dat in dit proefschrift de nadruk ligt op het uitvoeren van zeer betrouwbare, accurate, schaaloplossende stromingssimulaties door middel van de Lattice-Boltzmann vergelijkingen, gekoppeld met een akoestische analogie op basis van de van Ffowcs Williams Hawkings vergelijking, met als doel het identificeren, karakteriseren en voorspellen van de primaire bronnen van aerodynamisch geluid geassocieerd met open rotors, propellers en geïsoleerde ventilatoren in eVTOLs en nieuwe, niet-conventionele, vliegtuigconfiguraties.

Allereerst wordt het probleem van geluidsoverlast van een rotor, komend van de achterrand van het rotorprofiel bekeken, en wordt vervolgens de reductie ervan aangepakt voor een gewelfd profiel met een natuurlijke grenslaagovergang bij een gematigd Reynolds-getal, voor zowel een rechte als getande achterrand bij verschillende flap hoeken. Voor de rechte achterrand steken de numerieke resultaten gunstig af tegen de experimentele gegevens. De numerieke resultaten laten zien dat, wanneer de achterrand gekarteld is, de hoek van de gekartelde achterrand voornamelijk de geluidsonderdrukking beïnvloedt door een wijziging van: de effectieve hoek waaronder de turbulente structuren over de gekartelde rand worden verplaatst; de convectiesnelheid en coherentielengte langs de karteling; de intensiteit van de hydrodynamische wanddrukfluctuaties die verspreid zijn langs de gekartelde rand. Hierbij spelen het eerste en laatste fenomeen de belangrijkste rol bij de geluidsonderdrukking in het verre veld. De meest geschikte invalshoek van de getande achterrand, waarbij de meest efficiënte geluidsonderdrukking van achterrand geluid optreed, blijkt te liggen rond de gemiddelde stromingslijn ten opzichte van de raaklijn aan de gemiddelde camberlijn. Ten slotte blijkt het destructieve interferentiemechanisme tussen geluidsbronnen langs de getande rand grotendeels verminderd te zijn wanneer een vertanding optreedt onder een invalshoek.

Vervolgens wordt de voorspelling van breedband achterrand geluid, samen met die van tonale ruis en aerodynamische karakteristieken, uitgebreid tot een analyse van een complete propellergeometrie die roteert onder lage Reynolds-getallen. In deze numerieke simulaties wordt met name een benadering voor de grenslaagovergang gebruikt in de vorm van een transitie strip op de propellerbladen, om zo het numerieke schema van gemodelleerd naar schaaloplossend te sturen en de vorming van wervel structuren op te schalen om zo de complexiteit van een grenslaag met een laag Reynoldsgetal op het rotorblad na te bootsen. Er worden twee verschillende tripstrategieën getest door middel van de trip respectievelijk of op de 25% lijn langs het blad te plaatsen, of op de verwachte turbulente grenslaagovergangslijn te plaatsen. Opgemerkt wordt dat de positie van de trip de stuwkrachtvoorspelling nauwelijks beïnvloedt, en in marginale mate de torsie aanpast. Bovendien blijkt de tonale component van het geluid bij de karakteristieke rotor frequenties vrijwel ongevoelig te zijn voor de trippositie, terwijl het breedband achterrand geluid er iets meer door wordt beïnvloed. Dit is vooral het geval bij hoge voorwaartse verhoudingen waarbij de grenslaagovergang naar verwachting dichter bij de achterrand van het blad gepositioneerd is. Ten slotte demonstreert de numerieke resultaten een lage gevoeligheid voor de locatie van de transitie strip. Daarnaast laat de goede overeenstemming tussen de numerieke en experimentele resultaten zien dat de robuustheid van de voorgestelde aanpak uitermate geschikt is voor industriële toepassingen.

Dezelfde benadering kan vervolgens worden gebruikt bij een propeller met lage tip snelheden om de impact van de stromingshoek als gevolg van de incidentie en de gierhoek van de rotorbladen op tonaal en breedband geproduceerd geluid te bepalen. De numerieke geluidsvoorspellingen blijken zeer goed overeen te komen met de experimentele metingen, waarbij de op transitie strip gebaseerde berekening in staat is om sterke richtingsveranderingen van tonaal geluid te reproduceren, en de kleine variaties van de breedbandgeluidsniveaus uit de experimentele gegevens. De numerieke resultaten bevestigden dat de aanwezigheid van een stromingshoek verantwoordelijk is voor de straling van tonaal laadgeluid langs de propelleras; alsmede voor een verhoging/verlaging van het geluidsdrukniveau in het gebied van/naar de propeller waarin het vandaan/naartoe wordt gekanteld. In tegenstelling tot propellers die werken met hoge tip snelheden blijkt de verandering in de richting van het geluid nu alleen te worden bepaald door de toename van periodieke onstabiele belastingen, waarin de modulatie van de sterkte van de geluidsbronnen op het blad als gevolg van de periodieke variatie van het waarnemer-bron relatieve Mach-getal (in het roterende frame) verwaarloosbaar zijn. Ten slotte wordt zowel het verplaatsingsgeluid alsmede het achterrand geluid niet significant gewijzigd wanner de propeller onder een gierhoek wordt geplaatst.

Vervolgens wordt het probleem van tonaal geluid van een helikopter onder sterke blad-vortex-interactiecondities bekeken. De numerieke simulaties worden uitgevoerd door rekening te houden met een starre bladbeweging, maar er wordt tevens een numerieke benadering gebruikt om rekening te houden met de constante en onstabiele aerodynamische effecten die verband houden met de elastische vervormingen van het blad die door de toepassing van een grensvoorwaarde voor de transpiratiesnelheid een vloeistoflichaam-krachtveld en een vervormde bladvorm genereren. De voorspellingen van zowel onstabiele belasting als verre veld geluid komen overeen met de experimen-

tele gegevens, hoewel enkele intrinsieke onnauwkeurigheden in de numerieke resultaten worden waargenomen. Deze zijn voornamelijk het gevolg van het ontbreken van de elastische vervormingen van het rotorblad in de simulatie. Het is echter aangetoond dat de modellering van de aerodynamische effecten die samenhangen met de elastische vervorming van het rotorblad, leidt tot nauwkeurigere voorspellingen van de triminstellingen, onstabiele belastingen alsook de geluidsemissie.

Ten slotte wordt de Lattice-Boltzmann methode toegepast voor de analyse van de verschillende geluidsmechanismen, alsmede de kwantificering van de gerelateerde tonale en breedbandgeluidsemissies van een in de grenslaag opgenomen omringde roterende voortstuwingssysteem. De analyse wordt uitgevoerd door een aangepaste versie van de geluidsarme NASA SDT motor te gebruiken, die vervolgens geïntegreerd is in de ONERA NOVA-romp. Installatie-effecten als gevolg van opname van de motor in de lokale grenslaag worden gekwantificeerd door vergelijking met een geïsoleerde configuratie van de gemodificeerde stille SDT ventilator onder dezelfde stromingsomstandigheden, te weten een start onder stroomuitval. Het is aangetoond dat de grenslaag-innemende rotor wordt gekenmerkt door een sterke onstabiele hoek verdraaiende belasting van de ventilatorbladen, alsmede minder asymmetrische en coherente tangentiële snelheidsvariaties en hogere niveaus van snelheidsfluctuaties in het zog van de rotor in vergelijking met de geïsoleerde motor. Dit resulteert in geen extreme tonale componenten, maar wel in een hogere breedbandniveau tot 20 dB in het verre-veld geluid, en daarnaast ook in een toename van het cumulatieve geluidsniveau tot 18 EPNdB.

PREFACE

THE work presented in this dissertation is the outcome of research and development activities conducted by the author at Dassault Systemes Deutschland GmbH (formerly Exa GmbH) and in collaboration with the Technische Universiteit Delft. This thesis is primarily the result of my own work. It is addressed to engineers and researchers involved in the aeroacoustic design and analysis of rotor systems in novel aircraft/rotorcraft vehicle configurations. The original contributions of this thesis have been presented at international conferences and/or published in archival journals by the author. I would like to express my gratitude to my PhD promotor and company manager Prof. Dr. Damiano Casalino, for giving me the possibility to pursue a PhD at TU-Delft in parallel to my job as engineer, first at Exa Corporation and later at Dassault Systèmes. To my supervisors and colleagues at Dassault Systèmes and TU-Delft: I would like to thank you for your fruitful and useful collaboration that contributed to improve the quality of this dissertation. I would also like to acknowledge: Dr. Andreas Fischer from DTU for the provision of the experimental data that were used in Chapter 4, Edoardo Grande from TU-Delft for providing the propeller geometry and measurements used in Chapters 5 and 6, and the HART-II team for the experimental data and geometry used in Chapter 7. Moreover, the author wish to thank the Department of Aerodynamics, Aeroelasticity and Aeroacoustics of ONERA for the provision of the NOVA fuselage geometry, as well as Dr. Edmane Envia from NASA Glenn Research Center for providing the geometry and experimental data of the NASA SDT fan-stage, both used in Chapter 8. Finally, I would like to gratefully acknowledge Dassault Systemes Deutschland GmbH (formerly Exa GmbH) for providing the computational resources that have been used in this research work.

I hope you enjoy your reading.

Gianluca Romani
Stuttgart, August 2021

CONTENTS

1

INTRODUCTION

Considerate la vostra semenza:
fatti non foste a viver come bruti,
ma per seguir virtute e canoscenza.

Inferno XXVI 118-120, Divina Commedia, Dante Alighieri

Consider your origin:
you were not born to live like brutes,
but to follow virtue and knowledge.

Hell XXVI 118-120, The Divine Comedy, Dante Alighieri

This chapter provides some background on the growth of the civil aviation, the consequent development of novel aircraft/propulsion integration concepts aimed at reducing gas emissions and improving the propulsive efficiency, as well as on the emergence of a new class of air transport vehicles for Urban Air Mobility. These aspects are connected to the problem of community noise, the need to develop and assess new computational approaches for the prediction of the noise radiation associated to the propulsive systems of novel aircraft configurations, as well as the design of quieter flying vehicles. This is followed by the definition of the objectives and outline of this thesis.

1.1. AVIATION AND NOISE NUISANCE

NOWADAYS, aviation represents a key contributor to the world socio-economic growth by connecting people, businesses and places across the world. People rely on aviation as a fast long-range mean of transport for personal, tourism and business travels. Air transport also promotes foreign investment and international trade, by facilitating goods export from one country to another, and generates direct and indirect employment. A recent analysis of the International Civil Aviation Organization (ICAO) showed that almost 12 million passengers and USD 18 billion worth of goods are currently transported by more than 100000 flights daily, and that about 90% of business-to-consumer e-commerce parcels are carried by air transportation [1]. From an historical point of view, civil aviation is in continuous expansion, experiencing a growth rate of approximately 100% every fifteen years [1]. Forecasts predict that air passenger and freight traffics will double in the next two decades, with yearly growths of 4.1% and 3.6%, respectively [2].

Although several social and economic benefits can be ascribed to air transportation, aviation is also associated with a number of dangerous consequences for both climate and human health. Aircraft emit particles and gases primarily in the form of carbon dioxide (CO_2), nitrogen oxides (NO_x), sulfur oxides (SO_x), water vapor (H_2O) and soot [3]. Such emissions overall contribute to the climate change and have an important influence on the quality of air and human health [4]. The Intergovernmental Panel on Climate Change (IPCC) estimated that air transport contribution to the total radiative forcing accounts for 3.5% of the total anthropogenic agents [4]. Although aviation does not represent the main driver of the climate change, its contribution to the global warming remains remarkable and is required to be reduced. The minimization of carbon and other gases emissions becomes even more significant when considering that future scenarios of air transportation pollution for 2050 foresee an increase of radiative forcing associated with aviation by more than a factor of 3 over the early 2000s.

NOVEL PROPULSION CONCEPTS IN CIVIL AVIATION

A set of ambitious climate action goals have been defined by all the aviation stakeholders for the short-, medium- and long-term, respectively: improving of fuel efficiency by 1.5% per year between 2009 and 2020; achieving net carbon neutral increase from 2020; reducing global net aviation carbon emission by 50% with respect to 2005 by the year 2050 [5]. On the one hand, researchers and industries in the aerospace field have recently proposed innovative airframe concepts aimed at improving the aerodynamic efficiency to achieve these goals, such as strut-braced wing, blended-wing body, box-wing and double-bubble fuselage aircraft [5]. On the other hand, electric/hybrid-electric powered aircraft and novel propulsion technologies have also been proposed to further reduce carbon emissions through an increased propulsive and/or aero-propulsive efficiency [5]. Among these new propulsion concepts, the most promising one for medium-haul aircraft are represented by Distributed Electric Propulsion (DEP), Boundary-Layer Ingestion (BLI) and Contra-Rotating Open Rotors (CROR) [5]. Examples of these innovative propulsive systems are provided in Fig. 1.1, which depicts the DRAGON[1] DEP con-

---

[1] Distributed fans Research Aircraft with electric Generators by ONERA (DRAGON)

cept [6], the NOVA[2] BLI configuration [7], the full-electric DEP NASA X-57 aircraft [8] and the Safran Engine CROR demonstrator [9], respectively.

(a) *ONERA DRAGON DEP [6]*

(b) *ONERA NOVA BLI [7]*

(c) *NASA X-57 [8]*

(d) *Safran Aircraft Engine CROR [9]*

Figure 1.1: Example of novel propulsion concepts for propulsive efficiency increment and fuel consumption reduction.

URBAN AIR MOBILITY

On a parallel development path, the future of aviation is going to be shaped by the emerging Urban Air Mobility (UAM) market. In fact, the current road traffic situation is expected to become unsustainable in the near future, as a result of the rapid increase of populations in densely populated areas. In response to this scenario, the combined usage of passenger-carrying air-taxis and small-package delivery drones has the potential to improve people's mobility and parcels delivery, with a positive impact on society and environment [10]. In this context, several companies are already developing and prototyping electric Vertical Take-Off and Landing (eVTOL) concepts. These fully electric vehicles, in addition to alleviate road traffic congestion, will also generate zero in-flight gas emissions, thus providing a contribution towards considerably lower fuel fossil emissions [10]. Typical design targets for UAM vehicles are to accommodate up to six passengers or up to 3500 kg of payload, to perform missions up to 180 km of range at maximum altitude and cruise speed of 900 m and 100 m/s, respectively [11]. Moreover, they combine VTOL capabilities and distributed electric propulsion in different ways, each of them having advantages and drawbacks in terms of cruise efficiency, hover power requirements, vehicle control, design simplicity, costs and payload [10]. The most promis-

---

[2] NextGen ONERA Versatile Aircraft (NOVA)

ing approaches are represented by multi-rotor[3], vectored thrust[4] and "lift+cruise"[5] configurations [10]. An extensive, yet not exhaustive, example of recent Urban Air Mobility eVTOL concepts embodying this approaches is depicted in Fig. 1.2.

AIRCRAFT NOISE POLLUTION

While the aforementioned novel aircraft/propulsion concepts can bring benefits to climate change, human health and people's mobility, they also need to be made acoustically friendly before being accepted by the community. Aircraft noise pollution is another important cause of concern associated to civil aviation. Aircraft noise is not only a source of disturbance for those who live around airports, but it also represents a serious danger for the human health and wildlife. According to an analysis conducted by the World Health Organization (WHO) [20], a number of different human diseases and illnesses can be related to noise exposure, such as hearing impairment and pain, stress and sleep disturbance, cardiovascular and psycho-endocrine effects, task performance and productivity reduction, deficits in reading acquisition[6]. Such concerns can limit the expansion of existing airports or the construction of new ones [21], the increment of the number of flights per day and the change in take-off and approach flight paths from and to airports [22]. Concerning UAM, eVTOL vehicles are expected to operate directly overhead and in close proximity to populated areas. Hence, it is as important - if not more than for traditional aviation - that eVTOLs noise do not negatively influence urban communities. If flights for safety and/or medical reasons over urban areas are tolerated by people nowadays, any other high-volume usage of inter-city flights is expected to be disputed because of noise annoyance [10].

Aircraft pollution and noise emissions are regulated through standards to ensure the environment and public health protection [23, 24]. Such standards, applied when an aircraft is acquiring its airworthiness certification and becoming increasingly stringent, require that both the aircraft and its engines meet or fall below designated noise and pollutant emissions levels [25]. Therefore, it is essential that the aforementioned novel airframe/propulsion concepts are sustainable not only in terms of air pollution, but also for what concerns noise emissions, especially in view of the expected growth of aviation. Regarding Urban Air Mobility, well-defined and codified noise regulations do not exist yet, due to the fact that this is a relatively new growing field. However, a preliminary analysis conducted by Uber Elevate sets 62 dB $L_{A_{max}}$ (maximum A-weighted sound pressure level) at 500 ft altitude [10] as noise threshold for eVTOLs operating in proximity of vertiports, which corresponds to about one-fourth of the noise emitted by a four-seat helicopter currently on the market. From these considerations, it is evident that low-noise emissions represent one of the enabling factors for the widespread usage of eVTOL aircraft in the upcoming years.

---

[3] Multiple rotors used to generate lift and thrust force components simultaneously.

[4] Same tilting thrusters used both for hover and cruise conditions.

[5] Separate thrusters used for cruise and hover, respectively, without any thrust vectoring.

[6] Some of these disturbances require a long term exposure over several years (e.g living in close proximity of an airports); others, such as sleep disturbance, can be caused by the occurrence of one single event.

(a) *Airbus CityAirbus [12]* (b) *Volocopter VoloCity [13]*

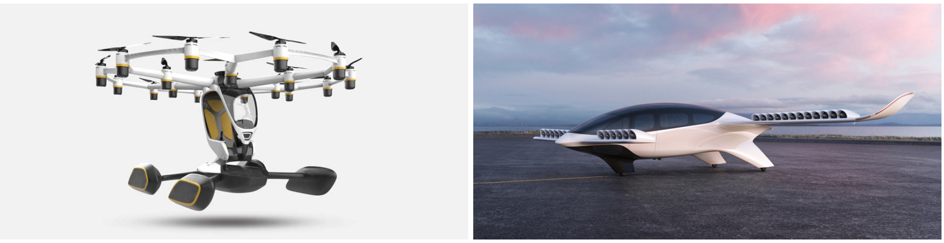

(c) *Lift HEXA [14]* (d) *Lilium Jet [15]*

(e) *Airbus A^3 Vahana [16]* (f) *Bell Nexus 6HX [17]*

(g) *Uber eCRM-003 [18]* (h) *Aurora Pegasus PAV [19]*

Figure 1.2: Recent multi-copter (a)-(c), vectored thrust (d)-(f) and "lift+cruise" (g)-(h) eVTOL concepts for Urban Air Mobility.

1.2. MOTIVATION AND OBJECTIVES

Aircraft noise is a very broad field, which spans from propulsion noise [26] and airframe noise [27], to noise control and management [28]. The first two areas respectively deal with the study of the noise generated aerodynamically by propulsive and non-propulsive aircraft components, while the latter involves the definition of low-noise flight procedures, as well as air spatial and ground management. Due to the wideness of this field, the area of interest of this research needs to be necessarily narrowed. Therefore, the focus of this thesis is restricted to the aeroacoustics of rotors in novel aircraft configurations. More specifically, this research aims to analyze and predict the primary sources of noise associated with two propulsive systems that can be found in eVTOLs and novel aircraft, namely open rotors/propellers and Boundary-Layer Ingestion (BLI) ducted-fans. Due to the unconventional integration of such propulsive systems with the airframe, and the possible different mission profiles characterizing these novel aircraft concepts, the acoustic signature associated to them might substantially differ from that generated by the same systems in traditional helicopters and general aviation aircraft [11]. A plethora of prediction tools and methods have been developed over the past years to compute the noise radiated by conventional aircraft. Although these can still be useful tools for the prediction of the noise associated to the next generation of eVTOLs and aircraft, yet new computational approaches and methods are required to be developed and assessed for the prediction of the noise impact of these innovative aircraft configurations [11]. Hence, the understanding of the change of the aerodynamic noise generation mechanisms associated to the above mentioned propulsion systems, as well as the availability of computational tools to accurately predict the related noise emissions, represents an essential ingredient to quantify their acoustic impact on society, and to drive the development of quieter flying vehicles.

The accurate prediction of open rotors/propellers and BLI ducted-fans aeroacoustics in eVTOLs and novel aircraft configurations is a quite challenging task, due to the fact that such rotors typically operate in highly distorted and non-homogeneous flows, with the rotating blades interacting with strongly non-uniform and turbulent flows. On the one hand, since eVTOLs are generally equipped with small-scale low blade-tip speed propellers/rotors[7], the prediction and simulation of phenomena related to low-Reynolds number flows and boundary-layer transition, such as laminar boundary-layer instability noise and turbulent boundary-layer trailing-edge noise, represent an additional challenge compared to large-scale high-speed rotors (such as turboprops, propfans or those used in conventional helicopter) [11]. On the other hand, intra-rotor and/or inter-rotor (tonal) blade-vortex interaction noise, as well as the impingement of the turbulence generated by upstream rotors and/or airframe components onto the propellers/rotors (responsible for broadband noise generation), are expected to be further relevant contributors to the overall noise emissions for the aforementioned novel aircraft configuration [11]. While analytical, semi-empirical and low-fidelity numerical models can provide quick and computationally inexpensive predictions that are suited for fast trend parameters identification, optimization and mission-level analysis purposes, their results may not be always reliable or poorly predictive for rotors and ducted-fans in unconventional aircraft layouts, due to the inadequacy of such models to fully account for the above mentioned complex flow phenomena. Moreover, additional development of such approaches is needed for UAM and unconventional aircraft vehicles [11]. On the other hand, scale-resolving high-fidelity Computational Fluid Dynamics (CFD) simula-

---

[7] With radius below 0.5 m and blade-tip Mach number $\approx 0.2-0.5$.

tions, such as Large Eddy Simulation (LES) [29], have the capability to capture most of the phenomena of interest, although at an often prohibitive computational cost for industrial applications, making their employment not possible in the early stages of the aircraft design.

In recent years, the Lattice-Boltzmann/Very-Large Eddy Simulation (LB/VLES) method [30–33], coupled with the Ffowcs Williams & Hawkings' (FW-H) acoustic analogy [34], has emerged as a faster scale-resolving alternative to LES for numerical simulations of unsteady turbulent flows of industrial relevance. Due to the fact that LB/VLES approach is low dissipative, compressible and provides an unsteady flow solution, it is intrinsically suited for aeroacoustic simulations, and for the prediction of both tonal and broadband noise generated by eVTOLs and unconventional aircraft layout propulsive systems. Hence, the development of relatively fast[8], accurate and reliable high-fidelity numerical models based on the LB/VLES approach can help to fully identify the noise sources associated to open rotors and ducted-fans in novel aircraft configurations, to predict the related noise emissions and to assess their acoustic nuisance on the community, thus guiding the development of quieter aircraft from the earlier design stages. In view of this, the main aim of this work is:

> *to develop and validate numerical methodologies based on the Lattice-Boltzmann/Very-Large Eddy Simulation approach for the identification, characterization and prediction of the primary sources of open rotors/propellers and ducted-fans noise in non-conventional aircraft configurations.*

As mentioned, due to the large number of new aircraft concepts that have been recently proposed, the field of the present work is restricted to two classes of propulsive systems, namely eVTOL open rotors and Boundary-Layer Ingestion (BLI) ducted-fan systems. The first four studies of the present thesis concern with the development and assessment of numerical models based on the LB/VLES method to predict, analyze and/or reduce the main sources of noise of open rotors in eVTOL configurations. Specifically,

- the first sub-goal is the development and validation of a computational model to predict free-transition turbulent boundary-layer trailing-edge noise at airfoil level, and investigate the impact of the serration flap angle upon add-ons noise reduction effectiveness;
- the second and third sub-goals pertain the development and validation of a LB/VLES computational approach to predict tonal and broadband noise for low-speed open rotors/propellers, with emphasis on the Reynolds number and angular inflow effects;
- the fourth sub-goal deals with the assessment of the LB/VLES numerical method to predict rotor blade-vortex interaction noise, with and without the inclusion of the aerodynamic effects associated to the blade elastic deformations.

On a parallel research path to the study of eVTOL open rotors systems,

---

[8] With respect to the level of fidelity provided by the method.

- the fifth and final sub-goal of this thesis is represented by the analysis, characterization and quantification of the noise generation mechanisms in boundary-layer ingestion turbofan systems by means of the LB/VLES approach.

1.3. OUTLINE OF THE THESIS

After having discussed the research topic, motivations and research objectives in the present introductory chapter, the rest of this thesis is organized into eight additional chapters. Chapter 2 serves as a comprehensive description of the noise sources in open rotors and ducted-fans that are considered in this work, whereas Chapter 3 provides a thorough description of the computational approach used throughout this research project, namely the LB/VLES method coupled with the FW-H acoustic analogy. Chapters 4 to 8, which represent the original contribution of this work, are based on journal articles and conference papers published by the author throughout the PhD research activity. A graphical outline of the these chapters is shown in Fig. 1.3.

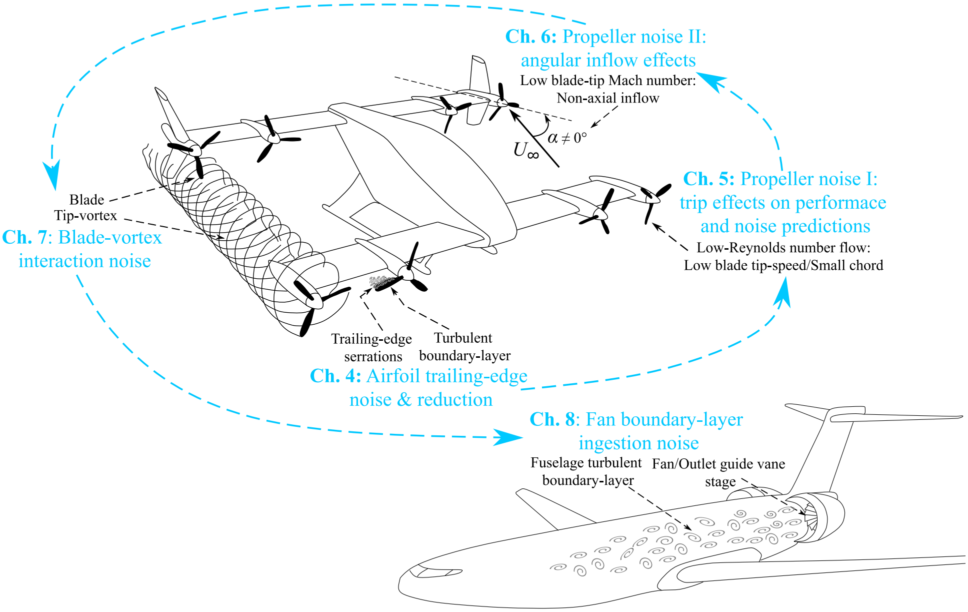

Figure 1.3: Graphical outline of the thesis.

In particular, Chapter 4 focuses on the analysis and prediction of the turbulent boundary-layer trailing-edge noise for a cambered airfoil operating at a moderate Reynolds number and undergoing natural boundary-layer transition, as well as to its reduction by means of serrations retrofitted to the airfoil section at different flap angles. Then, in Chapter 5, the focus is enlarged to prediction of both tonal and broadband noise for a complete propeller geometry operating at low-Reynolds numbers. Next, Chapter 6 addresses the impact of the most elementary source type of inflow distortion, namely the propeller angle of attack or yaw angle, on the physics behind the tonal and broadband acoustic signatures generated by a low blade-tip speed propeller. Chapter 7 deals with noise associated with a more complex type of inflow non uniformity, which is that related to the velocity field induced by the blade tip-vortices, when the rotor/propeller blades interact or pass in close proximity to the tip-vortices released by other blades or by the blade itself (blade-vortex interaction noise). Then, Chapter 8 presents the investigation of the noise generation mechanisms and the quantification of the related noise emissions in a boundary-layer ingesting ducted-fan/OGV (outlet guide vane) embedded propulsion systems. Finally, the main findings of this work are briefly summarized in Chapter 9, along with future perspectives and recommendations related to the present research.

2

SOURCES OF NOISE IN OPEN ROTORS AND TURBOFANS

> *Shall I refuse my dinner because I do not*
> *fully understand the process of digestion?*
>
> Oliver Heaviside

Chapter 1 introduced the problem of aircraft noise pollution, as well as the importance of developing accurate and reliable computational models to predict the associated acoustic impact on the community. This chapter provides a general description of the main sources of noise that characterize the propulsive systems considered throughout this thesis, namely open rotors and turbofans. The chapter is structured as follows. First, the main sources of broadband and tonal noise for open rotors/propellers are described in Sec. 2.1, with emphasis on rotor self-noise, blade-vortex and turbulence interaction noise, and the haystacking of the broadband noise. Then, Sec. 2.2 briefly addresses the additional noise generation and radiation mechanisms, such as in-duct noise propagation and rotor-stator interaction noise, that primarily characterize and differentiate turbofan engines from open rotors.

2.1. NOISE SOURCES IN OPEN ROTORS

PROPELLERS, rotors and fans are open or shrouded rotating blade devices designed to produce an area of low pressure on the suction side of the blades and high pressure on the pressure one, resulting in the generation of thrust for propulsion purposes [26]. In spite of the several aspects that can differentiate between propellers, rotors and fans (i.e. number of blades, blade planform and airfoil shapes, solidity, radius and/or characteristic rotational Mach number), the aerodynamic noise generation mechanisms are nearly the same for all of them. However, the noise sources that are generated and dominate over others depend on the particular application and operating condition [35]. The far-field noise spectrum associated to a rotating blade typically contains both tonal/harmonic and broadband contributions. The former is related to all the periodic and deterministic interactions between the blades and the flow, which typically result in the appearance of tones at discrete frequencies multiple of the blade-passing frequency, while the latter is generally due to random and stochastic interactions with the turbulent flow developing over the blades and/or impinging on them [35]. In some specific situations, the noise signature generated by a rotor/propeller may be quasi-periodic (i.e. it does not repeat exactly with time) and the resulting noise spectrum is characterized by narrow-band noise components with energy content spreading out around discrete frequencies [26]. A typical far-field noise spectrum of a rotor is sketched in Fig. 2.1.

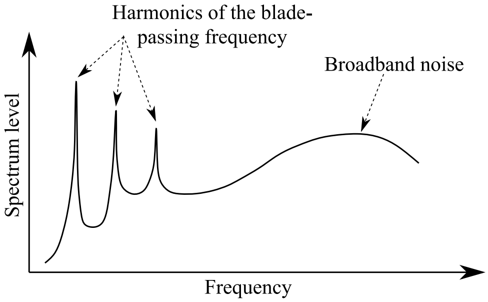

Figure 2.1: Example of a rotor far-field noise spectrum showing both tones at the harmonics of the blade-passing frequency and broadband noise.

The interaction of the blades with the turbulence in the incoming flow (leading-edge or turbulence impingement noise) and/or with their self-generated turbulence (self-noise) are typically recognized as the most relevant mechanisms of rotor broadband noise [36, 37]. Conversely, the turbulence mixing occurring in the rotor wake does not significantly contribute to the broadband noise generation [35]. Regarding the tonal component, steady and unsteady blade aerodynamic loadings (in the blade-fixed reference frame) represent the main sources of noise at relatively low blade-tip Mach numbers [35]. The steady loading noise is associated to the blade pressure distribution component that is steady in the blade-fixed reference frame, which results in a force that periodically varies direction and generates sound for a far-field observer as the blade rotates [35]. For propellers/rotors operating at low blade-tip Mach numbers, this can be a relatively weak source of noise in the presence of the unsteady loading noise, which arises when the propeller operates in a non-uniform distorted flow. Examples of deterministic unsteady loading noise are the blade-vortex interaction noise or the noise generated by a propeller/rotor when it operates at an angle of attack with respect to the free-stream [35]. In addition to loading noise, another important source of tonal noise, especially from moderate to high blade-tip Mach numbers, is represented by the thickness noise, which arises from the periodic displacement of fluid due to the volume of the passing blade [26]. Finally, at transonic or supersonic blade-tip speeds, shocks arise in the volume surrounding blade. Due to the blade rotation, these shocks apparently change for a far-field observer and thus generate sound. In the above, the most relevant rotor/propeller noise generation mechanisms have been briefly outlined. In the following sections, the above mentioned sources of propeller/rotor noise are discussed more in detail, with emphasis on those that are concerned in this thesis.

2.1.1. AIRFOIL BLADE SELF-NOISE

For a rotor operating in a homogeneous non-turbulent flow, Brooks *et al.* [37] identified five airfoil blade self-noise generation mechanisms associated to the interaction between the rotor blade with its self-generated boundary-layer and near-wake: laminar boundary-layer instability noise, turbulent boundary-layer trailing-edge noise, boundary-layer separation/stall noise, trailing-edge bluntness vortex shedding noise and blade tip-vortex noise. The first two mechanisms are relevant to the studies presented in this thesis, while the latter are not directly addressed and are, therefore, only briefly described. A sketch of the above mentioned airfoil self-noise mechanisms is provided in Fig. 2.2.

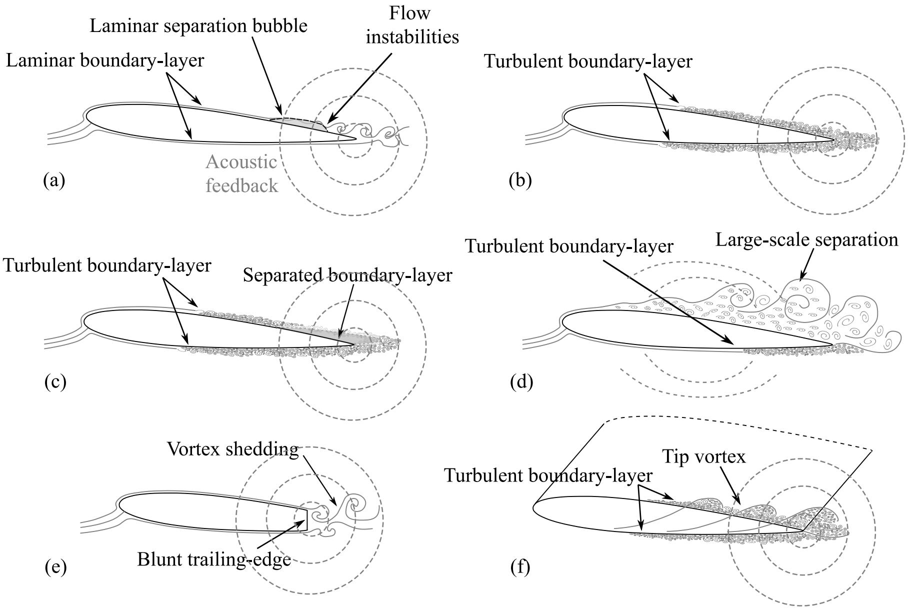

Figure 2.2: Different mechanisms of airfoil blade self-noise: (a) laminar boundary-layer instability noise, (b) turbulent boundary-layer trailing-edge noise, (c) boundary-layer separation and (d) stall noise, (e) trailing-edge bluntness vortex shedding noise and (f) tip-vortex noise. Adapted from Brooks *et al.* [37].

LAMINAR BOUNDARY-LAYER INSTABILITY NOISE

At low-to-moderate chord-based Reynolds numbers (i.e., $5 \cdot 10^4 < Re_c < 5 \cdot 10^5$; $Re_c = Uc/\nu$ with U being the free-stream velocity, c the airfoil chord and ν the fluid kinematic viscosity), airfoils can emit both tonal and broadband noise signatures [38]. Such a flow condition is characteristic of many rotary-wing applications, such as small wind turbines, cooling fans, compressors and rotors of drones/small-size urban air mobility vehicles. Several hypotheses have been proposed by different authors to explain the origin of the tonal noise, which can exceed the broadband noise levels up to 30 dB. Most of those theories invoke an amplification of the sound at certain frequencies, through an aeroacoustic feedback loop, as possible explanation for the tonal noise emissions [39–44].

In the above mentioned Reynolds number regime, the boundary-layer can remain laminar for a relatively large extension of the airfoil chord and possibly separates. The resulting separated shear-layer, depending on the airfoil angle of attack, Reynolds number, airfoil characteristics and incoming flow conditions, can reattach as either a laminar or turbulent boundary-layer and lead to the formation of a laminar separation bubble [43, 45], as depicted in Fig. 2.2(a). The hydrodynamic instabilities (i.e. the Tollmien-Schlichting waves [46]) within the laminar boundary-layer are amplified coherently in the laminar separation bubble and/or separated shear-layer and scattered as sound as they pass a surface discontinuity such as the airfoil trailing-edge. Then, the resulting acoustic disturbances can travel upstream and trigger the generation of further flow instabilities, which reinforce the sound radiation. Hence, an aeroacoustic feedback loop between the hydrodynamic and acoustic waves can be closed at those frequencies at which the phase of the upstream-traveling acoustic waves matches the phase of the hydrodynamic waves convected downstream. This can lead to a significant noise increment when the laminar separation bubble is sufficiently close to the trailing-edge [47], with narrowband tones over a broadband hump featuring the corresponding far-field noise spectrum for bi-dimensional airfoils [38]. In particular, the broadband noise is attributed to the scattering of incoherent eddies of different sizes and strengths, whereas the tonal noise emissions are related to the scattering of relatively coherent and strong vortical disturbances amplified through the feedback loop [38]. However, no definitive consensus on the position, length and physics of the activation of the aeroacoustic feedback loop has been reached yet.

For rotor operating at low-Reynolds numbers, the rotation of the blades introduces an additional modulation of the actual frequencies related the laminar boundary-layer instability noise radiation. Moreover, spanwise variable flow conditions experienced by the propeller blade can play against the effective establishment of an aeroacoustic feedback loop. In fact, a high frequency broadband hump has been reported in the far-field noise spectrum in the presence of a laminar separation bubble on the blade surface in previous experimental studies involving rotating blades, with [47] and without [47–49] the emergence of a strong tonal content strictly ascribable to the acoustic feedback loop. The presence of a broadband hump with no tonal contribution was associated to the mere trailing-edge scattering of instability waves without the occurrence of a proper acoustic feedback [47].

TURBULENT BOUNDARY-LAYER TRAILING-EDGE NOISE

At higher chord-based Reynolds numbers ($Re_c > 5 \cdot 10^5$), the boundary-layer over the rotor blades completely transitions from a laminar into a turbulent state, as illustrated in Fig. 2.2(b). Hence, the boundary-layer is no longer characterized by periodic coherent vortical structures, but rather by a broader distribution of eddies of different sizes and strengths compared to the previous mechanism. Similarly to the laminar boundary-layer instability noise, the pressure fluctuations within the turbulent boundary-layer are scattered as sound when they pass the trailing-edge [37], because of the Kutta's condition.[1] However, since the boundary-layer is now fully developed and characterized by a random and chaotic distribution of vortices, the resulting far-field noise spectrum is broadband in nature. Turbulent boundary-layer trailing-edge noise is recognized as the most important aerodynamic noise source for large wind-turbines, and as one of the most relevant broadband noise contributors for propellers and rotors operating in a homogeneous stationary flow [37, 50].

The scaling law of the turbulent boundary-layer trailing-edge noise can be shown by following the approach of Ffowcs Williams & Hall [51]. They idealized the airfoil trailing-edge noise problem considering a uniform turbulent flow interacting with a semi-infinite plate of zero thickness, as depicted in Fig. 2.3. The semi-infinite approximation holds as long as the airfoil chord is much larger than the wavelength of the radiated acoustic waves. In Fig. 2.3, U is the mean velocity of the flow which passes the trailing-edge with a sweep angle γ, $\mathbf{y}$ and $\mathbf{x}$ are the source and observer positions, b is the flat-plate span, while φ and θ are the angles of the observer measured from the trailing-edge and chord-line, respectively.

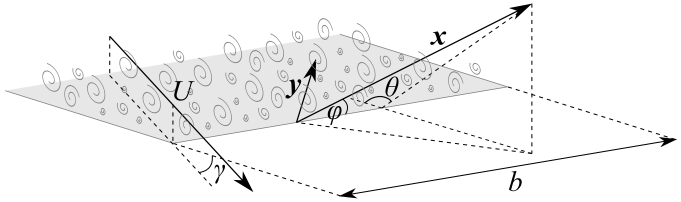

Figure 2.3: Idealization of the turbulent boundary-layer trailing-edge noise problem through the semi-infinite flat plate approximation. Adapted from Glegg and Devenport [35].

Ffowcs Williams & Hall characterized the acoustic pressure p' associated to scattering process of the turbulent fluctuations at the trailing-edge in terms of Fourier transformed solution of the Lighthill's equation, and used a tailored Green's function to fulfill the rigid wall boundary condition on the semi-infinite plate [35]:

$$\tilde{p}'(\mathbf{x},\omega) = \int_V \frac{\partial^2 \tilde{G}_T(\mathbf{x}|\mathbf{y},\omega)}{\partial y_i y_j} \tilde{T}_{ij}(\mathbf{y},\omega) \mathrm{d}\mathbf{y}, \tag{2.1}$$

where G_T is Green's function of the semi-infinite flat-plate problem, T_{ij} is the Lighthill's stress tensor, V is the volume of integration surrounding the turbulent flow around the

---

[1] Due to the Kutta's condition at the traling-edge, a very localized pressure disturbance convecting over the trailing-edge needs to the balanced by another pressure fluctuation, which ultimately propagates as sound, in such a way that their net sum is equal to zero.

semi-infinite flat plate, the tilde sign indicates a Fourier transform, while ω is the angular frequency. By introducing far-field and low-Mach number assumptions, they obtained that the far-field noise spectrum S_{pp} approximately scales as [35, 51]:

$$S_{pp}(\mathbf{x},\omega) \sim \frac{\rho_0^2 U^3 u^2 L b \sin(\varphi)\cos^2(\theta/2)\cos^2(\gamma)}{|\mathbf{x}|^2 c_\infty} S(\omega), \tag{2.2}$$

where $S(\omega)$ is the normalized spectral shape function, ρ_0 is the undisturbed fluid density, u represents the velocity scale of the turbulent fluctuations (which scales as U), while L is the length scale of the turbulence (that is typically the boundary layer displacement thickness at the trailing-edge, δ^*).

Equation (2.2) highlights different features of the turbulent boundary-layer trailing-edge noise. First, trailing-edge noise is inversely proportional to the square of the observer distance $|\mathbf{x}|$ from the edge, and linearly proportional to the airfoil span b and turbulent length scale L. Moreover, it scales with the fifth power of the flow velocity: the presence of a geometrical singularity such as the blade trailing-edge enhances the efficiency of the noise radiated by the turbulence, which would otherwise scale with the eighth power for unbounded flows[2] [53]. Another important characteristic revealed by Eq. (2.2) is that the trailing-edge noise manifests a cardiod directivity on a plane normal to the airfoil span ($\varphi = 90°$), as highlighted by the $\cos^2(\theta/2)$ term and depicted in Fig. 2.4(a). Hence, the noise radiation is maximum upstream, weak downstream and negligible along the airfoil wake. It is worth mentioning that, since the sound emitted by the suction side is in anti-phase with respect to that emitted by the pressure one, a destructive interference actually takes place upstream the airfoil leading-edge in practical applications for airfoils of finite chord [54]. Since the boundary-layer developing on the suction side is typically characterized by larger turbulent length scales than on the pressure one, the former contributes more at lower frequencies, while the pressure side contribution tends to dominate the broadband noise radiation at higher frequencies, as qualitatively sketched in Fig. 2.4(b).

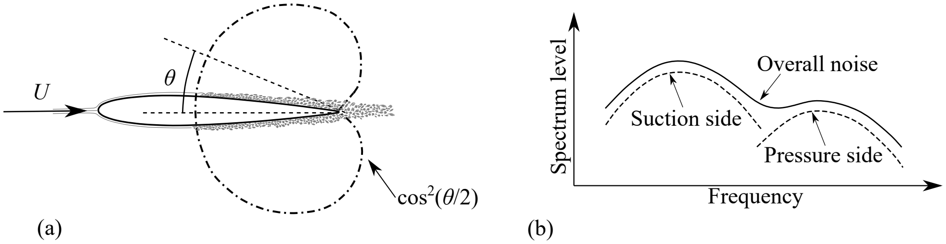

(a) (b)

Figure 2.4: Cardiod trailing-edge noise directivity for an observer in a plane normal to the trailing-edge (a); adapted from Glegg and Devenport [35]. Sketch of a typical trailing-edge far-field noise spectrum with relative contributions from the suction and pressure sides (b); adapted from Pröbsting [55].

A final relevant result from the Ffowcs Williams & Hall's analysis is that the far-field noise is proportional to a $\cos^2(\gamma)$ term, which indicates that the turbulent pressure fluc-

---

[2] To be rigorous, trailing-edge noise scales as $U^4 M$, while unbounded turbulence as $U^4 M^4$ (where M is the flow Mach number) [35]. Therefore, the noise generated by an eddy scattered at the trailing-edge is $\mathcal{O}(M^{-3})$ larger than that associated to the same eddy away from the edge [52].

tuations are scattered more efficiently when the convected eddy passes the trailing-edge perpendicularly to it (i.e. $\gamma = 0°$). Hence, a possible way through which trailing-edge noise can be reduced is by sweeping the trailing-edge with respect to the flow, namely by means of serrations [56], as illustrated in Fig. 2.5. Trailing-edge serrations are widely adopted for broadband noise reduction of wind turbines nowadays [56], and they are recently spreading to low-speed propeller applications as well [57, 58]. However, their benefit might be partially counteracted by the increment of the length of the serrated-edge compared to the straight one [35].

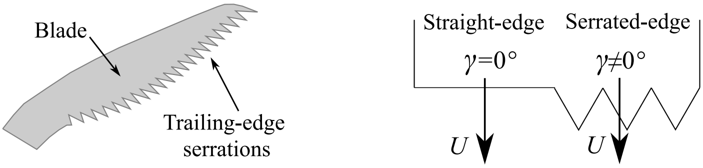

Figure 2.5: Example trailing-edge serrations applied to a propeller blade. Adapted from van der Velden [54].

BOUNDARY-LAYER SEPARATION AND STALL NOISE

In the previous two airfoil self-noise mechanisms, the boundary-layer is assumed to remain attached to the airfoil surface when approaching the blade trailing-edge. However, at relatively high values of the airfoil incidence, the flow can separate upstream of the trailing-edge on the suction-side and lead to the shedding of vortices, Fig. 2.4(c). The associated (boundary-layer separation) noise signature is quasi-tonal and characterized by a spectral hump at mid-to-high frequencies, due to the scattering of relatively small and coherent vortices separating from the airfoil surface [37]. If the angle of attack is further increased, the local airfoil section can experience a deep stall condition, with large-scale vortical structures separating from the airfoil surface, Fig. 2.4(d). As a result, low-frequency stall noise is radiated by the airfoil as a whole [37]. This source of noise can be mitigated by operating the blade at conditions away from the stall or through blade pitch control strategies.

TRAILING-EDGE BLUNTNESS VORTEX SHEDDING NOISE

When the ratio t/δ^* between the trailing-edge thickness, t, and the boundary-layer displacement thickness, δ^*, exceeds the critical value of 3.3, a von Kármán vortex shedding from a blunt trailing edge can take place [59], as shown in Fig. 2.4(e). The blunt trailing-edge promotes a large scale vortex shedding within the near wake that is limited to a narrow range of frequencies, since the dominant turbulent length scale is determined by the trailing-edge thickness. As a consequence, the resulting far-field noise spectrum is tonal or quasi-tonal, depending on the t/δ^* ratio [59]. Due to the large spanwise coherence of the vortices being shed from the blunt trailing-edge, the resulting noise can dominate over the turbulent boundary-layer trailing-edge noise. However, this source of noise can be reduced by designing a blade trailing-edge such that t/δ^* is below 3.3 under the expected blade operating conditions.

Tip-vortex noise

A final mechanism of airfoil self-noise is that related to the tip-vortex, which is generated due to the pressure difference between the suction and pressure sides at the tip of a blade. The tip-vortex, characterized by a thick viscous turbulent core, wraps-up around the blade tip, and the associated turbulent structures are scattered at the trailing-edge of the blade tip in a similar manner to the turbulent boundary-layer trailing-edge noise [37], as illustrated in Fig. 2.4(f). This source of noise may be reduced by limiting the interaction between the suction and pressure sides at the blade tip by means of optimal tip shapes or winglets.

2.1.2. Leading-edge/turbulence-impingement noise

Another broadband noise generation mechanism that involves the interaction of a rotor blade with the upstream generated inflow turbulence is the so called leading-edge noise or turbulence-impingement noise. This is an important source of noise in several aeronautical applications, such as turbofan engines and rotorcraft configurations undergoing blade-wake interactions. Although the radiated noise is largely dependent upon the characteristics of the incoming turbulent flow interacting with the leading-edge and the blade geometry, still some relevant results can be extracted from the theory under the assumption of a thin-plate immersed in a homogeneous turbulent flow. Following Glegg and Devenport [35], the spectral density of the far-field acoustic pressure radiated from a flat-plate airfoil of large span can be expressed as:

$$S_{pp}(\mathbf{x},\omega) \approx \left(\frac{\pi\omega x_2}{c_\infty r_e^2}\right)^2 \frac{S_{FF}\left(\omega, k_1^{(o)}, k_3^{(o)}\right)}{(2\pi)^4}, \tag{2.3}$$

where ω is the angular frequency, c_∞ is the free-stream speed of sound, r_e is observer distance with Prandtl-Glauert correction and x_2 is the observer coordinate in the direction normal to the blade (positive upwards and referred to the leading-edge, Fig. 2.6). Moreover, S_{FF} is the wavenumber-frequency spectrum of the unsteady blade loading produced by the airfoil, and $k_1^{(o)}$ and $k_3^{(o)}$ are the streamwise and spanwise acoustic wave number with Prandtl-Glauert correction.

Considering the von Kármán turbulence model for the planar wavenumber spectrum within the definition of S_{FF} and an observer in the mid-span plane, Eq. (2.3) can be written as [35]:

$$S_{pp}(\mathbf{x},\omega) \approx \frac{4}{9\pi}\left(\frac{\rho_0^2 U \overline{u^2} b M}{\pi k_e^2 r_e^2 (1+M)}\right)\left(\frac{(\omega/k_e U)^2}{\left[1+(\omega/k_e U)^2\right]^{7/3}}\right)\cos^2(\theta_e/2), \tag{2.4}$$

where b is the blade span, M is the Mach number, $\overline{u^2}$ and k_e are the velocity variance and wavenumber scale of the largest eddies, respectively, and $\theta_e = \tan^{-1}\left(x_2\beta/x_1\right)$, with x_1 being the streamwise observer coordinate (positive downstream and referred to the leading-edge, Fig. 2.6) and $\beta = \sqrt{1-M^2}$. Since $\overline{u^2}$ scales as U^2, the spectral density scales at the forth power of the flow velocity. If the spectral level is considered in place of the spectral density, a term $k_e U$ (related to the frequency bandwidth) would appear on the right hand side of Eq. (2.4), revealing that the turbulence-impingement noise scales with the fifth power of the flow speed. Moreover, under the assumption of semi-infinite plate, the noise radiation follows a cardiod directivity with the maximum and minimum noise radiation achieved respectively downstream and upstream the airfoil, as sketched in Fig. 2.6. These two results represent two significant differences with respect to the typical dipole scaling law and directivity for an acoustically compact surface (i.e. for vortical disturbances that are much larger than the chord of the blade), according to which the associated noise scales with the sixth power of the flow velocity and is radiated as $\sin^2(\theta_e)$. Finally, the spectral level (i.e. with bandwidth correction) further scales as $b/k_e{\sim}bL_f$, where L_f is an integral length scale of turbulence. Hence, the leading-edge noise can be generally reduced by reducing the turbulence integral length scale. However, as pointed out in Ref. [35], this would also modify the shape of the far-field noise spectrum, with an effective reduction of the noise levels taking place at low frequency and a general increment of the spectral content at high frequencies.

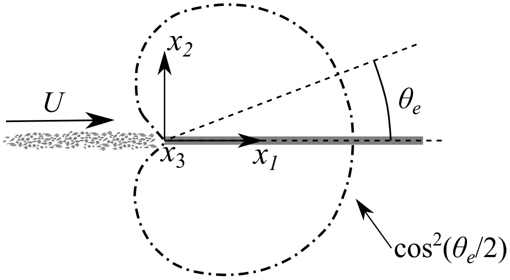

Figure 2.6: Sketch of leading-edge/turbulence impingement noise problem and directivity for a semi-infinite plate.

2.1.3. Loading noise

As previously mentioned, the loading noise is generated by the steady and unsteady pressure on the surface of a rotating blade. For an external observer, a force that is steady in the blade-fixed reference frame has a time-varying component projected in the direction of the observer, which is perceived as noise. In addition, a time variation of the loading in the blade-based reference is also a source of unsteadiness and, thus, of noise, regardless the fact that the observer is inside or outside the rotating reference frame. For propellers/rotors operating a low blade-tip Mach numbers, the loading noise represents the major contributor to the overall noise emissions [35]. Broadly speaking, all the aforementioned airfoil noise generation mechanisms, which involve the interaction of the blade surface with self-generated or ingested turbulence, are responsible for the generation of unsteady surface pressure fluctuations in the reference frame rigidly connected with the blade. Therefore, they can be generically considered as broadband loading noise sources. However, in this subsection, loading noise is strictly intended as the tonal noise associated to steady forces and/or unsteady loadings, with the latter associated to rotors operating at an angle of attack, in non-uniform distorted inflows and/or undergoing blade-vortex interactions.

In order to draw interesting considerations on the tonal loading noise of rotors operating at subsonic blade-tip speeds, it is useful to consider the case of a rotating force, as depicted in Fig. 2.7, and refer to the analytical frequency-domain expression of the far-field noise from a compact rotating dipole. In Fig. 2.7, a periodic force of magnitude $F(t)$ is generated by a blade element at the radial position r and tilted by an angle γ with respect to the rotor axis e_z. The observer position, $\mathbf{x}$, is defined by its distance R from the origin and by the angles θ and φ, while Mc_0 represents the tangential velocity of the source, where $M = \Omega r / c_0$ is the tangential Mach number, Ω the angular velocity of the source and c_0 the undisturbed speed of sound.

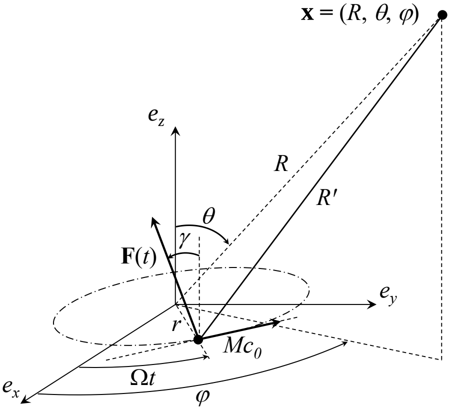

Figure 2.7: Problem definition for far-field tonal loading noise. Adapted from Roger and Moreau [60].

Under the assumptions of compact source, far-field observer and B equally spaced blades, the complex-valued sound pressure amplitude at the m-th harmonic of the angular Blade-Passing Frequency ($mB\Omega$) read as[3] [61]:

$$P_{mB}(\mathbf{x}) = \frac{imB^2\Omega}{4\pi c_0 R} \sum_{s=-\infty}^{\infty} F_s(r)\, e^{-i(mB-s)\frac{\pi}{2}}\, e^{i(mB-s)[\varphi-\Omega_s R/c_0]} \times J_{mB-s}(mBM\sin(\theta)) \left[-\frac{mB-s}{mB}\frac{\sin(\gamma)}{M} + \cos(\theta)\cos(\gamma)\right], \tag{2.5}$$

where $\Omega_s = mB\Omega/(mB-s)$, $F_s(r)$ are the complex-valued coefficients of the Fourier series of the periodic force, while J_{mB-s} are the Bessel's functions of the first kind of order $mB-s$. Equation (2.5) is characterized by several properties [61]. First, it shows that a periodic blade force produces a discrete-frequency noise at the blade-passing frequency ($B\Omega/2\pi$) and its harmonics, where each tone is the sum of free-field radiation modes. Moreover, the magnitude of each mode is proportional to the blade-harmonic loading F_s weighted by the Bessel's function J_{mB-s}, as a consequence of the Doppler effect introduced by the source motion with respect to the observer. Each radiation mode rotates

---

[3] Considering a rotor with B equally spaced blades, only the harmonics of the blade-passing frequency survive in the far-field, due to constructive-destructive interference between the acoustic signatures generated by the different blades. Each blade generates noise at harmonics multiple of the rotational frequency. However, if the blades are evenly spaced and the associated force is periodic, the contributions at the harmonics not multiple of the blade-passing frequency are canceled out.

with an equivalent speed Ω_s. For $s \neq mB$, the mode is called spinning mode and has no contribution on the rotor axis and for angles such that the quantity in the square brackets is zero. For $s = mB$, the mode is called symmetric mode and it is the most efficient one due to the favorably weighting of the Bessel's function J_0. Symmetric modes radiate along the rotor axis and are characterized by a vanishing directivity in the rotor plane. The case $s = 0$ (steady-loading noise) corresponds to the noise radiated by the steady component of the force and is the only contribution related to the thrust generated by the rotor. The steady-loading noise is typically smaller than the unsteady loading one for significant values of unsteady loading harmonics, since the Bessel's function corresponding to the steady loading component can assume much lower values compared to that modulating the unsteady loading harmonics. Indeed, the steady force F_0 is weighted by $nJ_n(nX)$, with $n \neq 0$ and $X = M\sin(\theta)$, while the first order blade-loading harmonics $F_{\pm1}$, for instance, are weighted by the factors $nJ_{n\pm1}(nX)$ [60]. These efficiency factors are shown in Fig. 2.8 as functions of n and for five different values of $X = 0.1, 0.3, 0.5, 0.7, 0.9$.

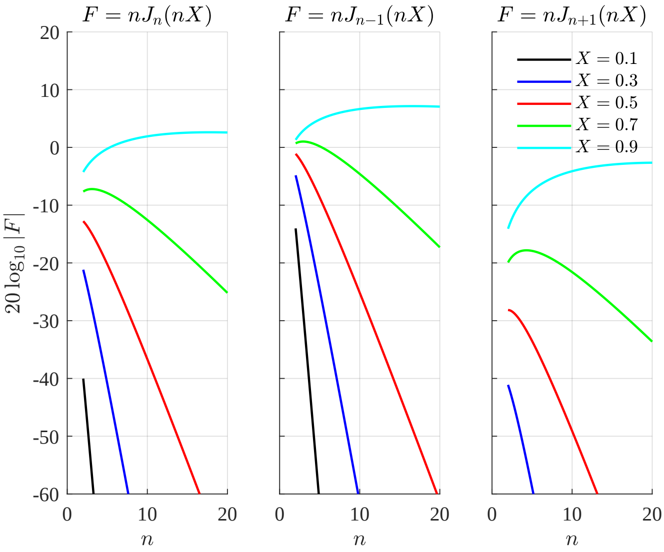

Figure 2.8: Weighting factors of the steady-loading noise (left) and of the first order blade-loading hamonics - $s = -1$ (center) and $s = +1$ (right) - of the unsteady-loading noise. Adapted from Roger and Moreau [60].

From Fig. 2.8 it can be inferred that, except for the inefficient $s = +1$ case, the efficiency associated to the unsteady loading noise ($s = -1$) is larger than that of the steady loading noise ($s = 0$), especially at low Mach numbers (i.e. for low values of X). Hence, the steady loading noise is a very efficient noise generation mechanism mainly at high blade-tip Mach numbers or in absence of significant blade unsteady loadings. Moreover, the rotor-locked noise has a zero radiation on the rotor axis, $|J_n(0)| = 0$ for $n > 0$, and in the area in front of the rotor for angles such that $\cos(\theta) = \tan(\gamma)/M$. Therefore, in the case that significant loading noise levels are perceived along the rotor axis, these are certainly related to the presence of unsteady forces. Finally, as a result of the Doppler effects, a given loading noise harmonic of order s contributes to the noise at the m-th blade-passing harmonic such that $s/(1+M|\sin(\theta)|) \leq mB \leq s/(1-M|\sin(\theta)|)$. Hence, as the rotational Mach number increases, the transfer of energy between frequencies of the blade loading and far-field noise farther apart from each other is possible.

2.1.4. BLADE-VORTEX INTERACTION NOISE

A particular case of deterministic/tonal unsteady loading noise is represented by the blade-vortex interaction (BVI) noise. When a rotor blade passes through or in close proximity of a blade tip-vortex, the blade experiences a rapid change of the local angle of attack and an impulsive change of the aerodynamic loading [62]. Blade-vortex interaction primarily occurs during descent flights or maneuvers at low advance ratios, during which the rotor wake is washed back into the plane of the rotor itself or can be ingested by neighboring rotors (e.g. in multi-rotor electric Vertical Take-Off and Landing - eVTOL - vehicles). BVI generates a loud thumping sound that is very impulsive and annoying. Thus, this type of noise is responsible for a significant disturbance towards the community and is one of the primary causes limiting the use of rotorcraft in urban environments [63].

A simple analytical model that highlights the most important aspects concerning BVI noise can be derived by considering the idealized situation sketched in Fig. 2.9, in which a three-dimensional vortex line of length L, circulation Γ, and convected with velocity U in the y_1 direction, interacts with the leading-edge of the blade at an angle Φ_v and with a vertical displacement or blade-vortex miss-distance h.

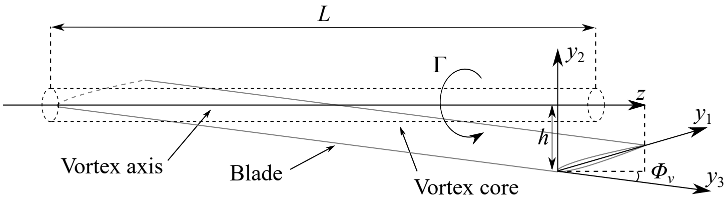

Figure 2.9: Sketch of a blade-vortex interaction. Adapted from Glegg and Devenport [35].

Following Glegg and Devenport [35], the Fourier transformed acoustic pressure from a leading-edge interaction can be approximately written as:

$$\tilde{p}(\mathbf{x},\omega) \approx \left(-\frac{i\omega\pi x_2 e^{ik_o r_e - ik_o M x_1}}{c_\infty r_e^2}\right)\frac{1}{2}\rho_0 c\,\tilde{\tilde{w}}_2\left(k_1^{(o)},k_3^{(o)}\right)\Lambda\left(k_1^{(o)},k_3^{(o)},\omega,M\right), \tag{2.6}$$

where k_o is the acoustic wavenumber with Prandtl-Glauert scaling, c is the blade chord, Λ is the non-dimensional blade acoustic response function for the acoustic far-field, while $\tilde{\tilde{w}}_2$ is the upwash velocity spectrum. All the remaining quantities have been defined in the above. For a blade-vortex interaction, $\tilde{\tilde{w}}_2$ can be expressed as [35]:

$$\tilde{\tilde{w}}_2(k_1^{(o)}, k_3^{(o)}) = \frac{i\Gamma L\left(k_3^{(o)}\sin\Phi_v - k_1^{(o)}\cos\Phi_v\right)e^{-k_{13}^{(o)}h}}{(2\pi)^2 2k_{13}^{(o)}} \times \left(\frac{\sin\left((k_1^{(o)}\sin\Phi_v + k_3^{(o)}\cos\Phi_v)L/2\right)}{(k_1^{(o)}\sin\Phi_v + k_3^{(o)}\cos\Phi_v)L/2}\right), \tag{2.7}$$

with $k_{13}^{(o)} = \sqrt{k_1^{(o)2} + k_3^{(o)2}}$.

From the previous equation, it is possible to derive a condition on the angle Φ_v for which blade-vortex interaction noise is significant, namely $\tan\Phi_v < \beta M$. If the interaction angle do not fulfill this conditions, the vortex interaction with the blade leading-edge would move subsonically along the blade and no significant noise is radiated [35]. Hence, BVI noise can be reduced by increasing Φ_v. This explains why the most severe blade-vortex interaction condition in terms of noise radiation occurs when the tip-vortex axis is nearly parallel to the blade leading-edge [63]. Conversely, when the axes of the tip-vortex and blade are perpendicular and lying on parallel planes, the blade-vortex interaction is significantly less intense and impulsive, and the resulting noise is characterized by a broadband content due to continuous interaction between the blade and the turbulent viscous core of the vortex [64]. Moreover, from Eqs. (2.6)-(2.7), it can be further deduced that the reduction of the vortex strength Γ and the increment of the blade-vortex miss-distance h both play in favor of a decrement of the noise associated to a blade-vortex interaction [35].

For traditional helicopter configurations, the above mentioned aspects may be achieved through a proper modification of the blade tip geometry and/or the implementation of blade loading control strategies (e.g. higher-harmonic control, individual blade control, active control flap or active twist rotor) to favorably alter the strength and the trajectory of the tip vortices with respect to the rotor blades [63, 65, 66]. For novel multi-rotor eVTOL vehicles, in which the blade-vortex interaction can occur between a certain rotor and the tip-vortices released by the neighboring rotors, a possible BVI noise mitigation strategy is to adopt specific flight trajectories such that the ingestion of a rotor wake by another one is minimized [67].

2.1.5. HAYSTACKING OF BROADBAND NOISE

For a propeller/rotor operating in turbulent inflow, the impingement of the incoming turbulence on the blade leading-edge can be a considerably source of noise, as discussed in Sec. 2.1.2. When the scales of turbulence are sufficiently small, so that the resulting pressure fluctuations on the blades are uncorrelated and characterized by the same statistics, the resulting noise spectrum is broadband. However, if the length scale of turbulence is sufficiently large and the vortical structures are elongated in the streamwise direction, it is possible that the same structure is cut multiple times by successive blades. This can result in blade-to-blade unsteady loading correlation that generates a quasi-periodic acoustic signature and a noise spectrum with broadband peaks in proximity of multiples of the blade-passing frequency [35]. This phenomenon is referred to as haystacking of broadband noise. In particular, the condition for the haystacking is that the blade-passing frequency ΩB is much higher than axial velocity U_a divided by the axial length scale of the turbulence L_a, namely $\Omega B L_a / U_a \gg 1$ [35].

Figure 2.10 illustrate the pressure signal and the corresponding noise spectrum for a rotor interacting with a small or large vortical structure, respectively. The case reported in Fig. 2.10(a) is representative of a situation in which the time scale of the interaction is relatively short, due to the small axial length scale and high axial flow velocity compared to the rotational speed of the rotor. As a result, some of the blades chop the eddy producing a pressure signature characterized by few pulses with intensity modulated by the varying strength of the eddy [35]. The resulting spectrum is quasi-broadband. Conversely, if the flow speed is sufficiently slow and the axial length scale of the eddy is large enough, compared to the rotational frequency, more blades can interact with the same vortical structure. This leads to the generation of a quasi-periodic pressure signal, with several pulses spaced by the blade-passing interval, whose spectrum is characterized by narrower peaks around the blade-passing frequency (BPF) [35], as depicted in Fig. 2.10(b).

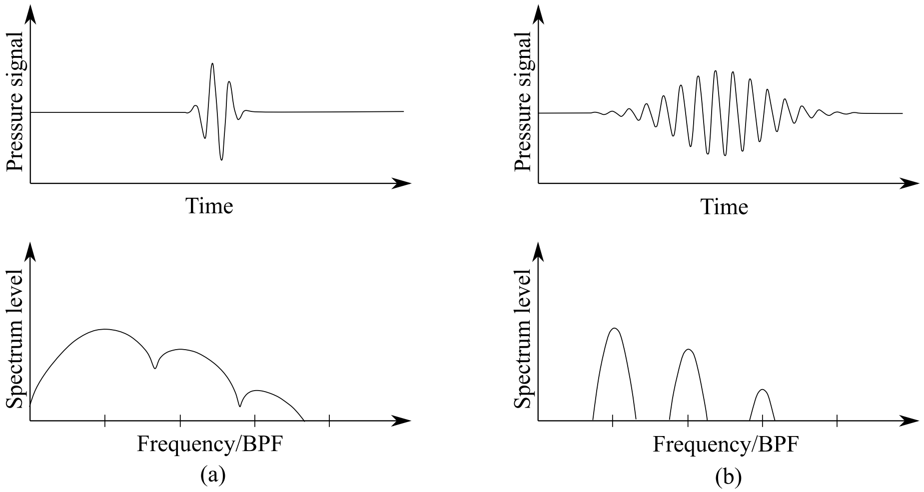

Figure 2.10: Example of pressure signal and spectrum from rotor blades interactions with a single small (a) and large (b) vortical structures. Adapted from Glegg and Devenport [35].

2.1.6. THICKNESS NOISE

When a rotor blade rotates, its volume generates a fluid displacement that is unsteady for an external observer and, thus, is perceived as noise. The resulting acoustic signature is a distinct pulse as the blade moves towards the listener. This source of tonal noise is referred to as thickness noise, since it is related to the thickness of the blade as it is shown in the following. A convenient way to highlight this aspect is to consider the thickness noise term from the Ffowcs Williams & Hawkings's (FW-H) equation [35]. Anticipating a result that will be introduced in Chapter 3, the thickness noise from the FW-H equation for an impermeable moving surface reads as:

$$p'_T(\mathbf{x},t) = \frac{\partial}{\partial t}\int_S \left[\frac{\rho_0 \mathbf{v}\cdot\hat{\mathbf{n}}}{4\pi r\,(1-M_r)}\right]_{\text{ret}} \mathrm{d}S(\mathbf{y}), \tag{2.8}$$

where $\mathbf{x}$ is the observer position, $\mathbf{y}$ is the source position on the integration surface S moving at the velocity $\mathbf{v}$, $\hat{\mathbf{n}}$ is the outward directed normal to the surface, M_r is the source Mach number projected in the direction of the observer and $r = |\mathbf{x}-\mathbf{y}|$. The subscript ret denotes that the integral needs to be computed at the retarded time $\tau = t - \left|\mathbf{x}-\mathbf{y}(\tau)\right|/c_0$, with t being the observer time and c_0 the undisturbed speed of sound. For thin blades, the integral over the blade surface S can be replaced by the integral over the blade planform Σ on the rotor plane, as follows [35]:

$$p'_T(\mathbf{x},t) = -\frac{\partial}{\partial t}\int_\Sigma \left[\frac{\rho_0 \mathbf{v}\cdot\nabla h}{4\pi r\,(1-M_r)}\right]_{\text{ret}} \mathrm{d}\Sigma(\mathbf{y}), \tag{2.9}$$

where $\nabla h = \nabla y_+ - \nabla y_-$, with y_+ and y_- respectively denoting the upper and lower coordinates of the blade such that the blade thickness is defined as $h = y_+ - y_-$. Equation (2.9) clearly highlights the dependence of the contribution of the blade thickness to the magnitude of the thickness noise source [35].

The acoustic efficiency of the thickness noise is larger than that of loading noise. Indeed, thickness noise scales as the fourth power of the flow velocity, against the sixth power scaling for the loading noise for acoustically compact sources [35]. Thickness noise is typically important at high blade-tip Mach numbers (i.e. above 0.7). Moreover, it is primarily directed along the rotor plane and can become significant for a rotor with a high number of blades for which the load of each blade can be relatively low. However, thickness noise is also often negligible for highly loaded rotors and/or in presence of highly efficient unsteady loading noise sources, and can be generally decreased by reducing the thickness/volume of the blades in the tip region [35] (thickness noise is reduced by 6 dB for every halving of the blade thickness).

2.2. NOISE SOURCES IN TURBOFANS

The previous section focused on the description of the primarily sources of aerodynamic noise in open rotors. However, in some aeronautical applications, such as high bypass-ratio turbofan engines, the previous sources of rotor noise can take place in a ducted environment. The main difference with respect to open rotors is that, for ducted fans/rotors, the propagation of the aeroacoustic sources is significantly modified by the presence of the duct. The duct causes a reorganization of the acoustic field of the rotor sources through successive reflections on the duct walls and generates particular guided waves [68]. Hence, these waves propagates outside the ducted environment in the far-field undergoing a diffraction process at the duct exit [68]. Moreover, in a turbofan configuration a stator is always positioned in the bypass duct downstream the fan in order to convert the kinetic energy in the swirling flow in the fan wake into additional thrust. The interaction of the fan blade wakes with the downstream stator (or Outlet Guide Vanes, OGV) represents an additional source of noise.

Figure 2.11 depicts the primarily sources of noise in the bypass duct of a turbofan engine. Note that additional noise sources are present when considering a complete turbofan engine, such as compressor and turbine noise, jet noise and combustion noise. However, the description of these sources is left out from the present discussion since they are not considered in this thesis. The first source of noise in a turbofan engine is represented by the fan self-noise. As for open rotors, the fan of a turbofan engine generates both tonal and broadband noise via several mechanisms, such as [35]: loading and thickness noise; unsteady loading noise and leading-edge noise through the interaction with the inflow/boundary-layer turbulence, respectively; tip flow noise due to the interaction of the fan blade tip with the flow between the tip and the duct wall; trailing-edge noise associated to the scattering of the turbulent boundary-layer developing over the fan blades; and quadrupole noise due to the appearance of shocks on the rotor blade at transonic blade-tip Mach numbers. Moreover, the interaction of the fan blade wakes with the downstream stator vanes is another source (typically the dominant one) of tonal and broadband noise for high bypass-ratio turbofan engines. However, due to the presence of the duct, only some acoustic modes at certain frequencies can propagate through the duct and radiate to the far-field outside the engine.

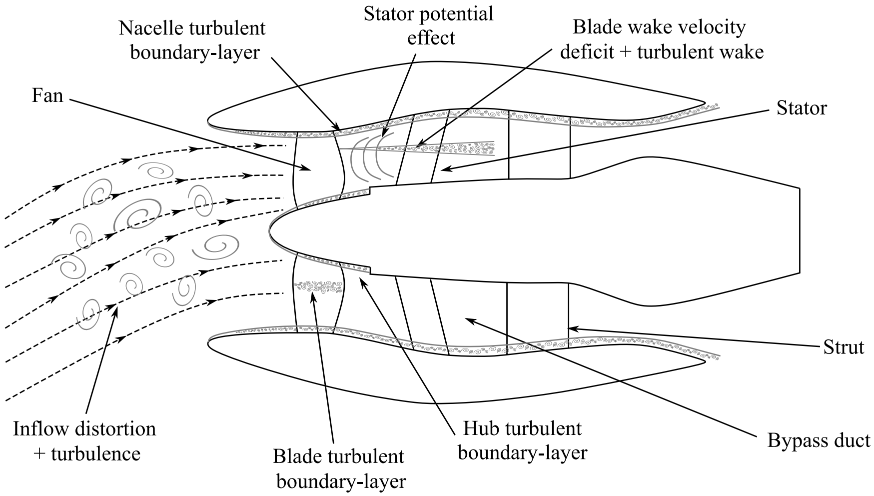

Figure 2.11: Sketch of a high bypass-ratio turbofan engine and primarily aerodynamic noise sources. Adapted from Moreau [69]

Before discussing the above mentioned noise sources for a turbofan engine, it is useful to briefly introduce some theoretical aspects related to the in-duct noise propagation and to the rotor-stator interaction noise, the latter representing an additional source of noise for turbofan engines with respect to those discussed in Section 2.1.

2.2.1. IN-DUCT NOISE PROPAGATION

As mentioned above, the presence of a duct alters the acoustic propagation of the aerodynamic noise sources inside the duct. How much the duct influences the noise propagation depends on the relative values of the acoustic wavelength and duct length. When the acoustic wavelength associated to a given noise source is small with respect to the characteristic lengths of the duct, the corresponding noise propagation is significantly modified by the duct. Conversely when a duct is relatively short compared to the wavelength, its effect becomes negligible [68]. Considering an infinite annular duct[4] with hard walls of outer and inner radii a and b, respectively, and homogeneous axial flow of constant velocity U, as sketched in Fig. 2.12, the acoustic pressure inside the duct can be determined as solution of the convected Helmholtz equation with rigid-wall boundary conditions and periodicity condition of period 2π on the azimuthal coordinate φ as [70]:

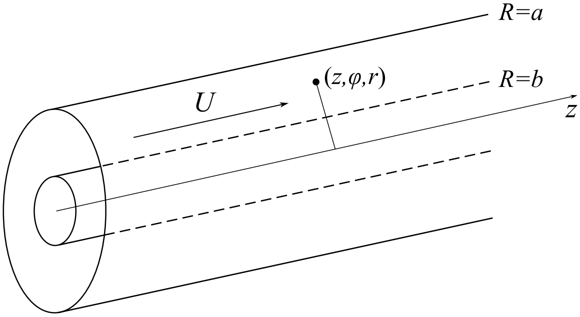

Figure 2.12: Cylindrical duct of radius a with center body of radius b.

$$p'_\omega(z,\varphi,r,t) = e^{-i\omega t} \sum_{m=-\infty}^{\infty} \sum_{j=0}^{\infty} P_{nj}(r) \left[\epsilon^+_{nj} e^{i\left(m\varphi + k^+_{nj} z\right)} + \epsilon^-_{nj} e^{i\left(m\varphi + k^-_{nj} z\right)} \right], \tag{2.10}$$

where $n = |m|$, ω is the angular frequency, t the time, and z, φ, r denote the streamwise, azimuthal and radial duct coordinates. Moreover, $\epsilon^\pm_{nj}$ are the modal coefficients depending on the noise source distribution[5], while $P_{nj}(r)e^{i(m\varphi + k^\pm_{nj} z)}$ are the acoustic modes of propagation in the duct, where:

$$P_{nj}(r) = f_{nj}(r) \left[\int_b^a r f^2_{nj}(r) \mathrm{d}r \right]^{-1/2} \quad \text{with} \quad f_{nj}(r) = J_n(K_{nj} r) + A_{nj} Y_n(K_{nj} r), \tag{2.11}$$

with J_n and Y_n being the Bessel's function of the first and second kind of order n, whereas A_{nj} and K_{nj} are constants to be determined by solving the boundary condition equation for f_{nj} [70]. The quantity $k^\pm_{nj}$ in Eq. (2.10) represents the axial wavenumber that defines whether a given mode can propagate or decays along the duct [70]:

$$k^\pm_{nj} = -\frac{kM}{\beta^2} \pm \bar{k}_{nj} = -\frac{kM}{\beta^2} \pm \frac{1}{\beta^2} \sqrt{k^2 - \beta^2 K^2_{nj}}, \tag{2.12}$$

where $M = U/c_0$ is the Mach number, $k = \omega/c_0$ and $\beta^2 = 1 - M^2$. Each mode is defined by the two indices n and j, which represents the number of azimuthal lobes and radial

---

[4] An annular duct, namely a cylindrical duct with a center body, can be used to approximately represent the bypass duct of a turbofan engine, while a simple cylindrical duct without a center body can be associated to the duct upstream the fan.

[5] All the quantities in Eq. (2.10) are determined by the duct geometry, while the modal coefficients $\epsilon^\pm_{nj}$ are related to the noise sources inside the duct [70].

nodes, respectively, while the amplitude of a certain mode along the radial coordinate is given by $P_{nj}(r)$. The case $n = 0$ correspond to a symmetric mode with no azimuthal dependence, while for $n \neq 0$ the mode is called spinning and is characterized by an equivalent rotation speed ω / m.

A very important result that follows from Eqs. (2.10) and (2.12) is that a mode can propagate along the duct only if $\bar{k}_{ij}$ is a real number, namely for $k > \beta K_{ij}$. On the other hand, for $k < \beta K_{ij}$, $k^{\pm}_{nj}$ has an imaginary part and the corresponding solution must be an exponentially decaying wave so that the amplitude can remain finite [68]. Hence, the mode does not propagate. The frequency ω such that $k > \beta K_{ij}$ is called cut-off frequency of the mode (n, j) and is an increasing function of the mode order. Modes that can propagate are called "cut-on" modes, while those which cannot are named "cut-off" [35]. The particular case $n = j = 0$ (where A_{nj} and K_{nj} are both zero) corresponds to the planar-wave mode that always propagate since its cut-off frequency is zero. How quickly a cut-off mode decays depends on the cut-off ratio $\chi_{nj} = \beta K_{nj} / k$. For $\chi_{nj} \gg 1$ the mode decays rapidly within a fraction of the acoustic wavelength, while for χ_{nj} slightly above one decays only very slowly [35]. The decay of cut-off modes is a relevant property of duct acoustics, since it can be exploited in the design of a turbofan so that some of the acoustic modes that are excited by the noise source are cut-off and do not radiate outside the duct, resulting in lower far-field noise emissions [70].

In the case of a duct without a center body (i.e. $b = 0$), due to the properties of the Bessel functions, it results that a mode propagates only if $ka > \beta K_{m1} a > \beta m$ [35]. Moreover, another important characteristic of a cut-on mode is that it has a supersonic speed at the outer duct wall. This implies that a fan blade at subsonic tip speed does not excite propagating acoustic modes [35].

It is worth mentioning that the above mentioned cut-off reduction mechanisms does not apply to non-periodic noise sources, such as the noise due to the interaction of the fan blades with the inflow turbulence or the duct wall boundary-layer, or the noise due to the impingement of the turbulent fan blade wakes on the stator [71]. Moreover, realistic turbofan configurations do not simply involve constant annular and circular duct cross-sections with uniform mean flow, but they are typically characterized by a variation of the duct cross-section, as well as by the presence of the non-uniform and swirling flows, which are responsible for a complex re-organization and modification of acoustic modes [70].

Finally, the acoustic modes propagating through the duct are subjected to a complex diffraction process at the duct exit [35], which results in the reflection of part of the incident sound (which is then propagated backwards in the duct) and in the radiation of part of the incident wave outside the duct. The sound field that is radiated outside is characterized by dominant lobes that represent the continuation of the oblique waves traveling inside the duct [70]. The modes that are quite beyond the cut-off frequency are efficiently transmitted, while those slightly above it are strongly reflected [70].

2.2.2. ROTOR-STATOR INTERACTION NOISE

The dominant noise source of a typical turbofan engine is due to the interaction between the turbulent wakes generated by the fan blades with the downstream stator vanes [72], as sketched in Fig. 2.11. Tonal and broadband noise are generated as a result of such an interaction, which propagates both upstream towards the turbofan inlet and downstream towards the bypass duct exit. During the upstream radiation, the acoustic waves can be partially impeded by the rotor and are subjected to some level transmission loss [73]. The broadband component is originated by the impingement of the blade wakes turbulent flow (uncorrelated from wake to wake and characterized by small time scales compared to the fan rotation frequency) on the stator vanes [73]. Since this is a modulated turbulent flow impinging on the stator vanes, the resulting broadband spectrum can be peaked around the blade-passing frequency when the modulation is significant [35]. Moreover, the overall broadband levels are related to both the length scale and intensity of the turbulence impinging on the stator vanes leading-edges [35].

The tonal noise is caused by the interaction between the coherent part (i.e. mean velocity deficit) of the fan wake with the stator vanes. Since this source of noise is subjected to the cut-on/cut-off mechanism described in the previous subsection, it is convenient to refer to the frequency-domain expression of the far-field acoustic pressure from a rotor-stator interaction noise (in free-space) for a rotor with B blades and a stator of V vanes. Specifically, if F_{mB} denotes the loading harmonic of order mB on a compact vane element, and γ is the stagger angle and α_0 is the azimuthal angle of the first vane (as sketched in Fig. 2.13), the far-field acoustic pressure for an acoustically compact vane segment can be written as [68]:

$$P_{mB}(\mathbf{x}) = \frac{imBV\Omega}{4\pi c_0 R} F_{mB}(r) \sum_{s=-\infty}^{\infty} e^{-i(mB-sV)(\frac{\pi}{2}+\alpha_0)} e^{i(mB-sV)[\varphi-\Omega_{sV}R/c_0]} \\ \times J_{mB-sV}(mBM\sin(\theta)) \left[\frac{mB-sV}{mB}\frac{\sin(\gamma)}{M} + \cos(\theta)\cos(\gamma) \right], \tag{2.13}$$

where $\Omega_{sV} = mB\Omega/(mB-sV)$ and M is the Mach number associated to the flow experienced by each vane. Again, J_{mB-sV} is the Bessel function of the first kind of order $mB-sV$ and c_0 is the undisturbed speed of sound. Note that since the B rotor blade wakes rotate at the rotor angular velocity Ω, the resulting tonal noise is at the blade-passing harmonics $\omega = mB\Omega$ of the rotor. Moreover, no Doppler effect takes place since the stator vanes are stationary. As a result, a given harmonic of the far-field noise spectrum is fed by the corresponding harmonic of the stator vane loadings.

Equation (2.13) shows that for a rotor of B blades operating with a stator of V vanes, the excited azimuthal modes at the blade-passing frequency harmonic m have the number of lobes $n = mB \pm sV$ and phase speed $\Omega_n = mB\Omega/(mB \pm sV)$. Moreover, for a rotor-stator configuration in a duct (under the assumptions made in the previous subsection), the mode (n, j) is cut-on if $mB\Omega > c_0\beta K_{nj}$, namely:

$$\frac{mB}{\beta}\frac{\Omega a}{c_0} > K_{nj}a \tag{2.14}$$

where $\Omega a/c_0$ is the blade-tip tangential Mach number and $K_{ij}a$ are tabulated eigenvalues [70]. Equation (2.14) is of fundamental importance, since it shows that the number of stator vanes V can be chosen with respect to the number of blades B in such a way that the lowest possible n is sufficiently high for the harmonic of interest to be evanescent[6] [71].

---

[6] Typically only the first harmonic can be effectively reduced following this rule [71].

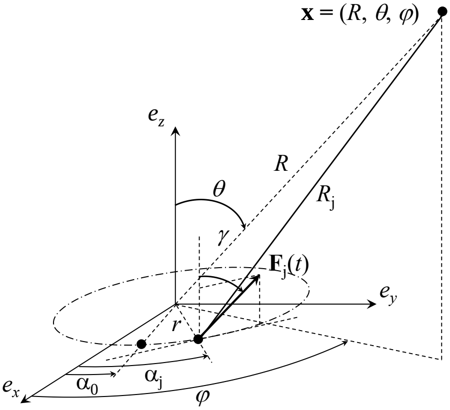

Figure 2.13: Problem definition for free-space far-field rotor-stator interaction noise. Adapted from Roger [68].

Finally, another source of noise introduced by the presence of a stator is the so called potential interaction-noise according to which the aerodynamic solution on the upstream rotor blades is influenced by the potential flow field around the stator vanes [68]. This mechanism generates unsteady periodic loadings on the fan blades, due to the relative motion between fan blades and stator vanes. As a result, the corresponding noise occurs at the blade-passing frequency and harmonics. In general, the rotor and the stator are placed at a distance sufficiently far from each other to minimize this source of tonal noise, but maintaining the propulsion benefit of a rotor-stator configuration.

2.2.3. FAN NOISE

Concerning the thickness noise generated by the fan blades, it can be shown that the resulting field in the duct is composed by harmonics of the blade-passing frequency $jB\Omega$ with a certain mode amplitude [35], where j is the harmonic count integer, B the number of blades and Ω the fan angular velocity. However, such modes can propagate outside the duct only if the corresponding wavenumber k is such that $ka/\beta > m$, where $m = jB$ is the mode order, a is the outer radius of the duct (i.e. of the turbofan intake) and $\beta = \sqrt{1 - M^2}$, with M being the flow Mach number. Since $k = |jB\Omega/c_0|$ (with c_0 being the undisturbed speed of sound), the cut-on condition for a duct mode excited by the thickness noise to propagate outside the duct is that $(\Omega a)/(\beta c_0) > 1$, which does not take place if the blade tip speed is subsonic and/or the axial flow is subsonic enough [35]. Hence, thickness noise does not propagate outside the duct unless the fan operates at transonic conditions or the duct is short enough so that the cut-off modes are not sufficiently decayed before escaping the engine intake.

Similarly, also the steady loading noise produced by the fan blades couples with propagating duct modes only when the blade tip speed reaches transonic conditions. However, in contrast to thickness noise, the loading noise at each harmonic of the blade-passing frequency is the superposition of multiple azimuthal modes. Not all of these modes can propagate outside the duct, but only those that satisfies the condition $ka/\beta > m$, where $m = jB - p$ is the mode order (with p an integer number ranging between $\pm\infty$). Since the frequency associated to a certain mode is $jB\Omega$, it follows that the duct modes excited by the unsteady loading noise propagates for any p such that $(\Omega a)/(\beta c_0) > |jB-p|/|jB|$ [35]. Hence, only a few modes for which $|p|$ is approximately equal to $|jB|$ can propagate outside the duct at subsonic blade tip Mach numbers. However, for $(\Omega a)/(\beta c_0)$ approaching one, a larger number of modes becomes cut-on [35].

The fan blades are also sources of broadband self-noise through the scattering at the trailing-edge of the turbulent pressure fluctuations developing over that blades. Trailing-edge noise from the fan blades can propagate both upstream and downstream, and can be an important contributor to the far-field noise at high-frequencies. Since the fan blades experience a flow speed higher than that of the stator vanes, trailing-edge noise from the fan typically overcomes that associated to the stator [35]. In addition, the fan-blades can generate broadband noise also due to the interaction with the inflow turbulence, the tip flow between the blade tip and the nacelle wall, and/or the turbulent boundary-layer developing over the hub and intake walls. In particular, the first mechanism can be a significant source of broadband noise for highly integrated turbofans, such as the boundary-layer ingesting ones, in which the engine can be partially buried into the aircraft airframe [7, 74], or rear-mounted to it [75], and the fan blades can ingest the turbulent boundary-layer developing over the airframe itself. For such configurations, a considerably amount of unsteady loading noise can be also generated by the fan blades, due to the fact that the mean flow approaching the fan disk is not circumferentially uniform [76].

Finally, at supersonic blade-tip conditions, shocks occur on the fan blades and radiate along the duct to the far-field. This sound, which propagates only in the upstream direction, is called Buzz-saw or multiple pure tones noise, and the resulting spectrum is rich of harmonics of the shaft rotational frequency [77]. Since the shocks are extremely sensitive to small variations of the blade geometry, blade-to-blade stagger angle variation is the main causes of the multiple pure tones occurrence [73].

3

COMPUTATIONAL METHODOLOGY

Science is facts; just as houses are made of stone,
so is science made of facts; but a pile of stones is not a house,
and a collection of facts is not necessarily science.

Jules Henri Poincaré

Chapter 2 provided a general description of the noise sources in open rotor and turbofan propulsive systems, with a particular attention to those that are addressed in thesis. The present chapter extensively describes the hybrid computational aeroacoustic approach that is used in this work, which is based on the coupling between the lattice-Boltzmann method and the Ffowcs Williams & Hawkings' acoustic analogy. After a brief introduction on computational aeroacoustics (Sec. 3.1), Sec. 3.2 illustrates the lattice-Boltzmann method, namely the numerical approach that is employed to compute the aerodynamic and aeroacoustic near-fields. Its derivation from the continuous Boltzmann equation to the discrete lattice-Boltzmann equation is outlined, along with a discussion on the inclusion of the turbulence modeling and the extension to high Mach number flows. Then, the Ffowcs Williams & Hawkings' acoustic analogy, which is used to compute far-field noise radiation from the flow solution provided by the lattice-Boltzmann method, is described in Sec. 3.3. A description of the Farassat's formulation 1A integral solution of the Ffowcs Williams & Hawkings' equation, as well as of the solid/permeable approaches and retarded/advanced time solutions, is presented.

3.1. INTRODUCTION

AEROACOUSTICS is that branch of the fluid mechanics that studies the generation and propagation of the aerodynamic sound produced by turbulent flows and/or moving bodies in a fluid medium. For a long time, research in aeroacoustics has been primarily conducted by experimental, semi-empirical and/or analytical methods in order to understand and predict the noise radiation associated to new technical products [29]. However, the enormous advances experienced by the computer technology in the past three decades has enabled numerical methods as feasible and quite accurate approaches to study the sound generation and propagation mechanisms associated to aeroacoustic problems involving complex geometrical configurations, inhomogeneous flows and flow-induced noise radiation [29].

All those numerical methods that describe the noise generation and/or radiation related to aerodynamic phenomena go under the name of Computational Aero-Acoustics (CAA). It is a vast discipline of research that includes, among others, acoustic transport methods such as the Lighthill's and Ffowcs Williams & Hawkings' acoustic analogies [34, 53], or the Kirchhoff method [78]; the Linearized Euler Equations (LEE) approach [29]; methods based on the Acoustic Perturbation Equations (APE) [79]; scale-resolving compressible Computational Fluid Dynamics (CFD) simulations, such as Direct Numerical Simulation (DNS), Large Eddy Simulation (LES), Detached Eddy Simulation (DES), Lattice-Boltzmann Method (LBM), hybrid RANS/LES [29, 80, 81], or their combination with integral methods [29]; Reynolds Averaged Navier-Stokes (RANS) equations coupled to semi-empirical statistical models or Stochastic Noise Generation and Radiation (SNGR) methods [82, 83]. All these approaches can be gathered under two broad categories, namely direct and hybrid methods. These are concisely summarized in the following, while for an extensive and systematic review on computational aeroacoustic approaches the reader may refer to Refs. [84–86].

DIRECT METHODS FOR NOISE PREDICTION

Direct methods aim at computing both the unsteady turbulent flow and the acoustic radiation together by solving a set of compressible flow equations, and are considered as the most exact prediction tools from a CAA perspective [29]. In a direct method, the computational domain includes the flow region where the noise is generated down to the far-field region where the observer is placed. Example of direct noise methods are compressible DNS, LES, DES, hybrid RANS/LES and LBM, in which an adequate computational grid must be employed to capture the noise generation mechanisms of interest, as well as the resulting acoustic propagation up to the far-field observer. These methods do not generally suffer from any modeling approximation of the noise sources, besides the possible usage of turbulence modeling [29]. Obviously, if turbulence modeling is used, only a range of energy-containing eddies is resolved, and the resulting sound field is only that associated to the flow dynamics that has been captured [84], provided that other issues of numerical nature have not affected the noise generation and propagation. Since the computational grid needs to fulfill strict requirements in terms of mesh quality and resolution, so that both the noise generation and propagation mechanisms can be properly captured [84], these kind of computations are generally very demanding in terms of computational cost, and only simple flow configurations can be concretely afforded by direct noise extraction methods. For this reason, hybrid methods are generally preferred to direct ones, especially for aeroacoustic problems of industrial relevance for which the latter are not still feasible nowadays.

HYBRID METHODS FOR NOISE PREDICTION

In order to alleviate the issue related to direct methods, the computation of the aerodynamic noise sources can be decoupled from the acoustic propagation to the far-field [29]. This is the idea behind the definition of an hybrid method. In such approaches, the sound sources are computed directly through a given scale-resolving CFD method (e.g. DNS, LES, DES, hybrid RANS/LES or LBM), on the body surface or in a near-field volume region, in order to provide the relevant flow data to an acoustic method for far-field noise extraction. Alternatively, they can be computed through semi-empirical models or SNGR methods, using information about turbulent time and length scales from RANS simulations and translating them into sound-source data to be used in analytical transport methods and acoustic analogies [29]. Hence, the radiation of the sound sources in the aerodynamic near-field can be carried out by computational or analytical transport/acoustic analogies approaches.

In a computational transport, some kind of partial differential equations are solved from the boundary of the noise-source region up to the far-field observer. In contrast to direct methods, only the acoustics (i.e. pressure disturbances propagation) is solved within the transport domain, with the full aerodynamic field no longer being simulated. Examples of computational transport methods are the numerical solution of the Linearized Euler Equations (LEE) [87], the Acoustic Perturbation Equations (APE) [79], the Perturbed Compressible Equations (PCE) [88] or simply the acoustic wave equation, in which the CFD data is used as boundary condition for the CAA simulation. The turnaround times of an hybrid method with computational transport is certainly reduced compared to direct approaches, yet it can be considerable since the whole domain between the aerodynamic near-field and the observer needs to be solved for. However, the computational cost associated to these approaches does not grow with the number of far-field observers, and their use is preferred over analytical transport methods when is required to compute the noise propagation in an extended far-field region [29].

A more computational efficient alternative is to use analytical transport (or integral) methods, such as the Lighthill's and Ffowcs Williams & Hawkings' (FW-H) acoustic analogies [34, 53], or the Kirchhoff's method [78], which allows to propagate a near-field information down to the far-field at a computational cost that is not related to the radiation distance, but only to the number of observers [89]. In these methods, the acoustic pressure at a location in the far-field is computed by integrating surface and/or volume source terms, depending on the particular method and formulation. The coupling between the CFD and CAA simulations is much easier compared to computational transport approaches, and their accuracy mainly rely on the proper representation of the noise sources by the CFD computation. However, due to the finite speed of the sound and the deterministic relationship between emission and observer times of a pressure signal, an interpolation of the source data at the retarded time, or of the pressure signals at the reception time, is needed [29, 89].

Figure 3.1 provides an overview of the noise prediction methods in CAA as discussed above.

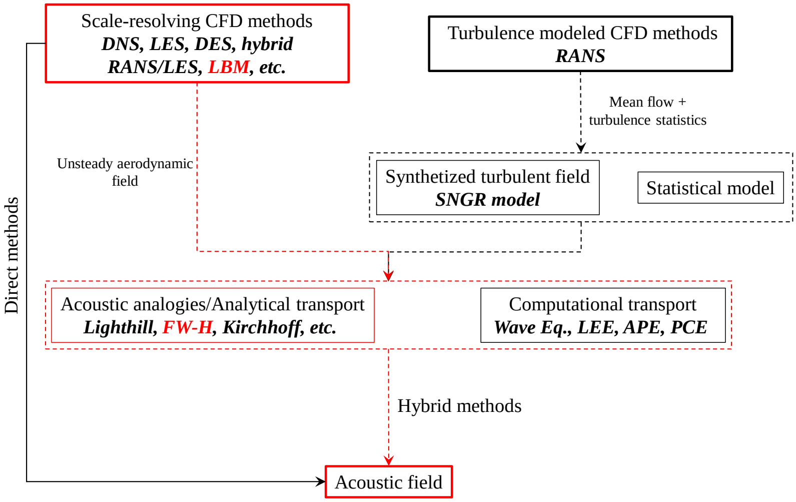

Figure 3.1: Overview of the noise prediction methods in CAA.

The main challenges and difficulties faced by CFD/CAA methods can be summarized as follows [29, 84, 85]:

- the fact that CFD methods need to deal with turbulence modeling (except for DNS), and/or complex phenomena such as laminar-to-turbulent transition and separation, may have an important impact on the correct representation of the physical noise sources and, in turn, on the resulting acoustic propagation/transport;
- the necessity for accurately propagating the near-field acoustic disturbances generated by the CFD simulation requires direct noise or computational transport methods with low-dissipation (error on the wave amplitude) and low-dispersion (error on the wave propagation speed and phase) properties;
- since there are several orders of magnitude between acoustic and hydrodynamic fluctuations, $P_a/P_h \approx 10^{-4}M^5$ (with M being the characteristic Mach number), the numerical simulation and computational grid should introduce as little numerical errors and artificial noise sources as possible, to avoid that the physical sound sources are overwhelmed by spurious ones;
- the coupling between a CFD method to a computational transport approach should guarantee a certain continuity and conservation of the flow quantities at the boundaries of the CFD/CAA domains, as well as avoid the generation of spurious noise sources at the interface;
- in direct methods or computational transport methods, the backwards reflection of outward going acoustic waves needs to be minimized through non-reflecting boundary conditions or sponge/buffer zones to avoid contamination of the physical noise solution;

- when dealing with integral/analytical transport methods, the non-linear source and propagation effects should be properly addressed by properly placing the integration surface and/or including volume contributions.

All the numerical simulations performed in this thesis are based on the use of one of the above mentioned hybrid CFD/CAA approaches, namely the lattice-Boltzmann method coupled to the Ffowcs Williams & Hawkings' acoustic analogy (highlighted in red in Fig. 3.1), where the former is used to extract the unsteady and compressible aerodynamic near-field, whereas the latter is used to compute the resulting far-field noise radiation. These two computational methods are discussed in the following.

3.2. THE LATTICE-BOLTZMANN METHOD

The mathematical description of the fluid dynamics can be carried out at different levels: macroscopic, mesoscopic and microscopic [81]. In the former, the fluid is described at fully-continuum level directly through macroscopic fluid quantities such as density, velocity and temperature. Macroscopic systems are governed by the compressible Navier-Stokes equation for viscous flows. In contrast, the microscopic description of a fluid is that in which the fluid is described at molecular level, by tracking and tracing the behavior of individual molecules whose dynamics obeys to the Newton's laws of motion. In between the previous two fluid representations lies the mesoscopic one. Instead of considering the behavior of the single molecules, the mesoscopic description tracks the dynamics of distributions or representative collections of molecules through the kinetic theory [81]. The LBM is based on the mesoscopic fluid description by means of the particle density distribution functions, with the macroscopic flow properties being the result of the moments of these particle distribution functions [30–32].

In recent years, the Lattice-Boltzmann Method (LBM) has been developed as an alternative CFD method for numerical simulations of unsteady turbulent flows. The key advantages of LBM, compared to Navier-Stokes based methods, are: the highly efficient parallelization (due to its explicit and local character), the ease of modeling various complex fluids, and the more straightforward handling of complex geometries and boundary conditions [31–33]. Moreover, due to the fact that LBM is low dissipative, compressible and provides an unsteady solution, it is intrinsically suited for aeroacoustic simulations. This has enabled the LBM as a very promising CFD method for large scale computations of complex industrial problems such as fixed-wing aircraft, both at component [90, 91] and full aircraft [92, 93] level, jet noise [94] and turbofan aeroacoustics [95, 96].

The following subsections provide a general, yet not exhaustive, description of the LBM as implemented in the commercial code SIMULIA PowerFLOW®, which is the LBM flow solver used throughout this thesis. Providing an in-depth description of the LBM is out of the scope of the present work, and the interested reader may refer to Refs. [81, 97, 98] for a thorough discussion of the theory underlying the lattice-Boltzmann method.

3.2.1. THE PROBABILITY DENSITY DISTRIBUTION FUNCTION

In the mesoscopic scale description, the behavior of collection of molecules can be represented through a particle distribution function $f_\eta(\boldsymbol{\xi},\mathbf{x},t)$ so that $\mathrm{d}\eta = f_\eta(\boldsymbol{\xi},\mathbf{x},t)\mathrm{d}\boldsymbol{\xi}\mathrm{d}\mathbf{x}$ represents the number of molecules in the mesoscopic volume $\mathrm{d}\mathbf{x}$, located around the spatial position $\mathbf{x}$ and in the infinitesimal time interval $(t, t + \mathrm{d}t)$, with microscopic velocity in the interval $(\boldsymbol{\xi}, \boldsymbol{\xi} + \mathrm{d}\boldsymbol{\xi})$. Considering all the particles to have the same molecular mass m, it is possible to define a probability density distribution function $f(\boldsymbol{\xi}, \mathbf{x}, t) = m f_\eta(\boldsymbol{\xi}, \mathbf{x}, t)$, which allows to retrieve the macroscopic fluid local density ρ, momentum density $\rho\mathbf{u}$ and total energy density ρE, as zeroth-, first- and second-order statistical moments of f, respectively [81, 98]:

$$\rho(\mathbf{x}, t) = \int f(\boldsymbol{\xi}, \mathbf{x}, t)\mathrm{d}\boldsymbol{\xi}, \tag{3.1}$$

$$\rho\mathbf{u}(\mathbf{x}, t) = \int \boldsymbol{\xi} f(\boldsymbol{\xi}, \mathbf{x}, t)\mathrm{d}\boldsymbol{\xi}, \tag{3.2}$$

$$\rho E(\mathbf{x}, t) = \int \frac{|\boldsymbol{\xi}|^2}{2} f(\boldsymbol{\xi}, \mathbf{x}, t)\mathrm{d}\boldsymbol{\xi}. \tag{3.3}$$

Assuming elastic collisions between particles (monoatomic gas), the total energy density of the fluid is the sum of the internal energy and kinetic energy densities [81, 98]:

$$\rho E(\mathbf{x}, t) = \rho e + \frac{1}{2}\rho|\mathbf{u}(\mathbf{x}, t)|^2 \quad \text{with} \quad \rho e(\mathbf{x}, t) = \int \frac{|\boldsymbol{\xi} - \mathbf{u}|^2}{2} f(\boldsymbol{\xi}, \mathbf{x}, t)\mathrm{d}\boldsymbol{\xi}, \tag{3.4}$$

while the thermodynamic temperature of the fluid can be computed as [81]:

$$T(\mathbf{x}, t) = e(\mathbf{x}, t)/c_v, \tag{3.5}$$

where $c_v = R(D/2)$ is the heat capacity at constant volume (with D denoting the number of spatial dimensions) and $R = k_B/m$ the gas specific constant with k_B being the Boltzmann constant.

By explicitly introducing the intrinsic velocity $\mathbf{c} = \boldsymbol{\xi} - \mathbf{u}$[1], the full second and third moments of the distribution function can be computed as follows [98]:

$$P_{ij}(\mathbf{x}, t) = \int f(\boldsymbol{\xi}, \mathbf{x}, t) c_i c_j \mathrm{d}\boldsymbol{\xi}, \tag{3.6}$$

$$Q_{ijk}(\mathbf{x}, t) = \int f(\boldsymbol{\xi}, \mathbf{x}, t) c_i c_j c_k \mathrm{d}\boldsymbol{\xi}, \tag{3.7}$$

with i, j, k denoting the Cartesian components. P_{ij} and Q_{ijk} have an important physical significance. The former represents the rate of momentum transfer from the i-direction into the j-direction, while the contracted third component of the latter represents the heat flux due to molecular motion:

$$q_i(\mathbf{x}, t) = Q_{iii}(\mathbf{x}, t) = \int f(\boldsymbol{\xi}, \mathbf{x}, t) c^2 c_i \mathrm{d}\boldsymbol{\xi}. \tag{3.8}$$

Moreover, the macroscopic pressure $p(\mathbf{x}, t)$ can be computed as the trace of Eq. (3.6), namely $p(\mathbf{x}, t) = P_{ii}(\mathbf{x}, t)/D = 2\rho(\mathbf{x}, t)\, e(\mathbf{x}, t)/D$ and, considering the temperature-internal energy relation for a monoatomic ideal gas, $e(\mathbf{x}, t) = DRT(\mathbf{x}, t)/2$, the ideal-gas equation of state can be recovered: $p(\mathbf{x}, t) = \rho(\mathbf{x}, t)\, RT(\mathbf{x}, t)$. Finally, the stress tensor $\boldsymbol{\sigma}$ is defined as $\sigma_{ij} = P_{ij} - p\delta_{ij}$, where δ_{ij} is the Kronecker's delta.

---

[1] It is more convenient to refer the full second and third moments of f to the reference frame moving with the bulk of the fluid flow.

3.2.2. THE BOLTZMANN-BGK EQUATION

The evolution in space and time of the particle density distribution function is described by the Boltzmann equation [98]:

$$\frac{\partial f}{\partial t} + \boldsymbol{\xi} \cdot \frac{\partial f}{\partial \mathbf{x}} + \boldsymbol{b} \cdot \frac{\partial f}{\partial \boldsymbol{\xi}} = \Omega(f), \tag{3.9}$$

where the left-hand side is a transport term, the right-hand side is a collision source term, while $\boldsymbol{b}$ represents the acceleration from an external body-force. The dot symbol in Eq. (3.9) denotes a scalar product. The collision term, also called collision operator, describes the variation of f due to the particles collisions and, thus, governs the evolution of the fluid towards a thermodynamic equilibrium. Since the collisions between particles conserve mass, momentum and energy for a monoatomic gas, the collision operator must fulfill these conservation constraints, which can be expressed as [81]:

$$\int \Omega(f)\varphi(\boldsymbol{\xi})\mathrm{d}\boldsymbol{\xi} = 0, \tag{3.10}$$

with $\varphi(\boldsymbol{\xi}) = 1$, $\boldsymbol{\xi}$ and $|\xi|^2/2$ for the mass, momentum and total energy conservation, respectively. A relatively simple collision operator that satisfies the aforementioned constraints is the so-called Bhatnagar–Gross–Krook (BGK) operator[2], which is given by [101]:

$$\Omega(f) = -\frac{1}{\tau}(f - f^{eq}) \tag{3.11}$$

where τ is the relaxation time parameter, which determines the speed at which the system of particles evolves towards the equilibrium, while f^{eq} is the local[3] Maxwell-Boltzmann equilibrium distribution function in a reference frame moving with the bulk of the flow [98]:

$$f^{eq} = \frac{\rho}{(2\pi RT)^{D/2}} \exp\left(-\frac{|\boldsymbol{\xi} - \mathbf{u}|^2}{2RT}\right). \tag{3.12}$$

Introducing the BGK collision operator (Eq. (3.11)) into the Boltzmann's equation (Eq. (3.9)) leads to the Boltzmann-BGK equation:

$$\frac{\partial f}{\partial t} + \boldsymbol{\xi} \cdot \frac{\partial f}{\partial \mathbf{x}} + \boldsymbol{b} \cdot \frac{\partial f}{\partial \boldsymbol{\xi}} = -\frac{1}{\tau}(f - f^{eq}). \tag{3.13}$$

It can be demonstrated that the mass, momentum and total energy conservation equations can be retrieved by respectively taking the zeroth- and first-order moments, and the trace of the second-order moments of the Boltzmann-BGK equation [98]. However,

---

[2] The original collision operator proposed by Boltzmann is in the form of a cumbersome double integral over the velocity space. The BGK collision operator is therefore often used for its simplicity and computational efficiency. However, the use of the BGK operator implies some repercussions on the conservation laws when applying the Chapman-Enskog to the equilibrium function f [99]. PowerFLOW® implements a regularized collision operator which results in a significantly higher numerical stability and accuracy compared to the classical BGK collision operator [100].

[3] The equilibrium distribution function is completely determined by local values of the macroscopic density, velocity and temperature.

the resulting macroscopic fluid mechanics equations thus obtained are not closed due to the appearance of high-order moments (i.e. P_{ij} and q_i), which are known only after f is known, in the equations for lower-order moments (i.e. momentum and total energy equations) [98]. A possible closure of the conservation equations can be obtained by considering the Chapman-Enskog expansion of the distribution function f in powers of the Knudsen number[4] ϵ around the equilibrium (or zeroth-order) distribution function $f^{(0)} = f^{eq}$ [102]:

$$f = f^{(0)} + \epsilon f^{(1)} + \epsilon^2 f^{(2)} + \ldots = \sum_{j=0}^{\infty} \epsilon^j f^{(j)}, \tag{3.14}$$

and considering a similar expansion in ϵ for the time and spatial derivative operators [98]. It can be shown that by substituting Eq. (3.14) into Eq. (3.13) and retaining only the zeroth ($f \approx f^{(0)}$) and first-order ($f \approx f^{(0)} + \epsilon f^{(1)}$) approximations of f, the Euler and Navier-Stokes equations can be respectively recovered from the Boltzmann-BGK equation under the constraints of small Knudsen numbers (i.e. $\epsilon < 0.01$) and unitary Prandtl number[5]. For more details on the recovery of the macroscopic flow governing equations from the Boltzmann-BGK equation with Chapman-Enskog expansion of f the reader may refer to Refs. [81, 98].

3.2.3. THE LATTICE-BOLTZMANN EQUATION

The Boltzmann equation, Eq. (3.13), can be solved numerically by first performing a discretization in the velocity $\boldsymbol{\xi}$-space along a set of discrete velocities $\boldsymbol{\xi}_i$ through a method based on Hermite polynomials and Gauss-Hermite quadrature [98]. The velocity-space discretization of the Boltzmann equation allows to reduce the continuous velocity space to only a certain number of discrete velocities without compromising the recovery of the flow governing equations at macroscopic level [81]. The so-called lattice-Boltzmann equation can be obtained by performing an additional discretization in the physical space and time of the discrete-velocity Boltzmann equation by means of the Characteristic Method [81]. Before going into the velocity, space and time discretization of the Boltzmann equation, it is convenient to express Eqs. (3.13) and (3.12) in non-dimensional form by scaling all velocities with respect to $c_0 = \sqrt{RT}$[6] and considering l_0 and $t_0 = l_0/c_0$ as characteristic length and time scales, such that $\tilde{\mathbf{x}} = \mathbf{x}/l_0$ and $\tilde{t} = tc_0/l_0$ [81]:

$$\frac{\partial \tilde{f}}{\partial \tilde{t}} + \tilde{\boldsymbol{\xi}} \cdot \frac{\partial \tilde{f}}{\partial \tilde{\mathbf{x}}} + \tilde{\boldsymbol{b}} \cdot \frac{\partial \tilde{f}}{\partial \tilde{\boldsymbol{\xi}}} = -\frac{1}{\tilde{\tau}}\left(\tilde{f} - \tilde{f}^{eq}\right), \tag{3.15}$$

$$\tilde{f}^{eq} = \frac{\tilde{\rho}}{(2\pi \tilde{T})^{D/2}} \exp\left(-\frac{|\tilde{\boldsymbol{\xi}} - \tilde{\mathbf{u}}|^2}{2\tilde{T}}\right), \tag{3.16}$$

---

[4] The Knudsen number ϵ is the ratio between the molecular mean free path ℓ_{mfp} and a characteristic length ℓ of the physical problem. For $\epsilon < 0.01$ the flow is considered continuum, while for $\epsilon > 1$ is considered molecular.

[5] The Prandtl number, Pr, is the ratio between viscosity and thermal conduction. The BGK collision operation predicts a wrong Pr equal to 1, while Boltzmann's original collision operator predicts the correct physical $Pr = 2/3$ for monoatomic gases [81]. Hence, the BGK collision operator is not appropriate for a accurate thermal simulations and other approaches, based on hybrid finite-difference/LBM models, double distribution functions or multiple relaxation time collision operators, are preferred [99].

[6] Note that c_0 denotes the speed of sound except for the square root of heat capacity ratio γ.

where:

$$\frac{\partial}{\partial \tilde{t}} = \frac{l_0}{c_0}\frac{\partial}{\partial t}, \quad \frac{\partial}{\partial \tilde{\mathbf{x}}} = l_0 \frac{\partial}{\partial \mathbf{x}}, \quad \frac{\partial}{\partial \tilde{\boldsymbol{\xi}}} = c_0 \frac{\partial}{\partial \boldsymbol{\xi}}, \tag{3.17}$$

$$\tilde{f} = f c_0^D/\rho_0, \quad \tilde{\boldsymbol{b}} = \boldsymbol{b} l_0/c_0^2, \quad \tilde{\rho} = \rho/\rho_0, \quad \tilde{T} = RT/c_0^2, \quad \tilde{\tau} = \tau/\tau_0. \tag{3.18}$$

with ρ_0 being a reference density and $\tau_0 = \epsilon t_0$ a reference relaxation time in which the Knudsen number is introduced [99]. For the sake of convenience, the tilde sign is dropped from Eqs. (3.15) and (3.16) from now on, and all the quantities are to be intended dimensionless.

VELOCITY DISCRETIZATION OF THE BOLTZMANN EQUATION

Following Shan *et al.* [98], the distribution function $f(\boldsymbol{\xi}, \mathbf{x}, t)$ can be expanded in Hermite ortho-normal polynomials in the $\boldsymbol{\xi}$-space as follows:

$$f(\boldsymbol{\xi}, \mathbf{x}, t) = \omega(\boldsymbol{\xi}) \sum_{n=0}^{\infty} \frac{1}{n!} \boldsymbol{a}^{(n)}(\mathbf{x}, t) : \mathscr{H}^{(n)}(\boldsymbol{\xi}), \tag{3.19}$$

where $\boldsymbol{a}^{(n)}$ and $\mathscr{H}^{(n)}$ are the dimensionless expansion coefficients and Hermite polynomials, both tensors of rank n, respectively defined as:

$$\boldsymbol{a}^{(n)}(\mathbf{x}, t) = \int f(\boldsymbol{\xi}, \mathbf{x}, t) \mathscr{H}^{(n)}(\boldsymbol{\xi}) \mathrm{d}\boldsymbol{\xi} \quad \text{and} \quad \mathscr{H}^{(n)}(\boldsymbol{\xi}) = \frac{(-1)^n}{\omega(\boldsymbol{\xi})} \nabla^{(n)} \omega(\boldsymbol{\xi}), \tag{3.20}$$

with $\nabla^{(n)}\omega(\boldsymbol{\xi})$ representing the n^{th}-order gradient tensor obtained by n-consecutive derivations with respect to $\boldsymbol{\xi}$ and $\omega(\boldsymbol{\xi})$ being the weighting function of the Hermite polynomials:

$$\omega(\boldsymbol{\xi}) = \frac{1}{(2\pi)^{D/2}} \exp\left(-\frac{\xi^2}{2}\right), \tag{3.21}$$

where $\xi = \boldsymbol{\xi} \cdot \boldsymbol{\xi}$. Note that the weighting function has the same form of the distribution equilibrium function f^{eq} in Eqs. (3.12) and (3.16). Moreover, the product between $\boldsymbol{a}^{(n)}$ and $\mathscr{H}^{(n)}$ in Eq. (3.19) is to be intended as a full contraction (i.e. summation over all the possible indices).

By substituting the Hermite polynomials into the first four expansion coefficients and sorting the resulting equations, the relevant thermodynamic variables can be expressed in terms of low-order Hermite expansion coefficients [98]:

$$\rho = \boldsymbol{a}^{(0)}, \tag{3.22}$$

$$\rho \boldsymbol{u} = \boldsymbol{a}^{(1)}, \tag{3.23}$$

$$\boldsymbol{P} = \boldsymbol{a}^{(2)} - \rho(\boldsymbol{u}^2 - \boldsymbol{\delta}), \tag{3.24}$$

$$\boldsymbol{Q} = \boldsymbol{a}^{(3)} - \boldsymbol{u}\boldsymbol{a}^{(2)} + (D-1)\rho \boldsymbol{u}^3, \tag{3.25}$$

$$\rho e = \frac{1}{2}[a_{ii}^{(2)} - \rho(u^2 - D)], \tag{3.26}$$

where $\boldsymbol{P} = \{P_{ij}\}$, $\boldsymbol{Q} = \{Q_{ijk}\}$ and $\boldsymbol{\delta} = \{\delta_{ij}\}$, while the power of the vector denotes vector products (e.g. $\boldsymbol{u}^3 = \boldsymbol{uuu}$) and $u^2 = |\boldsymbol{u}|^2$. Hence, the macroscopic density (ρ), velocity ($\boldsymbol{u}$), temperature ($T = 2e/D$) and momentum flux tensor ($\boldsymbol{P}$) and the stress tensor ($\boldsymbol{\sigma}$) can be recovered through the first three Hermite expansion coefficients, while for the heat flux $\boldsymbol{q}$ the fourth expansion coefficient is necessary. Hence, for $N = 4$ the full Navier-Stokes Fourier equations are recovered[7], while for $N = 3$ errors in the energy equation are introduced and the Navier-Stokes equations are recovered only under the isothermal hypothesis. Finally, for $N = 2$ further errors are introduced in the energy equation (the isothermal hypothesis becomes compulsory), and an error term of order $\mathscr{O}(M^3)$, with M being the Mach number, appears in the viscous stress tensor [99][8].

Thanks to the orthogonality of the Hermite polynomials, the Hermite expansion of f can be truncated at an order N without affecting the N lower-order Hermite moments of the distribution function (i.e. expansion coefficients), namely [98]:

$$f(\boldsymbol{\xi},\mathbf{x},t) \approx f^N(\boldsymbol{\xi},\mathbf{x},t) = \omega(\boldsymbol{\xi}) \sum_{n=0}^{N} \frac{1}{n!} \boldsymbol{a}^{(n)}(\mathbf{x},t) : \mathscr{H}^{(n)}(\boldsymbol{\xi}), \tag{3.27}$$

thus ensuring that $f^N(\boldsymbol{\xi},\mathbf{x},t)$ has the same velocity moments of the complete distribution function $f(\boldsymbol{\xi},\mathbf{x},t)$. In a similar manner, the distribution function at equilibrium f^{eq} must be expanded in Hermite polynomials according to Eq. (3.27) as:

$$f^{eq}(\boldsymbol{\xi},\mathbf{x},t) \approx f^{eq,N}(\boldsymbol{\xi},\mathbf{x},t) = \omega(\boldsymbol{\xi}) \sum_{n=0}^{N} \frac{1}{n!} \boldsymbol{a}_{eq}^{(n)}(\mathbf{x},t) : \mathscr{H}^{(n)}(\boldsymbol{\xi}), \tag{3.28}$$

with:

$$\boldsymbol{a}_{eq}^{(n)}(\mathbf{x},t) = \int f^{eq,N}(\boldsymbol{\xi},\mathbf{x},t)\mathscr{H}^{(n)}(\boldsymbol{\xi})\mathrm{d}\boldsymbol{\xi}, \tag{3.29}$$

as well as the body-force term on the left-hand side of the Boltzmann equation [98]:

$$F(\boldsymbol{\xi}) \approx F^N(\boldsymbol{\xi}) = \omega(\boldsymbol{\xi}) \sum_{n=1}^{N} \frac{1}{n!} \boldsymbol{b}\boldsymbol{a}^{(n-1)}(\mathbf{x},t) : \mathscr{H}^{(n)}(\boldsymbol{\xi}) \quad \text{where} \quad F(\boldsymbol{\xi}) = -\boldsymbol{b} \cdot \frac{\partial f}{\partial \boldsymbol{\xi}}. \tag{3.30}$$

For the sake of compactness, the subscript N in f^N, $f^{eq,N}$ and F^N is omitted in the following, implying that such quantities are to be intended as truncated to the order N of the Hermite polynomial expansion.

At this point, it is possible to discretize the Boltzmann equation in the $\boldsymbol{\xi}$-space by applying the Gauss-Hermite quadrature rule, namely to evaluate the integral in the Hermite coefficients expansion as a discrete sum over the polynomial evaluated at specific V abscissae $\boldsymbol{\xi}_i$, e.g. for Eq. (3.20) [81]:

$$\boldsymbol{a}^{(n)}(\mathbf{x},t) = \int f(\boldsymbol{\xi},\mathbf{x},t)\mathscr{H}^{(n)}(\boldsymbol{\xi})\mathrm{d}\boldsymbol{\xi} = \sum_{i=0}^{V-1} \frac{w_i}{\omega(\boldsymbol{\xi}_i)} f(\boldsymbol{\xi}_i,\mathbf{x},t)\mathscr{H}^{(n)}(\boldsymbol{\xi}_i), \tag{3.31}$$

---

[7] Some authors have pointed out that including higher expansion coefficients can be beneficial for the sake of accuracy and numerical stability [81].

[8] This type of truncation of the Hermite expansion is related to the well-known weakly compressibility limit of the LBM under isothermal hypothesis.

where w_i are the weights of the Gauss-Hermite quadrature and $\boldsymbol{\xi}_i$ the quadrature point in the $\boldsymbol{\xi}$ velocity space [98]. The choice of the discrete velocity set for the discretization of the Hermite expansion coefficients (i.e. the V abscissae $\boldsymbol{\xi}_i$), also called velocity lattices, must ensure that the polynomials with the highest degree can be properly integrated in order to fulfill all the relevant flow governing equations. Hence, if N is the order of the polynomial, at least $n \geq (N+1)/2$ abscissae, given by the roots of $\mathscr{H}^{(n)}(\boldsymbol{\xi}_i) = 0$, are needed to accurately evaluate the corresponding integral [81]. By applying the Gauss-Hermite quadrature one obtains the discrete-velocity Boltzmann equation (for more details the reader may refer to Ref. [98]):

$$\frac{\partial f_i}{\partial t} + \boldsymbol{\xi}_i \cdot \frac{\partial f_i}{\partial \mathbf{x}} = -\frac{1}{\tau}(f_i - f_i^{eq}) + F_i \quad \text{with} \quad (i = 1, \dots, V), \tag{3.32}$$

where $f_i(\mathbf{x}, t) = w_i f(\boldsymbol{\xi}_i, \mathbf{x}, t)/\omega(\boldsymbol{\xi}_i)$ and:

$$\begin{aligned} f_i^{eq} \equiv \frac{w_i}{\omega(\boldsymbol{\xi}_i)} f^{eq}(\boldsymbol{\xi}_i) = w_i \rho \Big\{ 1 + & \underbrace{\boldsymbol{\xi}_i \cdot \boldsymbol{u}}_{1^{st}\, order} + \underbrace{\frac{1}{2}[(\boldsymbol{\xi}_i \cdot \boldsymbol{u})^2 - u^2 + (T-1)(\xi_i^2 - D)]}_{2^{nd}\, order} \\ & + \underbrace{\frac{\boldsymbol{\xi}_i \cdot \boldsymbol{u}}{6}[(\boldsymbol{\xi}_i \cdot \boldsymbol{u})^2 - 3u^2 + 3(T-1)(\xi_i^2 - D - 2)]}_{3^{rd}\, order} + \dots \Big\}, \end{aligned} \tag{3.33}$$

$$\begin{aligned} F_i \equiv \frac{w_i}{\omega(\boldsymbol{\xi}_i)} F(\boldsymbol{\xi}_i) = w_i \rho \Big\{ & \underbrace{\boldsymbol{\xi}_i \cdot \boldsymbol{b}}_{1^{st}\, order} + \underbrace{(\boldsymbol{\xi}_i \cdot \boldsymbol{b})(\boldsymbol{\xi}_i \cdot \boldsymbol{u}) - \boldsymbol{b} \cdot \boldsymbol{u}}_{2^{nd}\, order} \\ & + \underbrace{\frac{1}{2\rho} \boldsymbol{a}^{(2)} : [(\boldsymbol{\xi}_i \cdot \boldsymbol{b}) \mathscr{H}^{(2)}(\boldsymbol{\xi}_i) - 2\boldsymbol{\xi}_i \boldsymbol{b}]}_{3^{rd}\, order} + \dots \Big\}. \end{aligned} \tag{3.34}$$

Hence, the (dimensionless) macroscopic hydrodynamic quantities can be computed as finite sums of f_i rather than through a continuous integration (Eqs. (3.1)-(3.4)), namely [98]:

$$\rho = \sum_{i=0}^{V-1} f_i \tag{3.35}$$

$$\rho \boldsymbol{u} = \sum_{i=0}^{V-1} f_i \boldsymbol{\xi}_i \tag{3.36}$$

$$\boldsymbol{P} + \rho \boldsymbol{u}\boldsymbol{u} = \sum_{i=0}^{V-1} f_i \boldsymbol{\xi}_i \boldsymbol{\xi}_i \tag{3.37}$$

$$\rho(DT + u^2) = \sum_{i=0}^{V-1} f_i \xi_i^2 \tag{3.38}$$

Different velocity lattices can be defined depending the flow physics that is required to be recovered. A LBM lattice is typically denoted with the $D_D Q_V$ nomenclature, where

D is the number of spatial dimensions and V is the number of discrete velocities $\boldsymbol{\xi}_i$. For three-dimensional cases, two different lattices are used in PowerFLOW®, namely the $D3Q19$ and $D3Q39$ models, which are respectively employed for the simulation of low-/high-subsonic and transonic/supersonic flows. The $D3Q19$ and $D3Q39$ models are sketched in Fig. 3.2, while more details on the weighting parameters w_i and discrete velocities $\boldsymbol{\xi}_i$ can be found in Shan *et al.* [98]. For low-subsonic flows (isothermal and weakly compressible, $M < 0.5$), the $D3Q19$ model is used with a second-order Hermite expansion of the distribution function. For high-subsonic flows ($0.5 < M < 0.95$), the $D3Q19$ model with a distribution equilibrium function approximated by a third-order Hermite expansion is coupled to an entropy equation to take into account the flow heating due to compression work and viscous dissipation[9] [103]. Finally, for transonic and supersonic flows, the $D3Q39$ model with a modified fifth-order Hermite expansion of the equilibrium distribution function is coupled to an entropy equation, and the capability to simulate flows up to $M \approx 2$ is achieved by introducing an interaction force in the lattice-Boltzmann scheme through which the speed of sound is artificially reduced[10] [103].

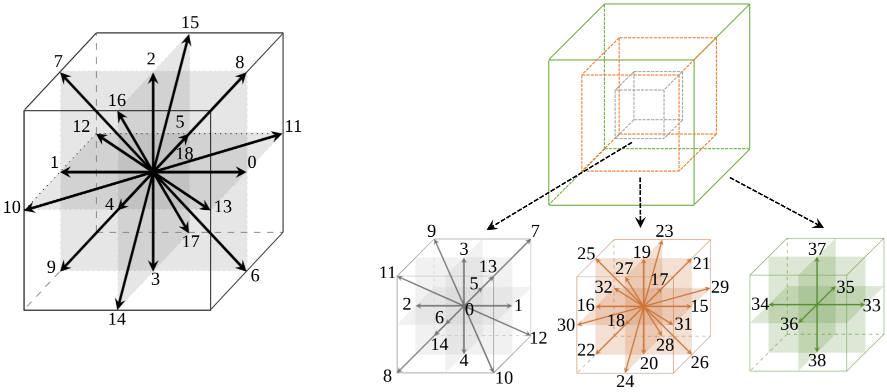

Figure 3.2: Sketches of the $D3Q19$ (left) and $D3Q39$ (right) models showing the discrete velocities $\boldsymbol{\xi}_i$ (adapted from Ref. [104]).

---

[9] Lattice-Boltzmann approaches with full energy conservation can suffer from numerical instability issues unless high-order Hermite expansion and Gauss-Hermite quadrature are used. To overcome these issues, a solution is to solve an additional scalar equation (e.g. for entropy or total energy) and to compute the temperature through it, rather than as a moment of the distribution function. This method allows to increase the dynamic range of the $D3Q19$ model to almost sonic conditions ($M < 0.95$).

[10] The full Navier-Stokes Fourier equations for a monoatomic gas can be completely recovered by a $D3Q121$ lattice-Boltzmann model. However, by increasing the number of velocity states from 39 to 121, the computational cost of the LBM scheme growths dramatically and its computational advantage with respect to Navier-Stokes based approached is largely reduced. Thus, to retain the computational efficiency of the LBM, coupling the $D3Q39$ model to an entropy/total energy equation is preferred, along with the introduction of an artificial interaction force to artificially reduce the speed of sound and increase the maximum Mach number that can be simulated [103].

SPACE AND TIME DISCRETIZATION: THE LATTICE-BOLTZMANN EQUATION

The discrete-velocity Boltzmann equation, Eq. (3.32), is a hyperbolic partial differential equation in the physical space and time. Hence, the *method of characteristics* can be used to integrate Eq. (3.32) along the i^{th} characteristic line $(\mathbf{x}+\boldsymbol{\xi}_i s, t+s)$, namely [81]:

$$\int_0^{\Delta t}\left(\frac{\partial f_i}{\partial t}+\boldsymbol{\xi}_i\cdot\frac{\partial f_i}{\partial \mathbf{x}}\right)\mathrm{d}s=\int_0^{\Delta t}\left(-\frac{1}{\tau}(f_i-f_i^{eq})+F_i\right)\mathrm{d}s, \tag{3.39}$$

where f_i, f_i^{eq} and F_i are to be intended as functions of the parameter s through the independent variables $(\mathbf{x}(s), t(s))$, and s is such that $\mathrm{d}t/\mathrm{d}s=1$ and $\mathrm{d}\mathbf{x}/\mathrm{d}s=\boldsymbol{\xi}_i$. The left hand side of Eq. (3.39) can be integrated exactly [81]:

$$\begin{aligned}\int_0^{\Delta t}\left(\frac{\partial f_i}{\partial t}+\boldsymbol{\xi}_i\cdot\frac{\partial f_i}{\partial \mathbf{x}}\right)\mathrm{d}s&=\\ \int_0^{\Delta t}\left(\frac{\partial f_i}{\partial t}\frac{\mathrm{d}t}{\mathrm{d}s}+\frac{\partial f_i}{\partial \mathbf{x}}\cdot\frac{\mathrm{d}\mathbf{x}}{\mathrm{d}s}\right)\mathrm{d}s&=\\ \int_0^{\Delta t}\frac{\mathrm{d}f_i}{\mathrm{d}s}\mathrm{d}s&=f_i(\mathbf{x}+\boldsymbol{\xi}_i\Delta t, t+\Delta t)-f_i(\mathbf{x},t),\end{aligned} \tag{3.40}$$

while the right-hand side of Eq. (3.39) can be computed through the trapezoidal rule [81]:

$$\begin{aligned}&\int_0^{\Delta t}\left(-\frac{1}{\tau}(f_i-f_i^{eq})+F_i\right)\mathrm{d}s=\\ &-\frac{\Delta t}{2\tau}\left(f_i(\mathbf{x}+\boldsymbol{\xi}_i\Delta t,t+\Delta t)-f_i^{eq}(\mathbf{x}+\boldsymbol{\xi}_i\Delta t,t+\Delta t)+f_i(\mathbf{x},t)-f_i^{eq}(\mathbf{x},t)\right)+\\ &\frac{\Delta t}{2}\left(F_i(\mathbf{x}+\boldsymbol{\xi}_i\Delta t,t+\Delta t)+F_i(\mathbf{x},t)\right)+\mathcal{O}(\Delta t^3),\end{aligned} \tag{3.41}$$

which results in a second-order accuracy time-implicit scheme. However, the scheme can be made explicit by introducing a "corrected" distribution function [81]:

$$\hat{f}_i(\mathbf{x},t)=f_i(\mathbf{x},t)+\frac{\Delta t}{2\tau}\left(f_i(\mathbf{x},t)-f_i^{eq}(\mathbf{x},t)\right)-\frac{\Delta t}{2}F_i(\mathbf{x},t), \tag{3.42}$$

which finally leads to the lattice-Boltzmann equation with BGK collision operator and a body-force term (combining Eqs. (3.40)-(3.42)):

$$\hat{f}_i(\mathbf{x}+\boldsymbol{\xi}_i\Delta t,t+\Delta t)=\hat{f}_i(\mathbf{x},t)-\frac{\Delta t}{\tau+\Delta t/2}\left(\hat{f}_i(\mathbf{x},t)-f_i^{eq}(\mathbf{x},t)-\tau F_i(\mathbf{x},t)\right). \tag{3.43}$$

where the relaxation time τ is related to the fluid kinematic viscosity ν and temperature T through $\nu=(\tau-\Delta t/2)T$ [105]. In Eq. (3.43) the left-hand side is associated to the integration along characteristics, while the right hand side is related to the local collision operator. Therefore, the lattice-Boltzmann equation can be interpreted as a streaming (or propagation) and collision algorithm [81]. In the collision step, f_i^{eq} and F_i are computed (respectively through Eqs. (3.33) and (3.34) with an appropriate order of truncation N), at time t and in a point $\mathbf{x}$ of the Cartesian grid, in order to evaluate the distribution function $\hat{f}_i^*$ after collisions:

$$\hat{f}_i^*(\mathbf{x},t) = \hat{f}_i(\mathbf{x},t) - \frac{\Delta t}{\tau + \Delta t/2}\left(\hat{f}_i(\mathbf{x},t) - f_i^{eq}(\mathbf{x},t) - \tau F_i(\mathbf{x},t)\right) \quad \text{for } i = 0,\ldots,V-1. \tag{3.44}$$

Then, in the propagation step, the resulting distribution functions $\hat{f}_i^*$ are streamed to the neighboring Cartesian grid nodes according to [81]:

$$\hat{f}_i(\mathbf{x}+\boldsymbol{\xi}_i\Delta t, t+\Delta t) = \hat{f}_i^*(\mathbf{x},t) \quad \text{for } i = 0,\ldots,V-1. \tag{3.45}$$

LBM ALGORITHM

In view of the above, the LBM algorithm can be summarized in the following steps:

1. Computation of external body-forces (if needed);
2. Evaluation of the macroscopic hydrodynamic quantities from Eqs. (3.35)-(3.38) based on the new variable $\hat{f}_i$ [81], with correction of the macroscopic velocity and temperature in the presence of body-forces according to $\boldsymbol{u}^* = \boldsymbol{u} + \Delta t\boldsymbol{b}/2$ and $T^* = T + \Delta t^2|\boldsymbol{b}|^2/(4D)$ (if needed) [106];
3. Calculation of f_i^{eq} and F_i through Eqs. (3.33) and (3.34), respectively;
4. Collision step (Eq. (3.44));
5. Streaming step (Eq. (3.45));
6. Application of boundary conditions;
7. Time step update and repetition from step 1 until the last time step.

As mentioned, the LBM scheme is solved on a Cartesian mesh composed of cubic volumetric elements (voxels). Different Variable Resolution (VR) regions can be defined within the fluid domain in order to increase the volume discretization in regions of interest or where high flow gradients are expected. Because a Cartesian mesh is employed by the solver, a variable grid resolution by a factor of two is allowed between two adjacent VRs. Moreover, because the solver uses an explicit time-marching scheme based on a unitary Courant-Friedrichs-Lewy condition (i.e. $\text{CFL} = |\boldsymbol{\xi}_i\Delta t|/|\Delta\boldsymbol{x}_i| = 1$), the time step is also varied by a factor of two between two adjacent VRs, with the solution in coarser VRs updated at a lower rate compared to finer VRs. Therefore, a balanced domain decomposition based on the equivalent number of voxels updated at every time step (i.e. Fine Equivalent Voxels, FEVoxels) allows for an efficient speed-up of the transient flow simulation.

The surface of solid bodies is automatically facetized within each voxel intersecting the wall geometry using planar surface elements (surfels). Therefore, complex arbitrary geometries can be treated automatically by the LBM solver, simplifying the cumbersome manual work typically associated with the volume meshing step using body-fitted CFD approaches. Moreover, in PowerFLOW®, boundary conditions are implemented through a particle reflection process, in which the changes in the momentum components perpendicular and tangential to a surfel correspond to pressure and friction (wall shear stress) forces, respectively. In particular, a boundary scheme based on a particle bounce-back process (in which both the normal and tangential components of f_i are inverted) and a specular reflection process (in which only the normal component of f_i is inverted, while the tangential one is unchanged) is respectively implemented to impose no-slip and slip wall boundary conditions at each surfel [31], as illustrated in Fig. 3.3 for a generic surfel aligned with the lattice. For surfels that are not aligned with the lattice, a more general volumetric boundary scheme is adopted. The interested reader can refer to Ref. [31] for further details.

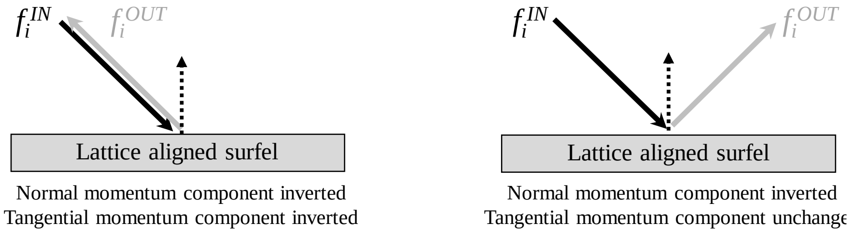

Figure 3.3: Implementation of boundary conditions in LBM for a lattice aligned surfel.

SIMULATION OF ROTATING GEOMETRIES

For simulations with a rotating geometry in time around a fixed axis, the computational domain is decomposed into an outer "ground-fixed" reference frame and an inner "body-fixed" Local Reference Frame (LRF). The latter is characterized by an axisymmetric volume grid which rigidly rotates with the rotating geometry in such a way that no relative motion between the LRF grid and the enclosed geometry occurs. Outside the LRF the fluid flow is solved using Eq. (3.43) without the body-force term, whereas the full Eq. (3.43) is used inside it, with the external body-force acceleration $\boldsymbol{b}$ corresponding to the inertial force related to the non-inertial rotating LRF [107]:

$$\boldsymbol{b}(\mathbf{x},t) = -\boldsymbol{\Omega}(t)\times\big(\boldsymbol{\Omega}(t)\times\boldsymbol{r}(\mathbf{x},t)\big) - 2\boldsymbol{\Omega}(t)\times\boldsymbol{u}^*(\mathbf{x},t) - \frac{\mathrm{d}\boldsymbol{\Omega}(t)}{\mathrm{d}t}\times\boldsymbol{r}(\mathbf{x},t), \tag{3.46}$$

where $\boldsymbol{\Omega}(t)$ is the angular velocity of the LRF, $\boldsymbol{r}$ is the radial vector from the center of rotation to the local voxel and $\boldsymbol{u}^*$ is the pre-collide fluid velocity $\boldsymbol{u}$ corrected by $\Delta t\boldsymbol{b}/2$, namely $\boldsymbol{u}^* = \boldsymbol{u} + \Delta t\boldsymbol{b}/2$. A surface treatment scheme is used between the boundaries of the outer and inner reference frames in such a way that the conservation laws are fulfilled across the LRF interface [107].

LBM-VLES TURBULENCE MODELING

The solution of the lattice-Boltzmann equation (Eq. (3.43)) is equivalent to perform a Direct Numerical Simulation (DNS) of the Navier-Stokes equations in the limit of the dynamic range (i.e. Mach number) that can be accurately covered by the lattice velocities $\boldsymbol{\xi}_i$ and of the grid resolution required to resolve the smallest scales of turbulence. However, for high Reynolds number flows, the computational cost associated to LBM-DNS simulations is prohibitively expensive, and the use of turbulence modeling is required. The LBM can be generally coupled to different turbulence modeling methods, such as one- or two-equation turbulence models, hybrid approaches or LES sub-grid scale models, through which evaluating a turbulent relaxation time (τ_{turb}) that is added to the viscous/laminar one (τ). Note that for a LBM-DNS or LBM-ILES[11] simulations such a turbulent relaxation time is zero.

In PowerFLOW®, turbulence modeling is incorporated into the LBM scheme [32] by applying a modified two-equation $k-\epsilon$ model, based on the re-normalization group (RNG) formulation [109, 110], on the unresolved scales [111], which are selected through a model based on the local flow swirl [112]. This approach is referred to as LBM-Very Large Eddy Simulation (LBM-VLES) and is conceptually similar to non-zonal hybrid RANS/LES, DES or Scale Adaptive Simulations approaches [80]. In particular, the two-equation RNG $k-\epsilon$ model, which is modified to incorporate a swirl correction and is solved on the same LBM grid with a second order time-explicit finite-difference scheme, is used to compute a turbulent relaxation time that is added to the viscous relaxation time, i.e. $\tau \rightarrow \tau_{eff}$:

$$\tau_{eff} = \tau + \tau_{turb} = \tau + C_\mu \frac{k^2/\epsilon}{T(1+\tilde{\eta}^2)^{1/2}}, \tag{3.47}$$

where $C_\mu = 0.09$, k and ϵ are the turbulent kinetic energy and dissipation, respectively, and $\tilde{\eta}$ is a function of a local strain parameter $\eta_s = k|S_{ij}|/\epsilon$, a local vorticity $\eta_\omega = k|\Omega_{ij}|/\epsilon$ parameter and a local helicity parameter. The swirl correction incorporated into the modified RNG $k-\epsilon$ model is employed to reduce impact of the modeled eddy viscosity in regions of high vorticity, in order to locally resolve large anisotropic vortical structures where the underlying computational grid is fine enough [113]. It should be pointed out that the above mentioned approach is not equivalent to use a RNG $k-\epsilon$ model as in a RANS method. In the present method, there is no explicit modification of the eddy viscosity in the sense that the modeled Reynolds stresses are not explicitly added to the governing equations, as in RANS approach. Instead, the RNG $k-\epsilon$ model is used to modify the evolution of the system of particles towards the thermodynamic equilibrium (through a variation of the relaxation time), in a way that is consistent with the characteristic time scales of a turbulent flow, leading to Reynolds stresses that are the result of the LBM computation and not of a semi-empirical modeling [33, 67].

WALL MODELING

Since the LBM employs a Cartesian mesh, different volume cell sizes along the three (or two) spatial dimensions, as well as a stretch of the grid only in the wall normal direction, is not possible. As a consequence, the resolution of the boundary layer down to the no-slip wall, which would require a wall-normal distance in viscous units (y^+) less than 1 [29], is prohibitively expensive in high Reynolds number applications. Therefore, a wall function approach is used in PowerFLOW® to model boundary layers on solid surfaces. The wall function model is an extension of the standard law-of-the-wall formula-

---

[11] In an Implicit Large Eddy Simulation (ILES) the inviscid energy cascade through the inertial range is captured by the numerical scheme and the inherent numerical dissipation acts as a sub-grid model [108].

tion [114], which includes the effects of favorable and adverse pressure gradients [111]:

$$u^+ = \begin{cases} y^+ & \text{if } y^+ \leq 5 \\ \frac{1}{\kappa}\ln\left(\frac{y^+}{A}\right) + B & \text{otherwise,} \end{cases} \tag{3.48}$$

where $u^+ = u_s/u_\tau$ and $y^+ = yu_\tau/\nu$ (with $u_\tau = \sqrt{\tau_w/\rho}$ and $\tau_w = \frac{1}{2}\rho C_f u_s^2$ being the friction velocity and the wall shear-stress) are the well-known dimensionless velocity and wall-distance coordinate, respectively. κ and B are empirically determined constants equal to 0.41 and 5 in the logarithmic region ($30 \leq y^+ \leq 300$). In the buffer region ($5 < y^+ < 30$), their values are adjusted to provide continuity between the equations used in the viscous sub-layer and logarithmic regions. The model takes into account the fact that the velocity profile slows down and expands due to an adverse pressure gradient through a function A. The expression of the scaling function A is given by:

$$A = \begin{cases} 1 + \ell \left|\frac{\mathrm{d}p}{\mathrm{d}\tilde{s}}\right| / \tau_w & \text{if} \quad \hat{\boldsymbol{u}}_{\boldsymbol{s}} \cdot \frac{\mathrm{d}p}{\mathrm{d}\tilde{s}} > 0 \\ 1 & \text{otherwise,} \end{cases} \tag{3.49}$$

where $\mathrm{d}p/\mathrm{d}\tilde{s}$ is the streamwise pressure gradient, $\hat{\boldsymbol{u}}_{\boldsymbol{s}}$ is the unit vector of the local slip velocity u_s and ℓ is a length-scale of the same order of the unresolved near-wall region. Equation (3.48) and $\tau_w = \rho u_\tau^2 = \frac{1}{2}\rho C_f u_s^2$ represent a system of two equations in the two unknowns C_f and u_τ, which is solved to specify a wall-shear stress for the wall boundary condition in the LBM scheme consistent with the law-of-the-wall [111]. The wall model is also used to provide the boundary conditions for the modified RNG $k-\epsilon$ turbulence model, namely $k = u_\tau^2/\sqrt{C_\mu}$ and $\epsilon = u_\tau^3/(\kappa y)$, where y is the wall-normal distance of the "slip" surface from the wall [111].

ACOUSTIC PROPERTIES OF THE LBM

As previously mentioned, the LBM is inherently unsteady and compressible, thus allowing the possibility to perform direct noise extraction from the CFD simulations. Brès *et al.* [115] have analyzed the acoustic properties of the LBM implemented in PowerFLOW® by considering the temporal decay of a standing planar wave in a periodic fluid domain, as well as the spatial decay of a propagating planar Gaussian acoustic pulse, both across a uniform computational grid. By comparison with theoretical predictions, they showed the low dispersive and dissipative errors[12] of the LBM, and hence the fact that the LBM can be used, in principle, for simulating acoustic propagation in the time-domain. Moreover, they performed both LBM-DNS and LBM-VLES simulations and pointed out that turbulence modeling, while does not introduce additional dispersion into the LBM scheme, increases the numerical dissipation inversely to the grid resolution or number of points per acoustic wavelength (N_{ppw}). Finally, they calculated the loss in dB, both per wavelength and per cell of propagation, in order to provide guidelines to estimate the resolution requirements for industrial applications. The showed that the former has an approximate $1/N_{ppw}$ dependency, while a $1/N_{ppw}^2$ scaling was found for the latter. Moreover, they estimated a loss of about 0.068 dB per wavelength

---

[12] An error introduced by a numerical scheme on the amplitude of a propagating wave is called dissipation error, whereas the dispersion error is related to acoustic waves of different wavelengths propagating at different speeds.

for $N_{ppw} = 12 - 16$ and of 0.0046 dB per cell of propagation at $N_{ppw} = 14$, both resulting in an attenuation of less than 1 dB at 5kHz and 1 m distance from the acoustic source.

However, for cases of industrial relevance, the coupling of the LBM with a Ffowcs Williams & Hawkings' acoustic analogy is typically necessary in order to relax the far-field grid resolution requirements and compute the noise in the acoustic far-field at an acceptable computational cost. Therefore, although direct noise computation is theoretically possible with the lattice-Boltzmann method, a hybrid LBM/FW-H approach is generally preferred. All the far-field noise computations performed throughout this thesis are based on this hybrid methodology, in which the LBM is used to accurately compute the near-field unsteady and compressible flow solution, and the FW-H acoustic analogy is used for computing the resulting far-field noise radiation. The following section presents a brief derivation and description of the FW-H acoustic analogy.

3.3. FFOWCS WILLIAMS & HAWKINGS' ACOUSTIC ANALOGY

This section describes the acoustic analogy that is used throughout this thesis to compute the sound generated aerodynamically by moving surfaces, with the flow data on the surface provided by transient and compressible LBM computations. It is based on the source-time dominant [89] solution of the formulation 1A proposed by Farassat [116] as solution of the Ffowcs Williams & Hawkings' (FW-H) equation [34]. Two different FW-H solvers are used in this thesis. The first is part of the post-processing software SIMULIA PowerACOUSTICS®, while the second, *Opty∂B*-PFNOISESCAN, is part of the SIMULIA *Opty∂B* toolkit. In this section, the FW-H equation is introduced first. Then, Farassat's formulation 1A of the FW-H equation is described. The retarded (observer-time) and advanced (source-time) time solutions of the FW-H equation are discussed along with the differences between solid and permeable formulations.

3.3.1. THE FFOWCS WILLIAMS & HAWKINGS' EQUATION

The Ffowcs Williams & Hawkings' equation [34, 117] represents an extension of the Lighthill's acoustic analogy [53] from an arbitrary region of turbulence surrounded by a quiescent unbounded fluid to flows confined by surfaces in arbitrary motion. The FW-H equation is an exact rearrangement of the Navier-Stokes' equations into an inhomogeneous wave equation that includes the effects of surfaces in arbitrary motion on the right-hand side. The key idea of an acoustic analogy is to separate the flow into a region of non-zero equivalent noise sources and an acoustic propagation region of quiescent fluid with vanishing sources. Another assumption behind the concept of acoustic analogy is that there is no flow-acoustic coupling occurs, namely the acoustic field does not influence the noise source.

The starting point of the FW-H acoustic analogy is the definition of a control surface S described by a function $f(\mathbf{x}, t) = 0$, which moves with velocity $\mathbf{v}(\mathbf{x}, t)$, with $\mathbf{x}$ and t being the observer position and (reception) time, respectively. The function f is such that is smaller than zero in the flow portion enclosed by the surface and larger than zero outside it, as depicted in Fig. 3.4.

In Fig. 3.4, $\hat{\mathbf{n}}$ is the normal unit vector to the surface S pointing in the outward direction, such that $\nabla f = \hat{\mathbf{n}}$. In addition, $\mathbf{u}$ and $\mathbf{v}$ are the flow and integration surface velocity

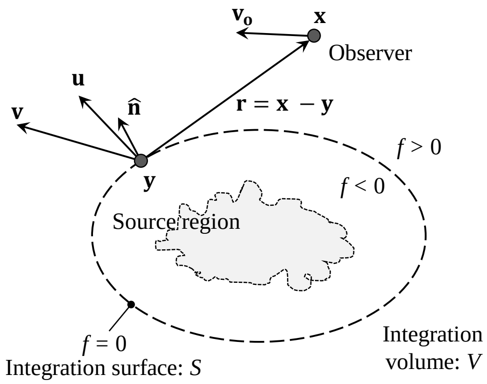

Figure 3.4: Problem definition of the FW-H acoustic analogy, adapted from Casalino [89].

vectors, while $\mathbf{y}$ denotes the position of the source. The observer moves at velocity $\mathbf{v}_\mathrm{o}$. It is assumed that the inner volume of the control surface is replaced with fluid at rest (ρ_0, p_0 and $u_i = 0$), where ρ, p and u_i are the flow density, pressure and velocity. To preserve the conservative character of the field a distribution of mass and momentum sources is imposed on the control surface. This can be expressed in term of generalized continuity and momentum equations making use of the Dirac $\delta(f)$ and Heaviside $H(f)$ generalized function as follows:

$$\frac{\bar{\partial}}{\partial t}\left[(\rho - \rho_0)\, H(f)\right] + \frac{\bar{\partial}}{\partial x_i}\left[\rho\, u_i\, H(f)\right] = Q\,\delta(f) \quad \text{with} \tag{3.50}$$

$$Q = \rho_0\, U_i\, \hat{n}_i \quad \text{and} \quad U_i = \left(1 - \frac{\rho}{\rho_0}\right) v_i + \frac{\rho\, u_i}{\rho_0}, \tag{3.51}$$

and

$$\frac{\bar{\partial}}{\partial t}\left[\rho\, u_i\, H(f)\right] + \frac{\bar{\partial}}{\partial x_j}\left[(\rho\, u_i\, u_j + P_{ij})\, H(f)\right] = L_i\,\delta(f) \quad \text{with} \tag{3.52}$$

$$L_i = P_{ij}\,\hat{n}_j + \rho\, u_i\,(u_n - v_n) \quad \text{and} \quad P_{ij} = (p - p_0)\,\delta_{ij} - \tau_{ij}, \tag{3.53}$$

where

$$\frac{\bar{\partial} H(f)}{\partial t} = \delta(f)\,\frac{\partial f}{\partial t} = -\delta(f)\, v_n \quad \text{and} \quad \frac{\bar{\partial} H(f)}{\partial x_i} = \delta(f)\,\frac{\partial f}{\partial x_i} = \delta(f)\,\hat{\mathbf{n}}, \tag{3.54}$$

denote generalized derivatives, while the terms on right-hand side of Eqs. (3.50) and (3.52) represent the mass and momentum source distributions on the integration surface S, respectively. In Eqs. (3.53), P_{ij} and τ_{ij} are the compressive and viscous stress tensors, while δ_{ij} indicates the well-known Kronecher's delta. Note that the presence of the Heaviside function $H(f)$ on the left-hand side terms of Eqs. (3.50) and (3.52) restores quiescent conditions inside the integration surface ($H(f) = 0$ inside S and $H(f) = 1$ outside it).

Equations (3.50) and (3.52) can be rearranged into an inhomogeneous wave equation, which includes the effects of surfaces in arbitrary motion on the right-hand side as source terms, by subtracting the divergence of Eq. (3.52) to the time derivative of Eq. (3.50), namely:

$$\overline{\Box}^2 \{p' H(f)\} = \frac{\bar{\partial}}{\partial t}\{Q\delta(f)\} - \frac{\bar{\partial}}{\partial x_i}\{L_i \delta(f)\} + \frac{\bar{\partial}^2}{\partial x_i \partial x_j}\{T_{ij} H(f)\}, \tag{3.55}$$

which represents the FW-H equation for the acoustic pressure p' in differential form[13], where $\overline{\Box}^2$ is the wave or D'Alembertian operator in three dimensional space (with generalized differential operators) and $T_{ij} = \rho u_i u_j + (p' - c_0^2 \rho')\delta_{ij} - \tau_{ij}$ being the perturbation form of the Lighthill's stress tensor. It follows from Eq. (3.55) that the pressure fluctuations in the fluid outside S are the same as those associated to an equivalent quiescent acoustic medium forced by three source terms. The first two terms on the right-hand side of Eq. (3.55), which have the mathematical form of monopole and dipole terms[14], respectively, represent surface source term distributions, as suggested by the presence of the Dirac function $\delta(f)$. On the other hand, the third term, known as quadrupole source, is a volume distribution due to the presence of the Heaviside function $H(f)$. For a control surface S coinciding with a solid (i.e. impenetrable) surface, all the three source terms have a physical meaning. In particular, the monopole (or thickness) term represents the fluid displacement effects generated by the movement of the body, while the dipole (or loading) term accounts for the unsteady loading applied by the surface on the surrounding fluid. Finally, the quadrupole term includes all physical sources and non-linear effects (e.g. shocks, turbulence/vorticity, non-linear propagation, etc.) in the volume outside the integration surface S ($f > 0$).

3.3.2. Farassat's formulation 1A of the FW-H equation

An integral representation of the FW-H equation can be derived by convoluting Eq. (3.55) with the free-space Green's function, defined as $G = \delta(g)/(4\pi r)$, with $g = t - \tau - r/c_0$, $r = |\mathbf{x} - \mathbf{y}|$ and τ representing the source (emission) time, and by using the Heaviside and

---

[13] Equation (3.55) is derived under the hypothesis of isentropic flow (reasonably valid for the typical source-observer distances commonly encountered in applications of practical interest), for which the density fluctuations are small and the pressure-density relationship can be approximated as:

$$p \approx p_0 + \left.\frac{\partial p}{\partial \rho}\right|_s (\rho - \rho_0) \rightarrow p' = c_0^2 \rho', \tag{3.56}$$

where $\rho' = (\rho - \rho_0)$ and $p' = (p - p_0)$ are the density and pressure fluctuations, while $c_0^2 = \left.\frac{\partial p}{\partial \rho}\right|_s$ is the isentropic speed of sound in the quiescent flow. Note that p' can be conceived as acoustic pressure only if $\rho'/\rho_0 << 1$.

[14] These are often referred to as thickness and loading terms, respectively. However, such a terminology is not appropriate for permeable surfaces, as they correspond to thickness and loading terms only if $u_n = v_n$ on the surface $f = 0$ (namely for impermeable surfaces).

Dirac functions properties:

$$\begin{aligned}4\pi\, p'(\mathbf{x},t) = {} & \frac{\partial^2}{\partial x_i \partial x_j}\int_{-\infty}^{t}\int_{f>0}\frac{\delta(t-\tau-r/c_0)}{r}\,T_{ij}\,\mathrm{d}V(\mathbf{y})\,\mathrm{d}\tau \\ & -\frac{\partial}{\partial x_i}\int_{-\infty}^{t}\int_{f=0}\frac{\delta(t-\tau-r/c_0)}{r}\,L_i\,\mathrm{d}S(\mathbf{y})\,\mathrm{d}\tau \\ & +\frac{\partial}{\partial t}\int_{-\infty}^{t}\int_{f=0}\frac{\delta(t-\tau-r/c_0)}{r}\,Q\,\mathrm{d}S(\mathbf{y})\,\mathrm{d}\tau. \end{aligned} \tag{3.57}$$

In the previous equation, the integration variable can be changed by considering that [89]:

$$\int_{-\infty}^{t}\mathscr{F}(\tau)\,\delta\big(g(\tau)\big)\,\mathrm{d}\tau = \sum_{n=1}^{N}\frac{\mathscr{F}}{\left|\partial g/\partial\tau\right|}(\tau_n^*) \quad \text{and} \quad \frac{\partial g}{\partial \tau} = -1 + M_r, \tag{3.58}$$

where the summation is to be taken over the zeros τ_n^* of the retarded time equation[15], $g = t-\tau-r/c_0 = 0$, and $M_r = M_i\hat{r}_i$ is the projection of the source Mach number vector $\mathbf{M} = \mathbf{U}/c_0$ (with $\mathbf{U} = \{U_i\}$) in the direction of the observer, defined by the unit vector $\hat{r}_i = (x_i - y_i)/r$. The absolute value of the source-time derivative of the retarded time equation, $|1-M_r|$ is the Jacobian of transformation from the τ variable to the g variable in Eq. (3.58), which represents the Doppler effects, namely the dilatation/contraction of the observer time scale with reference to the source time one, when the source moves away from/towards the listener. Hence, for a subsonically moving surface[16], Eq. (3.57) can be rewritten as:

$$\begin{aligned}4\pi\, p'(\mathbf{x},t) = {} & \frac{\partial^2}{\partial x_i \partial x_j}\int_{f>0}\left[\frac{T_{ij}}{r\,(1-M_r)}\right]_{\mathrm{ret}}\mathrm{d}V(\mathbf{y}) \\ & -\frac{\partial}{\partial x_i}\int_{f=0}\left[\frac{L_i}{r\,(1-M_r)}\right]_{\mathrm{ret}}\mathrm{d}S(\mathbf{y}) \\ & +\frac{\partial}{\partial t}\int_{f=0}\left[\frac{Q}{r\,(1-M_r)}\right]_{\mathrm{ret}}\mathrm{d}S(\mathbf{y}), \end{aligned} \tag{3.59}$$

where the subscript ret denotes that the integrals are computed at the retarded time $\tau = t - \left|\mathbf{x}(t)-\mathbf{y}(\tau)\right|/c_0$. By transforming space derivatives into time derivatives, moving the latter inside the integrals (for more details the interested reader may refer to Refs. [89, 116, 117]) and neglecting the quadrupole term $p'_Q(\mathbf{x},t)$ (which implies that all the linear sources outside the integration surface will be discarded), Eq. (3.59) can be rewritten as

---

[15] For a subsonically moving source there is only one solution of the retarded time equation for a given τ, while up to three zeros can exists for the case of a supersonically rotating source.

[16] The absolute value sign for $|1-M_r|$ can be dropped for subsonic moving sources since $1-M_r < 1$ always.

$p'(\mathbf{x},t) = p'_T(\mathbf{x},t) + p'_L(\mathbf{x},t)$, where:

$$\begin{aligned}
4\pi\, p'_T(\mathbf{x},t) &= \int_{f=0} \left[\frac{\rho_0 \left(\dot{U}_n + U_{\dot{n}}\right)}{r\,(1-M_r)^2} \right]_{\mathrm{ret}} \mathrm{d}S(\mathbf{y}) \\
&+ \int_{f=0} \left[\frac{\rho_0\, U_n \left(r\dot{M}_r + c_0\left(M_r - M^2\right)\right)}{r^2\,(1-M_r)^3} \right]_{\mathrm{ret}} \mathrm{d}S(\mathbf{y}), \qquad (3.60) \\
4\pi\, p'_L(\mathbf{x},t) &= \frac{1}{c_0}\int_{f=0} \left[\frac{\dot{L}_r}{r\,(1-M_r)^2} \right]_{\mathrm{ret}} \mathrm{d}S(\mathbf{y}) + \int_{f=0} \left[\frac{L_r - L_M}{r^2\,(1-M_r)^2} \right]_{\mathrm{ret}} \mathrm{d}S(\mathbf{y}) \\
&+ \frac{1}{c_0}\int_{f=0} \left[\frac{L_r \left(r\dot{M}_r + c_0\left(M_r - M^2\right)\right)}{r^2\,(1-M_r)^3} \right]_{\mathrm{ret}} \mathrm{d}S(\mathbf{y}), \qquad (3.61)
\end{aligned}$$

which represents the Farassat's formulation 1A used throughout this thesis. For an impermeable surface ($u_n = v_n$) Eqs. (3.60) and (3.61) assume the physical meaning of thickness and loading noise, respectively. In the above equations, dots on quantities denote time derivatives with respect to the source time τ (differing from the observer time t) observed in a reference frame fixed with undisturbed medium, the subscripts r and n denote the projections along the radiation and surface normal directions, respectively, while $U_{\dot{n}} = U_i \dot{\hat{n}}_i$ and $L_M = L_i M_i$. All the other quantities have been previously introduced.

RETARDED AND ADVANCED TIME SOLUTIONS OF THE FW-H EQUATION

Two different methods can be used to compute the integral solution of the FW-H equation (Eqs. (3.60) and (3.61)), which are referred to as *retarded-time* and *advanced-time* approaches [89].

In the retarded-time algorithm, the computational time considered is that of the observer, i.e. the reception time t. The acoustic disturbances that contribute to the acoustic signal perceived by the observer at the time t are generated at different retarded times τ and cover different distances $|\mathbf{x}(t) - \mathbf{y}(\tau)|/c_0$, depending on the specific source on the integration surface. This approach requires the evaluation of the roots[17] τ of the retarded-time equation, $t - \tau - |\mathbf{x}(t) - \mathbf{y}(\tau)|/c_0 = 0$, as well as the interpolation of the original discrete time-varying flow data at the time τ for each integration surface mesh element. For simple source motions, an analytical expression can be derived to determine the roots of the retarded-time equation. In general, for complex source motions an iterative scheme is usually required.

In the advanced-time approach, the computational time considered is that of the source, i.e. τ. For each integration surface element, the acoustic disturbance and the time at which it will reach the observer, namely $t = \tau + |\mathbf{x}(t) - \mathbf{y}(\tau)|/c_0$, are computed. Then, since t is not equally spaced for all the source elements because of Doppler effects, an interpolation of the acoustic disturbance time histories on an equally spaced reception time vector must be performed, prior to summing up all the contributions from the different surface elements. If the observer is stationary and/or moves at constant velocity, the observer time t can be computed explicitly [89].

---

[17] There might exist more than one solution for supersonically moving sources.

As previously mentioned, both the two FW-H solvers used in this thesis are based on the advanced-time solution of the FW-H equation. A first advantage of this formulation over the retarded-time one is its higher computational efficiency (i.e. fewer floating point operation required) for a large number of elements on the integration surface, for a large number of time steps in the observer time history and/or when the number of coordinate transformations to be computed is high [118]. Moreover, the advanced-time algorithm allows to compute the integrands in Eqs. (3.60) and (3.61) at those time instants that are already available in the flow data solution, without the need for time interpolation of the original discrete transient flow data at the retarded time. Hence, the advanced-time method needs to access to the integration surface data at just one source time step at a time, while retarded-time approaches call for continual access to a large portion of information regarding the integration surface (since the acoustic signal for a single observer is the sum of contributions from surface elements emitted at different source times) [119]. This makes advanced-time approaches more memory efficient than retarded-time ones [119]. Finally, another advantage of the advanced-time approach is the possibility to perform an on-the-fly aeroacoustic computation in parallel to the CFD simulation, without the need to store large amount of aerodynamic data [89].

SOLID AND PERMEABLE FW-H APPROACHES

In deriving the FW-H equation, Eq. (3.55), a generic *permeable* or *porous* integration surface S has been considered, not necessarily corresponding to the surface of a body. For an integration surface coinciding with a physical body, the velocity of the flow on a point on the surface is equal to that of a surface itself, namely $u_i = v_i$, and the FW-H approach is referred to as *solid* or impenetrable. In such a case, the terms:

$$Q = \rho_0 U_n \quad \text{and} \quad L_i = (p - p_0)\delta_{ij}\hat{n}_j - \tau_{ij}\hat{n}_j + \rho u_i(u_n - v_n), \tag{3.62}$$

in Eq. (3.55) respectively reduce to:

$$Q = \rho_0 v_n \quad \text{and} \quad L_i = (p - p_0)\delta_{ij}\hat{n}_j - \tau_{ij}\hat{n}_j, \tag{3.63}$$

and the thickness and loading noise terms recover their physical meaning as previously pointed out.

Several solutions of the FW-H equation, such as the formulation 1A by Farassat that is used in this thesis, neglect the quadrupole term $p'_Q(\mathbf{x}, t)$, due to the fact that its computation involves a volume integration that is time consuming and not straightforward to be performed. As previously mentioned, the quadrupole term accounts for all the noise sources in the volume V outside the integration surface: shocks, turbulence and non-linear propagation. Hence, adopting a solid FW-H approach without the volume term might result in erroneous computations whenever the quadrupole effects are relevant (e.g. for jets or rotors at transonic blade-tip Mach numbers). To overcome this problem, a permeable FW-H approach can be employed following the idea that all the quadrupole sources that provide a non-negligible contribution to the acoustic signature are included inside the porous integration surface [78, 117, 120].

As firstly shown by di Francescantonio for a helicopter rotor in hover condition [120], placing the integration surface away from the physical surface of the body allows to retrieve the quadrupole contributions within the surface through the surface source terms, namely Eqs. (3.60) and (3.61). Nevertheless, neglecting the volume integral in a permeable FW-H approach can lead to the generation of so-called *spurious noise* signals when all the relevant quadrupole sources are not completely included inside the integration surface [121]. In such a case, the assumption that all the quadrupoles are surrounded by the surface is no longer valid, and the choice of neglecting the volume integral can be questioned. Since the FW-H equation is an exact rearrangement of the continuity and momentum equations, it accounts for both hydrodynamic and acoustic phenomena. Moreover, the integral solution of the FW-H equation is based on the use of the free-space Green's function. Hence, vortical structures passing through the porous integration surface would radiate as (non-physical) sound [122]. This spurious noise would be canceled by the contribution associated to the volume integration of the quadrupole sources outside the integration surface. Thus, the spurious noise is a consequence of the fact that only the quadrupole sources inside the integration surface are accounted for, while those outside it are discarded [122].

When employing a permeable FW-H approach, the integration surface should be ideally placed in a region of high resolution of the CFD grid to ensure a proper simulation of turbulence-related phenomena (when concerned) and of the acoustic propagation up to the integration surface. This generally correspond to the near-body volume region. Placing the FW-H surface in too close proximity to the body, which would be beneficial in terms of computational cost, might be critical from the point of view of the spurious noise, as previously discussed. However, different strategies can be adopted to limit the generation of spurious noise for a permeable FW-H acoustic analogy. The most relevant ones from an industrial perspective are briefly summarized in the following.

The most simple approach is to use an *open integration surface* to exclude that surface portion contaminated by the hydrodynamic structures from the noise computation [122]. The main drawback of this method is that also the (physical) acoustic contribution from the same removed surface is discarded from the computation, thus introducing potential errors in the noise directivity, especially for observer angles perpendicular to the omitted surface.

Another possible solution is the definition of a *departure region*, in which the porous integration surface is extended far enough away from the body and a gradual coarsening of the underlying CFD mesh is carried out. The philosophy behind this approach is to let the simulation completely or partially dissipate, through numerical dissipation or subgrid-scale modeling, the small-scale turbulence before it crosses the permeable integration surface [123]. However, the definition of such a departure region is not trivial, since starting it too close from the body might influence the aerodynamic solution of the solid body itself. Moreover, it introduces a non-physical damping of the turbulent structures, which might result in accurately computing the noise associated to non-physical quadrupole sources.

A quite often employed and effective strategy is that based on the use of multiple porous surfaces with different downstream *end-caps* in which the noise evaluated from each surface is averaged in the time- or frequency-domain to filter the hydrodynamic spurious content out from the acoustic signature [124]. The idea behind this *cap-averaging* approach is that the noise signature computed with the FW-H equation collects the surface source contributions that travels towards the observer at the speed of sound. Hence, the contribution of a relatively large eddy on a certain end-cap, which generates spurious noise through the surface integrals of the FW-H equation and travels at the convective velocity, is substantially reduced by the averaging process that is carried out with the other end-caps, which do not simultaneously perceive the same vortical structure and thus do not emit the same spurious acoustic waves [123].

Finally, more complex methods based on approximate corrections under the assumption of frozen turbulence passing through the end-caps have been proposed by several authors [125–127]. However, although these approaches have been attempted with some success in the past years, their application remains challenging and impractical for cases of industrial relevance.

4

AIRFOIL BLADE TRAILING-EDGE NOISE & REDUCTION

We see only what we know.

Johann Wolfgang von Goethe

Chapter 3 introduced the computational aeroacoustic methodology that is used throughout this thesis, namely the hybrid Lattice-Boltzmann/Ffowcs Williams & Hawkings approach. This method is used in the present chapter to predict the most elementary, yet dominant, source of broadband noise for a rotating blade in a homogeneous stationary flow, namely the turbulent boundary-layer trailing-edge noise. Emphasis is given to its prediction for a cambered airfoil operating at a moderate Reynolds number and undergoing natural boundary-layer transition, as well as to its reduction by means of serrations retrofitted to the airfoil section at different flap angles. The aim of this chapter is to provide insights in the impact of the serration flap angle on the effectiveness of sawtooth serrations into reducing noise. Three different serration flap angles are considered. It is found that the serration flap angle primarily affects the trailing-edge noise reduction through a modification of: (i) the effective angle at which the turbulent structures are convected over the serrated edge; (ii) the convection velocity and spanwise coherence length along the serration; (iii) the intensity of the hydrodynamic wall-pressure fluctuations that are scattered along the serrated edge. The first and last phenomena are expected to play the most important role on the far-field noise reduction.

Parts of this chapter have been published in the AIAA journal (2021) [128].

4.1. INTRODUCTION

AIRFOIL blade self-noise, caused by the airfoil interaction with the self-generated flow disturbances, is widely considered as one of the most important sources of aerodynamic noise for applications involving rotating blades, such as helicopter rotors [129, 130], aircraft propellers [26, 35], low-speed fans [50, 131] and wind turbines [132, 133]. Among the different aerodynamic noise mechanisms that can be ascribed to airfoil self-noise [37], the turbulent boundary-layer trailing-edge noise is of primary interest, being the dominant broadband noise contributor for a rotating blade in a homogeneous stationary flow [37, 50]. As discussed in Sec. 2.1.1, trailing-edge noise is the sound associated to the scattering of the turbulent boundary-layer pressure fluctuations at the airfoil trailing-edge. When the boundary-layer pressure waves encounter a surface discontinuity, such as the airfoil trailing-edge, the hydrodynamic turbulent energy is converted into acoustic energy and radiated into the far-field [35, 37].

The rapid expansion of small rotary-wing Unmanned Aerial Vehicles (UAVs) for commercial, scientific or recreational applications, as well as the emergent aviation market of propeller-driven Personal Aerial Vehicles (PAVs) for on-demand aviation services, has recently renewed the interest in accurately predicting and reducing the acoustic signature associated to this type of airfoil self-noise mechanism. For such low-speed rotary-wing configurations, trailing-edge noise can be a significant source of acoustic annoyance, due to the efficient scattering mechanism of the turbulent boundary-layer fluctuations at low Mach numbers [51].

Starting from Howe's analytical studies on serrated trailing-edges [134, 135], several passive noise-mitigation solutions devoted to reducing the scattering efficiency (and thus eventually the trailing-edge noise) by means of diffraction effects, have been proposed and tested by various authors in the past years [56, 136–142]. Among them, sawtooth trailing-edge serrations represent the most popular ones due to their good compromise in terms of noise reduction and ease of manufacturing. Serrations are widely used for broadband noise reduction of wind turbines nowadays [56] and they are starting to spread to low-speed propeller applications as well [57, 58]. The mechanisms behind the trailing-edge noise mitigation have been extensively investigated and well understood for serrations at zero flap angle mounted on symmetric airfoils [143–145]. However, its aeroacoustic behavior has been poorly addressed for lifting airfoils retrofitted with serrations at incidence with respect to the incoming flow.

Vathylakis *et al.* [146] performed an experimental sensitivity study on airfoil self-noise reduction for different serration flap angles. They retrofitted a NACA 65(12)-10 airfoil with sawtooth serrations mounted at several flap angles, and measured the resulting far-field noise reduction with respect to the straight-edge case. They found that a flap-up position is generally more favorable for broadband trailing-edge noise reduction than a flap-down position.

The mean flow topology, the turbulence statistics and the noise emissions of a NACA 0018 airfoil with sawtooth serrations have been experimentally investigated by Arce-León *et al.* [142] for different combinations of flap angles and angles of attack. They found that the degree of serration-flow misalignment significantly affects the level of noise reduction provided by serrations. However, they observed discrepancies between experimental data and a simplified Howe's [135] model (corrected with the maximum local streamline angle deflection) at zero flap angle and angle of attack. Therefore, they concluded that the level of flow-misalignment could not fully explain the efficiency at which serrations reduce noise.

In a complementary experimental study, Arce-León *et al.* [147] further analyzed the effect of the trailing-edge serration-flow misalignment - due to the airfoil incidence and serration flap angle - on the noise levels. They confirmed the previous finding of Gruber *et al.* [148] that a serrated airfoil is typically noisier than a baseline airfoil beyond a Strouhal number, based on the boundary-layer thickness and free-stream velocity, approximately equal to 1. Moreover, they proposed a new Strouhal scaling based on the boundary-layer thickness and edge velocity, and noticed that the resulting crossover frequency exhibits a linear modification with changes in the angle of attack, while slightly varying with the free-stream velocity.

Although a few experimental studies have been conducted in the past on the impact of the serration flap angle on the noise reduction effectiveness of serrated trailing-edges, no further insights between the hydrodynamic near-field and noise emissions have been proposed. Therefore, a deeper understanding of the flow physics and noise generation mechanisms associated with serrated trailing-edges at incidence is needed. This situation is relevant for industrial applications where serrations retrofitted to wind turbine or propeller blades might be at incidence with respect to the incoming flow. Hence, the scope of the present study is to provide further connections between the hydrodynamic flow features and the resulting far-field noise for a serrated trailing-edge by means of high-fidelity CFD/CAA simulations. For this purpose, numerical simulations are more suitable than experiments due to their intrinsic capability to extract features of the hydrodynamic near-field without affecting the flow itself, and their better repeatability.

In this study, a detailed analysis of the unsteady flow properties in proximity of the straight trailing-edge of a free boundary-layer transition lifting NACA 64-618 airfoil is presented first. Then, the impact of the serration flap angle on the mean and the unsteady flows, and its connection with the radiated noise, is addressed. Cases 6 and 7 of the AIAA workshop on Benchmark Problems for Airframe Noise Computations (BANC-V) Category 1 are considered as reference for the straight trailing-edge cases. The numerical results are validated against the measurements made available in the framework of the workshop [149]. The Lattice-Boltzmann Method (LBM) based solver SIMULIA PowerFLOW® is used to obtain the numerical flow solution. The aerodynamic noise generated by the scattering of the hydrodynamic pressure fluctuations at the airfoil trailing-edge is further estimated by using an acoustic analogy based on Farassat's formulation 1A of the Ffowcs Williams & Hawkings' (FW-H) equation applied to the airfoil surface.

The rest of the chapter is organized as follows. In Sec. 4.2, the test case and computational setup are described. The numerical results are analyzed next. First, a validation of the numerical method for a straight-edge airfoil undergoing natural transition in provided in Sec. 4.3. Then, in Sec. 4.4, the impact of the flap angle upon the serration noise reduction effectiveness is discussed. Finally, the main conclusions of this study are drawn in Sec. 4.5.

4.2. TEST-CASES AND COMPUTATIONAL SETUP

In this study, a NACA 64-618 airfoil with a chord $c = 0.6$ m, a span $s = 0.1c = 0.06$ m and straight trailing-edge is investigated. Cases 6 and 7 from the AIAA BANC-V Workshop Category 1, are considered as experimental benchmark. They correspond to shallow negative and positive angle of attack conditions, respectively. A summary of the flow conditions for each case is reported in Tab. 4.1. In addition, for each airfoil angle of attack, the airfoil is retrofitted with sawtooth serrations mounted at different flap angles. The serration flap angle β is defined as the angle between the serration and the airfoil chord, positive clockwise. Three serration flap angles are considered, namely: $\beta = 0.0°$ (Serr-chord), $\beta = 6.6°$ (Serr-mid) and $\beta = 13.2°$ (Serr-camber). A sketch of the geometries, as well as of the employed Cartesian coordinate systems, is depicted in Fig. 4.1. The origin of the airfoil coordinate system (x, y, z) is set at the leading-edge midpoint. The x-axis is aligned with the airfoil chord, the y-axis is perpendicular to the former and directed upwards, whereas the z-axis coincides with the airfoil leading-edge with direction defined by the right-hand rule. The local serration coordinate system (x_s, y_s, z_s) has origin on the mid-point at the serration root. The x-axis is aligned with the serration chord, the y-axis is perpendicular to it and the z-axis aligns with the serration span. The sawtooth serration has a thickness $t_s = 0.001$ m, length $h = 0.1c = 0.06$ m and wavelength $\lambda = 0.5h = 0.03$ m, resulting in an aspect ratio of $h/\lambda = 2$. Overall 2 serrations are present along the span.

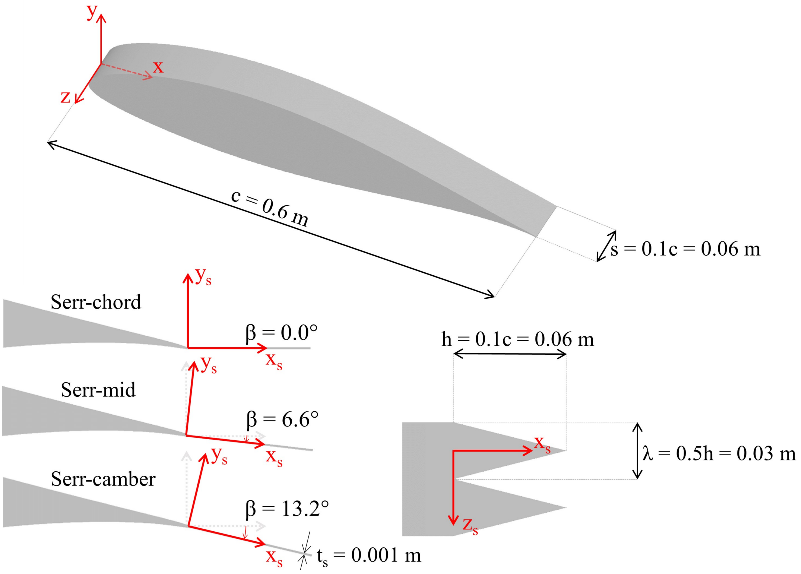

Figure 4.1: NACA 64-618 airfoil and serration geometries.

The computational domain consists of a box - of length equal to $100c$ in both streamwise and wall-normal directions - centered around the airfoil trailing-edge. Static pressure and free-stream velocity are prescribed at the outer boundary of the domain, and an acoustic sponge approach is used to damp the out-going acoustic waves, so that back-

	U_∞ [m/s]	M [-]	Re [-]	T_∞ [K]	ρ_∞ [kg/m^3]	p_∞ [Pa]	α [deg]
Case 6	45.03	0.126	$1.43 \cdot 10^6$	317.6	1.018	92180	−0.88
Case 7	44.98	0.126	$1.43 \cdot 10^6$	317.3	1.019	92180	4.62

Table 4.1: Flow conditions for cases 6 and 7 from AIAA BANC-V Workshop Category 1.

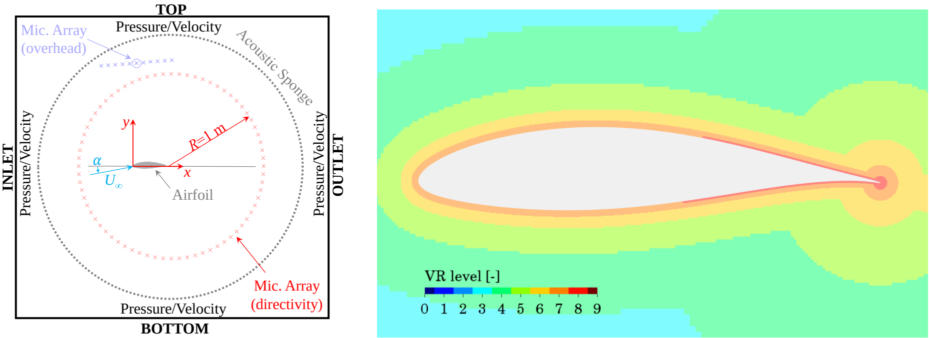

(a) *Computational setup (not to scale)* (b) *Near-body mesh (medium resolution)*

Figure 4.2: Sketch of the computational setup (a) and grid (b).

ward reflections from the outer boundary are minimized (Fig. 4.2(a)). Periodic boundary conditions[1] are applied at the side walls of the computational domain (2.5D simulation). The free-stream turbulence intensity is set to 0.1%. No transition trips are used to enforce the laminar-to-turbulent boundary-layer transition. Three different computational grids are investigated, hereinafter referred to as coarse, medium and fine. For each computational grid, the finest Variable Resolution (VR) region is set around the expected turbulent boundary-layer regions as defined by XFOIL [150] free-transition computations. The rest of the near-body volume around the airfoil is discretized a level coarser (Fig. 4.2(b)). A total of 8, 9 and 10 VRs are used to fill the fluid domain for the coarse, medium and fine grids, respectively. For each mesh, Tab. 4.2 shows the voxel size Δx in the finest VR, the corresponding physical time step (ts), the y^+ in proximity of the trailing-edge, the total number of voxels and the computational cost per flow passage (on Intel Xeon E5-2690 2.90 GHz platform of 360 cores). It is worth recalling that, for $5 \le y^+ \le 30$, the coefficients κ and B of the logarithmic law-of-the-wall are adjusted to provide continuity between the viscous sub-layer and logarithmic regions (see Sec. 3.2.3). Hence, for the medium resolution grid, a $y^+ \approx 5.5$ implies that k and B are adapted in such a way that the wall function is still a close approximation of the linear law-of-the-wall, namely $u^+ = \ln(y^+/A)/\kappa + B \approx \mathrm{y}^+$. A similar computational setup and near-wall resolution (in terms of y^+) returned a good agreement with experimental results in previous investigations of Avallone *et al.* [145] and Ragni *et al.* [151], where the LBM had been used to analyze the hydrodynamic flow around combed-sawtooth and

---

[1] With periodic boundary conditions, the flow entering or leaving one bounding face of the computational domain is equal to the flow leaving or entering the opposite bounding face of the domain.

slitted serrations.

In this study, simulations are performed by using an Implicit Large Eddy Simulation (ILES) approach, where the inviscid energy cascade through the inertial range is captured by the numerical scheme and the inherent numerical dissipation acts as a sub-grid model [108], in order to reduce the eddy viscosity and promote the natural transition of the boundary-layer from a laminar to a turbulent state (see Sec. 3.2.3). The low-subsonic version of the LBM implemented in SIMULIA PowerFLOW® 6-2019-R4 is used for computing the numerical flow solution (see Sec. 3.2). Moreover, the noise radiation is computed by using a FW-H analogy applied to a surface mesh fitted to the airfoil surface wall. The flow is sampled after 10 initial flow passes (0.13 sec of physical time) that constitute the transient phase of the simulation. The unsteady pressure on the airfoil surface is sampled at 84 kHz for a total of 8 flow passes (0.10 sec). Fourier transformed data is obtained with 50% overlap and Hanning windowing to further smooth the spectra.

Resolution	# VR	Δx [mm]	y^+ [-]	ts [s]	# Voxels	CPUh/flow pass
Coarse	8	0.234	10.8	$3.71 \cdot 10^{-7}$	$48.3 \cdot 10^{6}$	350
Medium	9	0.117	5.5	$1.86 \cdot 10^{-7}$	$14.2 \cdot 10^{7}$	2100
Fine	10	0.059	2.6	$9.28 \cdot 10^{-8}$	$50.8 \cdot 10^{7}$	15600

Table 4.2: Mesh resolution, grid size and computational cost.

4.3. STRAIGHT-EDGE: ANALYSIS AND SETUP VALIDATION

In this section, the numerical results for the straight trailing-edge airfoil are discussed and compared to the experimental data from the AIAA BANC-V Workshop Category 1 (cases 6 and 7). The quality of the numerical results is assessed in terms of surface pressure distribution, boundary-layer characteristics, wall-pressure spectrum, far-field noise and spanwise coherence length. In addition, a mesh resolution study is performed on both aerodynamic and aeroacoustic quantities in order to verify the grid independence of the numerical results.

4.3.1. PRESSURE DISTRIBUTION AND BOUNDARY-LAYER PROFILES

Figure 4.3 shows the mean pressure distribution against the experimental measurements. For both cases 6 and 7, the numerical results are in a very good agreement with the experimental data, except for $x/c \approx 0.6$ (case 6) and $x/c \approx 0.5$ (case 7), where the numerical results do not show the presence of the laminar-separation bubble occurring in the experiments. Preliminary simulations with turbulent intensity equal to 0.05%, comparable to that measured during the experiments [149], have also been attempted without showing any significant impact on the pressure-coefficient distribution and boundary-layer transition. Therefore, it is believed that the discrepancies observed on the pressure-coefficient distributions are primarily ascribable to artifacts of the numerical method. Overall, the pressure coefficient does not appear to be particularly sensitive to the three different grid resolutions considered, as expected due to the relatively low y^+ values. Only a minor difference between the coarse mesh and the finer ones around $x/c = 0.6$ on the suction side of the airfoil is observed. This result suggests that the coarse mesh could be used for purely aerodynamic calculations.

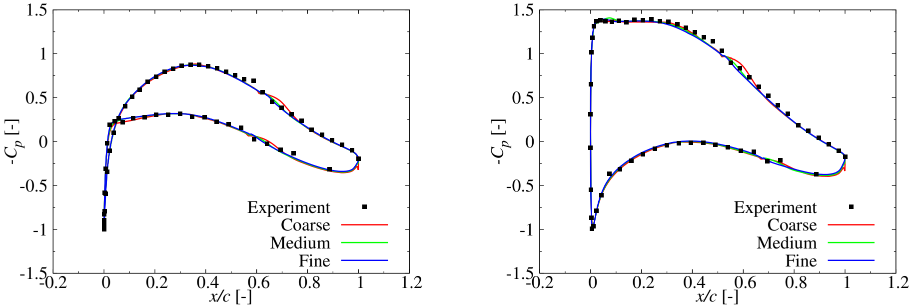

(a) *Case 6*, $\alpha = -0.88°$ (b) *Case 7*, $\alpha = 4.62°$

Figure 4.3: Time-average pressure coefficient distribution over the airfoil surface. Experimental results from Fischer [149].

The time-averaged streamwise velocity profiles $\langle u \rangle$ at $x/c = 0.975$ on the suction side are shown in Fig. 4.4. A satisfactory agreement is found between numerical results and hot-wire anemometer measurements for each case and resolution level, especially for $\alpha = -0.88°$ (case 6) and the inner part of the boundary-layer. Overall, the predicted boundary-layer edge velocity results to be relatively higher than the one measured for cases 6 and 7. The medium and fine resolution levels show a satisfactory convergence trend, while a much thicker boundary-layer is observed in the coarse grid.

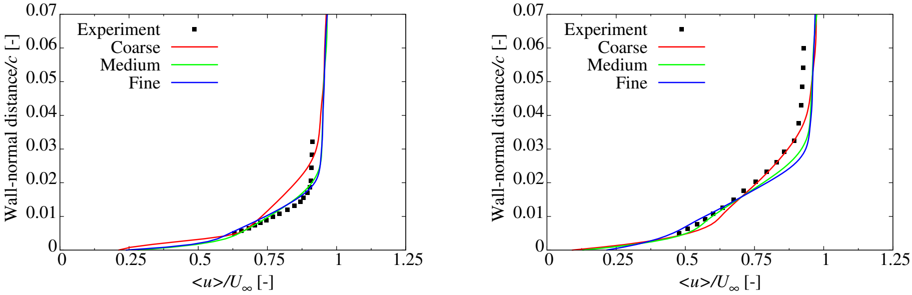

(a) *Case 6*, $\alpha = -0.88°$ (b) *Case 7*, $\alpha = 4.62°$

Figure 4.4: Mean streamwise velocity profile at $x/c = 0.975$ on the suction side. Experimental results from Fischer [149].

The time-averaged Reynolds stress profiles $\langle u'u' \rangle$, $\langle v'v' \rangle$ and $\langle u'v' \rangle$ at $x/c = 0.975$ on the suction side are depicted in Fig. 4.5. u' and v' represent the streamwise and wall-normal velocity fluctuation components, respectively. For both cases 6 and 7, the streamwise fluctuations $\langle u'u' \rangle$ are predicted with a satisfactory level of accuracy, with the numerical profiles correctly approaching the non-dimensional value of 0 outside the boundary-layer. Experimental data not fully converging to zero might be a result of the hot-wire calibration and averaging. A similar behavior can be also noticed for the wall-normal $\langle v'v' \rangle$ and shear $\langle u'v' \rangle$ components. The discrepancies observed between the numerical and experimental results could be related to the use of hot-wire anemometers, which might have resulted in erroneous velocity data due to the additional heat losses in proximity of the wall [152], as well as to the slightly delayed prediction of the boundary-layer transition process in the numerical simulation (as it will be shown in Sec. 4.3.2). Overall, a good level of grid convergence is observed between the medium and fine computational meshes, with only variations in the prediction of the maximum values of the boundary-layer velocity fluctuation profiles, especially for $\alpha = 4.62°$ (case 7).

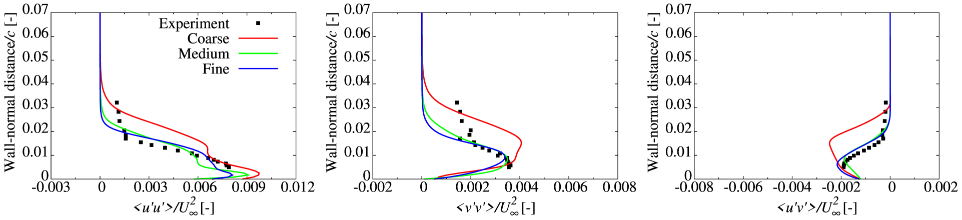

(a) *Case 6*, $\alpha = -0.88°$

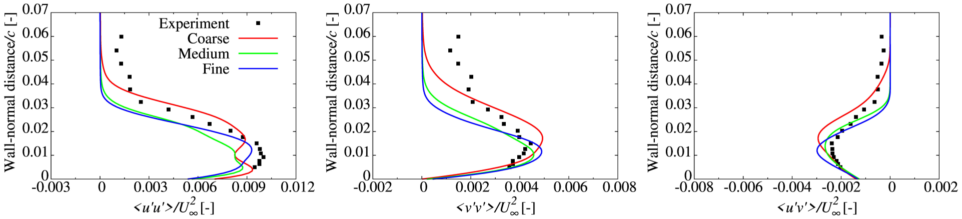

(b) *Case 7*, $\alpha = 4.62°$

Figure 4.5: Time-averaged Reynolds stress profiles at $x/c = 0.975$ on the suction side. Experimental results from Fischer [149].

4.3.2. LAMINAR-TO-TURBULENT BOUNDARY-LAYER TRANSITION

As introduced in Sec. 4.2, the free transition cases 6 and 7 of the AIAA BANC-V Workshop Category 1 are simulated in this study without enforcing the development of the turbulent boundary-layer by means of transition trips. Figure 4.6 qualitatively illustrates, for the medium resolution case, the natural laminar-to-turbulent boundary-layer transition process occurring on the suction and pressure sides of the airfoil for the two cases, by means of an instantaneous snapshot of the λ_2 [153] iso-surfaces colored by the velocity magnitude. To quantitatively assess the laminar-to-turbulent boundary-layer transition process, Tab. 4.3 shows the comparison between the measured transition locations and the numerical ones. Since the transition on the pressure side was not measured during the experimental campaign [149], the predictions from viscous XFOIL [150] simulations are also reported. In Tab. 4.3, the experimental and XFOIL results represent the effective transition points (i.e. the position where the boundary-layer is fully turbulent), whereas the numerical ones are provided in terms of initial and final locations of the transition process, which are based on the minimum and maximum chordwise values of the surface skin friction coefficient, respectively.

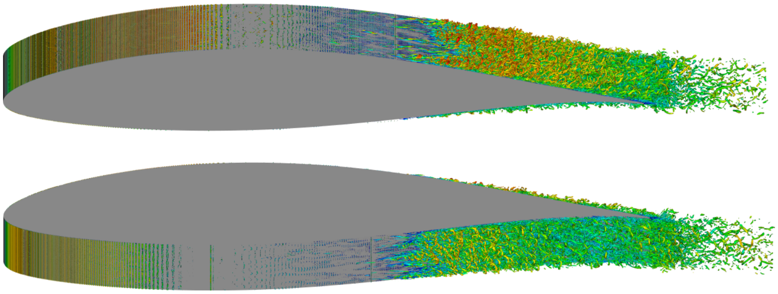

(a) *Case 6,* $\alpha = -0.88°$

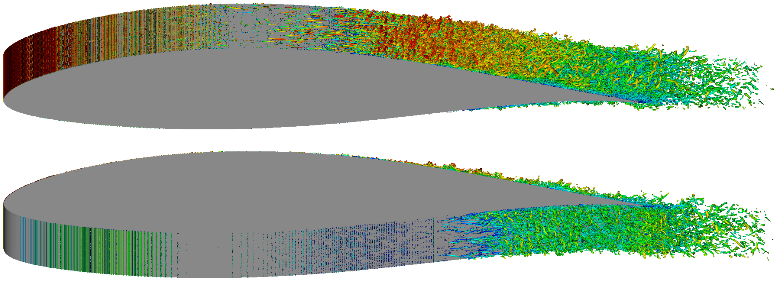

(b) *Case 7,* $\alpha = 4.62°$

Figure 4.6: $\lambda_2 = -1 \cdot 10^7\ 1/s^2$ iso-surfaces of the instantaneous flow around airfoil colored by the flow velocity magnitude for the medium resolution case; velocity magnitude limits: blue ($0.0U_\infty$) - red ($1.5U_\infty$).

Case 6	Experiment	XFOIL	Coarse	Medium	Fine
Suction side	0.65	0.62	$0.62 \div 0.80$	$0.63 \div 0.75$	$0.62 \div 0.73$
Pressure side	–	0.58	$0.60 \div 0.82$	$0.58 \div 0.70$	$0.58 \div 0.68$
Case 7	Experiment	XFOIL	Coarse	Medium	Fine
Suction side	0.56	0.52	$0.56 \div 0.71$	$0.54 \div 0.64$	$0.52 \div 0.61$
Pressure side	–	0.69	$0.74 \div 0.90$	$0.69 \div 0.79$	$0.67 \div 0.74$

Table 4.3: Laminar-to-turbulent boundary-layer transition location in percentage of chord (x/c). Experimental results from Fischer [149].

For the suction side, the chordwise position where the boundary-layer is fully turbulent is delayed from 15%, for the coarse grid and both angles of attack, to 8% ($\alpha = -0.88°$) and 5% ($\alpha = 4.62°$) for the finer mesh. Regarding the pressure side, no experimental data is available, but the same level of transition delay is expected by comparing numerical and XFOIL results, and considering how the latter correlates with the experiments on the suction side. However, a good convergence trend can be noted between the medium and fine meshes, for which the boundary-layer transition process takes place within roughly the same chordwise extension. The slightly delayed prediction of the end of the laminar-to-turbulent transition might be another cause for the slight over-prediction of the wall-normal $\langle v'v'\rangle$ and shear $\langle u'v'\rangle$ Reynolds stress peak values observed in Fig. 4.5.

4.3.3. WALL-PRESSURE FLUCTUATION SPECTRUM

Figure 4.7 shows the comparison between the numerical and experimental wall-pressure power spectral densities Φ_{pp} at $x/c = 97.5\%$ and $x/c = 95\%$ on the suction and pressure sides. In Fig. 4.7, Φ_{pp} is plotted as a function of the non-dimensional frequency expressed in terms of Strouhal number $St_c = fc/U_\infty$, based on the airfoil chord c and free-stream velocity U_∞.

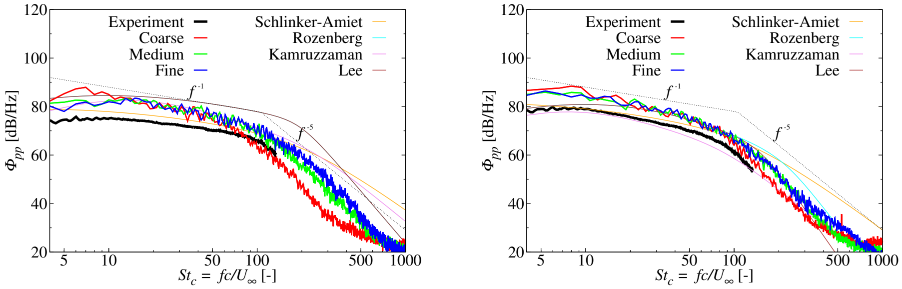

(a) *Suction side at* $x/c = 0.975$, *case 6,* $\alpha = -0.88°$ (b) *Suction side at* $x/c = 0.975$, *case 7,* $\alpha = 4.62°$

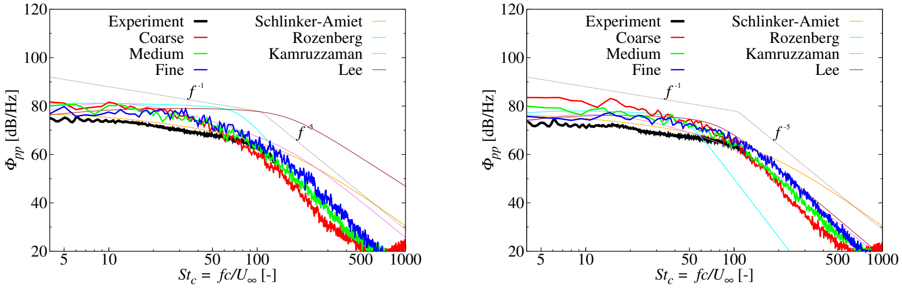

(c) *Pressure side at* $x/c = 0.95$, *case 6,* $\alpha = -0.88°$ (d) *Pressure side at* $x/c = 0.95$, *case 7,* $\alpha = 4.62°$

Figure 4.7: Power spectral density of the wall-pressure Φ_{pp} in proximity of the trailing-edge. Experimental results from Fischer [149]. Semi-empirical results from Schlinker & Amiet's [129], Rozenberg [154], Kamruzzaman's [155] and Lee's [156] models.

A good convergence trend is found between the medium and fine computational grids in the frequency of interest for turbulent boundary-layer trailing-edge noise ($4 < St_c < 100$) [132], with only small differences observed at low frequency on the pressure side (Figs. 4.7(c) and 4.7(d)), whereas the coarse mesh presents larger pressure fluctuations at low and mid frequencies. As expected, the numerical wall-pressure spectra show higher fluctuations as the resolution increases at very high frequencies ($St_c > 100$), due to capability of the computational mesh to capture smaller scales of turbulence. For each angle of attack, the numerical setup is able to reproduce the general shape and trend of the experimental wall-pressure fluctuation spectra, as well as the fact that the suction side (Figs. 4.7(a) and 4.7(b)) is more energetic than the pressure one (Figs. 4.7(c) and 4.7(d)). A power decay $\sim f^{-1}$ typical of a fully developed turbulent boundary-layer is found at mid-to-high frequencies, while at very high frequency the spectra show a slope $\sim f^{-5}$ as a consequence of the viscous dissipation [59]. Besides this, a large over-prediction up to 10 dB/Hz is observed in the numerical predictions compared to the measurements. To better clarify this aspect, the wall-pressure spectra computed with four different semi-empirical models are also compared to the numerical and experimental results in Fig. 4.7. The semi-empirical models are Schlinker & Amiet's [129], Rozenberg's [154], Kamruzzaman's [155] and Lee's [156] (see Appendix A), which are fed with boundary-layer parameters extracted from XFOIL computations (reported in Tab. 4.4).

Suction side at $x/c = 0.975$			Case 6	Case 7
Edge velocity	U_e	[m/s]	42.32	43.33
Boundary-layer thickness	δ	[m]	0.0134	0.0133
Displacement thickness	δ^*	[m]	0.0031	0.0055
Momentum thickness	Θ	[m]	0.0021	0.0022
Wall shear stress	τ_w	[N/m^2]	4.87	1.59
Pressure gradient	$\mathrm{d}p/\mathrm{d}x$	[Pa/m]	1629.0	2045.7
Pressure side at $x/c = 0.95$			**Case 6**	**Case 7**
Edge velocity	U_e	[m/s]	36.05	35.15
Boundary-layer thickness	δ	[m]	0.0155	0.0114
Displacement thickness	δ^*	[m]	0.0034	0.0032
Momentum thickness	Θ	[m]	0.0023	0.0016
Wall shear stress	τ_w	[N/m^2]	3.76	2.25
Pressure gradient	$\mathrm{d}p/\mathrm{d}x$	[Pa/m]	-633.9	-967.4

Table 4.4: Boundary-layer parameters extracted from XFOIL computations used in semi-empirical wall-pressure spectrum model [129, 154–156] and semi-analytical trailing-edge noise model [50].

As expected, the four different semi-empirical models show a certain sensitivity to the input data. The semi-empirical results tend to generally over-predict the amplitude of the wall-pressure spectrum with respect to both numerical and experimental data at high frequency (except for the Rozenberg's model on the pressure side for $\alpha = 4.62°$). However, they compare more favorably with the numerical predictions compared to the experiments, except for the Schlinker-Amiet's model on the suction side for both $\alpha = -0.88°$ and $\alpha = 4.62°$, and for the Kamruzzaman's model on the suction side for $\alpha = 4.62°$. On the one hand, these results suggest that the experimental wall-pressure spectra might be affected by some measurement errors. On the other hand, having performed a wall-modeled implicit large eddy simulation (ILES) does not guarantee that the numerical wall-pressure spectra correspond to those extracted from a fully resolved direct numerical simulation (DNS). A companion far-field noise analysis by means of Roger & Moreau's [50] semi-analytic trailing-edge model, fed with the experimental wall-pressure spectra, is performed in the next subsection for further clarification of such discrepancies.

4.3.4. FAR-FIELD NOISE

In Fig. 4.8, far-field noise computations carried out using the FW-H acoustic analogy, Eqs. (3.60) and (3.61), applied to the airfoil surface are validated against the experimental beamforming data. The far-field noise is obtained by approximating the experimental beamforming array [149] using a line of 11 streamwise microphones centered on the experimental array center ($x = 0.19$ m, $y = 1.62$ m, $z = 0$ m) and averaging over them. This (overhead) numerical microphone array is depicted in blue in Fig. 4.2(a). The far-field sound pressure level in 1/3-octave band is normalized for a reference observer distance $R_r = 1$ m and span length $s_r = 1$ m in order to allow for comparison with the experiments, where a span of 0.6 m resulting from the beamforming integration region is used. The following formula is used for scaling [59]:

$$\Phi_{aa} = \Phi_{aa}^{\mathrm{raw}} + 20\log_{10}(R/R_r) - 10\log_{10}(s/s_r) \tag{4.1}$$

where Φ_{aa} represents the normalized sound pressure level and Φ_{aa}^{raw} is the raw computed/measured sound pressure level for a generic observer radius R and span s. To shed more light on the discrepancies observed between the numerical and measured wall-pressure spectra (Fig. 4.7), the far-field noise predictions computed with Roger & Moreau's semi-analytical trailing-edge noise model [50] (see Appendix B), fed with the experimental wall-pressure spectra at the trailing-edge, are also shown in Fig. 4.8. In addition to the wall-pressure spectra at the trailing-edge, Roger & Moreau's model also requires the spanwise coherence length l_z as input. In this study, the spanwise coherence length supplied to the analytical trailing-edge model is estimated with the Corcos' model [157], namely:

$$l_z(f) = \frac{b_c u_c}{2\pi f}, \tag{4.2}$$

where b_c is a constant, typically chosen between 1.2 and 1.7 [158], while u_c is the convection velocity. u_c is computed as $u_c = \zeta U_e$, where U_e is the edge velocity and ζ a parameter usually taken between 0.6 and 0.8. To account for the influence of such parameters on the far-field noise predicted by Roger & Moreau's trailing-edge noise model, which is proportional to b_c and ζ through the Corcos's model, the semi-analytical results are computed for ($b_c = 1.2, \zeta = 0.6$) and ($b_c = 1.7, \zeta = 0.8$). This allows to identify the range between the lowest and highest far-field noise levels predictable by Roger & Moreau's model fed with the available experimental wall-pressure spectra.

For case 6 (Fig. 4.8(a)), a good agreement is found between numerical and experimental results, with only 1-2 dB over-estimation for the medium and fine grids. Regarding case 7 (Fig. 4.8(b)), the FW-H prediction fits the experimental data up to $St_c = 20$, whereas for higher frequencies a certain over-prediction can be observed. It is worth mentioning that a similar over-prediction at high frequency was also found by Lee

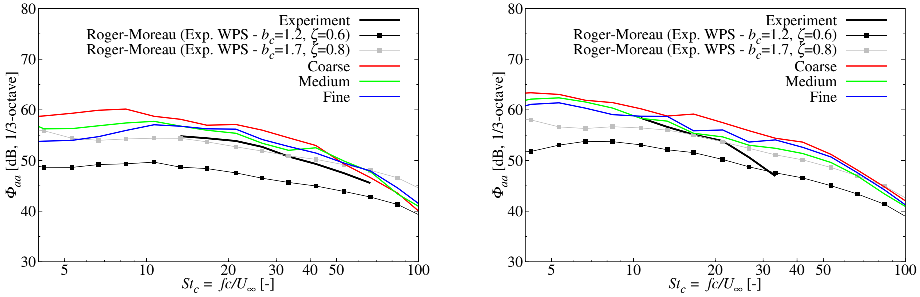

(a) *Case* 6, $\alpha = -0.88°$

(b) *Case* 7, $\alpha = 4.62°$

Figure 4.8: Far-field sound pressure level in 1/3-octave band Φ_{aa} at (x = 0.19 m, y = 1.62 m, z = 0 m). Experimental results from Fischer [149]. Roger & Moreau's trailing-edge model [50] fed with the experimental wall-pressure spectra.

et al. [159] by using Howe's trailing-edge model [160] fed with empirical wall-pressure spectra [156] for the same benchmark case. Overall, a good convergence trend is observed between the medium and fine cases for both the angles of attack, with only a minor scatter of the numerical predictions within 1 dB throughout the frequencies of interest. Regarding the results from Roger & Moreau's trailing-edge model fed with experimental wall-pressure spectra, a certain under-estimation of the far-field noise levels is observed for ($b_c = 1.2, \zeta = 0.6$), while a good agreement with the experiments is found for ($b_c = 1.7, \zeta = 0.8$), especially for case 6. Interestingly, both numerical and semi-analytical predictions show similar sound pressure level slopes, which differ from the experimental one in the range $20 < St_c < 30$, for case 7. The fact that the numerical far-field noise is overall higher than the measured one might be a consequence of the over-prediction of the numerical wall-pressure spectra in proximity of the trailing-edge (Fig. 4.7). On the other hand, the semi-analytical predictions falling on average below the experimental far-field noise results might be associated to the relatively low values of the experimental wall-pressure spectra shown in Fig. 4.7. In view of the above, the discrepancies observed in the wall-pressure spectra and far-field noise results could be ascribable to a combination of factors in both simulations and experiments. Future studies based on wall-resolved LES or DNS computations, as well as independent measurements for similar flow configurations, might help to resolve the origin of the aforementioned differences.

4.3.5. WALL-PRESSURE SPANWISE COHERENCE AND COHERENCE LENGTH

The straight-edge analysis and validation are concluded by focusing on the spanwise turbulent flow statistics, which is known to play a relevant role for trailing-edge noise, as the scattering process is related to the properties of the vortical field in proximity of the trailing-edge [50]. In this sense, an important parameter to track is the spanwise coherence length l_z, as the far-field noise spectrum is proportional to l_z according to Howe's trailing-edge noise theory [160]. This parameter can be conceived as the length of a source term scattering at the trailing-edge and is a function of the frequency f:

$$l_z(f) = \lim_{L\to\infty} \int_0^L \sqrt{\gamma^2(f,\eta)}\mathrm{d}\eta, \tag{4.3}$$

where $\gamma^2(f,\eta)$ is the squared coherence function of the wall-pressure signals between two points spaced by η along the spanwise direction z. The squared coherence function γ^2 is in turn defined as the squared magnitude of the cross-spectrum $\mathrm{C}(f,z_1,z_2)$ of the two signals, sampled at two points z_1 and $z_2 = z_1+\eta$ along the spanwise coordinate z, divided by the auto-spectrum of both signals at each frequency, namely:

$$\gamma^2(f,\eta) = \frac{|\mathrm{C}(f,z_1,z_2)|^2}{|\mathrm{C}(f,z_1,z_1)||\mathrm{C}(f,z_2,z_2)|}. \tag{4.4}$$

In order to compare the numerical coherence length to the experimental one, the squared coherence function has to be evaluated first. Figure 4.9 depicts the contours of the spanwise squared coherence function at $x/c = 0.975$ on the suction side.

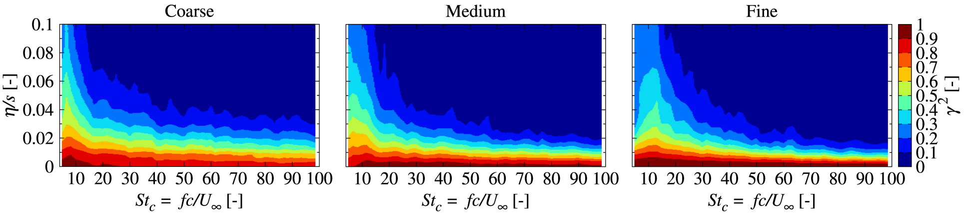

(a) *Case 6*, $\alpha = -0.88°$

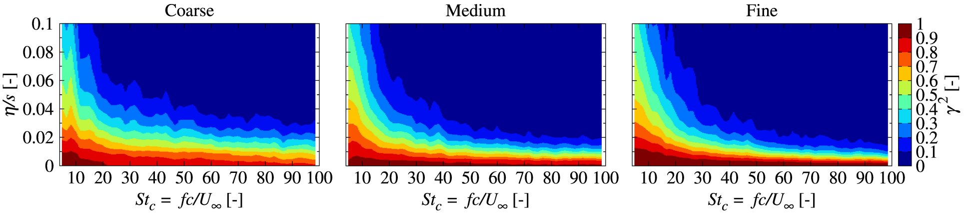

(b) *Case 7*, $\alpha = 4.62°$

Figure 4.9: Magnitude of the spanwise squared coherence function γ^2 at $x/c = 0.975$ on suction side. Spanwise separation distance η normalized by the simulated airfoil span s.

For both cases 6 and 7, a peak around $St_c = 10$ is observed, after which γ^2 decays as the frequency increases, as expected for turbulent flows. In addition, the spanwise squared coherence drops down to relatively low values for separation distances within 10% of the airfoil span. This implies that the simulated span is large enough to include source regions that radiate noise independently from the neighboring ones in a statistical sense [161]. For a given frequency, a more rapid decay of γ^2 is observed as the resolution increases. This suggests that a refinement of the computational mesh, especially from the coarse grid to medium one, leads to the prediction of less coherent turbulent structures for larger spanwise separation distances. Overall, a good convergence trend is observed between medium and fine resolutions, especially in the mid to high frequency range.

In Fig. 4.10, the comparison between the experimental coherence length l_z at $x/c = 0.975$ on the suction side and the numerical ones is shown. It should be pointed out that the numerical coherence length is not rigorously computed by using Eq. (4.3), as the squared coherence function does not approach zero for large separation distances η, thus leading to convergence issues of the direct integration of γ [162]. To overcome this issue, the spanwise coherence length l_z is evaluated by means of a curve fitting approach based on an exponential function [163, 164] and performed on the spanwise coherence $\gamma(f,\eta)$ for each discrete frequency, namely:

$$\gamma(f,\eta) = \mathrm{e}^{-|\eta|/l_z(f)}. \tag{4.5}$$

For each discrete frequency, the exponential fitting is performed by neglecting those separation distances for which the coherence function γ does not show a convergent trend towards 0 [128]. For case 6 (Fig. 4.10(a)), the agreement between the measured and numerical spanwise coherence length is satisfactory for all the frequencies. The only discrepancy is observed around $St_c = 6$, where the sharp peak of the measured coherence length is not reproduced in the numerical ones. This might be a consequence of the larger bandwidth used in the numerical results. For case 7 (Fig. 4.10(b)), the numerical results also match the experiments in a quite satisfactory way, although a slight overprediction is found below $St_c = 6$. Again, the medium and fine resolution meshes show a quite good convergence trend.

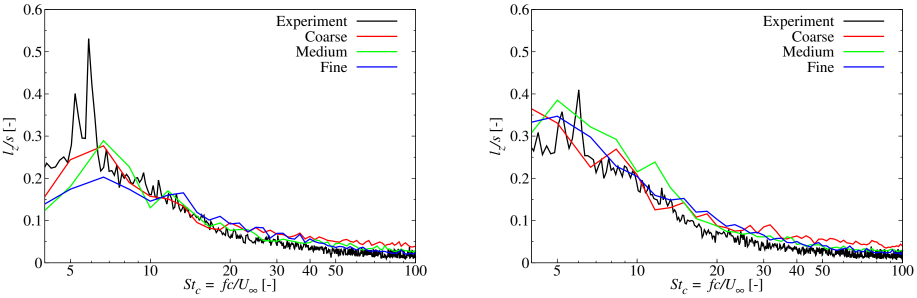

(a) *Case 6*, $\alpha = -0.88°$ (b) *Case 7*, $\alpha = 4.62°$

Figure 4.10: Spanwise coherence length l_z normalized by the simulated airfoil span s at $x/c = 0.975$ on the suction side. Experimental results from Fischer [149].

Overall, the medium resolution setup provided quite similar flow statistics in proximity of the trailing-edge and noise predictions compared to the fine one, with a computational time almost one order of magnitude lower (Tab. 4.2). Therefore, in order to keep the computational cost relatively low without significantly affecting the numerical results, the medium resolution grid is used in what follows to investigate the effect of the serration flap angle on the hydrodynamic near-field and acoustic far-field.

4.4. SERRATED-EDGE: ANALYSIS OF FLAP ANGLE EFFECTS

In this section, the effect of the flap angle upon the aerodynamic and acoustic behavior of the serrated edge is numerically investigated. For each airfoil angle of attack, the NACA 64-618 profile is retrofitted with sawtooth serrations mounted at three different flap angles: $\beta = 0.0°$, $\beta = 6.6°$ and $\beta = 13.2°$. The former corresponds to a condition such that the serration is aligned with the airfoil chord (Serr-chord), whereas the latter with the local tangent to the suction side at $x/c = 0.99$ (Serr-camber). The $\beta = 6.6°$ case represents an intermediate condition to the previous ones (Serr-mid). No experimental data is available for such serrated cases. Therefore, only numerical results are shown, obtained using the computational setup validated in Sec. 4.3. Although not shown for the sake of conciseness, it is verified that for the cases under examination the presence of the serrations and their flap angle do not significantly affect the natural boundary-layer transition process, the wall-pressure fluctuations spectrum, integral boundary-layer parameters and spanwise pressure coherence length upstream the trailing-edge. Finally, it should be recalled that the typical coherence length at the frequencies of interest for the present study (where significant noise reduction due the serration can occur, i.e. $4 < St_c < 32$ as it will be shown in Sec. 4.4.2) must be substantially smaller than the spanwise extent of the computational domain for the results to be reliable. This requirement is satisfied by the employed computational setup, as observed in Fig. 4.10, which shows that for both cases the coherence length in the range $4 < St_c < 32$ is considerably lower than the simulated airfoil span extension.

4.4.1. PRESSURE DISTRIBUTION

Figure 4.11 shows the influence of the serration flap angle on the time-average pressure coefficient distribution over the airfoil surface for $\alpha = -0.88°$ and $\alpha = 4.62°$. The pressure coefficient distributions are extracted on a longitudinal plane passing through the serration tip. Although not shown for the sake of brevity, it is observed that the time-average pressure distribution is independent from the spanwise position of the plane of extraction for $0 \leq x/c \leq 1$. Table 4.5 shows the impact of the flap angle on the sectional lift and drag coefficients for both $\alpha = -0.88°$ and $\alpha = 4.62°$.

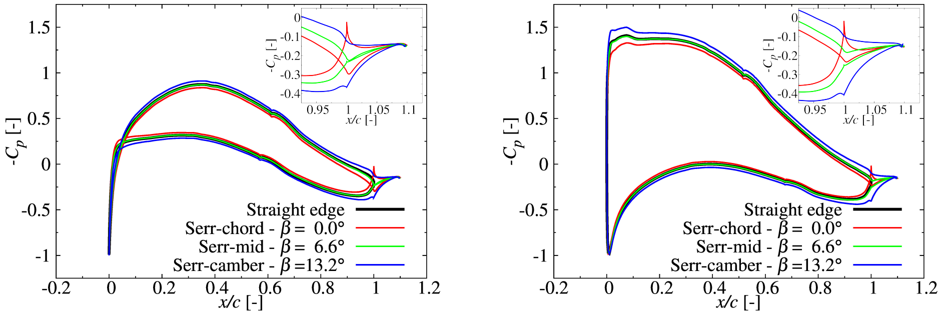

(a) *Case 6*, $\alpha = -0.88°$

(b) *Case 7*, $\alpha = 4.62°$

Figure 4.11: Time-average pressure coefficient distribution over the airfoil and serration surfaces.

For both angles of attack, the serration being at incidence with respect to the upcoming flow results in a change of the circulation and, in turn, of the loading of the airfoil. On the one hand, the chord-aligned serration ($\beta = 0.0°$) induces a reduction of the lift generated by the airfoil compared to the straight edge configuration, as well as a favorable pressure gradient going from the suction to the pressure side of the serration. On the other hand, the camber-aligned serration ($\beta = 13.2°$) yields to an increment of the airfoil lift with respect to the non-serrated case and to the generation of an adverse pressure gradient between the suction and pressure sides of the add-on. A more neutral behavior is exhibited by the intermediate serration case ($\beta = 6.6°$) for which, being the add-on more aligned with the mean-flow streamlines leaving the airfoil trailing-edge (as it will be shown in Sec. 4.4.5), there is no evident variation of the airfoil lift and only a weak adverse pressure gradient is generated across the serration tooth, moving from the suction to the pressure side.

Case 6 ($\alpha = -0.88°$)	C_L [-]	C_D [-]
Straight edge	0.419	0.007
Serr-chord - $\beta = 0.0°$	0.328	0.006
Serr-mid - $\beta = 6.6°$	0.411	0.007
Serr-camber - $\beta = 13.2°$	0.508	0.008
Case 7 ($\alpha = 4.62°$)	C_L [-]	C_D [-]
Straight edge	1.060	0.009
Serr-chord - $\beta = 0.0°$	0.982	0.010
Serr-mid - $\beta = 6.6°$	1.066	0.011
Serr-camber - $\beta = 13.2°$	1.179	0.012

Table 4.5: Effect of serration flap angle on sectional lift and drag coefficients.

Serration flap angles that increase the overall blade loading might impose additional challenges from a structural viewpoint and require the addition of additional mass and stiffness to the retrofitted blade, especially for wind turbine rotors. In terms of noise radiation, the change in the steady airloads can affect both the steady loading noise and turbulent boundary-layer trailing-edge noise generation. First, a serrated blade generating more/less lift would eventually produce more/less steady loading noise at blade-passing frequencies falling in the frequency range where turbulent boundary-layer trailing-edge noise reduction due to serrations may occur. Second, a more loaded blade might cause an earlier laminar-to-turbulent boundary-layer transition and yield to higher turbulent pressure fluctuations approaching the serrated trailing-edge. This can have an impact on the turbulent boundary-layer trailing-edge noise generation, in addition to that associate to the local changes of the hydrodynamic field induced by a certain serration flap angle. In view of this, the potential benefits on trailing-edge noise reduction given by a specific serration flap angle, should be evaluated in conjunction with its impact on rotor performances, aerodynamic loading, steady tonal noise and boundary-layer transition. As mentioned earlier, for the configurations examined in this study, the serrations and their flap angle do not significantly influence the boundary-layer transition process and the pressure statistics of the flow approaching the serrated trailing-edge. Therefore, it is expected that the turbulent boundary-layer trailing-edge noise variations with respect to the straight edge (Secs. 4.4.2 and 4.4.3) are primarily due to local flow changes induced by the serration itself.

4.4.2. FAR-FIELD NOISE REDUCTION

The effect of the serration flap angle on the far-field trailing-edge noise reduction with respect to the straight trailing-edge is analyzed in this subsection. For the three different flap angles, Fig. 4.12 depicts the 1/3-octave band sound pressure level reduction with respect to the straight trailing-edge, $\Delta\Phi_{aa} = \Phi_{aa}^{\mathrm{str}} - \Phi_{aa}^{\mathrm{serr}}$ (where Φ_{aa}^{str} and $\Phi_{aa}^{\mathrm{serr}}$ are the far-field noise spectra of the straight and serrated edge, respectively), at the center of the overhead microphone array ($x = 0.19$ m, $y = 1.62$ m, $z = 0$ m) for $\alpha = -0.88°$ and $\alpha = 4.62°$. The normalized frequency range examined here is $4 < St_c < 32$, which corresponds to a dimensional frequency ranging from 300 Hz to 2400 Hz. As expected, for each case the noise reduction varies with the frequency, but different trends are observed between the three different flap angles. The intermediate serration flap angle ($\beta = 6.6°$) shows the best noise suppression behavior among the three examined serration configurations, except for $\alpha = -0.88°$ and $St_c < 7$. For this configuration, a noise reduction is observed throughout the frequency range of interest, with a maximum noise attenuation of 4 dB at low and mid frequencies, for $\alpha = -0.88°$ (Figure 4.12(a)), and 6 dB at $St_c \approx 6$, for $\alpha = 4.62°$ (Figure 4.12(b)). On the contrary, the serrations aligned with the airfoil chord and camber do not exhibit consistent trends as the airfoil angle of attack varies. Specifically, for $\alpha = -0.88°$ the camber-aligned serration outperforms the chord-aligned one by providing a noise reduction up to $St_c \approx 13$, after which an increment of the sound levels is observed. A lower noise reduction is found for the latter. The opposite is observed for the positive angle of attack case ($\alpha = 4.62°$), for which the chord-aligned serration provides noise reduction up to $St_c \approx 20$, with the highest attenuation of 5 dB at $St_c \approx 8$, whereas the camber-aligned one reduces noise only up to $St_c \approx 13$, with the maximum reduction of 5.5 dB at low frequency.

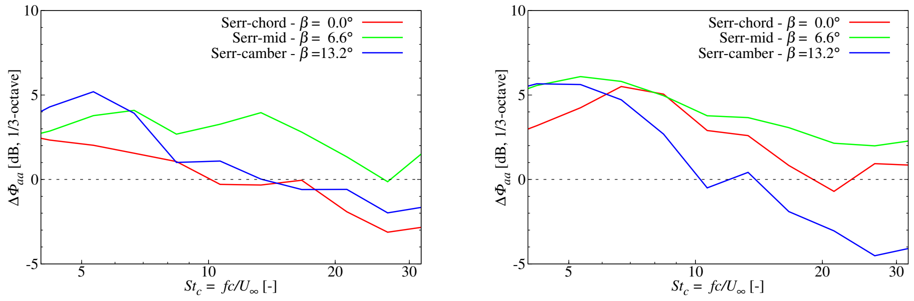

(a) *Case 6*, $\alpha = -0.88°$ (b) *Case 7*, $\alpha = 4.62°$

Figure 4.12: Far-field noise reduction in 1/3-octave band $\Delta\Phi_{aa}$ at ($x = 0.19$ m, $y = 1.62$ m, $z = 0$ m). A positive value of $\Delta\Phi_{aa}$ has the meaning of noise reduction with respect to the straight trailing-edge.

These results are in line with earlier observations from Vathylakis *et al.* [146] for a NACA 65(12)-10 airfoil. They experimentally observed that flap-up positions of the serration (with respect to a camber-aligned configuration) are more favorable for broadband noise reduction, with the maximum noise reduction achieved for flap angles around 5°. Such a flap angle is similar to the $\beta = 6.6°$ cases of the present study, which also showed the best turbulent boundary-layer trailing-edge noise suppression behavior among the three examined flap angles. As previously shown in Fig. 4.11 and Tab. 4.5, the intermediate flap angle case ($\beta = 6.6°$) has only a negligible effect on the airfoil lift and drag generation. Hence, in a serrated rotor/propeller configuration, it is not expected to considerably affect the rotor performances and steady loading noise radiation, contrarily to the chord- and camber-aligned cases.

4.4.3. FAR-FIELD NOISE DIRECTIVITY

To investigate the serration flap angle influence on the far-field noise pattern, Fig. 4.13 depicts the directivity plots of $p_{\text{rms}}(\theta)/\overline{p_{\text{rms}}}$ for the straight and serrated cases and for three different non-dimensional frequency ranges: $4 < St_c < 8$, $8 < St_c < 16$ and $16 < St_c < 32$. They are obtained by evaluating the acoustic pressure through a FW-H approach at 72 equally spaced microphones placed over a circular array of radius $R = 1$ m centered around the airfoil trailing-edge (Fig. 4.2(a)). The far-field noise levels are reported in terms of the root mean square of the acoustic pressure $p_{\text{rms}}(\theta)$ normalized by the mean value $\overline{p_{\text{rms}}}$ along the circular array of the straight edge case (where θ is the trailing-edge observation angle: $\theta = 0°$ denotes the downstream aligned direction, whereas $\theta = 90°$ denotes the suction side chord-normal view towards the trailing-edge).

For all cases and frequency ranges examined, a non-compact dipolar pattern is observed, as expected by the value of Helmholtz number based on the airfoil chord, which is higher than 0.5 for the lowest frequency band. As the frequency increases, the non-compact behavior becomes more significant: the dipolar pattern tends to become asymmetric with respect to the streamwise flow direction and secondary lobes are visible. For each case, most of the noise is radiated along the chord-normal and upstream directions, as known from the trailing-edge noise theory in the non-compact regime [37]. Moreover, the lobe on the pressure side results to be generally more significant than that on the suction side one for the cases examined here. Similar to what observed for the overhead microphone array, the intermediate flap angle ($\beta = 6.6°$) provides the highest noise suppression for both positive and negative angles of attack and all the frequency ranges considered, except for $4 < St_c < 8$. Moreover, for $\alpha = -0.88°$, the camber-aligned serration shows noise reduction for all directions only at low frequency ($4 < St_c < 8$), whereas the chord-aligned one also reduces noise in the mid frequency range ($8 < St_c < 16$) for some directivity angles ($195° - 270°$). At high frequency ($16 < St_c < 32$), both the chord- and camber-aligned serrations increase the noise levels compared to the straight trailing-edge for most of the observer angles. For $\alpha = 4.62°$, the camber-aligned serration reduces noise at low frequency ($4 < St_c < 8$), while increases it at high frequency ($16 < St_c < 32$) for all directions. A similar far-field noise directivity to that of the straight edge is observed at mid-frequency ($8 < St_c < 16$). A better noise suppression behavior is shown by the chord-aligned serration, which manifests noise reduction also at mid frequency for all directions, and at high frequency for some directivity angles ($180° - 270°$). Finally,

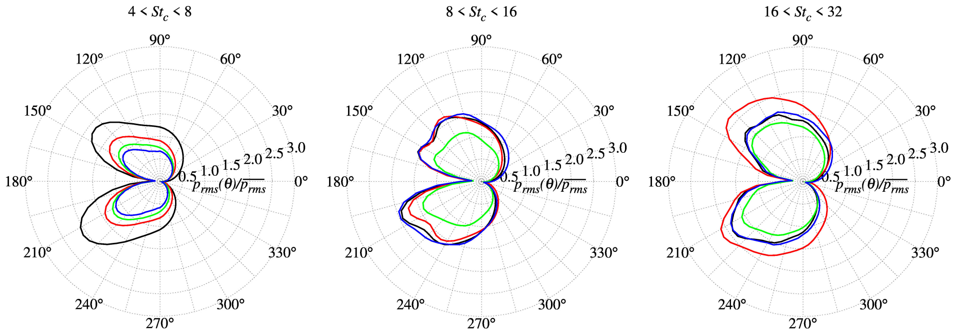

(a) *Case 6*, $\alpha = -0.88°$

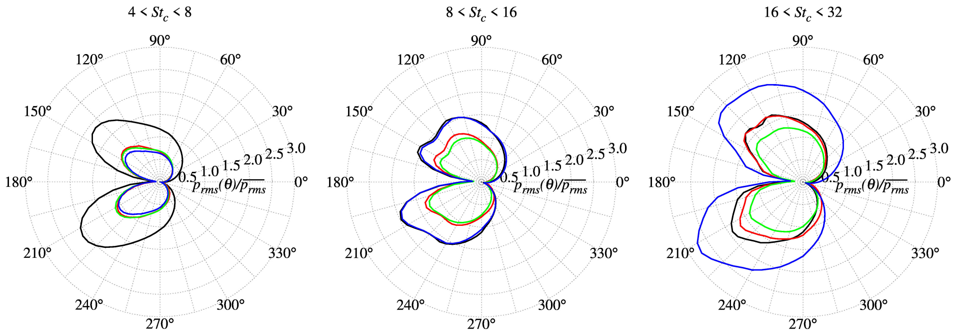

(b) *Case 7*, $\alpha = 4.62°$

Figure 4.13: Far-field noise directivity patterns for three non-dimensional frequency ranges: $4 < St_c < 8$, $8 < St_c < 16$ and $16 < St_c < 32$. Straight edge (—), Serr-chord - $\beta = 0.0°$ (—), Serr-mid - $\beta = 6.6°$ (—) and Serr-camber - $\beta = 13.2°$ (—).

it is interesting to note that the serration flap angle not only alters the amount of noise reduction or increment, but also the overall orientation of the non-compact dipole, with the two lobes that tend to be tilted along the direction perpendicular to the serration chord.

4.4.4. SERRATED TRAILING-EDGE SCATTERING

In this subsection, the effect of serration flap angle on the serrated trailing-edge scattering is analyzed. This analysis follows that proposed by Avallone *et al.* [145] for the analysis of the scattering of sawtooth and combed-sawtooth serrations retrofitted to a NACA 0018 under zero lift conditions. The serration region, which extends from the last 2.5% of the airfoil surface up to the serration tip, is split into 10 strips, each of which is independently used to compute the acoustic signature $p'(t)$ in the far-field ($x = 0.19$ m, $y = 1.62$ m, $z = 0$ m) by means of the FW-H acoustic analogy. The strips are numbered from 1 to 10 and the strip 0 is used to account for the entire serration region, as depicted in Fig. 4.14. The acoustic signature from each strip is used to compute the

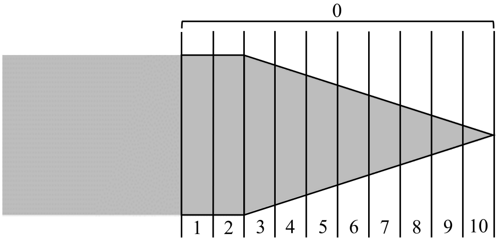

Figure 4.14: Sketch of the serration surface partition for scattering analysis.

Fourier transform of the cross-correlation between strips, i.e the cross-spectral density $\mathrm{C_{ij}}(f)$, in order to highlight constructive and/or destructive interference of noise sources distributed along the serration edge:

$$\mathrm{C_{ij}}(f) = \int_{-\infty}^{\infty}\left[\int_{-\infty}^{\infty} p'_{\mathrm{i}}(t)p'_{\mathrm{j}}(t+\tau)\mathrm{d}\tau\right]\mathrm{e}^{j2\pi f t}\mathrm{d}t. \tag{4.6}$$

The results from the cross-spectral density analysis are further integrated over the three frequency bands considered so far and presented in Fig. 4.15 and Fig. 4.16 for $\alpha = -0.88°$ and $\alpha = 4.62°$, respectively. In Figs. 4.15 and 4.16, the colored inner matrix shows the magnitude of the cross-spectral density $|\mathrm{C_{ij}}|$ between the i-th and j-th strips normalized by the magnitude of the auto-spectral density of the entire serration region $|\mathrm{C_{00}}|$. This matrix is symmetric by definition. Therefore, its main diagonal represents the magnitude of the auto-spectral density of the contribution from the i-th strip. The outer grey matrix represents the values of $\cos(\phi_{\mathrm{i0}})$, where ϕ_{i0} is the phase angle of the cross-spectral density $\mathrm{C_{i0}}$ between the i-th strip and the entire serration region. If $\cos(\phi_{\mathrm{i0}})$ is close to 1, the contribution of the i-th strip is in phase with that of the overall serration, thus leading to constructive interference. The opposite situation occurs for $\cos(\phi_{\mathrm{i0}})$ close to -1. It should be pointed out that this analysis would, in principle, neglect the constructive and/or destructive interference between the different serration teeth. However, as previously mentioned, it has been verified that the spanwise coherence length upstream the serrated trailing-edge is not significantly affected by the presence of the serration. Therefore, considering Fig. 4.10 and that $s = 2\lambda$, it can be inferred that the pressure coherence length is smaller than the serration wavelength λ and no coherent interference is expected between the different serrations. The spanwise coherence length averaged along the serration will be shown in Sec. 4.4.6 to further support this point. Finally, it is worth mentioning that each serration strip might contain scattered noise from the other strips due to the compressible nature of the LBM scheme. However, its contribution to the far-field noise is expected to be a small compared to that associated to the hydrodynamic pressure fluctuations.

The magnitude of the cross-spectral density shows that, regardless of the flap angle and airfoil incidence, the dominant sources of noise are mainly located at the root of the serration. However, whilst at low frequency the main noise sources are confined to the very beginning of the serration, they are much more distributed along the serrated edge as the frequency increases. This is consistent with the findings of Avallone

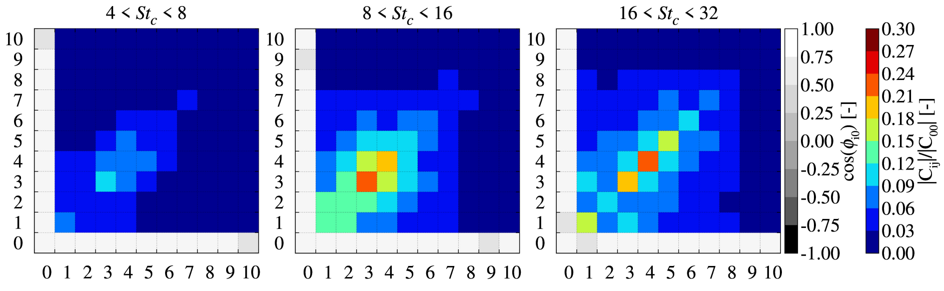

(a) *Serr-chord* - $\beta = 0.0°$

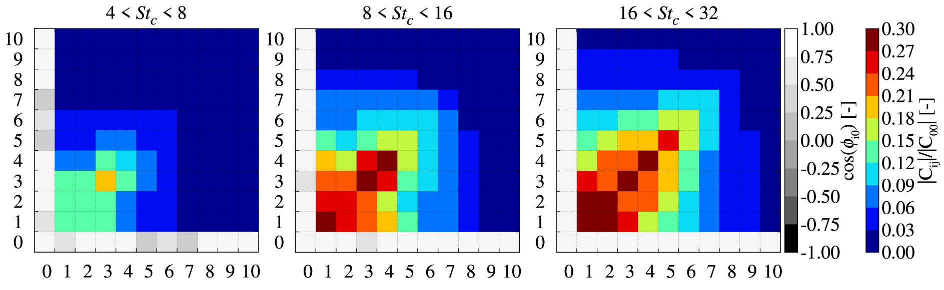

(b) *Serr-mid* - $\beta = 6.6°$

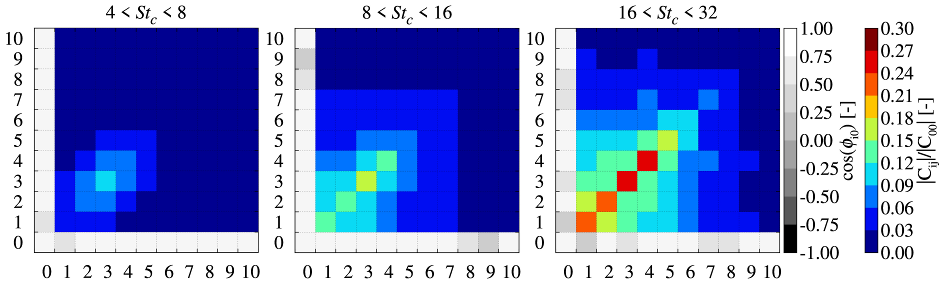

(c) *Serr-camber* - $\beta = 13.2°$

Figure 4.15: Normalized cross-spectral density matrix (colored scale) between the different serration strips and phase information (grey scale) with respect to the overall serration region, case 6 ($\alpha = -0.88°$).

et al. [145] for a symmetric airfoil retrofitted with sawtooth serrations at zero flap angle and angle of attack. On the other hand, the phase angle results of the cross-spectral density tend to partially differ from those of the above mentioned study. Indeed, they found that the scattered waves at the central part of the serration destructively contribute to the low-frequency far-field noise radiated by the entire serration region [145]. In the present study, none of the strips shows a strong out-of-phase noise radiation (i.e. $\cos(\phi_{i0}) < -0.5$) and only some moderate phase differences between the scattered waves are found. This aspect is observed for all the angles of attack and flap angles examined here. These findings suggest that, as the serration is at incidence with respect to the flow,

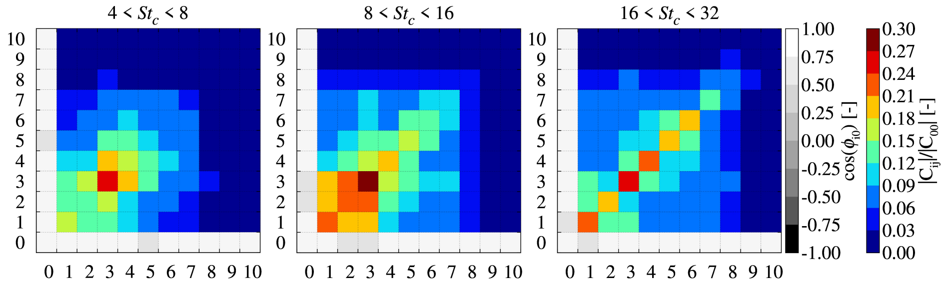

(a) *Serr-chord* - $\beta = 0.0°$

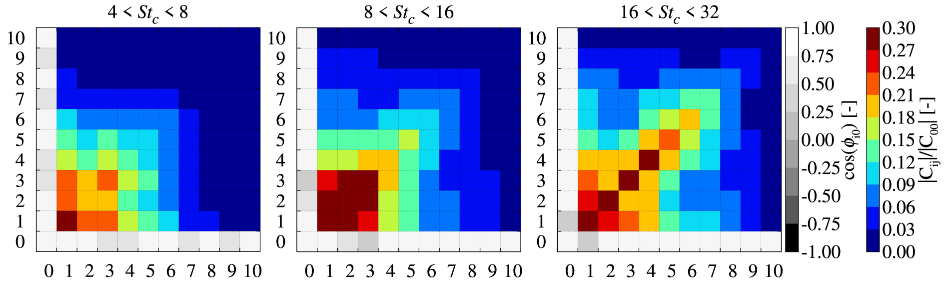

(b) *Serr-mid* - $\beta = 6.6°$

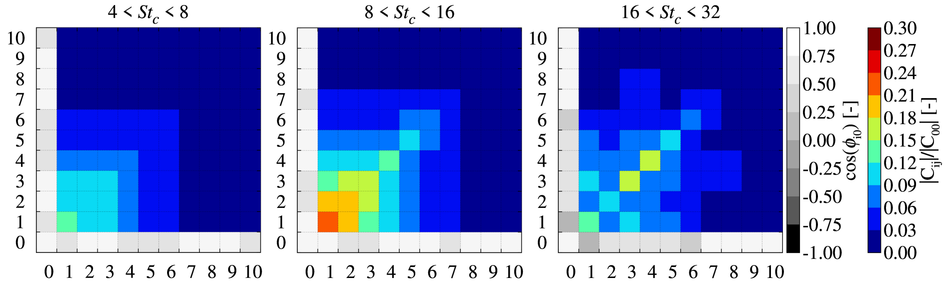

(c) *Serr-camber* - $\beta = 13.2°$

Figure 4.16: Normalized cross-spectral density matrix (colored scale) between the different serration strips and phase information (grey scale) with respect to the overall serration region, case 7 ($\alpha = 4.62°$).

a lower destructive interference among the noise sources distributed along the serrated edge is promoted compared to zero incidence serrations, thus resulting in a lower noise suppression effectiveness of the serration itself. Interestingly, for the shallow negative angle of attack case ($\alpha = -0.88°$), the mid-aligned serration (Fig. 4.15(b)) shows more uniform values of the auto-spectral density, as well as larger phase differences between the waves scattered from the noisiest strips and the overall serration region compared to the chord- and camber-aligned ones (Figs. 4.15(a) and 4.15(c), respectively). These aspects are responsible of a larger noise reduction [145, 165]. Similar results are observed for $\alpha = 4.62°$ (Fig. 4.16), although, for this angle of attack, also the chord-aligned serration shows quite distributed noise sources along the serrated edge (Fig. 4.16(a)) and some phase differences between the acoustic signatures radiated from the noisiest strips and the overall serration.

4.4.5. MEAN FLOW AROUND THE SERRATED TRAILING-EDGE

The far-field noise analysis showed that for both the angles of attack considered in this study, the serration mounted at an intermediate flap angle between the chord- and camber-aligned configurations manifested the highest noise reduction. Moreover, the analysis of the scattering behavior of the serration showed that, although the noise sources are mainly localized at the serration root for each flap angle, they are more distributed along the serrated edge for the $\beta = 6.6°$ case. This might be caused by a modification of the mean flow organization for different serration flap angles. Earlier studies conducted by Howe [134], Chong & Vathylakis [140], Arce-León *et al.* [147] and Avallone *et al.* [145] indicated that the flow alignment with respect to the serrated edge represents one of the driving mechanisms that positively contributes to the noise reduction. In order to verify this finding, Figs. 4.17 and 4.18 depict the time-averaged flow deflection angle φ over the serration, extracted at the closest voxels layer to the add-on surface, with near-wall streamlines superimposed. The angle φ represents the deflection angle between the undisturbed and actual (local) streamlines, and is defined as $\varphi = \tan^{-1}(\langle w \rangle / \langle u \rangle)$, where $\langle u \rangle$ and $\langle w \rangle$ are the wall-parallel (i.e. directed as x_s) and spanwise (i.e. directed as z_s) time-averaged flow velocity components, respectively. One can note that a modification of the deflection angle φ results in a change of the effective angle (i.e. the angle between the serrated edge and the local streamline) at which the turbulent structures are convected over the slanted edge.

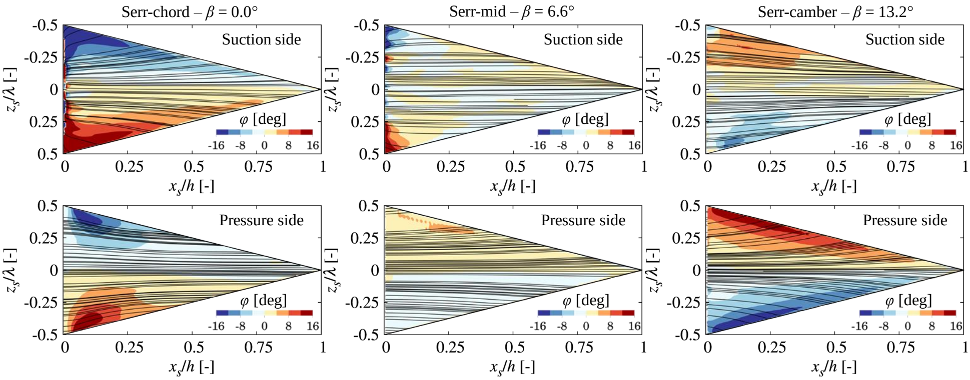

Figure 4.17: Contours of time-averaged near-wall flow deflection $\varphi = \tan^{-1}(\langle w \rangle / \langle u \rangle)$ and streamlines, case 6 ($\alpha = -0.88°$).

For the shallow negative angle of attack case (Fig. 4.17) and flap angle $\beta = 0.0°$, the flow exhibits a pronounced outward motion (i.e. from the centerline of the serration towards the serration edge) on the suction side at the root of the serration. On the pressure side, a weaker inward motion (i.e. from the serration edges towards the centerline of the serration) is visible. The opposite situation occurs for the camber-aligned serra-

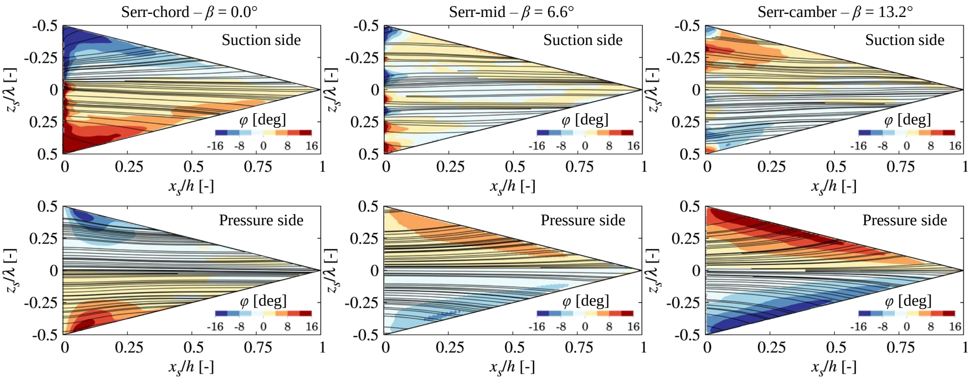

Figure 4.18: Contours of time-averaged near-wall flow deflection $\varphi = \tan^{-1}(\langle w\rangle \,/\, \langle u\rangle)$ and streamlines, case 7 ($\alpha = 4.62°$).

tion ($\beta = 13.2°$), whereas the $\beta = 6.6°$ case shows an intermediate condition with respect to the chord- and camber-aligned configurations, with the near-wall streamlines mostly aligned with the streamwise direction. These aspects can be related to the overall noise reduction performance of the intermediate configuration: the outward flow motion enhances the efficiency of the noise scattering of the sources on the serrated edge, as the streamlines are more perpendicular to the local edge (i.e. larger effective angle). Moreover, for the chord and camber aligned cases, the large outward flow motion near the root, on the suction side for $\beta = 0.0°$ and on the pressure side for $\beta = 13.2°$, might explain why the strongest noise sources are more localized towards the root for these angles, whereas are more distributed along the edge for $\beta = 6.6°$. Similar considerations can be argued for the positive angle of attack case (Fig. 4.18). However, although the level of misalignment between the local streamline and the serrated edge considerably influences the efficiency of the noise radiation, it cannot be used to completely explain the noise reduction, as pointed out by Arce-León *et al.* [142]. This might explain why the camber-align serration ($\beta = 13.2°$) performs similarly to (for $\alpha = 4.62°$) or even better then (for $\alpha = -0.88°$) the intermediate one ($\beta = 6.6°$) at low frequency, despite the large flow deflection of the former on the pressure side.

Figure 4.19 depicts the time-averaged streamwise vorticity component $\langle\omega_x\rangle$ for various combinations of angles of attack and flap angles at five different uniformly spaced cross-flow planes, spanning from the root to the tip of the serration. In addition, mean-flow streamlines around the serration tooth are also shown. Streamwise contra-rotating vortices generated around the slanted edges are visible for each case. The circulation associated to these horseshoe vortices tends to be more affected by the serration flap angle than the airfoil angle of attack, as expected, due to the larger values of the former compared to the latter. For the chord-aligned serration, these vortex pairs reveal a downwash motion between the serrations and an upwash motion on the tooth itself. This effect occurs for both $\alpha = -0.88°$ and $\alpha = 4.62°$, but it is more significant for the former. The opposite situation takes place for the mid- and camber-aligned serrations, although it turns out to be much more evident for the positive angle of attack case ($\alpha = 4.62°$). This transverse flow motion is induced by the pressure difference generated between upper and lower sides of the serrations, being the serration at incidence with respect to the incoming flow, as previously shown in Fig. 4.11. It is interesting to note that the intensity of the above mentioned streamwise vortices, which is more pronounced at the root of the serration, is directly correlated with the level of flow misalignment with respect to the streamwise direction observed in Figs. 4.17 and 4.18. A similar flow behavior was experimentally observed by Arce-León *et al.* [142] for a NACA 0018 airfoil retrofitted with sawtooth serrations for different combinations of flap angles and angles of attack. Moreover, it is interesting to note that the configurations that simultaneously show the larger horseshoe vortex intensity and its closer proximity to the serration tooth (Serr-chord/camber for $\alpha = -0.88°$ and Serr-camber for $\alpha = 4.62°$) are also characterized by the lower levels of far-field noise reduction. Presumably, the more intense three-dimensional vortex dynamics leads to additional sound generation by interacting with the surfaces, thus reducing the benefit of the serrations. From the far-field noise results (Fig. 4.12) and the mean-flow streamlines around the serration (Fig. 4.19), it can be argued that the best-suited orientation of the add-on in terms of turbulent boundary-layer trailing-edge noise reduction is that for which the serration is oriented as the mean streamlines deviation angle with respect to the tangent to the camber line.

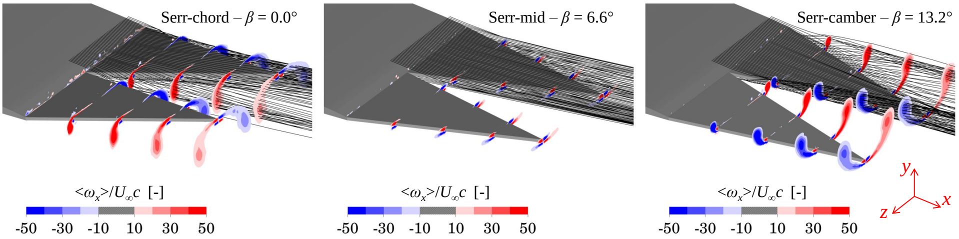

(a) *Case 6,* $\alpha = -0.88°$

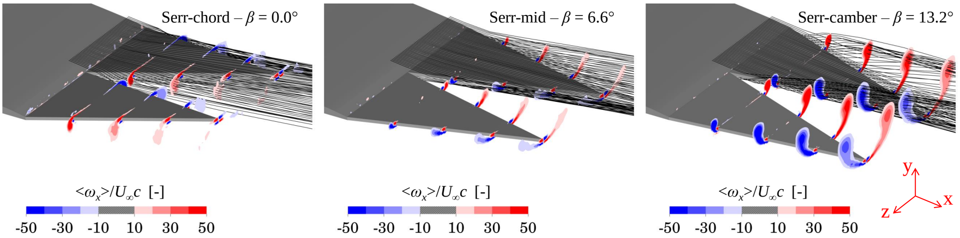

(b) *Case 7,* $\alpha = 4.62°$

Figure 4.19: Contours of time-averaged normalized streamwise vorticity component with fluid streamlines around the serrated trailing-edge (values $-10 < \langle\omega_x\rangle / U_\infty c < 10$ not shown).

4.4.6. WALL-PRESSURE STATISTICS ALONG THE SERRATED EDGE

As already mentioned in Sec. 4.4.5, it is known that the level of serration-flow misalignment plays a relevant role upon the efficiency of the noise scattering of a serrated trailing-edge. However, it may not be sufficient to fully explain the resulting far-field noise [142]. Therefore, the pressure over the serrated edge is further investigated in terms of power spectral density, spanwise coherence length and convection velocity, in order to correlate the wall-pressure statistics to the radiated sound. These quantities are considered as they are those used in Amiet's trailing-edge analytical model [166]. According to this theory, higher wall-pressure spectrum, spanwise coherence length and convection velocity lead to higher far-field noise radiation for a straight trailing-edge.

Figures 4.20 and 4.21 show the wall-pressure power spectral density Φ_{pp} for $\alpha = -0.88°$ and $\alpha = 4.62°$, respectively. The wall-pressure spectra, directly obtained from the LBM simulation, are computed along the slanted edge at three different streamwise locations ($x_s/h = 0.2$, $x_s/h = 0.5$ and $x_s/h = 0.8$) on both suction and pressure sides. For each case presented, the magnitude of the wall-pressure fluctuations tends to generally decrease from the root to the tip of the serration, confirming the observation that the intensity of the noise sources is higher in proximity of the root. Low frequencies tend to dominate the wall-pressure spectrum at the root of the serration, whereas a richer high frequency content is observed in proximity of the tip. These results are in line with the findings of Avallone *et al.* [145]. In addition, for both angles of attack, the mid-aligned serration shows a much more uniform wall-pressure spectrum implying a more uniform distribution of the noise sources along the serrated edge compared to the other two flap angles. These results are consistent with the previous cross-spectral density analysis shown in Sec. 4.4.4. For $\beta = 6.6°$, the wall-pressure fluctuations are generally smaller than (or comparable to) those of the chord- and camber aligned serrations. This suggests that another possible cause for the better noise suppression behavior of the mid-aligned serration can be ascribable to the overall lower intensity of the pressure fluctuations scattered at the serrated edge, which is related to the way the turbulent structures convect over the serrated edge as a consequence of the specific serration flap incidence.

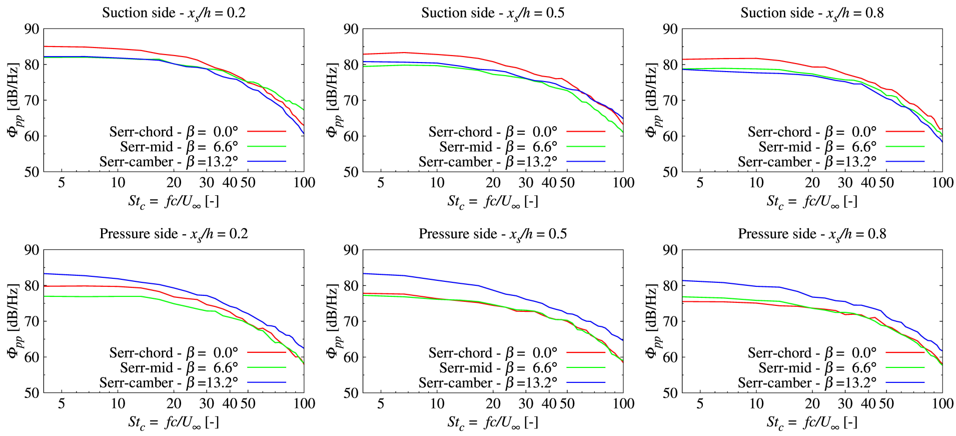

Figure 4.20: Wall-pressure spectra Φ_{pp} along the serrated edge for three streamwise locations ($x_s/h = 0.2$, $x_s/h = 0.5$, $x_s/h = 0.8$) on the suction and pressure sides, case 6 ($\alpha = -0.88°$).

Since the serration flap angle might alter the way the turbulent structures are convected and distributed over the serrated edge, Figs. 4.22 and 4.23 show the spanwise

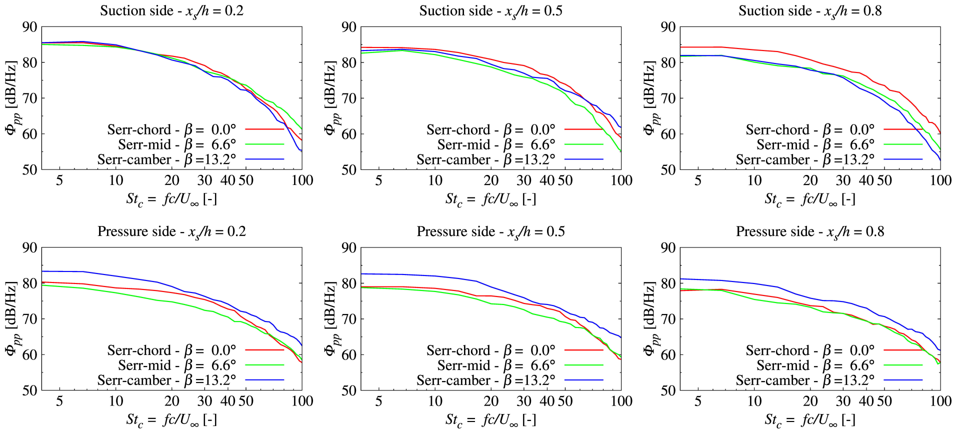

Figure 4.21: Wall-pressure spectra Φ_{pp} along the serrated edge for three streamwise locations ($x_s/h = 0.2$, $x_s/h = 0.5$, $x_s/h = 0.8$) on the suction and pressure sides, case 7 ($\alpha = 4.62°$).

coherence length l_z, the convection velocity u_c and their product $u_c l_z$ for $\alpha = -0.88°$ and $\alpha = 4.62°$, respectively. For both suction and pressure sides, the spanwise coherence length l_z is evaluated using Eq. (4.5) on the coherence function γ computed at three different streamwise locations on the serration (i.e. $x_s/h = 0.2$, $x_s/h = 0.5$ and $x_s/h = 0.8$) and averaging among them. Correspondingly, the convection velocity u_c is calculated along the serrated edge at the same streamwise locations on both suction and pressure sides, using the spectral approach proposed by Romano [167] and adopted by Chong & Vathylakis [140]:

$$u_c(f) = 2\pi\eta\left[\frac{\partial\phi}{\partial f}\right]^{-1}, \tag{4.7}$$

where ϕ is the phase calculated from the cross-spectral density of the wall-pressure signals between two points spaced by η along the local flow direction (i.e. the local streamline). Then, u_c is further averaged over the three streamwise locations for suction and pressure sides, respectively. This simplification of averaging l_z and u_c is carried out in order to retrieve single frequency-dependent curves to be used for comparisons among the different serration flap angles, similarly to [145]. Although not shown for the sake of conciseness, it is noted that the spanwise coherence length l_z generally decreases from the root to the tip of the serration, for each angle of attack and serration flap angle examined. For each case, it is observed that the convection velocity u_c tends to increase from the root to the tip of the serration, in agreement with previous experimental evidences [144, 147].

For a given side of the serration, similar trends of the spanwise coherence length l_z and convection velocity u_c are found for the three different flap angles between $\alpha = -0.88°$ and $\alpha = 4.62°$. For each case examined, l_z decreases as the frequency increases, showing a different decay rate depending on the flap angle and angle of attack considered. For the mid- and camber-aligned serrations, l_z generally shows higher values compared to the chord-aligned one on the suction side, while on the pressure side

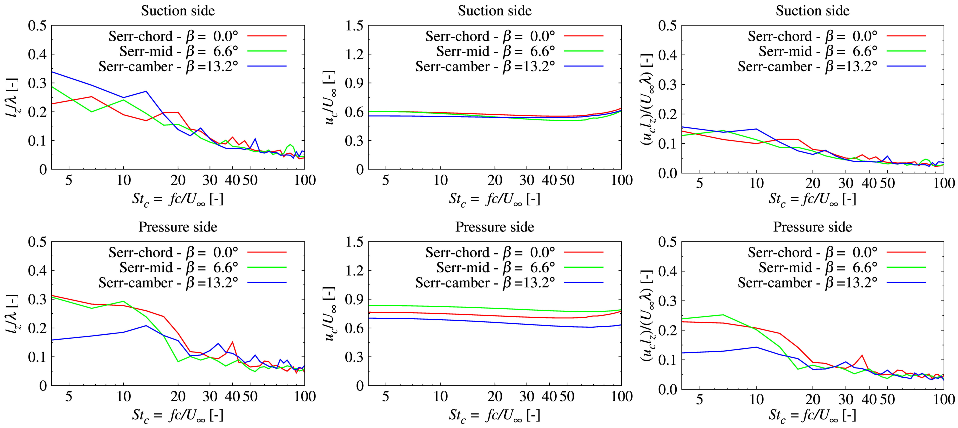

Figure 4.22: Spanwise coherence length l_z (left), convection velocity u_c (center) and their product $u_c l_z$ (right) on the suction (top) and pressure (bottom) sides, case 6 ($\alpha = -0.88°$).

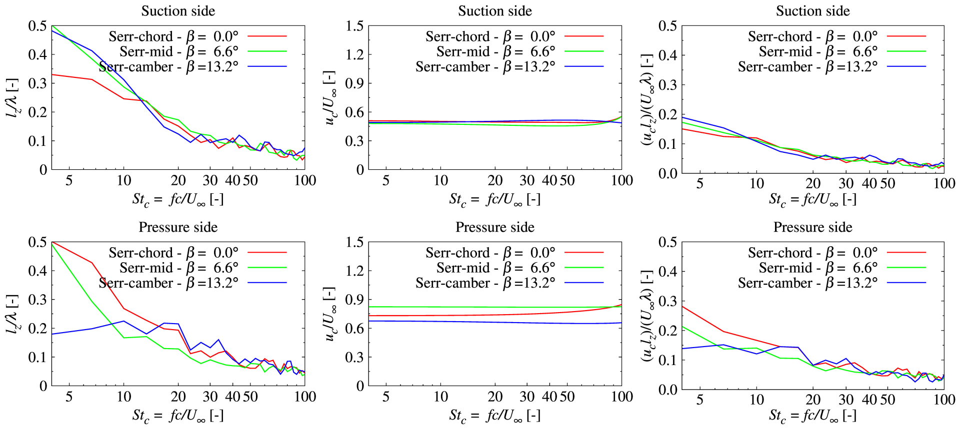

Figure 4.23: Spanwise coherence length l_z (left), convection velocity u_c (center) and their product $u_c l_z$ (right) on the suction (top) and pressure (bottom) sides, case 7 ($\alpha = 4.62°$).

the chord- and mid-aligned cases show an overall larger spanwise coherence length than the camber-aligned one. This is observed for both angles of attack and is more significant for $\alpha = 4.62°$. Interestingly, for each flap angle, the different l_z curves tend to collapse on each other for $St_c > 20$. This is in agreement with previous findings obtained by Jones & Sandberg [168] and Avallone *et al.* [145], who observed that serrations do not affect the flow characteristics for high non-dimensional frequencies. A larger flow outward motion along the serrated edge results in a smaller spanwise coherence length at low frequency (and vice-versa), as shown in Figs. 4.17 and 4.22, and Figs. 4.18 and 4.23.

Regarding the convection velocity, rather constant curves of u_c with respect to frequency are found, with larger values observable on the pressure side of the serration. While on the suction side the three flap angles show very similar values of u_c, a larger scatter of the data is observed on the pressure side, with the mid- and camber-aligned serrations showing the largest and the lowest values of u_c, respectively. The larger convection velocity for the mid- and chord-aligned cases might be associated to the presence of a more uniform flow over the serration compared to the camber aligned one, as previously highlighted in Figs. 4.17 and 4.18. Note that the non-dimensional u_c curves fall within the commonly expected values of 0.5 and 0.8 [158].

According to the straight trailing-edge noise theory [166], larger values of u_c and l_z would result in higher far-field noise levels. In contrast, for a serrated edge at zero incidence, while an increment of u_c might still result in a larger noise radiation, a higher l_z could be beneficial for noise reduction, due to the fact that it might promote destructive interference effects among scattered pressure waves within one correlation length [145, 165]. The results shown in Figs. 4.15 and 4.16 indicated that, for each angle of attack and serration flap angle, the noise sources distributed along the slanted edge are characterized by only small or moderate phase differences. This suggests that a larger spanwise coherence length would still result in a penalty in terms of noise reduction for the examined serrated cases, as for the convection velocity. For this reason, it is worth assessing the combined effect of u_c and l_z on the effectiveness of sawtooth serrations at incidence in reducing noise, by considering their product $u_c l_z$. As depicted in Figs. 4.22 and 4.23, the three different flap angles show quite similar $u_c l_z$ on the suction side for both angles of attack. Conversely, on the pressure side, the camber-aligned serration shows a smaller $u_c l_z$ at low frequency compared to the mid- and chord-aligned serrations. This aspect might explain why, at low frequencies, the camber-aligned serration showed a noise reduction higher than that associated to the other two flap angles (Figs. 4.12 and 4.13), despite the more pronounced outer motion of the flow convecting over it compared to the mid- and chord-aligned cases (as shown in Figs. 4.17 and 4.18).

In view of the above, one could conclude that the primary mechanisms by which the serration flap angle affects the trailing-edge noise reduction effectiveness of sawtooth serrations are by means of a variation of: (i) the effective angle at which the turbulent structures are convected over the trailing-edge; (ii) the convection velocity and spanwise coherence length along the serration; (iii) the intensity of the hydrodynamic wall-pressure fluctuations that are scattered along the slanted edge. Among them, the variation of the hydrodynamic wall-pressure fluctuations and the flow effective angle are believed to be the most essential mechanisms through which the serration flap angle influences the way a sawtooth serration reduces noise. This is suggested by the larger level of correlation with the far-field noise reduction showed by the modification of the aforementioned flow quantities compared to the variation of both spanwise coherence length and convection velocity.

4.5. CONCLUSIONS

The flow field around a NACA 64-618 airfoil with and without serrations and its resulting turbulent boundary-layer trailing-edge noise were investigated at different airfoil angles of attack and serrations flap angles. The natural boundary-layer transition cases of the AIAA BANC-V Workshop Category 1 (cases 6 and 7) were considered as benchmark for the validation of the computational setup for the straight trailing-edge cases. The numerical flow solution was obtained by using the fully explicit, transient and compressible lattice-Boltzmann equation implemented in the CFD/CAA solver SIMULIA PowerFLOW®. The aerodynamic noise generated by the scattering of the hydrodynamic pressure fluctuations at the airfoil trailing-edge was estimated by using an acoustic analogy based on Farassat's formulation 1A of the FW-H equation applied to the airfoil surface.

A grid convergence study was conducted for the straight trailing-edge cases to verify the independence of the numerical results from the computational mesh. It was carried out in terms of mean pressure distribution, turbulent boundary-layer pressure and velocity statistics in proximity of the trailing-edge and far-field noise radiation for three different computational grids. It showed a good level of grid convergence for the medium resolution grid, which was consequently used for the analysis of the serration flap angle effects. Overall, the numerical results compared satisfactorily against the experimental data in terms of airfoil pressure distribution, boundary-layer profiles, far-field noise radiation and spanwise coherence length. A large over-prediction of the wall-pressure spectrum in proximity of the straight trailing-edge was observed for both cases 6 and 7. However, semi-empirical wall-pressure spectrum predictions were found to compare more favorably with the numerical results. A cross comparison between numerical results, experiments, and semi-analytical far-field noise predictions (fed with experimental wall-pressure spectra) suggested that the discrepancies observed between the numerical and experimental results could be due to a combination of factors in both simulations and experiments.

After the assessment of the computational setup for the straight trailing-edge cases, the influence of the serration flap angle on their noise reduction effectiveness was investigated. The NACA 64-618 airfoil was retrofitted with sawtooth serrations mounted at three different flap angles for both cases 6 and 7. Chord- and camber-aligned serrations, as well as an intermediate flap angle configuration, were considered for each airfoil angle of attack. The analysis was carried out in terms of mean airfoil pressure distribution, far-field noise radiation, serration scattering and near-wall hydrodynamic flow topology and statistics. For the angles of attack considered, the mid-aligned serration was found to have a minimal impact on the airfoil pressure distribution and to generate only a low pressure gradient across the serration, implying that this configuration should not considerably affect the performances and steady loading noise when retrofitted to a rotor/propeller blade. Moreover, it manifested the overall best noise suppression behavior for each angle of attack examined, except at very low frequencies, while the chord- and camber-aligned ones showed opposite noise reduction behaviors depending on the specific airfoil angle of attack. The analysis of the add-ons scattering effects showed that, for all the angles of attack and flap angles considered, no large phase differences between the acoustic waves scattered by each serration strip and the overall serration occur. This suggested that no (or only minimal) destructive interference among noise sources distributed along the serrated edge is promoted when a serration is at incidence, compared to zero incidence cases. For each case examined, it was observed that most of the noise was generated at the root of the serration, although the mid-aligned one showed a more uniform distribution of the noise sources along the slanted edge compared to the two other configurations.

The serration flap angle was found to affect the far-field noise emission primarily through a modification of: (i) the effective angle at which the turbulent structures are convected over the serrated edge; (ii) the convection velocity and spanwise coherence length along the serration; (iii) the intensity of the hydrodynamic wall-pressure fluctuations that are scattered along the serrated edge. Among them, the first and last phenomena are expected to play the most important role upon the far-field noise reduction, while the combined variation of the convection velocity and spanwise coherence length is found to influence the noise mitigation mainly at low frequency.

5

PROPELLER NOISE I: TRIP EFFECTS ON PERFORMANCE AND NOISE PREDICTIONS

> *Against that positivism which stops before phenomena, saying "there are only facts", I should say: "no, it is precisely facts that do not exist, only interpretations".*
>
> Notebooks (Summer 1886 – Fall 1887), Friedrich Wilhelm Nietzsche

Chapter 4 presented the prediction and investigation of airfoil broadband trailing-edge noise for a blade segment at incidence, with and without serration, and undergoing natural laminar-to-turbulent boundary-layer transition. In the present chapter, the focus is enlarged to a complete propeller geometry operating at low-Reynolds numbers. Broadband self-noise prediction of low-Reynolds number propellers is particularly challenging, due to the requirement for the employed computational method to emulate the complexity of the laminar/turbulent boundary-layer behavior on the blade. A zig-zag transition trip on the propeller blades is used in the numerical setup to reproduce resolved turbulent pressure fluctuations in the boundary-layer for broadband noise computation at engineering level and relatively low computational cost. The effect of using a transition trip to simulate low-Reynolds number propellers, as well as the impact of its chordwise position on the calculation of performances and radiated noise, is outlined. The trip position marginally affects the thrust and to a slightly larger extent the torque prediction. Tonal noise at the blade-passing frequencies does not show a relevant sensitivity to it, whereas broadband noise is found to be slightly more influenced by the chordwise position of the trip, especially at high advance ratios. The low sensitivity of the numerical results to the trip location, as well as their good agreement with loads and noise measurements carried out in the A-Tunnel of TU-Delft, demonstrates the robustness of the proposed approach for industrial applications.

Parts of this chapter have been published in the AESCTE journal (2021) [169].

5.1. INTRODUCTION

IN recent years, the aeroacoustics associated to low-Reynolds number propellers ($Re_c < 1 \cdot 10^5$ based on the chord at 75% of the blade radius) has significantly gained the attention in the aerospace community [170–174], due to the rapid expansion of small rotary-wing UAVs[1] for commercial, scientific or recreational applications, as well as to the emergent market of propeller-driven PAVs[2] for on-demand urban air transport [10]. Since these are full-electric and battery-powered vehicles that are expected to operate in densely populated areas, high propulsive efficiency and low-acoustic footprint represent essential target of their design process, with the aim of increasing endurance and limiting noise nuisance towards the community [10].

Due to the lower blade tip velocity of small-scale propellers compared to traditional helicopter rotors, broadband self-noise - in the form of turbulent boundary-layer trailing-edge noise - becomes a relevant contributor to the far-field acoustics in addition to steady/unsteady loading and thickness noise [11]. Turbulent boundary-layer trailing-edge noise is associated to the scattering of the hydrodynamic pressure fluctuations, within the turbulent boundary-layer developing over the blade surface, when they pass a geometrical singularity such as a sharp trailing-edge [35], as discussed in Sec. 2.1.1. Moreover, the performance and noise signature of propellers operating at low-Reynolds numbers can be significantly affected by the behavior of the boundary-layer developing over the blades. In the low-Reynolds number regime, the boundary-layer remains laminar for a relatively large extension of the blade chord and possibly separates. The resulting separated shear layer, depending on the local angle of attack, Reynolds number, airfoil characteristics and incoming flow conditions, can reattach as either a laminar or turbulent boundary-layer and lead to the formation of a laminar separation bubble [43, 45]. The position and length of the laminar separation bubble are mainly influenced by the local airfoil angle of attack and Reynolds number [45], and can have a detrimental impact on both propeller performances [175] and noise emissions [48].

The presence of a laminar separation bubble can significantly alter the airfoil pressure distribution, resulting in an increment of the drag generated by the local blade section [176]. Furthermore, a feedback loop between hydrodynamic instability waves in the boundary-layer and acoustic waves, associated to the scattering of such instabilities at the trailing-edge, can lead to a significant noise increment when the laminar separation bubble is sufficiently close to the trailing-edge [47], with narrowband tones over a broadband hump featuring the corresponding far-field noise spectrum for 2D airfoils [38], as discussed in Sec. 2.1.1. In rotor applications, a high frequency broadband hump was reported in the far-field noise spectrum in the presence of a laminar separation bubble on the blade surface in previous experimental studies, with [47] and without [47–49] the emergence of a strong tonal content strictly ascribable to the acoustic feedback loop. The presence of a broadband hump with no tonal contribution was associated to the mere trailing-edge scattering of instability waves without the occurrence of a proper acoustic feedback [47].

The accurate prediction of low-Reynolds number propellers aerodynamics and aeroacoustics is a quite challenging topic from a computational perspective. Low-

---

[1] Unmanned Aerial Vehicles.

[2] Personal Aerial Vehicles.

fidelity approaches such as BEMT[3]-2D viscous panel methods for propeller loading computation (in which 2D viscous panel method computations are used to provide the sectional force coefficients for the BEMT calculation) [49] coupled with compact monopole/dipole FW-H formulations for far-field noise radiation [177], can provide very good forces prediction [49], as well as tonal noise estimation within 2-5 dB accuracy [49, 171], at a negligible computational cost. However, the accuracy of such approaches is limited as far as turbulent boundary-layer trailing-edge noise prediction is also concerned, due to the relatively low predictive capability of the semi-empirical wall-pressure spectrum models that are often used in their semi-analytical trailing-edge noise models [11, 49]. A recent benchmark study on a small-scale propeller aeroacoustics conducted by Casalino *et al.* [49] showed a large sensitivity of broadband noise to the particular wall-pressure spectrum model employed, with a scatter of broadband noise predictions within 30 dB among the different models.

Higher fidelity scale-resolving methods, such as DES[4] [29], hybrid RANS/LES[5] [29] or LBM/VLES, represent more accurate approaches to compute both tonal and broadband rotor/propeller noise at computational cost that is lower than that required by LES and complies with industrial turnaround times. Nevertheless, these hybrid CFD methods may suffer in accurately predicting flows characterized by shallow regions of boundary-layer separation and re-attachment [80]. Moreover, they typically rely on the presence of a sufficiently high level of flow instabilities in the numerical solution to switch from modeled to scale-resolving turbulence mode, and thus to generate an unsteady resolved turbulent content [178], which is essential for the sake of turbulent boundary-layer trailing-edge noise prediction. Such shortcomings make capturing laminar separation bubbles and laminar-to-turbulent boundary-layer transition, as well as the associated trailing-edge noise radiation, quite challenging problems to be addressed with these hybrid CFD methods.

In this chapter, the commercial CFD/CAA solver SIMULIA PowerFLOW®, based on a Lattice-Boltzmann Method hybridized with a Very Large Eddy Simulation (LBM-VLES) model for turbulence, is employed with a computational approach to emulate the flow complexity of low-Reynolds number propellers and predict the resulting far-field noise radiation. The aerodynamic noise generated by the propeller is evaluated by using an acoustic analogy based on Farassat's formulation 1A of the Ffowcs Williams & Hawkings' (FW-H) equation applied to the propeller surface. Similarly to DES or global hybrid RANS-LES approaches, the LB-VLES method used in this work relies on the presence of some instabilities in the numerical flow solution to force the VLES turbulence model to enter into the scale-resolving mode. This paper proposes a computational approach based on the usage of a low-intrusive zig-zag transition trip to address this aspect. The zig-zag trip constitutes a geometric imperfection on the blade surface that guides the VLES turbulence model towards a scale-resolving mode and triggers the formation of vortical structures, with scales able to emulate the complexity of the low-Reynolds boundary-layer on the blade, which is required for turbulent boundary-layer trailing-edge noise computation. The validation of such an approach is accomplished

---

[3] Blade Element Momentum Theory.

[4] Detached Eddy Simulation.

[5] Reynolds-Averaged Navier-Stokes/Large Eddy Simulation.

by comparison with forces and noise measurements carried out in the A-Tunnel of TU-Delft. Two different tripping approaches are considered by placing the trip arbitrarily on the quarter-chord line of the blade, and along the expected turbulent boundary-layer transition line, as predicted by a BEMT code coupled with a 2D viscous panel method. With this regard, the present study is aimed at: (i) assessing the proposed computational approach to predict the performances and noise radiation associated to low-Reynolds number propellers; (ii) analyzing the impact and limitations of using a transition trip for low-Reynolds number propeller simulation, as well as to investigate the effect of the trip line location on the propeller loads and noise radiation.

The rest of the chapter is organized as follows. Section 5.2 describes the propeller geometry, operating conditions and computational setup that are used in this study. The numerical results are presented and discussed in Sec. 5.3. Finally, the main conclusions of this work are summarized in Sec. 5.4.

5.2. TEST-CASE AND COMPUTATIONAL SETUP

The geometry used in this study (shown in Fig. 5.1(a)) is a two-bladed propeller designed at TU-Delft and derived from an APC 9x6 propeller. It is characterized by a radius R of 0.15 m and NACA 4412 airfoil sections, which are merged with the propeller hub by elliptical sections (for $r < 0.01$ m). The airfoil chord and twist spanwise distributions are shown Fig. 5.1(b).

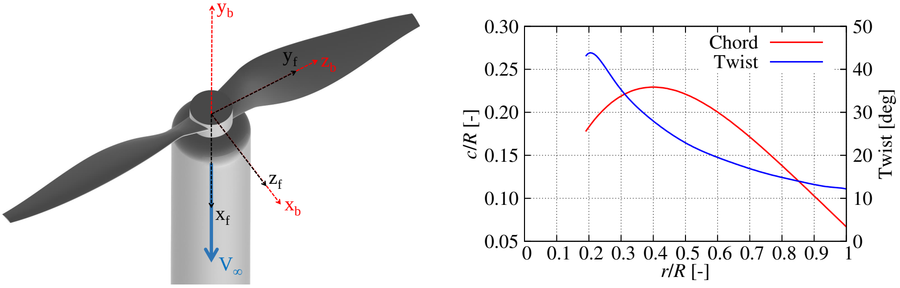

(a) *Propeller and coordinate systems* (b) *Airfoil chord and twist distributions*

Figure 5.1: Propeller geometry, coordinate systems, airfoil chord and twist spanwise distributions.

The propeller hub radius is 1.25 cm and connected to a nacelle of 5 cm diameter and 52 cm length. The propeller geometry under examination has been experimentally tested in the A-Tunnel of TU-Delft and used for low-Reynolds number propeller benchmarking. A detailed description of the propeller geometry and experiment that is used as benchmark in this work can be found in Refs. [49, 179]. Figure 5.1(a) shows the free-stream (x_f, y_f, z_f) and blade coordinate (x_b, y_b, z_b) systems that are used in this study. The former is rigidly connected to a ground-fixed reference frame, whereas the latter rigidly rotates with the blade geometry. The free-stream velocity V_∞ is directed along the x-axis of the free-stream coordinate system. The propeller is operated at fixed angular velocity (n = 83.33 rps, i.e. ω = 523.6 rad/s) and five different advance ratios

$J = 0.0, 0.24, 0.4, 0.6, 0.8$ (where $J = V_\infty/(nD)$, with n denoting the revolutions per second (rps) and D the propeller diameter), by varying the free-stream velocity from 0 to 20 m/s. The resulting tip Mach number is 0.23 and the Reynolds number based on the local airfoil chord and velocity ranges between $5 \cdot 10^4$ and $1 \cdot 10^5$ across the different section and axial velocity conditions. The free-stream static pressure and temperature considered are $p_\infty = 99000$ Pa and $T_\infty = 293.15$ K, respectively.

Figure 5.2(a) depicts the computational setup used in this study. The computational fluid domain is a spherical volume of $325D$ radius centered around the propeller. Free-stream static pressure and velocity, and turbulence intensity of 0.1% of the free-stream velocity are prescribed on its outer boundary. The experimental wind tunnel geometry is not modeled in the computational setup. An acoustic sponge is used to dissipate the out-going acoustic waves and minimize the backward reflection from the outer boundary and reproduce a full anechoic digital environment. The acoustic sponge is defined by two concentric spheres of radius $15D$ and $55D$, respectively, centered around the propeller. The fluid kinematic viscosity is gradually increased starting from its physical value within the inner sphere, up to an artificial value two orders of magnitude higher outside the outer one.

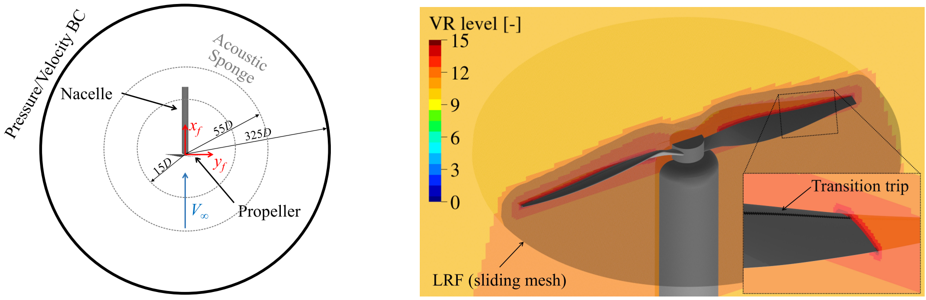

(a) *Computational setup*

(b) *Near body mesh*

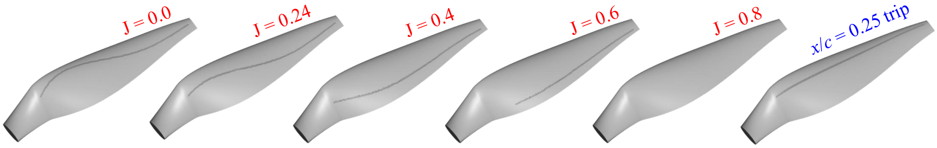

(c) *Trip line distributions: Opty∂B*-BEMT *trips (red) and* $x/c = 0.25$ *trip (blue)*

Figure 5.2: Sketch of (a) computational setup (not drawn to scale), (b) near body mesh and (c) trip line distributions on the blade suction side.

Since one of the goals of the present study is to predict trailing-edge noise of low-Reynolds number propellers, with turnaround times feasible for industrial applications, it is necessary to resolve part of the energy spectrum associated to the turbulent pressure fluctuations in the simulated boundary-layer. Hence, a zig-zag transition trip of 0.17 mm thickness, 0.9 mm amplitude and wavelength is used on the suction side of the blade (for $r/R > 0.2$) to drive the LBM-VLES scheme from turbulence modeling to scale-resolving behavior and trigger the formation of vortical structures, with scales capable of emulating the complexity of a low-Reynolds number boundary-layer at a relatively low computational cost. The zig-zag topology is preferred to other trip shapes due to its high efficiency and low critical roughness height-based Reynolds number in initiating transition [180]. The height of 0.17 mm, corresponding to three finest voxels, is selected to ensure that the flow volume surrounding the trip is sufficiently discretized, according to the employed computational mesh, and that the trip is able to initiate transition regardless its chordwise position for the sake of industrial robustness. Indeed, the blade suction side is tripped considering two different strategies: (i) trip line arbitrary positioned at 25% of the chord; (ii) trip distributed along the expected boundary-layer transition line (i.e. at the end of the laminar separation bubble) as predicted by *Opty∂B*-BEMT, a BEMT code coupled with a 2D viscous panel method developed by Dassault Systèmes. The former is a modeling choice that might be followed in absence of any information on the boundary-layer transition process, while the latter represents an approach more consistent with the physics of the problem, according to which transition is likely to occur across the laminar separation bubble reattachment line. For both cases, no trip is placed on the blade pressure side, since no laminar-to-turbulent boundary layer transition is expected to occur by the BEMT/2D-viscous panel method code. Figure 5.2(c) shows the trip line positions predicted by the BEMT model for the different advance ratios considered, as well as the configuration with trip located at 25% of the blade chord. Portions of the trip line above the 80% of the chord were omitted from the generation of the zig-zag trip to avoid placing the trip excessively close to the blade trailing-edge and promoting an undesired flow separation.

Figure 5.2(b) shows the details of the computational setup and mesh in proximity of the propeller geometry. The propeller and hub are encompassed by a volume of revolution that defines the Local Reference Frame (LRF), namely the rotating sliding mesh domain used to reproduce the propeller rotation. The solid FW-H integration surface used to compute the far-field noise radiation coincides with the propeller, hub and nacelle surfaces. A total of 16 Variable Resolution (VR) regions are used to discretize the whole fluid domain, with the finest resolution level (VR15) placed around the blade trip and trailing-edge. A resolution of 200 voxels along the mean chord (22.85 mm) is used in the second finest resolution level (VR14), resulting in a smallest voxel size of 0.06 mm, a mean $y+ \approx 5$ on the blade surface and an overall mesh size of 107 million voxels. Simulations are performed using the low-subsonic LBM/VLES solver implemented in SIMULIA PowerFLOW® 6-2019-R4 (see Sec. 3.2). The computational cost is 840 CPUh/rev on a 430 cores cluster with Intel Xeon CPU E5-2697 2.6 GHz. The whole fluid domain is initialized with the instantaneous flow solution from a statistically converged coarser simulation. Hence, after a settling time corresponding to 2 propeller revolutions, the sampling of relevant flow data is started for 10 additional revolutions. Acoustic data is sampled at 365 kHz with spatial averaging of 0.5 mm on the solid FW-H integration surface. Fourier transformed data is obtained with 2 Welch blocks, 50% overlap and Hanning windowing, corresponding to a bandwidth of 16.6 Hz (BPF[6]= 0.1).

---

[6] Blade-Passing Frequency.

5.3. NUMERICAL RESULTS

In this section, the LBM-VLES results, obtained by tripping the blade suction side at $x/c = 0.25$ and along the boundary-layer transition line location predicted by *Opty∂B*-BEMT, are presented. The numerical results are compared against the measurements carried out in the A-Tunnel of TU-Delft to assess the capability of the employed computational approach to predict the performances and aeroacoustics of low-Reynolds number propellers at engineering level. No transition trip was employed in the experimental data reported in the following. Since no acoustic data was measured at $V_\infty = 20$ m/s, due to the relatively high background noise in the experimental setup, the aeroacoustic analysis is limited to only J between 0.0 and 0.6. Hence, results for $J = 0.8$ are presented only in terms of thrust and torque coefficients. The grid independence of the numerical results was verified in a previous study carried out by the author [49].

5.3.1. MEAN THRUST, TORQUE AND PROPULSIVE EFFICIENCY

Figure 5.3 shows the comparison between the experimental and numerical thrust (C_T) and torque (C_Q) coefficients, and propulsive efficiency (η) at different advance ratios, which are computed as follows:

$$C_T = \frac{T}{\rho n^2 D^4}, \quad C_Q = \frac{Q}{\rho n^2 D^5} \quad \text{and} \quad \eta = \frac{JC_T}{2\pi C_Q}, \tag{5.1}$$

with T and Q being the mean propeller thrust and torque, n the number of revolutions per second and D the diameter.

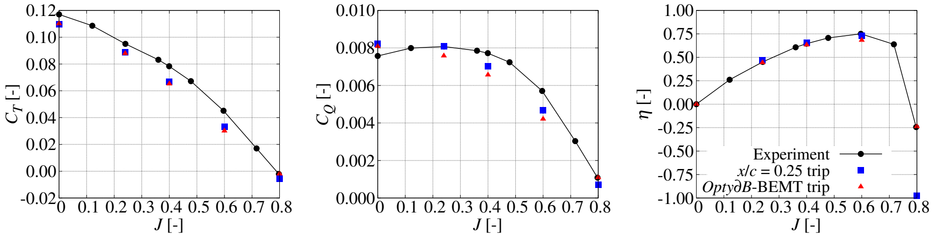

Figure 5.3: Thrust (left), torque (center) and propulsive efficiency (right) coefficients at different advance ratios ranging between $J = 0.0$ and $J = 0.8$. Comparison between measurements and numerical solutions obtained with the $x/c = 0.25$ and *Opty∂B*-BEMT trips.

As shown in Fig. 5.3, the thrust coefficient is predicted in a satisfactory way. The C_T is quite insensitive to the two different ways of tripping the blade suction side between $J = 0.0$ and $J = 0.6$, where the two C_T curves, obtained by tripping the blade at $x/c = 0.25$ and along the expected boundary-layer transition line, provide almost identical thrust values. Contrarily, a small difference is observed between the two numerical solutions at $J = 0.8$, as no zig-zag trip is applied on the blade suction side for the *Opty∂B*-BEMT trip case at this advance ratio (since the BEMT-trip line position completely exceeded the 80% of the chord for the entire blade span, see Fig. 5.2(c)). Overall, the numerical results tend to slightly underestimate the thrust generated by the propeller, except at $J = 0.8$ for the untripped numerical solution (*Opty∂B*-BEMT trip case). Although not shown for the sake of conciseness, it is observed that at $J = 0.8$ the presence of the trip causes a slightly reduction of the suction peak at the leading-edge, thus yielding to a certain thrust decrease, compared to the untripped case (i.e. *Opty∂B*-BEMT). This trip effect on the pressure coefficient distribution will be briefly illustrated in Sec. 5.3.6, while discussing the sensitivity of the numerical results to the reduction of the trip thickness for $J = 0.0$.

Regarding the torque coefficient, the numerical predictions are in a good agreement with the experimental results for low and high values of the advance ratio, although the numerical C_Q does not show the slope sign inversion around $J = 0.24$ observed in the measurements. For intermediate J, the agreement between numerical and experimental results decreases, with the former generally showing lower values compared to the latter. A transition trip is known to provide a local increment of the skin friction across the trip itself, in addition to that associated to an earlier transition, and thus to provide some drag increment of the local airfoil section compared to an untripped case [181]. However, as previously mentioned, the trip is also responsible for a certain attenuation of the suction effect at the leading-edge in the current computations, which in turn is associated to a lower local airfoil drag generation. In addition, due to the presence of the trip, no laminar separation bubbles occur in the numerical simulations, which are known to increase the local airfoil drag [182] and thus the overall propeller torque. These aspects might represent the causes of the torque under-prediction in the numerical results despite the use of a transition trip.

Finally, the propulsive efficiency of the propeller is predicted in a very satisfactory way, except at $J = 0.8$ for the computational setup with trip at 25% of the chord. However, it should be recalled that the propulsive efficiency becomes very sensitive to even small discrepancies in the prediction of C_T and C_Q at nearly non-thrusting advance ratios, such as $J = 0.8$ in the present study, due to the relatively low values of both thrust and torque at such conditions. Interestingly, the thrust and torque discrepancies at low-to-intermediate J tend to cancel out in the computation of η. The fact that thrust, torque and propulsive efficiency are weakly sensitive to the trip chordwise location highlights the industrial robustness of the proposed approach, which can be used with sufficient confidence for the sake of low-Reynolds number propeller performance prediction.

5.3.2. FAR-FIELD NOISE

Figure 5.5 shows, for J between 0.0 and 0.6, the comparison between numerical and experimental far-field noise power spectral densities Φ_{aa} against the frequency f normalized by the Blade-Passing Frequency (BPF = 167 Hz). Two different microphones in the free-stream coordinate system are considered: Mic. 7 (0.0 m, 1.2 m, 0.0 m) and Mic. 11 (-0.75 m, 1.2 m , 0.0 m), respectively located in and out of the propeller plane, as depicted in Fig. 5.4. For each microphone and advance ratio, the unloaded (i.e. without the propeller) electric motor noise (in orange) and the background noise (in green) of the wind tunnel are reported to further support the discussion. To support the analysis of the numerical results, it is worth mentioning that the main sources of uncertainty in the experimental spectra are represented by: (i) the background noise below the wind tunnel cut-off frequency (~200 Hz), which is responsible for the large broadband noise levels at low frequencies; (ii) the loaded electric motor noise and the non-perfect balance of the blades that cause the rise of low-frequency tones at harmonics of the shaft frequency (BPF 0.5, 1, 1.5, etc.); and (iii) the unloaded electric motor noise, which generally adds mid-frequency tonal contributions (approximately between BPF 5 to 25) to the far-field noise spectrum [49, 179].

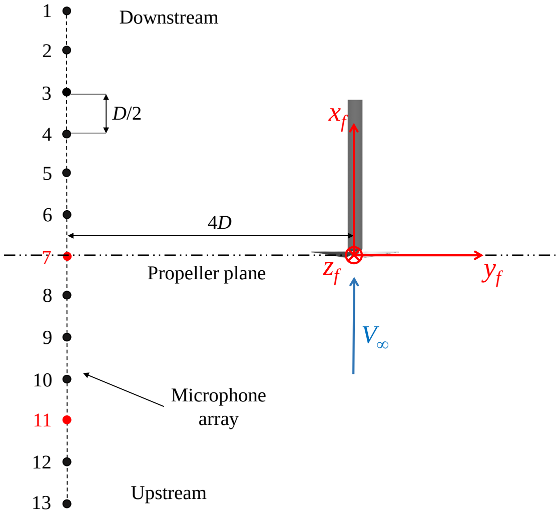

Figure 5.4: Sketch of the microphone array used of far-field noise computation (drawn not to scale).

As shown in Fig. 5.5, the position of the transition trip on the blade suction side does not significantly affect the tonal noise component generated by propeller, even at high advance ratios where the $x/c = 0.25$ and *Opty∂B*-BEMT trip lines are distributed in a rather different way. For $J = 0.0$, the amplitude of the tone at BPF 1 is nearly the same for both the $x/c = 0.25$ and *Opty∂B*-BEMT trip cases. For increasing advance ratios, the tone at BPF 1, for the solution with trip at 25% of the chord, tends to be slightly larger than that with the BEMT trip, up to a maximum difference of about 1 dB at $J = 0.6$. This aspect is consistent with the thrust results presented in the previous section, which showed that the different trip position has a negligible impact on the thrust generation. Overall, the prediction of the BPF 1 tone is quite satisfactory compared to the measurements for all the operation conditions considered. However, while for the microphone upstream the propeller (Mic. 11), the value of the tone at BPF 1 is predicted within 1 dB difference with respect to the measurements, its prediction worsen up to an under-prediction of 3-4 dB for in-plane observer positions. Such a directional increase of the BPF 1 tone mismatch, that was also observed when comparing the measurements against BEMT-compact dipole/monopole FW-H noise computations [49], cannot be solely attributed to the lower thrust prediction observed in Fig. 5.3, whose impact on the radiated tonal noise is expected to be about 1.5 dB according to BEMT-compact monopole/dipole FW-H computations [49]. It might be also related to the experimental imperfect balance of the blade loading that leads to the generation of harmonics of the shaft frequency, as well as the wind-tunnel acoustic confinement effect at low frequency (i.e. test room not fully anechoic below 200 Hz).

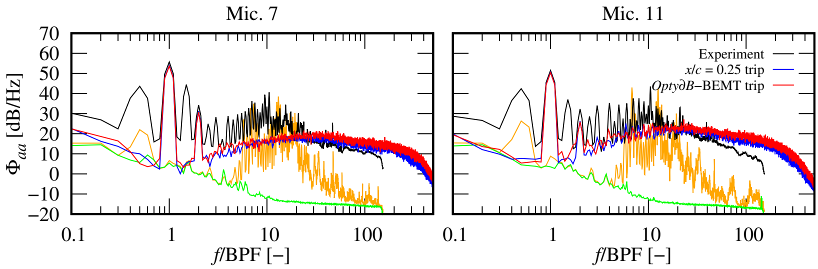

(a) $J = 0.0$

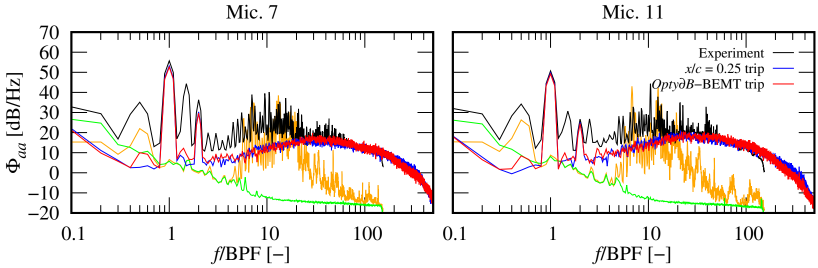

(b) $J = 0.24$

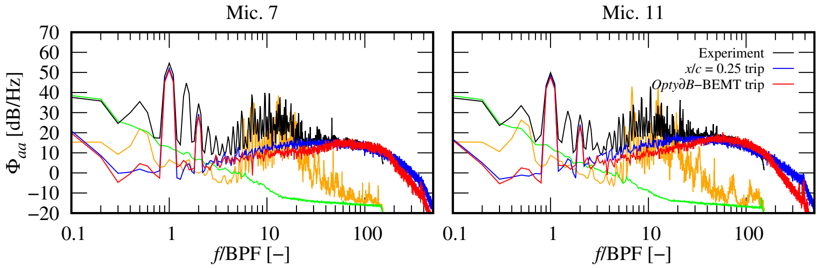

(c) $J = 0.4$

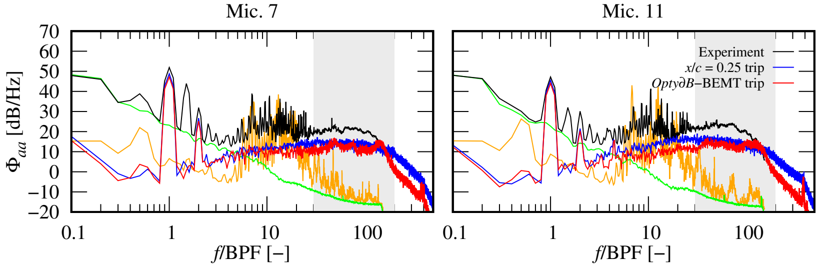

(d) $J = 0.6$

Figure 5.5: Far-field noise power spectral density Φ_{aa} for in-plane (Mic. 7) and out-of-plane (Mic. 11) observer positions. Comparison between measurements and numerical solutions obtained with $x/c = 0.25$ and *Opty∂B*-BEMT trips. Unloaded electric motor noise (–) and facility background noise (–) reported for reference.

As expected, the numerical results do not show the multitude of tones at the harmonics of the shaft frequency, not strictly related to the BPF, that characterize the experimental data. As previously mentioned, such tones are associated to some imperfections of the experimental setup and, in particular, to the loaded electric motor noise and the non-perfect balance of the blades (below BPF 5), and to the unloaded electric motor noise (approximately between BPF 5 to 25).

Contrarily to the tonal component of the noise, broadband noise is more influenced by the chordwise distribution of the trip line. Since the BEMT-predicted trip lines are distributed similarly to the $x/c = 0.25$ case at low advance ratios than at high ones, it is reasonable to expect that similar boundary-layer development and turbulent boundary-layer trailing-edge noise emissions take place at low J in the numerical simulations, and that opposite situation occurs at large advance ratios. This aspect begins to be noticeable at $J = 0.4$, although it is more clearly visible at $J = 0.6$. For intermediate advance ratios ($J = 0.24 - 0.4$), the agreement between measurements and numerical solutions is fairly good. On the other hand, in hover ($J = 0.0$) and at high advance ratio ($J = 0.6$), the numerical results show a certain over-prediction and under-estimation of the broadband noise levels, respectively.

For $J = 0.0$, the larger broadband noise might be attributed to excessively high turbulent pressure fluctuations generated in the boundary-layer, promoted by the presence of a transition trip in combination with high blade loading conditions. Under such conditions, the flow experiences a higher local acceleration on the blade suction side, which would in principle require a lower trip height to initiate transition compared to higher advance ratio cases and/or more downstream trip placements, according to considerations based on the critical roughness height-based Reynolds number [181]. Hence, it is reasonable to expect that the same zig-zag trip height can lead to the development of higher turbulent fluctuations in boundary-layer under higher blade loading, as it will be qualitatively illustrated in Sec. 5.3.3. A sensitivity study of the numerical results to the trip thickness for $J = 0.0$ will be presented in Sec. 5.3.6 to further discuss - in the limit of the employed near-wall resolution - the boundary-layer over-tripping and the broadband noise over-prediction in hover.

Regarding the under-prediction of broadband noise for $J = 0.6$, it can be attributed to the absence of the laminar separation bubble and the associated acoustic feedback mechanism in the numerical solution. Such phenomena, which were observed to be the cause for the high frequency noise increment and broadband hump in the experimental data [49], are not captured in the present numerical results. This is due to the usage of a transition trip to force the turbulence model to enter into scale-resolving mode and initiate transition. However, it is worth mentioning that even in absence of the tripping device, the laminar separation bubble would be unlikely captured in the numerical solution, due to the intrinsic difficulties of the employed numerical method in capturing shallow regions of boundary-layer separation and reattachment. This aspect motivates once more the choice of using a zig-zag trip for such low-Reynolds number cases for the sake of broadband noise prediction at engineering level.

This subsection concludes the validation of the proposed computational approach, which is aimed at providing an industrial solution for the prediction of performances and tonal/broadband noise of propellers operated at low-Reynolds numbers. The following subsections provide some insights on the numerical results to further support the discussion on the effect of using a transition trip to simulate low-Reynolds number propellers, as well as the impact of its chordwise position on performances and radiated noise.

5.3.3. MEAN AND TURBULENT VELOCITY FIELDS

Figures 5.6 and 5.7 respectively show the contours of the time-averaged velocity magnitude (V_r, expressed in the non-inertial reference frame rotating at the propeller angular velocity ω) and of the root-mean-square (V_{rms}) for the two numerical solutions obtained with trip at $x/c = 0.25$ and along the BEMT-predicted transition line for $J = 0.0-0.6$. The airfoil section considered is that at 70% of the blade span, which is expected to be representative of the overall aerodynamic behavior of the blade. The time-averaged velocity magnitude and the rms values are then normalized by the free-stream velocity experienced by the airfoil section in the body-fixed reference frame rigidly rotating with the blade, i.e. $V_{r_\infty} = \sqrt{V_\infty^2 + (\omega r)^2}$.

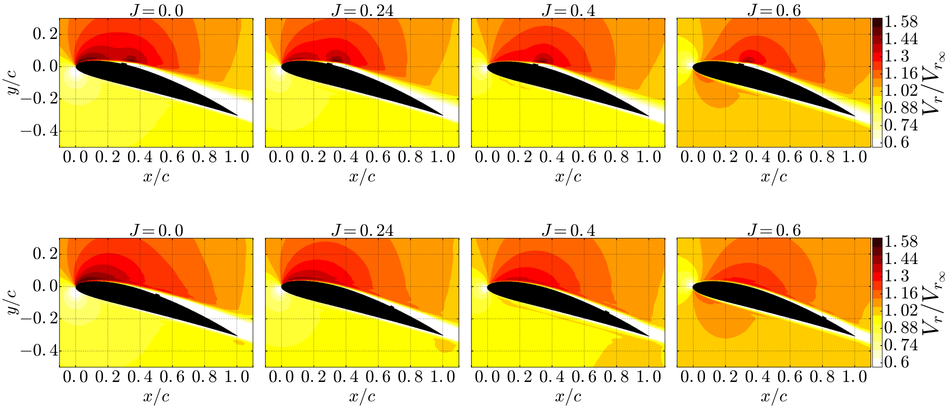

Figure 5.6: Time-averaged velocity magnitude contours for the blade section at $r/R = 0.7$. Comparison between $x/c = 0.25$ (top) and *Opty∂B*-BEMT (bottom) trip computational setups.

Interestingly, the time-averaged velocity magnitude fields (Fig. 5.6) show the more intrusive nature of the trip located at $x/c = 0.25$ compared to the trip distributed along the expected laminar-separation bubble reattachment line, which leads to a less pronounced flow acceleration around the blade leading-edge, a higher flow acceleration around the trip and the growth of a thicker boundary-layer downstream it. Although not reported for the sake of brevity, the inspection of the pressure coefficient distributions on the airfoil at $r/R = 0.7$ showed that the trip at 25% of the chord is responsible for a certain reduction of the suction effect at the leading-edge of the blade compared to the BEMT-predicted trip cases. However, this effect is found to be balanced out by a larger low-pressure area generated downstream the trip, which is consistent with the rather similar C_T predictions between the two different tripping strategies observed in Fig. 5.3.

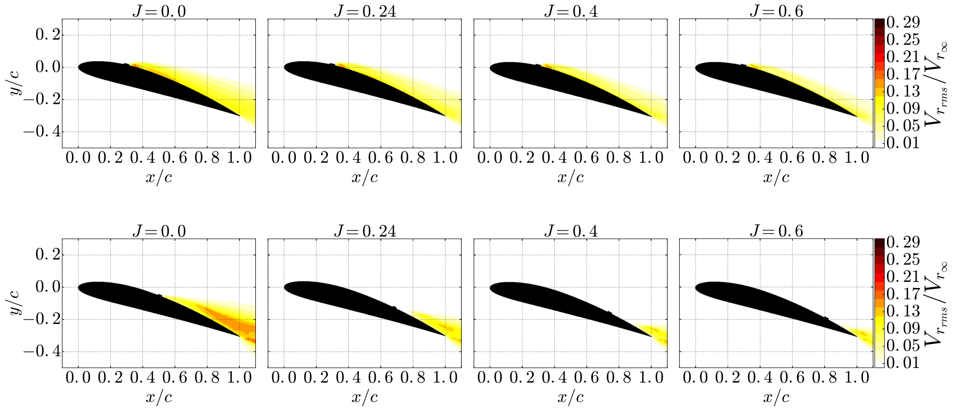

Figure 5.7: Root-mean-square velocity contours for the blade section at $r/R = 0.7$. Comparison between $x/c = 0.25$ (top) and *Opty∂B*-BEMT (bottom) trip computational setups.

For all the numerical solutions with trip located at 25% of the blade chord, a similar rms velocity pattern is found, although the level of the velocity fluctuations tends to decrease as the advance ratio increases. As J increases, the local blade angle of attack and flow acceleration on the suction side decrease (Fig. 5.6). As a result, the same trip line experiences a slower incoming flow for increasing J and lead to the generation of lower turbulence levels in the boundary-layer downstream it (Fig. 5.7). Interestingly, for increasing J, the decreasing rms velocity correlates with the slight reduction of the broadband noise shown in Fig. 5.5, which is associated to the scattering of the turbulent boundary-layer pressure fluctuations at the blade trailing-edge. Similarly to the cases with trip at 25% of the chord, higher advance ratio conditions correspond to a more intense velocity fluctuations in the boundary-layer also for the BEMT-predicted trip simulations. However, in such cases, the rms velocity levels decrease more rapidly as the advance ratio increases. Since the BEMT trip lines move towards the blade trailing-edge as J increases, the trip is subjected to a lower relative velocity and thicker incoming boundary-layer (as shown in Fig. 5.6). As a consequence, both the perturbation of the incoming flow and the generation of the fully turbulent boundary-layer by the trip are gradually mitigated for increasing J.

5.3.4. WALL-PRESSURE SPECTRUM AT THE TRAILING-EDGE

According to Amiet's trailing-edge noise theory [166], turbulent boundary-layer trailing-edge noise is proportional - among other quantities - to the level of wall-pressure fluctuations in proximity of the trailing-edge. Hence, the numerical wall-pressure power spectral densities Φ_{pp} on the suction side at 95% of the chord for different spanwise sections ranging between 50% and 95% of the blade radius are analyzed in this subsection (Fig. 5.8). It can be noted that when the blade is tripped at 25% of the chord, the boundary-layer reaches a fully-turbulent state in proximity of the trailing-edge for all the advance ratios considered, at least above $r/R = 0.5$. This can be inferred from the shape of the power spectra densities, which exhibit the typical power decay laws of a fully-developed turbulent boundary-layer, respectively proportional to $f^{-7/3}$ and f^{-5} in mid-high and very high frequency ranges [59]. In contrast, the simulations with trip line predicted by *Opty∂B*-BEMT show that a fully turbulent boundary-layer is generated only at low advance ratios ($J = 0.0 - 0.24$). For $J = 0.4$ and $J = 0.6$, only the last 30% of the blade span exhibits significant levels of wall-pressure fluctuations. These results are consistent with the rms velocity contours shown in Fig. 5.7 and with the broadband noise content in the far-field noise spectra shown in Fig. 5.5. In particular, it can be appreciated the correlation between the wall-pressure spectrum levels at the trailing-edge on the suction side and the broadband noise levels in the far-field noise computations, with the *Opty∂B*-BEMT trip case generally showing broadband noise levels higher ($J = 0.0$) or lower ($J \geq 0.4$) than those of the $x/c = 0.25$ trip case in correspondence of higher or lower resolved wall-pressure fluctuations generated at the trailing-edge, respectively. These results suggest, once more, the importance of using a transition trip in the present computational setup, without which not enough resolved turbulent pressure fluctuations in the boundary-layer would be generated in the numerical solution for the sake of trailing-edge noise prediction.

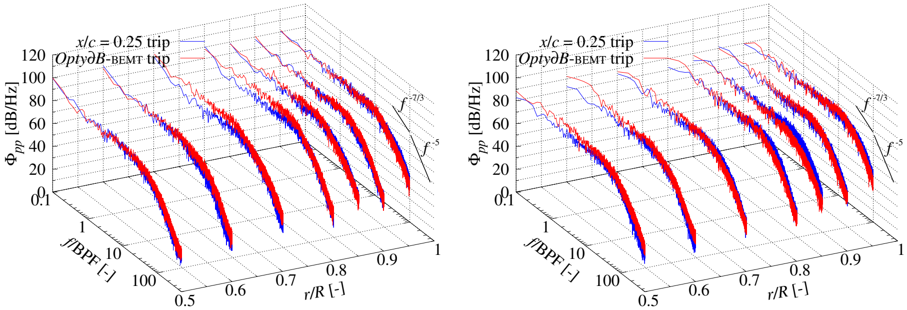

(a) $J = 0.0$ (b) $J = 0.24$

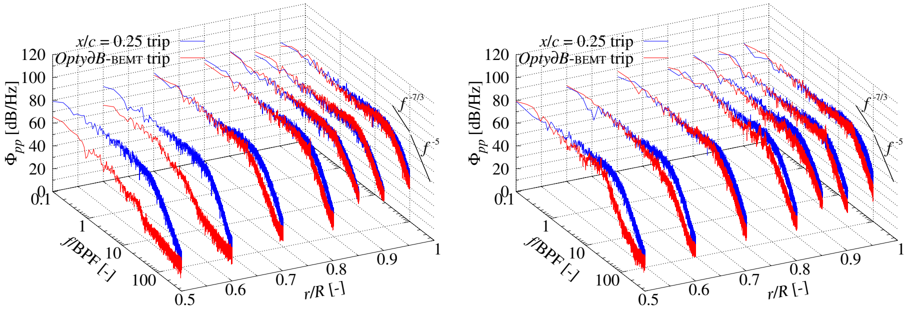

(c) $J = 0.4$ (d) $J = 0.6$

Figure 5.8: Wall-pressure power spectral density Φ_{pp} on the blade suction side at $x/c = 0.95$ for different spanwise sections. Comparison between $x/c = 0.25$ and *Opty∂B*-BEMT trip computational setups.

5.3.5. BEAMFORMING NOISE SOURCE LOCALIZATION

The comparison between Clean-SC [183] beamforming noise maps on the blade suction side for the two different computational setups is shown in Fig. 5.10, for $J = 0.0 - 0.6$. The digital beamforming analysis is performed to ensure that the dominant source of broadband noise in the numerical results is due to turbulent boundary-layer trailing-edge noise and that spurious broadband noise sources, such as those potentially introduced by the usage of the trip, do not sensibly affect the far-field noise spectrum. The noise maps are computed from FW-H acoustic signals evaluated from a single blade on a spiral array of 226 microphones of $60R$ radius, which is defined in a reference frame rigidly rotating with the propeller for broadband noise source localization. The array, shown in Fig. 5.9, is centered around the propeller hub and located at $4R$ distance from it in the upstream direction. The beamforming antenna resolution at the minimum (BPF 10 = 1666 Hz) and maximum (BPF 100 = 16666 Hz) frequencies of interest is approximately equal to 30% and 3% of the mean chord, respectively. The employed Clean-SC deconvolution algorithm is implemented in the beamforming code *Opty∂B*-BF developed by Dassault Systèmes.

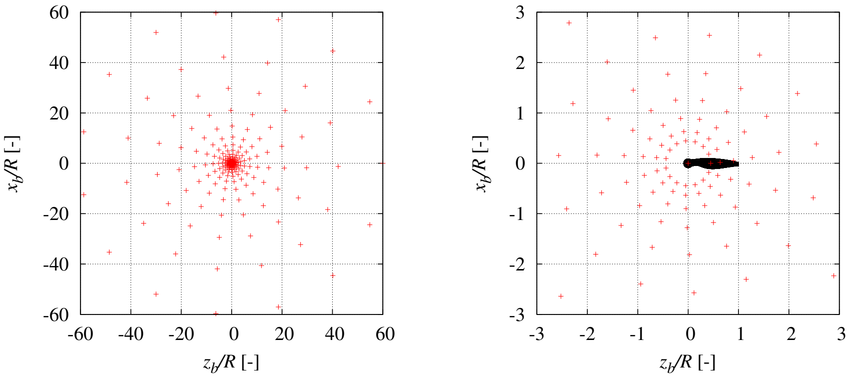

Figure 5.9: Microphone array used for the beamforming noise source localization: full array (left) and array close-up view (right).

For both setups, the main broadband noise contributor between BPF 10-100 is the blade trailing-edge, through the scattering of the pressure fluctuations within the turbulent boundary-layer developing on the blade suction side, with no relevant contribution to the far-field noise clearly ascribable to the zig-zag transition trip. Both cases show that the noisiest trailing-edge region is that in proximity of the blade tip, due to higher Mach number and efficiency of the scattering process. However, while for the propeller tripped at 25% of the chord the broadband noise sources at the trailing-edge are quite uniformly distributed along the span, these are more clustered in the outer part of the blade for the BEMT-trip cases, especially as J increases. Moreover, the $x/c = 0.25$ trip configurations exhibit rather similar acoustic source images across the different advance ratios considered, with only a minor variation of their intensity and locations as J increases.

The opposite situation occurs for the numerical results with trip line distribution computed by *Opty∂B*-BEMT. Overall, for all the cases examined, the beamforming noise maps magnitude variation for increasing J correlates quite well with the broadband noise reduction observed in the far-field noise spectra presented in Fig. 5.5. As a final remark, it is worth pointing out the presence of broadband noise sources between 80-90% of the radius on the leading-edge for the blade tripped at $x/c = 0.25$, in hover conditions. Such sources, which are not detected by the beamforming algorithm in the numerical simulations with BEMT-predicted trip, are related to the impingement of secondary turbulent structures braking down from the blade tip-vortex of the preceding blade. This breakdown phenomenon, which was observed to be more pronounced for the $x/c = 0.25$ case, is expected to be related to the occurrence of a different boundary-layer/tip-vortex interaction due to the different chordwise trip location at the tip of the blade.

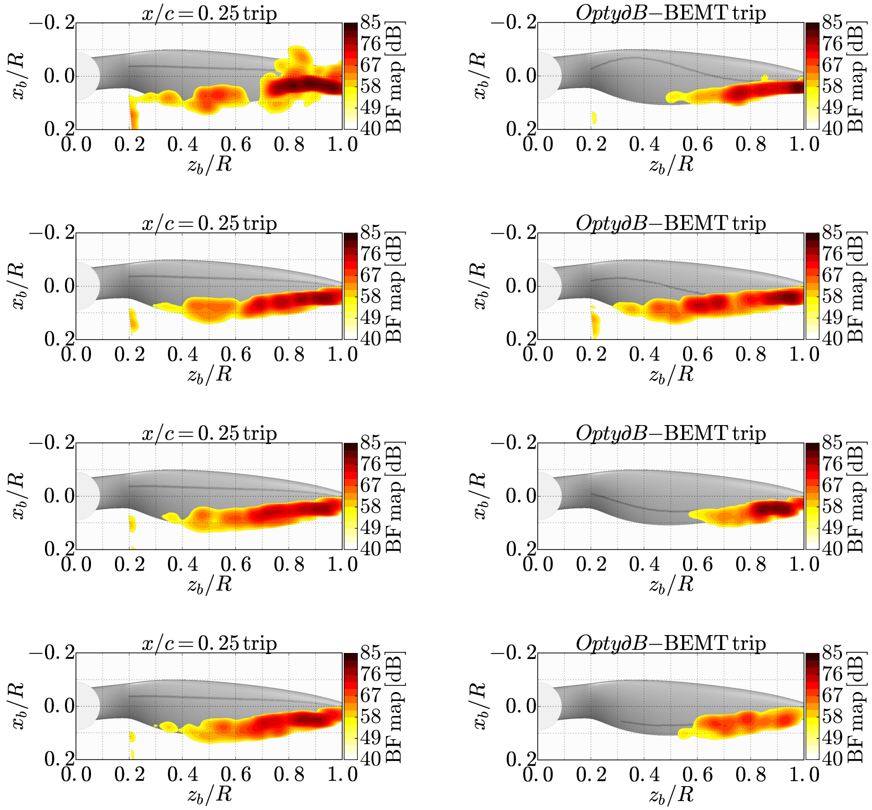

Figure 5.10: Clean-SC beamforming noise maps on the blade suction side between BPF 10-100 (1666-16666 Hz) for $J = 0.0$, $J = 0.24$, $J = 0.4$ and $J = 0.6$ from top to bottom. Values below 55 dB are not shown. Comparison between $x/c = 0.25$ and *Opty∂B*-BEMT trip computational setups.

5.3.6. LOADS AND NOISE SENSITIVITY TO TRIP THICKNESS IN HOVER

Figure 5.5(a) showed a certain broadband noise over-prediction for $J = 0.0$ for both the trip strategies adopted, from 5 dB for observers in the propeller plane up to 10 dB for out-of-plane positions. It was conjectured that this could be related to the excessively large boundary-layer fluctuations and boundary-layer thickness promoted by a trip of 0.17 mm thickness under high blade loading conditions, compared to those that would be experienced by the blade for a fully natural transitional case. Hence, a study on the sensitivity of the numerical results to the trip thickness is presented in this subsection for $J = 0.0$ and the computational setup with trip located at 25% of the chord, with the aim of shedding more light on the cause of the aforementioned discrepancies. As part of this analysis, also the sensitivity of thrust and torque to the trip height is investigated. Two additional zig-zag trips of thickness respectively equal to 0.11 mm and 0.06 mm (corresponding to a height of 2 voxels and 1 voxel, respectively), are considered in addition to the trip of 0.17 mm (3 voxels) that was considered in the previous subsections. It is worth recalling that the 0.06 mm trip thickness (corresponding to 1 finest voxel) represents the lowest trip height that can be achieved with the current computational grid.

Table 5.1 reports the variation of the thrust and torque coefficients with respect to the trip height. It can be observed that the reduction of the trip thickness leads to an improvement of the C_T prediction, from a under-estimation of −6% for the thicker trip, to an under-prediction of about −3% for the thinner one. Conversely, the torque coefficient shows a lower sensitivity to the trip height, with a minor over-prediction increment by 1%, most likely consequence of the increased induced drag due to the increased lift distribution generated along the span.

Case	C_T [-]	C_T rel. err.	C_Q [-]	C_Q rel. err.
Experiment	0.117	-	0.00756	-
$x/c = 0.25$ trip (3 vox.)	0.110	−6.2%	0.00839	+10.4%
$x/c = 0.25$ trip (2 vox.)	0.113	−3.5%	0.00839	+10.4%
$x/c = 0.25$ trip (1 vox.)	0.114	−2.6%	0.00851	+11.8%

Table 5.1: Thrust and torque coefficients sensitivity to the trip thickness for $J = 0.0$ and trip located at $x/c = 0.25$.

Figure 5.11 depicts the pressure coefficient, time-averaged velocity magnitude and root-mean-square contours for the blade section at 70% of the radial coordinate. As for the time-averaged velocity magnitude and root-mean-square, also the C_p is normalized considering the dynamic pressure based on the local free-stream velocity experienced by the airfoil. The pressure coefficient contours show that a larger low-pressure area is generated around the blade leading-edge on the suction side as the trip height is reduced. At the same time, the region downstream the trip is characterized by a slower recovery of the free-stream pressure for the smaller trip height. These aspects are consistent with the larger thrust generation observed in Tab. 5.1. The C_p contours also show the trivial consideration that a thinner trip exert a less intrusive action on the surrounding flow. This aspect is also clearly noticeable from the time-averaged velocity magnitude contours, which further illustrates that a progressively lower flow acceleration is established around the trip as the trip height is reduced. Furthermore, a reduced trip thickness leads to the generation of a higher flow acceleration around the blade leading-edge, which is consistent with the increment of the pressure suction effect described above. Concerning the root-mean-square of the velocity, the trip thickness is seen to play a major role on the turbulent development right downstream the trip (i.e. bypass transition process [184]) rather than on the ultimate levels of fluctuations that are achieved in proximity of the blade trailing-edge.

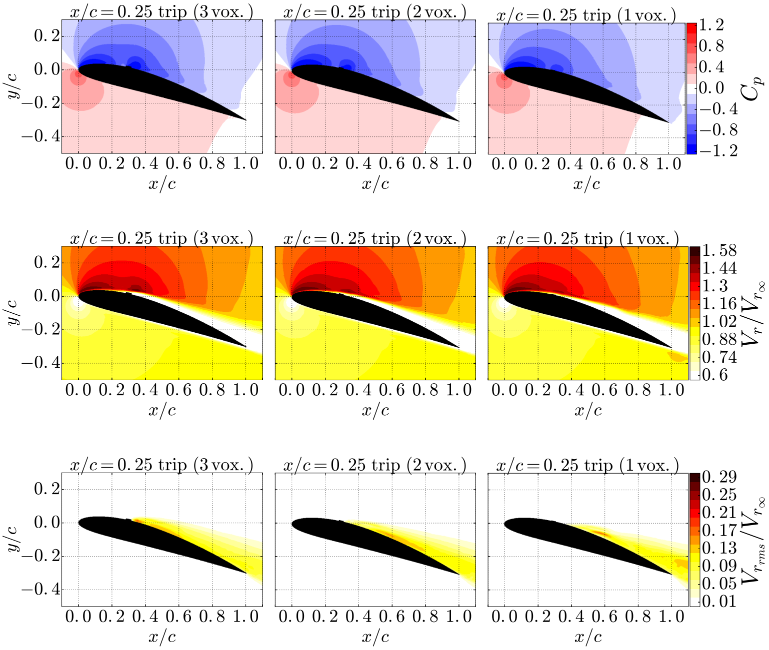

Figure 5.11: Pressure coefficient (top), time-averaged velocity magnitude (center) and root-mean-square velocity (bottom) contours for the blade section at $r/R = 0.7$. Comparison between three trip thicknesses for the computational setup with trip at $x/c = 0.25$.

Finally, Fig. 5.12 shows the far-field noise sound pressure level $L_{p(1/3)}$ plotted in 1/3-octave frequency bands to better discern high-frequency broadband noise variations for the three different trip heights considered. The two microphone positions are the same as in Sec. 5.3.2. Similarly to what has been previously observed regarding the trip chordwise position, it can be noted that also trip thickness has no influence on the tonal component of the noise, at least for the three trip heights analyzed in this study, for which no flow separation is induced by the trip itself. Moreover, also the broadband component of the noise shows a very minor sensitivity to the three trip thicknesses considered, for a zig-zag trip placed at 25% of the chord and under hover conditions. Although this aspect is to some extent surprising, it could have been expected based on the root-mean-square velocity contours shown in Fig. 5.11, which qualitatively showed comparable turbulence levels in proximity of the trailing-edge, thus suggesting similar turbulent boundary-layer trailing-edge noise radiations. Surprisingly, the smallest trip height generates slightly higher broadband noise emissions for frequencies above BPF 100 compared to the two other trip thicknesses. This might be the consequence of smaller scales of turbulence being triggered by a smaller trip within the transition process taking place downstream it.

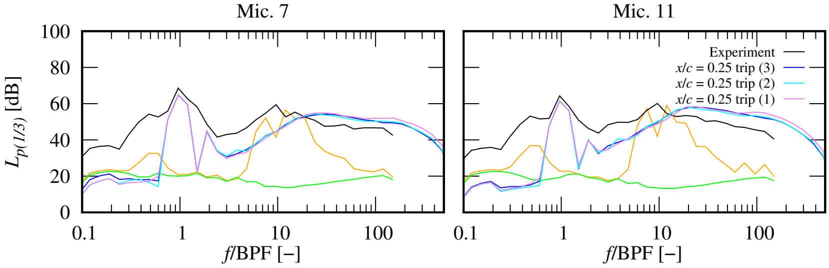

Figure 5.12: Sound pressure level in 1/3-octave band $L_{p(1/3)}$ for in-plane (Mic. 7) and out-of-plane (Mic. 11) observer positions. Comparison between measurements and numerical solutions obtained with $x/c = 0.25$ and three different trip thicknesses. Unloaded electric motor noise (–) and wind tunnel background noise (–) reported for reference.

Figure 5.12 shows that for the two additional trip heights of 0.11 mm and 0.05 mm broadband noise is also over-estimated from 5 to 10 dB for $J = 0.0$. For three-dimensional tripping devices, Van Rooij and Timmer [185] proposed a critical roughness height-based Reynolds number $Re_k = 200$ (where $Re_k = uk/\nu$, with u being the local flow velocity and ν the kinematic viscosity) to define a minimum trip thickness k to trigger transition. Based on this criterion, and considering a local velocity of the flow approaching the trip $u \approx 1.4V_{r_\infty}$ (see Fig. 5.11) a critical trip thickness of approximately 0.04 mm can be determined for $r/R = 0.70$ for initiating transition in hover. With this regard, all the three trip thickness considered would lead to an over-tripped boundary-layer above 70% of the blade span, which might explain the origin of the broadband noise over-prediction for $J = 0.0$. Nevertheless, the low sensitivity of loads and broadband noise radiation to the trip thickness, in addition to that to the trip chordwise position discussed above, plays in favor of the robustness of the proposed approach for industrial applications.

5.4. CONCLUSIONS

This chapter presented a computational approach based on the LB/VLES method to predict the performances and noise signature associated to a two-bladed propeller operated at low Reynolds numbers. The numerical flow solution was obtained by solving the explicit, transient and compressible lattice-Boltzmann equation implemented in the CFD/CAA solver SIMULIA PowerFLOW®. The aerodynamic noise generated by the propeller was computed by using an acoustic analogy based on Farassat's formulation 1A of the FW-H equation applied to the propeller/nacelle surfaces. A transition trip was included in the computational setup to force the numerical scheme to switch from modeled to scale-resolving turbulence, and to trigger the formation of vortical structures with scales able to emulate the complexity of the low-Reynolds number boundary-layer on the blade. Two different tripping strategies were attempted by positioning the trip along the quarter-chord and the expected turbulent boundary-layer transition lines, respectively.

Numerical results were compared against loads and noise measurements carried out in the A-Tunnel of TU-Delft. Overall, thrust and torque predictions were found to be in a satisfactory agreement with respect to the experimental results, although some discrepancies were observed for the former at low and middle advance ratios, and at intermediate ones for the latter. The trip position marginally affected the thrust, and to a slightly greater extent the torque predictions. Both tonal and broadband prediction compared favorably against the experimental data, especially for intermediate advance ratios. A certain over-prediction of the broadband noise levels were found for the hover case, due to excessively high levels of turbulence generated by the trip under high blade loading conditions. Contrarily, at $J = 0.6$ the numerical results did not show the measured high-frequency broadband hump associated to the laminar bubble separation noise, with both the computational setups predicting lower broadband noise. Tonal noise did not show a significant sensitivity to the trip chordwise position, whereas broadband noise levels were found to be affected to a slightly larger extent by the chordwise position of the trip.

A further investigation of the rms velocity fields and wall-pressure spectra at the trailing-edge on the blade suction side revealed that the formation of a fully-turbulent boundary-layer is achieved for most of the blade span for the blade tripped at 25% of the chord. Contrarily, the simulations with trip derived from BEMT calculations exhibited a lower spanwise extension of high turbulent activity regions as the advance ratio increases. These results were confirmed by Clean-SC beamforming noise maps calculations, which showed that broadband noise sources generated at the trailing-edge are more uniformly distributed along the span for the propeller tripped at 25% of the chord, in contrast to the BEMT-trip cases, especially for increasing advance ratios. The beamforming results further showed that the trip did not contribute in a tangible way to the broadband noise levels.

The satisfactory agreement of thrust, torque and tonal/broadband noise numerical results with respect to the experimental measurements validated the proposed approach for the prediction of performances and noise radiation associated to low-Reynolds number propellers at engineering level. Moreover, the robustness of the proposed method for industrial studies was corroborated by the low sensitivity of the trip chordwise location and height.

6

PROPELLER NOISE II: ANGULAR INFLOW EFFECTS

> *It would be possible to describe everything scientifically,*
> *but it would make no sense;*
> *it would be without meaning,*
> *as if you described a Beethoven symphony*
> *as a variation of wave pressure.*
>
> Albert Einstein

Chapter 5 presented a computational approach based on the use of a zig-zag transition trip to predict the performance and tonal/broadband noise radiation of a two-bladed propeller operating at low Reynolds numbers and axial inflow conditions. In the present chapter, the same approach is used to address the impact of a non-axial inflow on the aeroacoustics of propellers operating at low blade-tip speed conditions. It is found that the presence of an angular inflow is responsible for: (i) a radiation of tonal loading noise along the propeller axis; (ii) an increment (reduction) of the sound pressure level in the region from (to) which the propeller is tilted away (towards). However, contrarily to propellers operating at high blade-tip Mach numbers, the noise directivity change is found to be governed only by the rise of periodic unsteady loadings, with the modulation of the strength of the noise sources on the blade, associated to the periodic variation of the observer-source relative Mach number (in the blade reference frame), being negligible. Moreover, thickness noise and turbulent boundary-layer trailing-edge noise are not significantly altered when the propeller is yawed with respect to the free-stream.

Parts of this chapter have been published in the AESCTE journal (2021) [186].

6.1. INTRODUCTION

THE use of small-to-medium size fully-electric flying vehicles in large metropolitan areas, from drones and Unmanned Aerial Vehicles (UAVs) for goods delivery to Personal Aerial Vehicles (PAVs) for people mobility, is envisaged in the near future as a solution to roads congestion [10, 67]. A number of different electrically propelled Vertical Take-Off and Landing (eVTOL) vehicles have been recently prototyped by several companies and research centers [14, 16, 187–189]. Most of them feature a common key characteristic, namely distributed electric propulsion systems consisting of low-speed thrust vectoring rotors/propellers, with radius below 0.5 m and blade-tip Mach number $\approx 0.2 - 0.5$. However, several aspects need to be addressed in order to make possible the implementation of this new technology in the upcoming years. In particular, those related to noise pollution play a primary role upon the public acceptance of Urban Air Mobility/Advanced Air Mobility (UAM/AAM), as this emerging class of flying vehicles aims at operating in close proximity of densely populated areas, where noise annoyance towards the community needs to be contained [190]. Since such vehicles are supposed to fly at relatively low forward flight velocities for which airframe self-noise is not a primarily concern [26], rotors/propellers self and installation noise are expected to be the most dominant sources of acoustic nuisance [26].

It is well known that propellers generate both broadband and tonal (harmonic) acoustic signatures [26]. The interaction of the blades with the turbulence in the incoming flow, the potential separation of the flow on the blade and the scattering of the turbulent flow at the trailing-edge of the blade are typically recognized as the most relevant mechanisms of broadband noise [36, 37] (see Sec. 2.1.1). Concerning the tonal component, steady and unsteady blade aerodynamic loadings (in the blade-fixed reference frame) represent the main sources of noise at the relatively low blade-tip Mach numbers [35] (see Secs. 2.1.3 and 2.1.6). The steady loading noise is associated to the steady (in the blade-fixed reference frame) blade pressure distribution, which results in a force that periodically varies direction and generates sound for an observer in an inertial reference frame as the blade rotates [35]. For propellers operating at low blade-tip Mach numbers, this may be a relatively weak source of noise in the presence of unsteady loading noise. The latter takes place when the propeller operates in a non-uniform inflow or is set at a yaw angle, which results in a periodic and/or impulsive change of the local blade angle of attack. Examples of unsteady loading noise are the blade-vortex interaction noise or the noise generated by a propeller when it operates with the axis misaligned with respect to the free-stream direction [35]. The focus of the present study is on this last noise generation mechanism for propeller operating at low blade-tip Mach numbers.

During the takeoff, landing and conversion stages of the profile mission, when eVTOLs/drones generally fly in closer proximity to the ground, a propeller can operate with its shaft at a non-zero yaw angle. Under such conditions, the acoustic field radiated by the propeller may significantly differ from that of the same propeller at zero yaw angle, with a general noise increase (reduction) in the region with respect to which the propeller is tilted away (towards), resulting in a non-axisymmetric directivity pattern [191–194]. Previous computational studies on high-speed propellers attributed this asymmetry of the noise field to a periodic variation of the blade incidence, which gives rise to unsteady loading components and alters the rate of momentum injection at the blade surface, and to an in-plane convective effect, for which the efficiency of a generic acoustic source on the blade periodically varies along the azimuth [195]. The most relevant research (to the author's knowledge) on the modeling, prediction and characterization of the aeroacoustics of propeller at incidence is outlined in the following.

A method for rotating steady line sources (acoustically compact), accurate to the first order in the in-plane Mach number, was formulated by Mani [194]. He included, in a frequency domain far-field method, the effect of the propeller yaw angle on the radiation of both the steady loading and thickness noise, in addition to that of the unsteady loading. He was the first to point out that, for highly-loaded high-speed propellers with large number of blades, the change in the azimuthal asymmetry of the noise was more affected by a non-axisymmetric modulation of the steady loading/thickness noise due to the in-plane velocity component than by the once-per-rev unsteady loading variation.

An extension of Mani's work to high yaw angles was carried out by Krejsa [196]. He demonstrated that modeling additional yaw angle effects, such as the source motion along the free-stream velocity vector direction and the blade loading direction variation, in addition to the blade loading magnitude variation, significantly improved the comparison with the experimental data. In addition, he showed that the inclusion of higher order effects of the yaw angle (i.e. higher modes in the frequency domain far-field method as a way to remove the small yaw angle limitation of Mani's approach) changed the predicted noise at far forward and aft angles, while it had a small impact near the propeller plane.

Envia [197] proposed a frequency domain formulation based on a moving-medium variant of the Ffowcs Williams & Hawkings' equation to predict the noise from a propfan operating at incidence. His approach involved the use of the Airy's function and its derivatives, as alternative to numerical integration, and incorporated both in-plane convective effects and loading unsteadiness with no limitations on the source chordwise compactness, showing a rather favorable agreement with the experimental data.

Hanson [198] developed far-field noise formulas by applying the free-space Green's function for the convected wave equation to loading noise point sources for a propeller tilted at any angle to the flight direction. He showed that the inflow angle influences the noise through the rise of efficient radiation modes associated to the unsteady loading, and introduced the concept of *wobbling modes*, according to which the radiation efficiency of the modes changes during the rotation due to the variation of the Mach number of the sources relative to the observer.

The noise generated by a propeller in an angular inflow was numerically computed by Frota *et al.* [199] by using a time-domain Ffowcs Williams & Hawkings' acoustic analogy applied to unsteady blade pressure measurements, who confirmed once again the role of both the unsteady loadings and kinematic/acoustic sources strength amplification on the variation of the noise radiated by a high-speed propeller at incidence.

More recently, Roger and Moreau [60] proposed an analytical model for loading noise based on the free-space Green's function and an expansion of the fluctuating forces on the blades as circular distributions of acoustic dipoles, and computed airframe installation and propeller disk angle of attack effects on the tonal noise of a quadrotor. By considerations based on the Bessel's functions, they stressed that, for low blade-tip Mach numbers and low number of blades, unsteady-loading noise can potentially exceed that associated to the steady lift, due to the considerably higher efficiency of the 1/rev blade loading harmonics compared to that of the steady loading, even at relatively low levels of angular inflow.

Although a number of computational and experimental aeroacoustic studies have been conducted by several authors in the past on angular inflow installation effects, most of those were focused on high-speed propellers. On the one hand, experimental campaigns did not provide a thorough understanding of the change of the noise mechanisms when a propeller is operated at incidence with respect to the free-stream. On the other hand, previous computational aeroacoustic studies (mostly based on analytical models or acoustic analogies) focused only on the investigation of deterministic phenomena (i.e. periodic unsteady loadings and in-plane convective effects), and did not include in the analysis the potential change of stochastic noise generation mechanisms such as turbulent boundary-layer trailing-edge noise. Moreover, for propellers operated at low blade-tip Mach numbers, the kinematic/acoustic source strength modulation might not play a role as relevant as for high-speed propellers, due to the relatively low in-plane velocity periodic variation typically experienced by their blades compared to propellers operated at higher blade-tip Mach numbers. Hence, previous research can only be considered as a first step towards a better understanding of the noise radiation mechanisms of low-speed propellers at non-zero yaw angles, which is essential to drive the design of quieter UAM/AAM vehicles and satisfy noise certification regulations and environmental concerns [190].

In view of the above, the present work aims at numerically investigating the impact of non-axial inflow conditions on the tonal and broadband noise radiated by a low blade-tip Mach number propeller, as well as at providing differences of the underlying physics with respect to high-speed propellers. The Lattice-Boltzmann/Very-Large Eddy Simulation (LB/VLES) method is employed to simulate flow around a two-bladed drone propeller. The aerodynamic noise generated by the propeller is then estimated by using an acoustic analogy based on Farassat's formulation 1A of the Ffowcs Williams & Hawkings' (FW-H) equation applied to the propeller surface. The numerical findings are supported by the validation of the numerical setup against loads and noise measurements carried out at Delft University of Technology (TU-Delft).

The rest of the chapter is organized as follows. In Sec. 6.2, the propeller geometry and computational setup used in this study are described. The validation of the computational setup is briefly outlined in Sec. 6.3, while the discussion on angular inflow effects on the aerodynamics and aeroacoustics of low blade-tip speed propellers is reported in Sec. 6.4. The main findings and conclusions of this work are summarized in Sec. 6.5.

6.2. TEST-CASE AND COMPUTATIONAL SETUP

The same propeller geometry presented in Chapter 5 is considered in this study. It is a two-bladed propeller designed at TU-Delft and derived from an APC 9x6 propeller (Fig. 6.1(a)) and characterized by a radius R of 0.15 m and NACA 4412 airfoil sections, which are merged with the propeller hub by elliptical sections (for $r < 0.01$ m). The airfoil chord and twist spanwise distributions are shown Fig. 6.1(b). The propeller hub radius is 1.25 cm and connected to a nacelle of 5 cm diameter and 52 cm length. Figure 6.1(a) shows the free-stream (x_f, y_f, z_f) and the ground-fixed (x_g, y_g, z_g) reference frames. The propeller axis coincides with the x-axis of the ground-fixed reference frame (x_g), while the azimuthal position of the blade ψ is referred to its z-axis (z_g). The free-stream reference frame is rotated by the propeller yaw angle α around the y-axis (y_g) of the ground-fixed one. The free-stream velocity V_∞ is directed along the x-axis of the former in such a way that the free-stream velocity vector is decomposed into axial V_{x_∞} and in-plane V_{z_∞} velocity components in the ground-fixed coordinate system, respectively. The propeller is operated at fixed angular velocity ($n = 83.33$ rps, i.e. $\omega = 523.6$ rad/s) and free-stream velocity of 10 m/s, resulting in an advance ratio $J = 0.4$ (where $J = V_\infty/(nD)$, with n denoting the revolution per seconds and D the propeller diameter). The resulting tip Mach number is 0.23 and the Reynolds number based on the chord at 75% of the radius is about $9 \cdot 10^4$. Two different values of the propeller yaw angle are considered to investigate the effects of an angular inflow, namely $\alpha = 0°$ and 15°. The free-stream static pressure and temperature considered are $p_\infty = 99000$ Pa and $T_\infty = 293.15$ K, respectively.

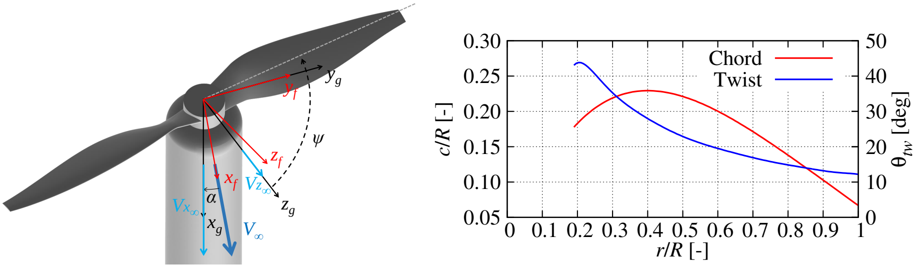

(a) *Propeller and coordinate systems*

(b) *Airfoil chord and twist distributions*

Figure 6.1: Propeller geometry, coordinate systems, airfoil chord and twist spanwise distributions.

Figure 6.2(a) illustrates the computational setup used in this study. The computational fluid domain is a spherical volume of 325D radius centered around the propeller. Free-stream static pressure and velocity, and turbulence intensity of 0.1% of the free-stream velocity are prescribed on its outer boundary. The experimental wind tunnel geometry is not modeled in the computational setup. An acoustic sponge is used to dissipate the out-going acoustic waves and minimize the backward reflection from the outer boundary and reproduce a digital anechoic environment. The acoustic sponge is defined by two concentric spheres of radius 15D and 55D, respectively, centered around the propeller. The fluid kinematic viscosity is gradually increased starting from its physical value within the inner sphere, up to an artificial value two orders of magnitude higher outside the outer one. A zig-zag transition trip is employed on the suction side of the blade to drive the LBM/VLES scheme switching from turbulence modeling to a scale-resolving behavior, thus allowing the formation of resolved turbulent structures within the boundary-layer for the sake of turbulent boundary-layer trailing-edge noise broadband calculation. The zig-zag trip is characterized by a thickness of 0.17 mm, amplitude and wavelength of 0.9 mm, and is placed at 25% of the chord on the suction side of the blade for $r/R > 0.2$ (Fig. 6.2(b)). No trip is placed on the blade pressure side, since no laminar-to-turbulent boundary layer transition is expected to occur based on BEMT/2D viscous panel method computations. This approach has been presented and successfully validated for axial flow conditions in Chapter 5 and in previous studies [49, 169].

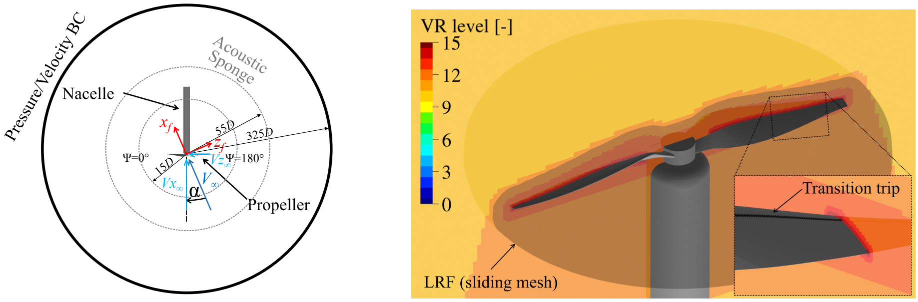

(a) *Computational setup* (b) *Near body mesh*

Figure 6.2: Sketch of (a) computational setup (not drawn to scale) and (b) near body mesh.

Figure 6.2(b) shows the details of the computational setup and mesh in proximity of the propeller geometry. The propeller and hub are encompassed by a volume of revolution that defines the Local Reference Frame (LRF), namely the rotating sliding mesh domain used to reproduce the propeller rotation. The solid FW-H integration surface used to compute the far-field noise radiation coincides with the propeller, hub and nacelle surfaces. A total of 16 Variable Resolution (VR) regions are used to discretize the whole fluid domain, with the finest resolution level (VR15) placed around the blade trip and trailing-edge. A resolution of 200 voxels along the mean chord (22.85 mm) is used in the second finest resolution level (VR14), resulting in a smallest voxel size of 0.06 mm, a mean $y+ \approx 5$ on the blade surface and an overall mesh size of 107 million voxels. Simulations are performed using the low-subsonic LBM/VLES solver implemented in SIMULIA PowerFLOW® 6-2019-R4 (see Sec. 3.2). The computational cost is 840 CPUh/rev on a 430 cores cluster with Intel Xeon CPU E5-2697 2.6 GHz. The whole fluid domain is initialized with the instantaneous flow solution from a statistically converged coarser simulation. Hence, after a settling time corresponding to 2 propeller revolutions, the sampling of relevant flow data is started for 10 additional revolutions. Acoustic data is sampled at 365 kHz with spatial averaging of 0.5 mm on the solid FW-H integration surface. Fourier transformed data is obtained with 2 Welch blocks, 50% overlap and Hanning windowing, corresponding to a bandwidth of 16.6 Hz (BPF[1] = 0.1).

6.3. NUMERICAL SETUP VALIDATION

The validation of the numerical setup under axial inflow conditions has been carried out in Chapter 5. In this section, the numerical results are compared against forces and noise measurements carried out in the A-Tunnel of TU-Delft to validate the employed computational setup for angular inflow cases. No transition trip was employed in the

---

[1] Blade-Passing Frequency

experimental data reported. A more detailed discussion on the yaw effects on propeller loads and noise will follow in Sec. 6.4.

6.3.1. MEAN THRUST, TORQUE AND PROPULSIVE EFFICIENCY COEFFICIENTS

The comparison between the experimental and numerical time-averaged thrust (C_T) and torque (C_Q) coefficients, and propulsive efficiency (η) at the two different propeller yaw angles ($\alpha = 0°$ and $15°$) is shown in Fig. 6.3. C_T, C_Q and η are computed as follows, respectively:

$$C_T = \frac{T}{\rho n^2 D^4}, \quad C_Q = \frac{Q}{\rho n^2 D^5} \quad \text{and} \quad \eta = \frac{J C_T}{2\pi C_Q}, \tag{6.1}$$

where T and Q are the mean propeller thrust and torque, n is the number of revolutions per second and D is the propeller diameter. From Fig. 6.3, a certain under-prediction of thrust and torque coefficients can be observed for both axial ($\alpha = 0°$) and angular ($\alpha = 15°$) inflow conditions. As pointed out in Chapter 5, for the same propeller operating at zero incidence with respect to the free-stream, the presence of the trip (which is used to generate resolved turbulent pressure fluctuations in the boundary-layer for trailing-edge noise generation) can be the cause for such discrepancies. Conversely, the propulsive efficiency results to be predicted in a more satisfactory way, as the aforementioned under-prediction of C_T and C_Q tend to cancel out in the computation of η. Interestingly, the increase of thrust, torque and efficiency coefficients with the increase of the propeller yaw angle is also captured by the numerical simulations, although to a lower extent with respect to the experimental data variation.

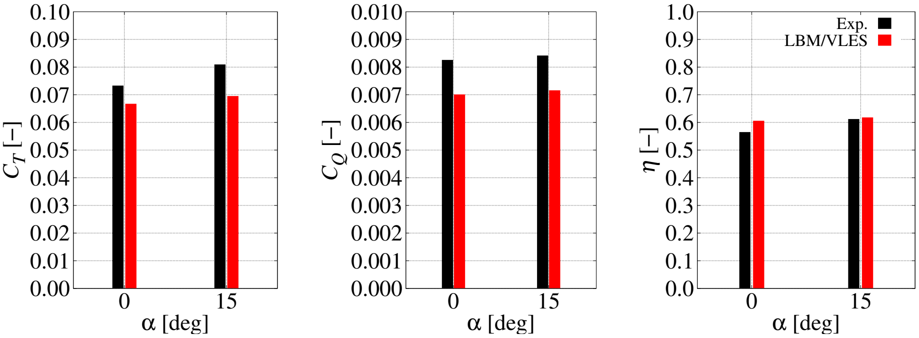

Figure 6.3: Thrust (left), torque (center) and propulsive efficiency (right) coefficients variation with the propeller yaw angle α.

6.3.2. FAR-FIELD NOISE SPECTRA

After the assessment of the thrust and torque predictions, the capability of the numerical setup to capture the effect of the propeller yaw angle on both its tonal and broadband acoustic signatures is hereinafter analyzed. Two different microphones in the free-stream coordinate system are considered: Mic. 7 (0.0 m, 1.2 m, 0.0 m) and Mic. 11 (-0.75 m, 1.2 m , 0.0 m), respectively located in and out of the propeller plane (for $\alpha = 0°$), as depicted in Fig. 6.4. The corresponding far-field noise spectra are reported in Figs. 6.5

and 6.6, respectively. Results are reported in 1/12-octave band sound pressure spectrum $L_{p(1/12)}$ versus the frequency f normalized by the Blade-Passing Frequency (BPF = $n_f B$ = 167 Hz, with n_f the shaft frequency in Hz and B the number of blades). In each figure, two different microphones array positions are considered, namely array 1 and array 2, away from and towards which the propeller is respectively tilted for a non-zero α. For each microphone, the unloaded (i.e. without the propeller) electric motor noise (orange curve) and the background noise (green curve) of the wind tunnel are reported to further support the discussion. Note that the background noise always refers to the $\alpha = 0°$ condition and that the same numerical and experimental spectra are shown on arrays 1 and 2 for the axial flow conditions, due to the axial symmetry of noise radiation. Moreover, it is worth mentioning that the main sources of experimental uncertainty are represented by: (i) the background noise below wind tunnel cut-off frequency (~200 Hz), which is responsible for the large broadband noise levels at low frequency; (ii) the loaded electric motor noise and the non-perfect balance of the blades that cause the rise of harmonics of the shaft frequency (BPF 0.5, 1, 1.5, etc.); and (iii) the unloaded electric motor noise, which generally adds mid-frequency tonal contributions (approximately between BPF 5 to 25) to the far-field noise spectrum [49, 179].

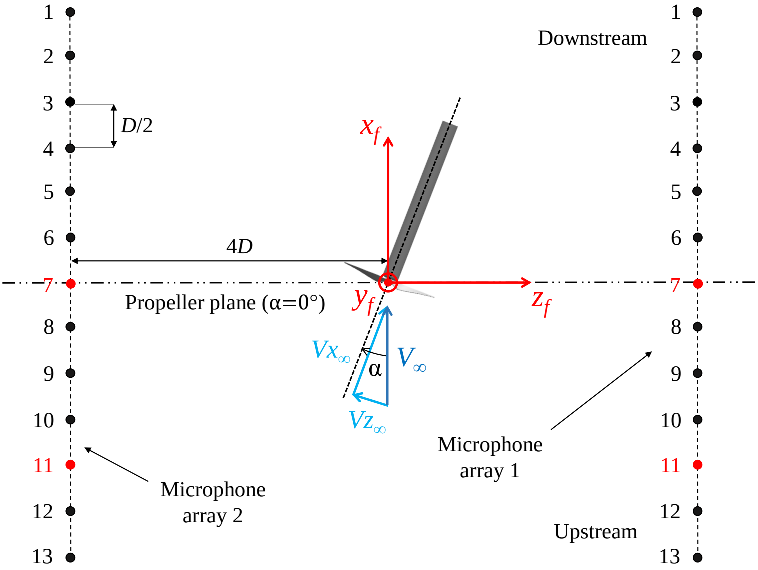

Figure 6.4: Sketch of the microphone array used of far-field noise computation (drawn not to scale).

The prediction of tonal and broadband noise is quite satisfactory for both axial ($\alpha = 0°$) and angular ($\alpha = 15°$) inflow conditions. For what concerns harmonic noise, the tone at BPF 1 is quite well predicted within 2-3 dB of under-prediction depending on the observer position considered. Such a moderate mismatch of the BPF 1 tone, might be attributed to the lower thrust and torque predictions observed in the numerical prediction (Fig. 6.3), whose impact is estimated to be around 1.5 dB based on BEMT/FW-H compact monopole/dipole computations, as well as to the experimental imperfect balance of the blade loading (that leads to the generation of harmonics of the shaft frequency) and the wind-tunnel acoustic confinement effect at low frequency (i.e. test chamber not completely anechoic below 200 Hz). Nevertheless, the expected increment of tonal noise at BPF 1 in that region from which the propeller is tilted away (array 1), as well as the reduction of noise in the opposite region (array 2), are well captured by the numerical setup. A similar behavior is also observed for the tone at BPF 2 in the numerical results, with a noise increment on array 1 and a reduction on array 2. However, this trend is not uniquely found in the experimental data. Possible reasons for such an unexpected behavior might be related to the presence of spurious tonal noise components at low frequency harmonics of the shaft rotation (BPF 0.5, 1, 1.5, etc.), which could be relevant when compared to the weak BPF 2 tone to such an extent to considerably affect its variation with the propeller yaw angle change.

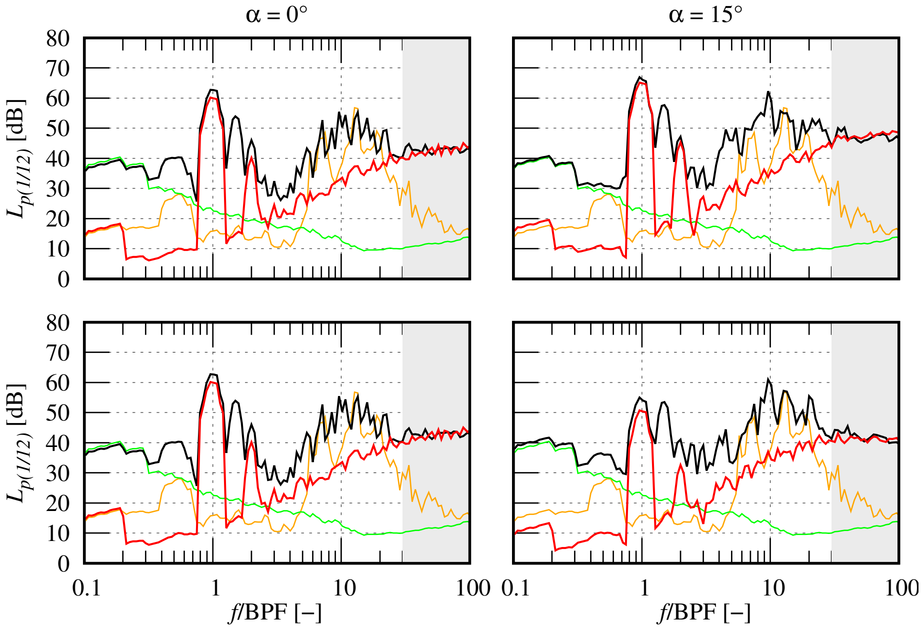

Figure 6.5: Far-field noise sound pressure level in 1/12-octave band $L_{p(1/12)}$ variation with the propeller yaw angle α for Mic. 7; array 1 (top) and array 2 (bottom). Experiment (—), LBM/VLES (—), electric motor noise (—) and wind tunnel background noise (—).

Regarding the broadband noise, levels are very well predicted for frequencies lying between BPF 30 and 100 (highlighted by the grey rectangle). For intermediate frequencies (BPF 5 to 25), the experimental electric motor noise contaminates the broadband noise due to turbulent boundary-layer trailing-edge noise, and no direct assessment of the numerical results against the experimental data can be drawn. Interestingly, the em-

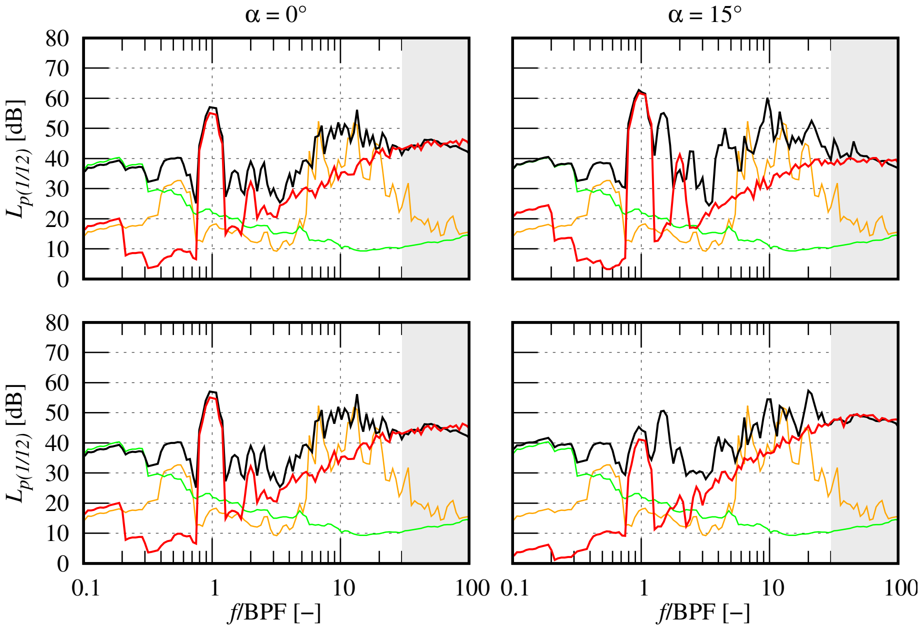

Figure 6.6: Far-field noise sound pressure level in 1/12-octave band $L_{p(1/12)}$ variation with the propeller yaw angle α for Mic. 11; array 1 (top) and array 2 (bottom). Experiment (—), LBM/VLES (—), electric motor noise (—) and wind tunnel background noise (—).

ployed computational approach - which is based on the use of a zig-zag transition trip to promote the generation of resolved pressure fluctuations within the boundary-layer that are scattered as sound at the blade trailing-edge - is able to capture the moderate changes of the broadband noise levels at high frequency due to the change of the propeller yaw angle. Such variations are less pronounced compared to those occurring to the tones at the first two BPFs, and do not follow the same trends manifested by the tonal components. More specifically, Mic. 7 on the array 1 shows some high-frequency broadband noise increment for $\alpha = 15°$ (Fig. 6.5) and almost no variation on the array 2, compared to the axial flow case ($\alpha = 0°$). Conversely, for Mic. 11 (Fig. 6.6), a slightly reduction and increment of the broadband noise component can be respectively noted on the arrays 1 and 2, when the propeller is operated at incidence.

6.4. ANALYSIS OF ANGULAR INFLOW EFFECTS

6.4.1. VELOCITY AND ANGLE OF ATTACK DISTRIBUTIONS

In order to correlate the effect of the propeller yaw angle on the blade aerodynamic loading variations, the flow experienced by a propeller blade during a revolution is investigated first. Figure 6.8 shows the axial (V_a) and tangential (V_t) velocity components and angle of attack (α_s) for $\alpha = 0°$, as well as their variations ($\Delta V_a = V_{a,15°} - V_{a,0°}$,

$\Delta V_t = V_{t,15°} - V_{t,0°}$ and $\Delta\alpha_s = \alpha_{s,15°} - \alpha_{s,0°}$) under angular inflow conditions ($\alpha = 15°$), experienced by the different blade sections along a propeller revolution. The azimuthal coordinate ψ indicates the blade position on the propeller disk (see Fig. 6.1(a)), while the radial coordinate represent the spanwise section location normalized by the propeller radius, r/R. The circular and straight arrows indicate the direction of the rotational velocity and in-plane free-stream (cross-flow) velocity for the tilted propeller, respectively.

The extraction of the sectional angle of attack from phase-locked averaged simulation data is carried out following the *3-points* method proposed by Rahimi *et al.* [200, 201]. It consists in extracting, for each radial section and blade azimuthal position, the velocity vectors (in the non-inertial reference frame rigidly rotating with the blade) in correspondence of six points, three located on the suction side (1, 3 and 5) and three on the pressure side (2, 4 and 6) at 25, 50 and 75% of the chord at a distance of approximately one chord away from the local airfoil aerodynamic center in the normal direction (Fig. 6.7). For each couple of points at the three different chordwise locations (I, II and III), the velocities are averaged by using an interpolating function (arithmetic mean in the present work), resulting in three velocity vectors for each station: $\mathbf{V}_I = (\mathbf{V}_1 + \mathbf{V}_2)/2$, $\mathbf{V}_{II} = (\mathbf{V}_3 + \mathbf{V}_4)/2$ and $\mathbf{V}_{III} = (\mathbf{V}_5 + \mathbf{V}_6)/2$. Then, the velocity vector perceived by the local airfoil is computed as arithmetic average of the three previous velocities, $\mathbf{V} = (\mathbf{V}_I + \mathbf{V}_{II} + \mathbf{V}_{III})/3$, and decomposed into axial and tangential components to extract the induction angle ϕ that, subtracted to the blade geometrical twist θ_{tw}, provides the local airfoil angle of attack: $\alpha_s = \theta_{tw} - \phi = \theta_{tw} - \tan^{-1}(V_a/V_t)$.

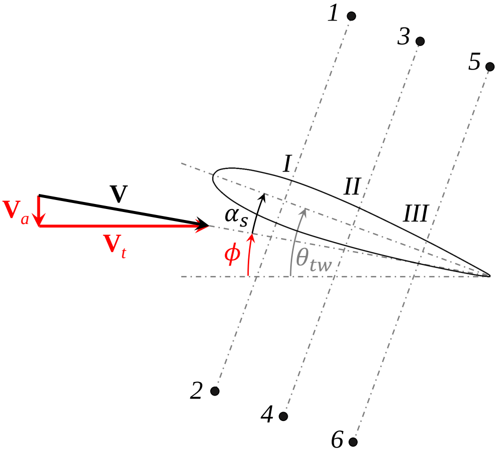

Figure 6.7: Sketch of the 3-points method for the local airfoil angle of attack extraction [200, 201].

For the propeller operating at zero yaw angle, the axial and tangential velocity components and the local airfoil angle of attack show the expected axisymmetric pattern, with dependency on the radial coordinate only, and constant values along the azimuth. In particular, the axial velocity component (Fig. 6.8(a)) is increased by the propeller rotation up to 40% of its undisturbed value for $0.4 < r/R < 0.8$, whereas the tangential component (Fig. 6.8(c)) and the sectional angle of attack (Fig. 6.8(e)) increase and decrease, respectively, along the blade span.

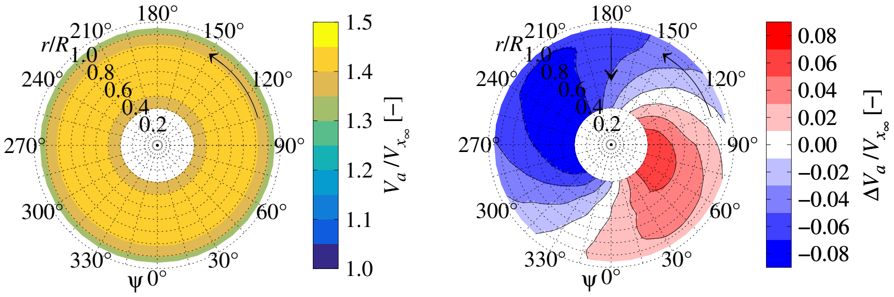

(a) Axial component, $\alpha = 0°$ (b) Axial component, $\alpha = 15°$

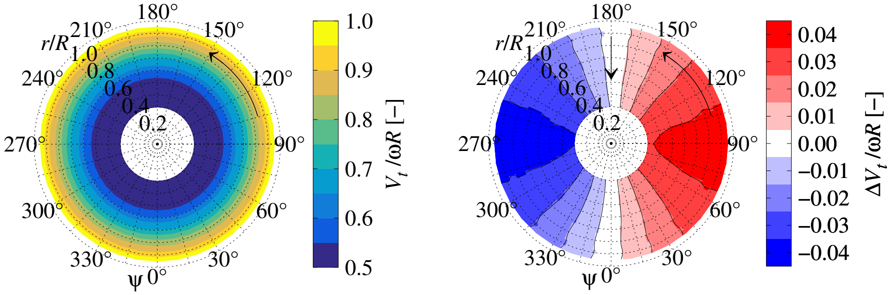

(c) Tang. component, $\alpha = 0°$ (d) Tang. component, $\alpha = 15°$

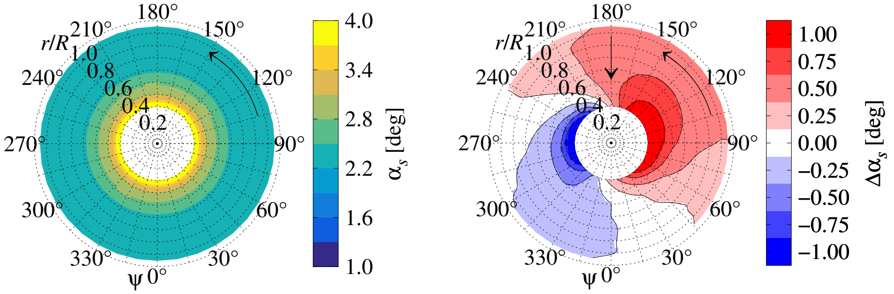

(e) Angle of attack, $\alpha = 0°$ (f) Angle of attack, $\alpha = 15°$

Figure 6.8: Axial and tangential velocity components and angle of attack distributions for axial flow ($\alpha = 0°$) and their variations under angular inflow conditions ($\alpha = 15°$).

Regarding the case with the propeller at incidence, more interesting results can be found. First, Fig. 6.8(d) shows the expected result that, when the propeller is operated at incidence with respect to the free-stream, the tangential velocity component experienced by the local airfoil section is increased on the blade advancing side ($0° < \psi < 180°$) and decreased on the retreating one ($180° < \psi < 360°$), due to the rise of an in-plane free-stream velocity component. Less foreseeable is the variation of the axial velocity component induced by the non-zero propeller yaw angle, which shows spanwise maxima and minima roughly in correspondence of $\psi = 45°$ and $\psi = 225°$, respectively. The advancing side of the blade is mostly characterized by an increment of the axial velocity, while the opposite phenomenon occurs on the retraining side. However, the axial and tangential velocity components variation do not appear to be in phase, with the former being 30° delayed with respect to the latter. As previously pointed out, the combination of both axial and tangential sectional velocities defines the local airfoil angle of attack (Fig. 6.7), whose variation for $\alpha = 15°$ is shown in Fig. 6.8(f). In particular, an increment of the axial velocity is responsible for a reduction of the local angle of attack experienced by the blade, whereas an increase in the tangential velocity results in higher α_s. This explains why the blade angle of attack is not purely increasing (decreasing) on the blade advancing (retreating) side when the propeller is at incidence, rather it shows a periodic variation with a phasing of about 30-45° delay with respect to the ideal blade angle of attack variation (i.e. that based on the tangential velocity only).

6.4.2. UNSTEADY THRUST AND TORQUE DISTRIBUTIONS

Next, the influence of the propeller yaw angle on the unsteady loading is investigated. Figure 6.9 shows the sectional thrust ($C_{\partial_r T}$) and torque ($C_{\partial_r Q}$) coefficient (per unit span) distributions for $\alpha = 0°$, as well as their variations ($\Delta C_{\partial_r T} = C_{\partial_r T,15°} - C_{\partial_r T,0°}$ and $\Delta C_{\partial_r Q} = C_{\partial_r Q,15°} - C_{\partial_r Q,0°}$) for $\alpha = 15°$, of a single propeller blade as functions of the azimuth and radial coordinates. The thrust and torque coefficients distributions are computed as follows:

$$C_{\partial_r T} = \frac{\partial_r T}{\rho n^2 D^3} \quad \text{and} \quad C_{\partial_r Q} = \frac{\partial_r Q}{\rho n^2 D^4}, \tag{6.2}$$

where $\partial_r T = \partial T/\partial r$ and $\partial_r Q = \partial Q/\partial r$ represent the blade thrust and torque per unit span, respectively. For the axial inflow case, the thrust and torque show axisymmetric distributions over the rotor disk with the highest values around 80% of the radial coordinate (Figs. 6.9(a) and 6.9(b)). The root and tip regions generate a lower amount of sectional thrust due to the relatively lower flow velocity and tip-vortex induced lift deficit, respectively. Similar considerations can be drawn for the torque for inboard blade sections (Fig. 6.9(b)). Conversely, the outer part of the blade shows a lower relative torque reduction compared to that observed for the thrust, due to the fact that the former is equally dependent from the local airfoil pressure distribution and skin friction through the sectional drag.

When the propeller axis is tilted with respect to the free-stream velocity component, both the section thrust and torque distributions exhibit a periodic variation along the blade azimuth, with the highest and lowest values reached slightly after $\psi = 90°$ and $\psi = 270°$, respectively. Such unsteady loading variations are not perfectly in phase with that of the tangential velocity component (which dominates the total velocity change perceived by the blade sections), due to its dependence from the sectional angle of attack as well. For $\alpha = 15°$, the sectional thrust and torque coefficients increments on the blade advancing side are larger than their corresponding reductions occurring on the retreating one.

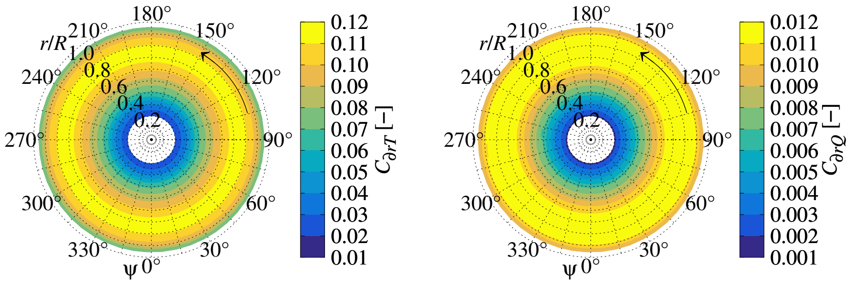

(a) Thrust, $\alpha = 0°$ (b) Torque, $\alpha = 0°$

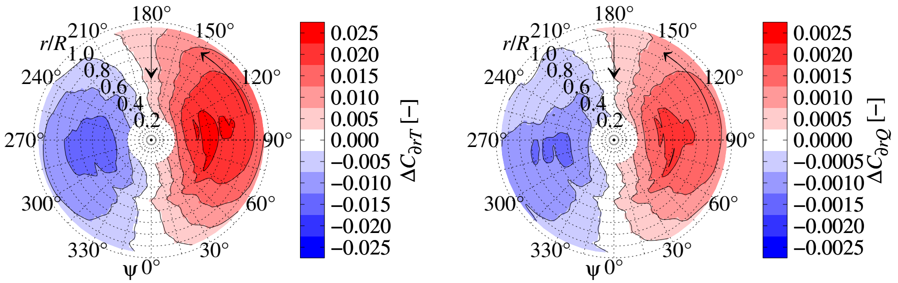

(c) Thrust, $\alpha = 15°$ (d) Torque, $\alpha = 15°$

Figure 6.9: Thrust and torque coefficients (per unit span) distributions for axial flow ($\alpha = 0°$) and their variations under angular inflow conditions ($\alpha = 15°$).

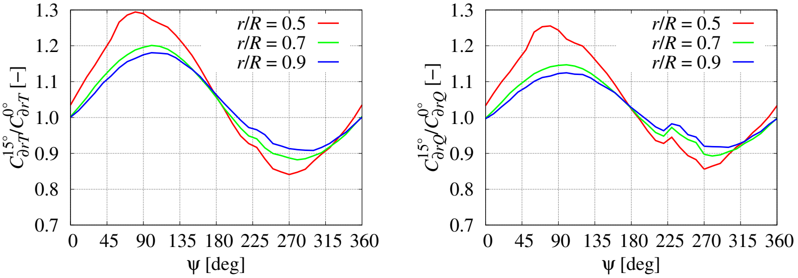

(a) Thrust ratio (b) Torque ratio

Figure 6.10: Ratio of the thrust and torque coefficients between $\alpha = 15°$ and $\alpha = 0°$ cases for three spanwise locations.

This is further highlighted in Fig. 6.10 for three spanwise locations ($r/R = 0.5, 0.7, 0.9$), which shows the ratio between the sectional thrust and torque coefficient (per unit span) between the yawed and axial cases. Specifically, it can be observed that the increment of sectional thrust and torque on the advancing side is roughly two times larger than the corresponding reduction occurring on the retreating one. This aspect can explain the moderate increase of the mean thrust and torque coefficients observed in Fig. 6.3 and is primarily related to the larger local airfoil angle of attack increase on the advancing side compared to its reduction taking place on the retreating one. Moreover, this phenomenon is expected to take place to a larger extent in the experiment, due to the larger increment of C_T and C_Q observed in the measurements when the propeller is at incidence. The use of a zig-zag transition trip in the computational setup, which is known to slightly reduce the pressure suction effect at the blade leading-edge as discussed in Chapter 5, might have limited the occurrence of the aforementioned phenomenon in the numerical simulation.

6.4.3. FAR-FIELD NOISE DIRECTIVITY

The far-field noise noise directivities in the plane of the propeller (y_g-z_g plane) and along its axis (x_g-z_g plane) are respectively shown in Figs. 6.11 and 6.13 for both the axial ($\alpha = 0°$) and angular ($\alpha = 15°$) inflow cases. These are computed on two circular arrays of $10R$ radius centered on the propeller hub and composed by 25 evenly spaced microphones. The circular and straight arrows in Fig. 6.11 indicate the propeller angular velocity and the free-stream in-plane velocity component directions, while the straight arrow in Fig. 6.13 represents the free-stream velocity vector direction. The propeller is sketched in grey in each plot. For both the in-plane and out-of-plane directivities, the total far-field noise (in red) is further decomposed into its thickness (in green) and loading (in blue) components according to Eqs. (3.60) and (3.61), respectively. The far-field noise directivity is presented in terms of Sound Pressure Level (SPL), with the root-mean-square of the acoustic pressure integrated over three different blade-passing frequency ranges: BPF 0.1-100, BPF 1 and BPF 10-100. The former is representative of the overall sound pressure level directivity (hence, hereinafter defined as OASPL) around the propeller. Moreover, as it can be inferred from Figs. 6.5 and 6.6, the latter is a measure of the directivity associated to the broadband component of the noise dominated by the turbulent boundary-layer trailing-edge noise, while the SPL around BPF 1 provides information about the directivity of the tonal noise at the most dominant harmonic.

Previous research pointed out that the effect of the propeller yaw angle on the far-field noise radiation has a twofold nature: one aerodynamic, related to the rise of unsteady loading sources, and one kinematic or acoustic, associated to the phase modulation of the strength of all the sources due to a periodic variation of the observer-source relative Mach number (for an observer rigidly rotating with the blade) [195, 198]. For low-speed propellers, the first mechanism is still relevant because of the high radiation efficiency of the unsteady loading modes [60]. Contrarily, the kinematic/acoustic effect may play a minor or negligible role due to the relatively low free-stream Mach, and consequently of its in-plane component responsible for the source strength modulation. The relative importance of this effect for $\alpha = 15°$ is investigated in this work by performing FW-H computations without the free-stream cross-flow velocity component, whose corresponding total far-field noise directivities are depicted by the black crosses in Figs. 6.11 and 6.13.

IN-PLANE NOISE DIRECTIVITY

For axial inflow conditions ($\alpha = 0°$), the far-field noise shows the expected axisymmetric in-plane directivity for all the three frequency ranges considered. The tonal noise at BPF

1 (Fig. 6.11(c)) contributes the most to the overall sound pressure level (Fig. 6.11(a)) in the plane of the propeller compared to the broadband component (Fig. 6.11(e)). Moreover, the loading noise represents the most important contributor to the total acoustic pressure for all the frequency ranges considered. While for the SPL at BPF 1 thickness noise is still relatively important when compared to loading noise (Figs. 6.11(c) and 6.11(d)), the latter is the only relevant contributor to noise in the BPF range 10-100 (Figs. 6.11(e) and 6.11(f)). However, it should be pointed out the different nature of these loading noise sources for the two different frequency ranges. At the BPF 1, the loading noise is associated to the presence of steady forces generated by the rotating blades in a frame that is not inertial with respect to a far-field observer (see Sec. 2.1.3). Conversely, the broadband noise in the frequency range BPF 10-100 is due to the presence of stochastic unsteady loadings in the reference frame rigidly connected to the blade. Such non-deterministic unsteady loadings are those related to the turbulent pressure fluctuations in the boundary-layer over the blade suction side, which are scattered as sound at the blade trailing-edge (see Sec. 2.1.1).

Similar considerations can be inferred for the case with the propeller axis at an angle of attack with respect to the free-stream velocity direction ($\alpha = 15°$), except for the axial symmetry of the noise directivity, which is significantly altered by the presence of a cross-flow velocity component. In line with previous studies [191–194], the total far-field noise is increased in that region from which the propeller is tilted away ($90° < \phi < 270°$) and decreased in the opposite one ($270° < \phi < 90°$). However, this noise directivity change is only related to the generation of periodic blade unsteady loadings (shown in Fig. 6.9), due to the periodic variation of the incidence and velocity experienced by the blade. Indeed, FW-H computations without the cross-flow velocity components (black crosses in Figs. 6.11(b), 6.11(d) and 6.11(f)) provide almost identical results to those in which the in-plane convective effects are considered, thus implying that the aforementioned kinematic/acoustic modulation effect of the source strength can be neglected for the case under examination. As shown in Fig. 6.11(d), the presence of unsteady loading of the blade is responsible for a SPL increment of the loading noise at the first BPF up to 6 dB at $\phi = 195°$, and for a reduction up to 12 dB in the diametrically opposite direction, which in turn affects the directivity of the total far-field noise. The circumferential positions of the maximum and minimum noise are located 90° ahead of the locations of maximum and minimum blade loading, respectively. This is a consequence of the fact that the noise generated by the propeller blade mainly radiates perpendicularly to it. Conversely, thickness and broadband noise are not significantly altered in the plane of rotation when the propeller is at incidence with respect to the free-stream. This can be ascribed to the relatively low periodic variations of both the section angle of attack and velocity, respectively below 0.5° and 5% of the undisturbed local airfoil free-stream velocity for outboard blade sections, resulting in a negligible unsteady (in the rotor frame) flow displacement and turbulent boundary-layer properties, which respectively underlie thickness and trailing-edge noise generation.

To complement the SPL directivity plots reported in Fig. 6.11, Fig. 6.12 shows the narrow band spectra in 1/12-octave bands at two in-plane observer angles, $\phi = 0°$ and $\phi = 180°$, corresponding to the regions of maximum noise increment and reduction under yawed conditions ($\alpha = 15°$), respectively. Once again, an increment of the total noise

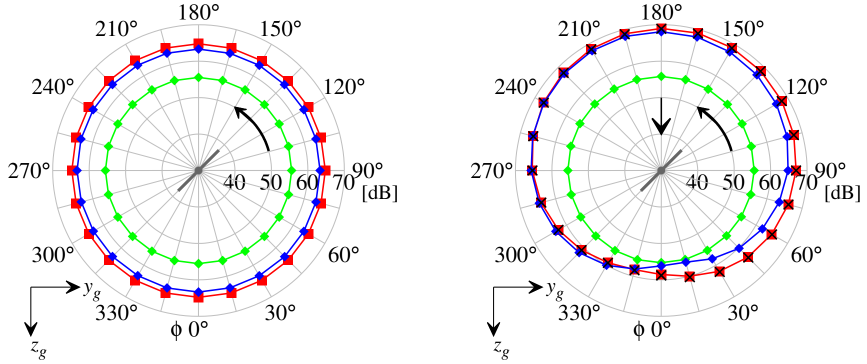

(a) OASPL, $\alpha = 0°$ (b) OASPL, $\alpha = 15°$

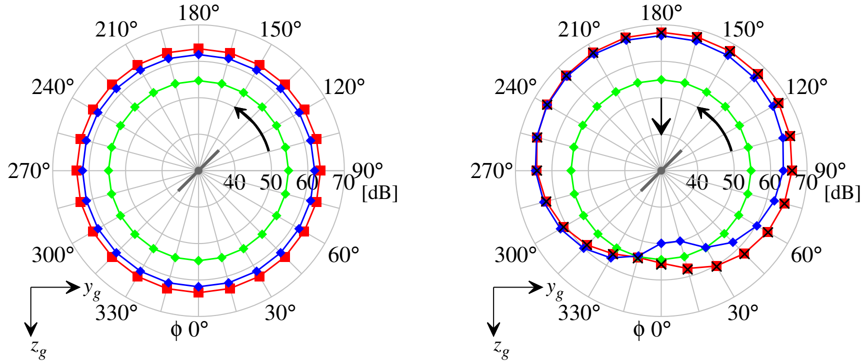

(c) SPL (BPF 1), $\alpha = 0°$ (d) SPL (BPF 1), $\alpha = 15°$

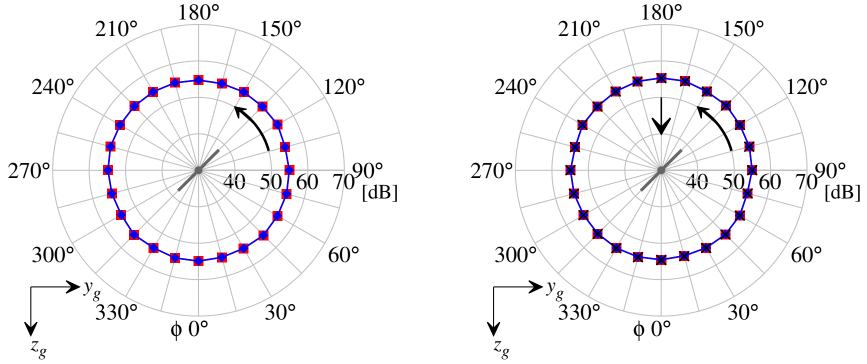

(e) SPL (BPF 10-100), $\alpha = 0°$ (f) SPL (BPF 10-100), $\alpha = 15°$

Figure 6.11: SPL in-plane directivity of total (■), thickness (◆) and loading noise (◆) for $\alpha = 0°$ and $\alpha = 15°$. Total noise without cross-flow velocity component for $\alpha = 15°$ (✕).

at the first two BPFs can be observed for the observer position from which the propeller is titled away ($\phi = 180°$) with respect to the axial flow case ($\alpha = 0°$), while a noise reduction of BPF 1 and 2 takes place in the opposite region ($\phi = 0°$). Conversely, no significant broadband noise variation can be appreciated between the yawed and axial cases.

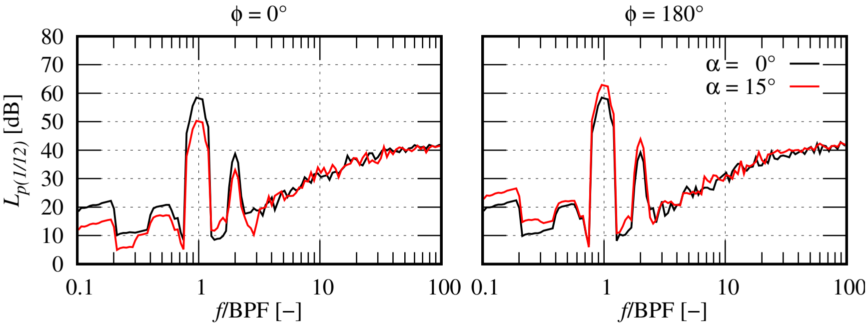

Figure 6.12: Sound pressure level in 1/12-octave band $L_{p(1/12)}$ of the total noise for $\alpha = 0°$ and $\alpha = 15°$ at two different in-plane observer positions: $\phi = 0°$ and $\phi = 180°$.

It should be pointed out that the negligible variation of the (broadband) sound pressure level within the frequency range BPF 10-100 observed in Fig. 6.11 is not antithetical to the moderate high-frequency broadband changes illustrated in Figs. 6.5 and 6.6. Indeed, the far-field noise spectra in Figs. 6.5 and 6.6 are reported in 1/12-octave bands to better discern tonal noise at low frequency and broadband noise at mid- to high-frequencies. However, this leads the p'_{rms} to be integrated over frequency bands of increasing width as the frequency increases, resulting in an apparent larger contribution of higher frequencies to the overall broadband noise energy. Although not shown for the sake of brevity, the far-field noise spectra in constant frequency bands highlight a more balanced broadband energy distribution across mid and high frequencies, so that the moderate changes of the high-frequency broadband noise do not significantly influence the SPL integrated within BPF 10-100.

OUT-OF-PLANE NOISE DIRECTIVITY

Next, the out-of-plane (axial) noise directivity (i.e. on the x_g-z_g plane shown in Fig. 6.1(a)) is analyzed. As a first result, it can be noticed that tonal noise propagates mainly in the propeller plane for axial flow conditions ($\alpha = 0°$), with almost no noise radiation occurring of along propeller axis (Fig. 6.13(c)), as expected. Conversely, broadband noise shows (Fig. 6.13(e)) a more uniform out-of-plane directivity with the largest noise levels radiated perpendicularly to the propeller plane. This is consistent with the turbulent boundary-layer trailing-edge noise theory according to which the noise radiates following a dipolar/cardioid pattern approximately symmetric with respect to the local airfoil chord [26]. As a result, both tonal and broadband noise contribute to the out-of-plane OASPL directivity (Fig. 6.13(a)), with the former dominating along the propeller plane, while the latter on the propeller axis.

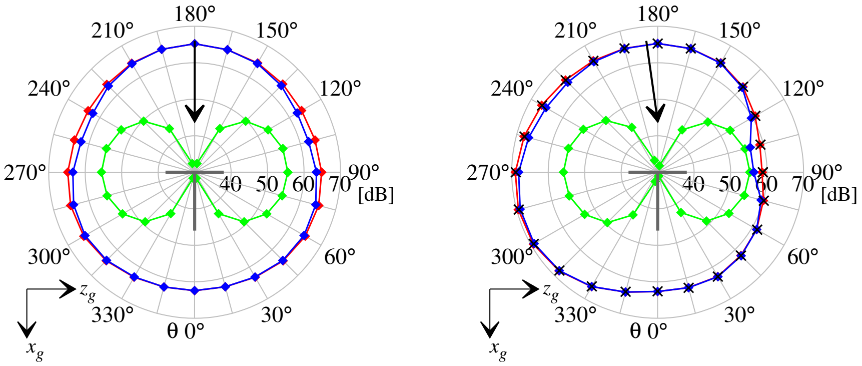

(a) OASPL, $\alpha = 0°$ (b) OASPL, $\alpha = 15°$

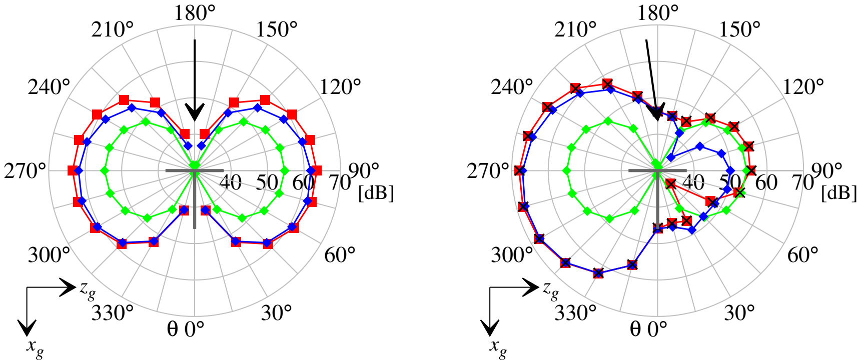

(c) SPL (BPF 1), $\alpha = 0°$ (d) SPL (BPF 1), $\alpha = 15°$

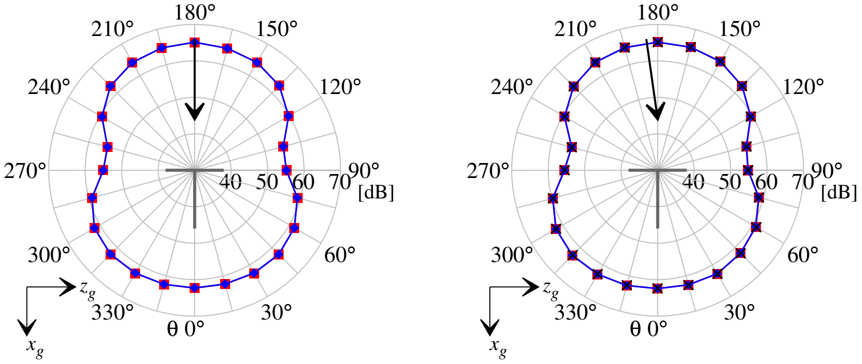

(e) SPL (BPF 10-100), $\alpha = 0°$ (f) SPL (BPF 10-100), $\alpha = 15°$

Figure 6.13: SPL out-of-plane directivity of total (—■—), thickness (—◆—) and loading noise (—◆—) for $\alpha = 0°$ and $\alpha = 15°$. Total noise without cross-flow velocity component for $\alpha = 15°$ (✕).

For the propeller with a non-zero yaw angle, the OASPL along the propeller plane is increased in that area from which the propeller is tilted away and reduced in the opposite one (Fig. 6.13(b)), as already shown in the in-plane directivity plots. This noise directivity change is governed by the modification of the loading noise at BPF 1 (Fig. 6.13(d)), with broadband noise directivity modifications being negligible (Fig. 6.13(f)). Interestingly, loading noise at BPF 1 dramatically increases along the propeller axis, as further shown by the noise spectra in Fig. 6.14 for two on-axis observers above ($\theta = 180°$) and below ($\theta = 0°$) the propeller plane. This is clearly the indication of the presence of unsteady loading harmonics that, contrarily to the noise associated to the steady contribution of the force (i.e. rotor-locked noise), lead to the propagation of noise in the direction of the propeller axis. As previously shown for the in-plane directivity, convective modulation effects on the noise sources on the blade are negligible also for what concerns the radiation along the propeller axis. Finally, it is interesting to point out that, for some particular observer angles (i.e. $345° < \phi < 30°$ for in-plane observers and $45 < \theta < 150°$ for out-of-plane ones) the loading noise decreases to such an extent that thickness noise becomes the most important noise source at BPF 1 (Figs. 6.11(d) and 6.13(d)), due to the forces reduction occurring around $\psi = 270°$ (Figs. 6.9(c) and 6.9(d)).

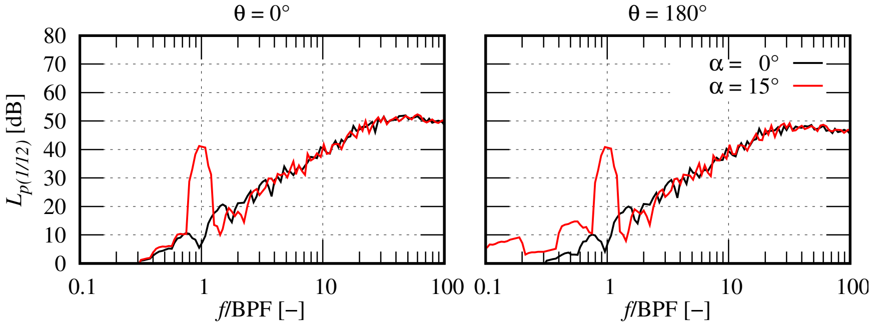

Figure 6.14: Sound pressure level in 1/12-octave band $L_{p(1/12)}$ of the total noise for $\alpha = 0°$ and $\alpha = 15°$ at two different out-of-plane observer positions: $\theta = 0°$ and $\theta = 180°$.

Although not shown for the sake of conciseness, considerations similar to that derived above for the SPL at BPF 1 can be inferred for the noise directivity variation of the second BPF harmonic.

6.4.4. NOISE POWER LEVEL

The survey on the propeller yaw angle effects on the resulting radiated field is concluded with the analysis of the source power level, which is representative of the acoustic energy generated by the propeller regardless the distance and the observation angle. The source Power Level (PWL) spectrum is evaluated by integration of the Power Spectral Densities (PSDs) of the (total) acoustic signature computed through the FW-H acoustic analogy over a spherical array of $10R$ radius centered around the propeller hub, using the following formula:

$$\mathrm{PWL}(f) = \int_0^{2\pi} \int_0^{2\pi} R_s^2 \sin(\theta) \frac{[1 + M_0 \cos(\theta)]^2 \mathrm{PSD}(f,\phi,\theta)}{2\rho_0 c_0} \mathrm{d}\phi \mathrm{d}\theta \tag{6.3}$$

where f is the frequency, R_s is the sphere radius, θ and ϕ are the angular coordinates defined in Fig. 6.11 and Fig. 6.13, respectively, while M_0, ρ_0 and c_0 are the free-stream Mach number, density and speed of sound. A total of 625 microphones, 25 per each angular coordinate, have been used for the PWL calculation. Figure 6.15 shows, for the axial ($\alpha = 0°$) and angular ($\alpha = 15°$) inflow cases, the one-sided source power level spectrum computed using Eq. (6.3), with the PWL converted from W/Hz to dB/Hz considering a reference sound power $\mathrm{PWL}_{\mathrm{ref}} = 10^{-12}$ W. The PWL spectrum reveals that the source power is increased by 3.4 dB and 2.1 dB at BPF 1 and 2, respectively, when the propeller is tilted incidence by 15° with respect to the free-stream velocity direction, regardless the presence of regions of sound pressure level increment and reduction around the propeller. Conversely, no variation of the broadband component of the source power can be appreciated, as expected from the negligible in-plane and out-of-plane sound pressure level directivity variations shown in Figs. 6.11 and 6.13.

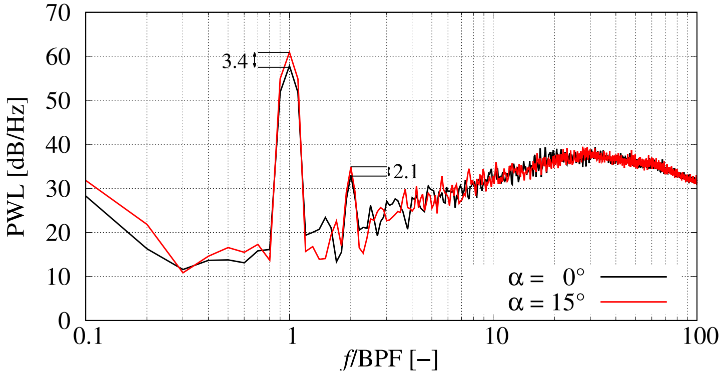

Figure 6.15: Source power level variation with the propeller yaw angle.

As a final result, the sectional source power level variation with α at the first BPF is analyzed. Specifically, the two blades of the propeller are both split into ten evenly spaced strips between root and tip. Then, FW-H acoustic signals from each couple of strips at iso-radius are evaluated on the aforementioned spherical array in order to compute the contribution of each strip to the whole propeller source power. The corresponding results for BPF 1 are reported in Fig. 6.16 with respect to the blade section count, where 1 and 10 respectively correspond to the root and tip strips. The total source power (red) is further decomposed into thickness (green) and loading (blue) noise-related PWL contributions. Under axial inflow conditions (Fig. 6.16(a)), the outer part of the blade contributes the most to the far-field noise radiation, with loading noise being the dominant source of noise. As the propeller is set at incidence with respect to the free-stream velocity, the outer part of the blade is still largely responsible for the overall noise emissions, although the relative contribution of the inner blade sections increases more than that associated to outer ones. This is a consequence of the fact that the innermost blade sections experience the largest loading and fluid displacement variations relative to the axial inflow case, due to the largest local angle of attack and velocity changes occurring at those spanwise locations. Similar considerations can be drawn for the BPF 2, whose results are not reported for the sake of conciseness.

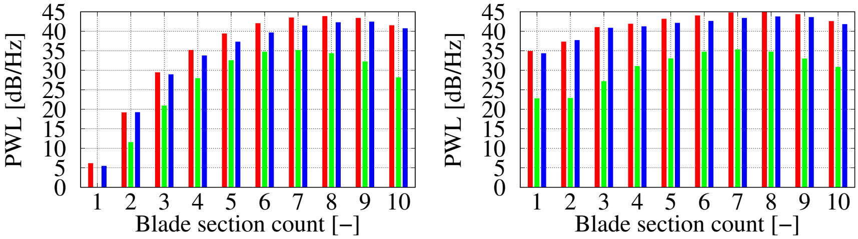

(a) BPF 1, $\alpha = 0°$ (b) BPF 1, $\alpha = 15°$

Figure 6.16: Sectional source power level at BPF 1 of total (—), thickness (—) and loading (—) noise.

6.5. CONCLUSIONS

This chapter presented a computational study on flow incidence effects on the aeroacoustics associated to low-speed propeller operated at a yaw angle with respect to the free-stream. The numerical flow solution was obtained by solving the explicit, transient and compressible lattice-Boltzmann equation implemented in the CFD/CAA solver SIMULIA PowerFLOW®. The aerodynamic noise generated by the propeller was computed by using the Farassat's formulation 1A of the FW-H equation applied to the propeller/nacelle surfaces. A transition trip was used on the suction side of the propeller blades in the computational setup to force the numerical scheme to switch from modeled to scale-resolving turbulence mode and trigger the formation of turbulent structures for the sake of turbulent boundary-layer trailing-edge noise generation.

Numerical results were compared against forces and noise measurements carried out in the A-Tunnel of TU-Delft to assess the capability of the employed computational setup to predict loads, tonal and broadband noise modifications due to a non-zero propeller yaw angle. Both absolute values and variations, due to the propeller yaw angle change, of the time-averaged thrust and torque were reasonably captured by the computational setup, although to a lower extent compared to those observed in the experimental data. A quite satisfactory agreement between numerical and experimental data was found for both tonal noise at BPF 1 and broadband noise above BPF 30, with the numerical setup able to capture the large tonal noise variation, as well as the moderate high-frequency broadband changes, at different observer locations due the modification of the propeller yaw angle.

The analysis of the velocity field for the propeller at incidence revealed a nearly symmetric variation (in absolute value) of the tangential velocity experienced by the different blade sections with respect to the in-plane free-stream velocity component, with an increment on the advancing side and a reduction on the retreating one. The sectional angle of attack azimuthal variation was found to take place with a phase shift of 30° in advance with respect to that of the tangential velocity, which dominates the total velocity experienced by the blade section, causing the unsteady aerodynamic loadings to reach the highest and lowest values slightly after $\psi = 90°$ and $\psi = 270°$, respectively. Moreover, larger sectional thrust and torque increments were observed on the blade advancing side compared to the reductions occurring on the retreating one, explaining the higher mean propeller thrust and torque coefficients found in both numerical and experimental data.

Similarly to previous studies on high-speed propellers, the effect of the propeller yaw angle on the far-field noise resulted in a large increment of the noise radiated along the propeller axis, and an increase of the sound pressure level in the region from which the propeller is tilted away and a decrease in the opposite one. However, contrarily to a propeller experiencing high cross-flow Mach number components, such a noise directivity change was found to be related only to the rise of deterministic unsteady loadings on the blade due to the periodic variation of the incidence and velocity experienced by the blade. FW-H computations without the cross-flow velocity component provided nearly identical results to those in which the in-plane convective effects were considered, thus implying that the kinematic/acoustic modulation effect of the sources strength can be neglected for low-speed propellers at incidence. Finally, thickness and broadband noise did not show a significant directivity variation due to the propeller yaw angle, as a consequence of the moderate variation of the sectional angle of attack and velocity, which could have resulted in a negligible unsteady flow displacement and turbulent boundary-layer properties changes at the blade trailing-edge.

7

ROTOR BLADE-VORTEX INTERACTION NOISE

> *There are in fact two things, science and opinion;*
> *the former begets knowledge, the latter ignorance."*
>
> Hippocrates

Chapter 6 discussed, for rotating blades operating at low blade tip speeds, the effects of the most simple type of inflow distortion that can be experienced by a rotor/propeller, namely that associated to the propeller yaw angle or angle of attack. The present chapter focuses on another and more complex type of inflow non uniformity, which is that related to the velocity field induced by a blade tip-vortex, when a rotor/propeller blade interacts or passes in close proximity it. In particular, the scope of this chapter is to assess the accuracy and computational performances of the LBM to predict blade-vortex interaction noise, which can represent an important source of noise for open rotors/propellers of rotorcraft performing low advance ratio maneuvers and/or descent flights. The employed benchmark configuration is the 40% geometrically and aeroelastically scaled model of a BO-105 4-bladed main rotor tested in the framework of the HART-II project. Simulations are performed by considering a rigid blade motion, but a computational approach is employed to account for the steady and unsteady aerodynamic effects associated to the blade elastic deformations. This is based on the application of a transpiration velocity boundary condition, a fluid body-force field and the steady deformed blade shape. It is shown that the modeling of the aerodynamic effects related to the elastic deformation of the rotor leads to more accurate predictions of trim settings, unsteady airloads and noise footprint.

Parts of this chapter have been published in the AESCTE journal (2019) [202] and in the 75th VFS Conference proceedings (2019) [203].

7.1. INTRODUCTION

THIS chapter describes the application of the Lattice-Boltzmann Method (LBM) to the evaluation of the aerodynamic and aeroacoustic fields around helicopter rotors in Blade-Vortex Interaction (BVI) conditions. Helicopter BVI is a phenomenon which occurs when a rotor blade interacts very closely with the tip vortices released by the other blades or the blade itself, and it typically takes place during descent flights or maneuvers at moderate advance ratios, when the wake of the main rotor remains in closer proximity to the rotor itself [63]. In more innovative rotorcraft configurations, such as electric Vertical Take-Off and Landing (eVTOL) vehicles characterized by non-conventional layouts with distributed propellers/rotors [13, 14, 16, 18, 19, 188, 189], the occurrence of BVI can concern the interaction between the blade of a rotor/propeller with the tip vortices released by the blades of a different rotor/propeller.

The BVI-induced fluctuations of the blade aerodynamic loads represent one of the main sources of rotorcraft community noise and airframe vibration. Therefore, BVI noise is considered as one of the major limitations of rotorcraft operations in urban areas, and it is strongly correlated with hundreds of dormant heliports/vertiports worldwide. The physics of BVI is governed by the strength and trajectory of the tip vortices, and in particular by the minimum distance from the rotor blade for the blade section and azimuth considered, which is referred to as blade-vortex miss distance [63] (see Sec. 2.1.4). For this reason, in order to successfully predict BVI phenomena, it is required to adopt an aerodynamic solver able to accurately predict three-dimensional unsteady flows and the spatial evolution of the rotor wake vorticity, as well as to take into account the periodic elastic deformation of the rotor blades.

In the last two decades, many researchers have focused their efforts on the experimental characterization and numerical prediction of BVI. In this framework, the second Higher-Harmonic Control (HHC) Aeroacoustic Rotor Test (HART-II), which is the experimental reference considered in the present study, represents the best-known benchmark for rotor BVI aerodynamics, aeroelasticity and aeroacoustics [204–208]. The HART-II experiments were conducted in the large low-speed facility of the German-Dutch wind tunnel (DNW) in 2001 by an international cooperation between DLR, Onera, DNW, US Army AFDD and NASA Langley. The experimental database includes blade deflections, section airloads, wake geometry, PIV (Particle Image Velocimetry) and acoustic radiation measurements. Due to the large and comprehensive data sets available, this database is widely used by the rotorcraft research community for the validation of numerical solvers. An assessment of the state-of-the-art of the comprehensive/engineering codes used within the HART-II International Workshop for the sake of BVI aerodynamic/aeroacoustic prediction is illustrated in Refs. [209, 210], while in Refs. [211, 212] a review of the state-of-the-art of higher-fidelity Computational Fluid Dynamics methods coupled with Computational Structural Dynamics codes (CFD/CSD) can be found.

Comprehensive codes are typically based on finite element beam formulations as structural model, and two-dimensional blade-section theories, enhanced by corrections for unsteadiness, free-wake vortex lattice approaches and roll-up models to include the rotor wake influence on the aerodynamic loads. Among the plethora of comprehensive codes, those based upon the coupling of beam-like models for the blade structural dynamics and Boundary Element Methods (BEMs) for its aerodynamics deserve a special mention due to their wide usage and good accuracy in predicting the aero-acousto-elastic behavior of rotors in BVI [213, 214]. The main advantage of comprehensive codes is the significantly lower computational cost and memory requirement compared to CFD/CSD approaches, making them suitable for fast trend parameters identification, optimization and mission-level analysis purposes. On the other hand, comprehensive codes typically require the tuning of some of the parameters involved in their aerodynamic modules to obtain a good agreement between experimental data and numerical results [215], and they offer a lower potential in terms of accuracy with respect to that provided by CFD-based methods [210]. For both the aforementioned approaches, the noise radiation is typically evaluated using formulations based on the Ffowcs Williams & Hawkings' (FW-H) acoustic analogy [34] applied to the rotor aerodynamic solution.

The primary goal of this study is to assess the accuracy, capabilities and the computational performances of the LBM to predict the unsteady loadings, the rotor wake development and the noise radiation of rotors undergoing BVI conditions. In this study, the HART-II baseline configuration, without Higher-Harmonic Control (HHC)[1], is simulated by using a recently released version (6-2020-R3) of the LBM-based solver SIMULIA PowerFLOW®, which implements a hybrid high-subsonic/transonic LBM formulation [103]. The benchmark study is conducted by assuming rigid blades. The effects of mesh resolution on the numerical results is investigated first. Then, the impact of including different blade deformation modeling assumptions on the accuracy of the aerodynamic and aeroacoustic results, such as the steady blade deformation and the application of transpiration velocity/fluid body forces for retrieving deformation effects on the blade loadings, is analyzed.

The present study represents the first attempt, to the author's knowledge, of application of the LBM to predict the aerodynamics and aeroacoustics associated to an helicopter rotor in strong BVI conditions. The performances of the solver are reported for the sake of comparison with those of conventional CFD methods based on the discretization of Unsteady Reynolds Average Navier-Stokes (URANS) equations, which are supposed, for this application, to generate an equivalent amount of flow information at an equivalent level of fidelity.

The rest of the chapter is organized as follows. In Sec. 7.2 the test case and computational setup are described. Section 7.3 illustrates the computational approach adopted to take into account the aerodynamic effects due to the elastic motion of the blades. In Sec. 7.4, the validation of the numerical setup is carried out, while Sec. 7.5 is focused on the impact of the modeling of the blade elastic deformation aerodynamic effects on the accuracy of the numerical predictions. The main conclusions of this study are summarized in Sec. 7.6.

---

[1] The HHC is an active vibration and noise control system in which the rotor blade pitch angle is periodically varied at harmonics higher than that of the shaft angular velocity. The pitch angle due to the HHC is then superimposed on the main rotor trim controls, causing a slight variation in them (compared to a situation without HHC) and producing different blade flap and torsion deformations, unsteady airloads and tip-vortices dynamics.

7.2. TEST-CASE AND COMPUTATIONAL SETUP

All the simulations performed in this chapter are based on the same rotor operating condition, which is the HART-II baseline configuration without HHC, corresponding to a descent flight in strong BVI conditions. The effective rotor shaft angle[2] is $\alpha_{eff} = \alpha_s + \Delta\alpha = 4.5°$ (with $\alpha_s = 5.3°$ being the rotor shaft angle and $\Delta\alpha = -0.8°$ the wind tunnel interference angle, respectively) and its radius is $R = 2\,\text{m}$. The blade chord of the NACA 23012 airfoil composing the four rotor blades is $c = 0.121$ m. The advance ratio is $\mu = U_\infty \cos(\alpha_s)/(\Omega R) = 0.15$, where $U_\infty = 32.9$ m/s is the free-stream velocity and $\Omega = 109.12$ rad/sec is the rotational speed of the rotor. This angular velocity corresponds to an hover blade-tip Mach number of 0.639 and a Blade-Passing Frequency (BPF) of 69.47 Hz. The ambient temperature and pressure are 290.45 K and 100970 Pa, respectively. Starting from the experimental collective ($\theta_0 = 3.80°$), lateral ($\theta_c = 1.92°$) and longitudinal ($\theta_s = -1.34°$) cyclics blade pitch commands as initial guess, a Newton-Raphson iterative method (see Appendix C) is used to trim the main rotor to the experimental thrust, $T = 3300$ N, and hub rolling and pitching moment, $M_x = 20$ Nm and $M_y = -20$ Nm, respectively[3].

A spherical simulation volume of radius $100R$ centered around the helicopter is used. Static pressure and the free-stream velocity are prescribed on the outer boundary, and an acoustic sponge approach is used to damp the out-going acoustic waves and thus minimize the backward reflection from the outer boundary. The acoustic sponge is defined by two concentric spheres of radius $10R$ and $80R$, respectively, and centered around the helicopter hub. Hence, the fluid kinematic viscosity is gradually increased starting from its physical value within the inner sphere, up to an artificial one two orders of magnitude higher outside the outer one. Figures 7.1(a) and 7.1(b) show the computational grid used for all the simulations presented in this chapter. Overall, 13 Variable Resolution (VR) levels are used to discretize the entire fluid domain. In particular, the finest VR level is set around the blade leading-edge and tip, the second finest VR is used to discretize the region surrounding the blade, while the third finest VR encompasses the volume annulus swept by the outer part of the blade as depicted in Fig. 7.1(b). Nested Local Reference Frames (LRFs) are used to manage the rigid motion of the rotor blades. More specifically, four inner LRFs are used to define the sliding mesh volumes used to prescribe the periodic blade pitching motion due to the cyclic commands. These inner LRFs are in turn nested into an external sliding mesh (i.e. the outer LRF) employed to rotate the entire rotor geometry according to the rotor angular velocity, as sketched in Fig. 7.1(c). Simulations are performed using the hybrid high-subsonic/transonic LBM solver implemented SIMULIA PowerFLOW® 6-2020-R3, in which the transonic solver is used within the LRFs (where high values of the Mach number are expected) and the high-subsonic solver is

---

[2] Defined as the angle between the rotor shaft and the axis perpendicular to the undisturbed free-stream velocity and positive when the rotor shaft is tilted backwards.

[3] A conventional helicopter is controlled by the following four commands: main rotor collective θ_0, lateral cyclic θ_c, longitudinal cyclic θ_s and tail rotor collective θ_{tr}. The first three parameters contribute to the definition of the pitch of the main rotor blades, $\theta(\Psi) = \theta_0 + \theta_c \cos(\Psi) + \theta_s \sin(\Psi)$, with Ψ being the blade azimuth referred to the tail of the helicopter. In particular, the collective θ_0 contributes to the definition of the thrust produced by the rotor, while the cyclics θ_c and θ_s are used to govern the roll and pitch of the rotorcraft. Finally, the control of the directional dynamics is delegated to the tail rotor collective. Hence, the blade pitch angle θ varies periodically with the main rotor rotational frequency (1/rev).

used elsewhere (see Sec. 3.2).

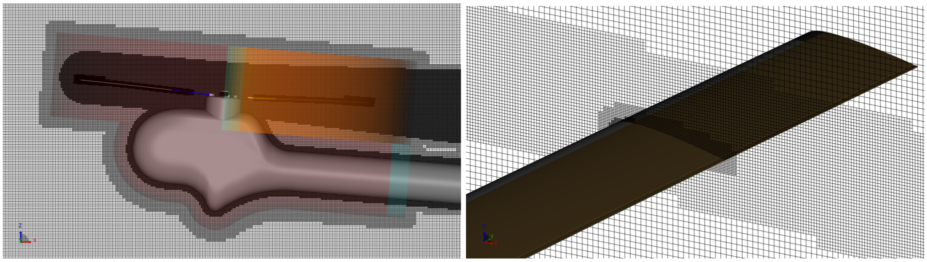

(a) *Mesh side view* (b) *Blade mesh close-up view*

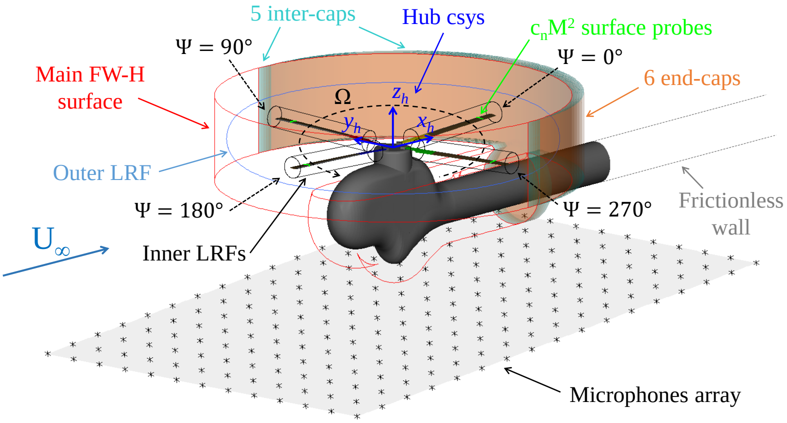

(c) *Sketch of the computational setup*

Figure 7.1: Details of the numerical setup: computational grid, hub coordinate system, LRFs, FW-H permeable surface and far-field noise microphones array.

In this study, the noise radiation is computed by using a FW-H acoustic analogy applied to a permeable surface encompassing the whole helicopter model, as sketched in Fig. 7.1(c). Since the FW-H approach adopted in this study neglects the volume (quadrupole) term, spurious signals might arise when the permeable surface is intersected by vortical structures [122], such as the blade tip-vortices and the turbulent structures within the rotor and hub wakes (see Sec. 3.3). Therefore, cap-averaging of the flow solution on 5 overlapping inter-caps and 6 staggered end-caps[4] on the permeable wakes

---

[4] The 6 end-caps are 6 identical surfaces staggered along the longitudinal direction downstream of the rotor (with the end-cap #1 being the most upstream one and the end-cap #6 the most downstream one), while the 5 inter-caps are 5 surfaces of different area partially overlapping on each other and connecting the main FW-H (open) surface to the end-caps. Therefore, the topology of the permeable FW-H surface used in this study is such that the main FW-H (open) surface is closed downstream by the end-cap #1, and that the inter-caps #1, #2, ..., #5 respectively connect the main FW-H (open) surface to the end-caps #2, #3, ..., #6.

surface being intersected by the rotor wake is adopted to filter out the noise signature associated to the vortical structures passing through the integration surface [124]. Table 7.1 shows the weighting parameters assigned to each face of the permeable FW-H integration surface for the far-field noise computation.

Acoustic data are sampled on the FW-H permeable surface at 69.5 kHz along 2 rotor revolutions on a sampling mesh which ensures at least 20 points-per-wavelength at BPF 40, after reaching the experimental trim conditions (3-4 rotor revolutions) for the thrust, and hub rolling and pitching moments. Fourier transformed data of the near-field pressure are evaluated using a bandwidth of 35.3 Hz, 40% window overlap coefficient and Hanning weighting.

FW-H surface face	#	Weight [-]	Note
Main surface	1	1	–
Inter-cap	5	$(6-n)/6$	$n = 1, \dots, 5$
End-cap	6	$1/6$	$\forall$ cap

Table 7.1: FW-H surface weighting parameters.

7.3. MODELING OF BLADE ELASTIC DEFORMATIONS AERODYNAMIC EFFECTS

As previously pointed out, the main affecting parameters of the BVI phenomenon are the blade-vortex miss distance, which results from the instantaneous position of the convected tip vortices and the deformed blades, and the tip-vortex circulation (see Sec. 2.1.4). Moreover, BVI mechanisms are also strongly related to the azimuthal positions of the interactions, which influence the angle of interaction between the blade and tip-vortices axes. Hence, in order to successfully predict BVI-related phenomena, it is crucial to fulfill the following three aspects:

- the accurate prediction of the vortex trajectory, which mainly depends on the good convection of the rotor wake;
- the capability of the solver to convect vorticity with low dissipation, thus preserving the vortex coherence over a sufficient number of rotor revolutions;
- the accurate prediction of the instantaneous position of the different blade sections, which relies on the capability of the solver to simulate elastic blade deformations under inertial and aerodynamic loads.

Therefore, two-way-coupled low-dissipative high-fidelity CFD/CSD approaches represent the ultimate frontier of BVI noise prediction. In the present work, only the modeling of the aerodynamic effects associated to the blade elastic deformation is concerned. Such a modeling choice is imposed by a main limitation of the LBM solver employed throughout this thesis, which can simulate combinations of rigid rotations, but not time-dependent deformations of the geometry. The computational mesh is indeed generated automatically by the solver in a pre-processing stage and is used throughout the simulation without possibility of update, whereas rigid rotations of parts respect to others are managed by sliding meshes called LRFs [107].

The analytical reconstruction of the blade elastic motion of the HART-II baseline case provided by van der Wall [216] - which was obtained by projecting Fourier components of the measured deformation on a basis of low-order FEM-computed modal shapes - is used in this study as starting point for the modeling of the associated aerodynamic effects. Following Ref. [216], the experimental flap (z), lead-lag (y) and torsion (ϕ) deformations[5] for each blade can be respectively written as:

$$z(r,\Psi) = \sum_{i=1}^{3} q_{z_i}(\Psi)\phi_{z_i}(r) \tag{7.1}$$

$$y(r,\Psi) = \sum_{i=1}^{2} q_{y_i}(\Psi)\phi_{y_i}(r) \tag{7.2}$$

$$\phi(r,\Psi) = \sum_{i=1}^{2} q_{x_i}(\Psi)\phi_{x_i}(r), \tag{7.3}$$

where ϕ_{z_i}, ϕ_{y_i}, ϕ_{x_i} are the modal shapes, functions of the radial coordinate r:

$$\phi_{z_i}(r) = \sum_{j=0}^{7} c_{z_{ij}} \left(\frac{r/R - 0.075}{1-0.075}\right)^j \tag{7.4}$$

$$\phi_{y_i}(r) = \sum_{j=0}^{7} c_{y_{ij}} \left(\frac{r/R - 0.075}{1-0.075}\right)^j \tag{7.5}$$

$$\phi_{x_i}(r) = \sum_{j=0}^{7} c_{x_{ij}} \left(\frac{r/R - 0.075}{1-0.075}\right)^j, \tag{7.6}$$

with R rotor radius, and q_{z_i}, q_{y_i}, q_{x_i} are the generalized coordinates:

$$q_{z_i}(\Psi) = \sum_{k=0}^{6} [a_{z_{ik}}\cos(k\Psi) + b_{z_{ik}}\sin(k\Psi)] \tag{7.7}$$

$$q_{y_i}(\Psi) = \sum_{k=0}^{6} [a_{y_{ik}}\cos(k\Psi) + b_{y_{ik}}\sin(k\Psi)] \tag{7.8}$$

$$q_{x_i}(\Psi) = \sum_{k=0}^{6} [a_{x_{ik}}\cos(k\Psi) + b_{x_{ik}}\sin(k\Psi)], \tag{7.9}$$

which reproduce the periodic time dependency and magnitude of each elastic deformation component through the azimuthal angle $\Psi = \Omega t$, with Ω denoting the rotational speed of the rotor and t the time. The coefficients of the modal shapes (Eqs. 7.4-7.6) are identical for each blade, whereas those of the generalized coordinates (Eqs. 7.7-7.9)

---

[5] Assuming a blade with zero geometrical twist, the flap deformation is the local blade displacement in the chord-normal direction, while the lead-lag one occurs in the chordwise direction. The torsion deformation is the rotation of the local blade section around the blade elastic axis.

slightly differ for the four blades due to their non identical elastic deformations measured during the experiment. All the previous coefficients are available in van der Wall's technical report [216].

For the sake of completeness and to help the discussion of the numerical results, Fig. 7.2 depicts the analytical reconstruction of the blade flap, lead-lag and torsion deflection data, averaged over the four blades, as functions of the radial coordinate and the azimuthal angle. As illustrated in Fig. 7.2(a), the flap motion mainly shows a 1/rev content, with a relatively large downward motion in the advancing side (0° – 180°) and a less pronounced upward motion in the retreating side (180° – 360°). The lead-lag deflection also shows a 1/rev variation with a maximum lag motion around 180° in the azimuth (Fig. 7.2(b)). Finally, the torsional response (Fig. 7.2(c)) is predominantly 2/rev and negative, thus being responsible for an overall reduction of the angle of attack of the different blade sections.

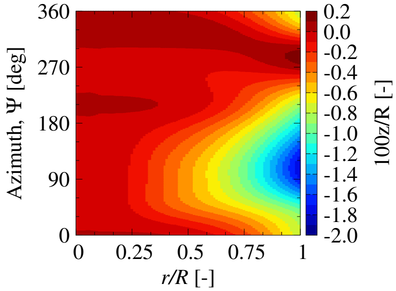

(a) *Flap deflection (positive upwards)*

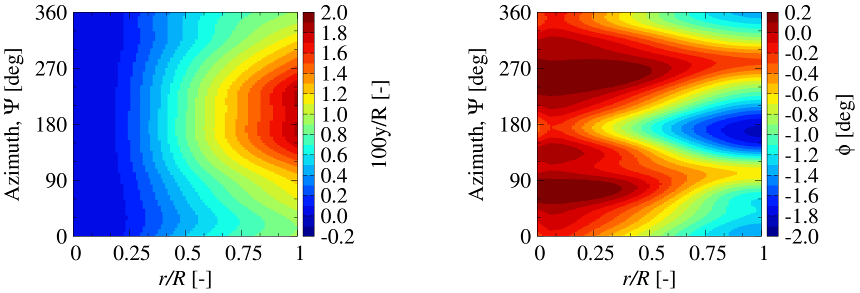

(b) *Lead-lag deflection (positive backwards)* (c) *Torsion deflection (positive pitch-up)*

Figure 7.2: Analytical reconstruction of the HART-II baseline blade deflection data along the radial and azimuthal coordinates [216].

In this work, the aerodynamic effects associated to the blade elastic deformations are modeled by prescribing a combination of a transpiration velocity boundary condition applied on the surface of the blade, for the flap displacement, and a semi-empirical fluid body-force field imposed within a fluid region surrounding the blade, for the torsion deformation, as depicted in Fig. 7.3. Both the transpiration velocity and fluid body-force models are related to the kinematics of the blade associated to the elastic deformation as described in the following. Since the lead-lag deformation is not expected to affect the BVI phenomenon significantly, its modeling in terms of aerodynamic effect is neglected in the present study.

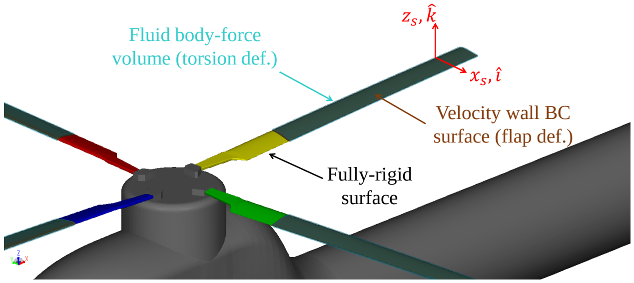

(a) *Surface and volume partitioning for the modeling of elastic deformation aerodynamic effects*

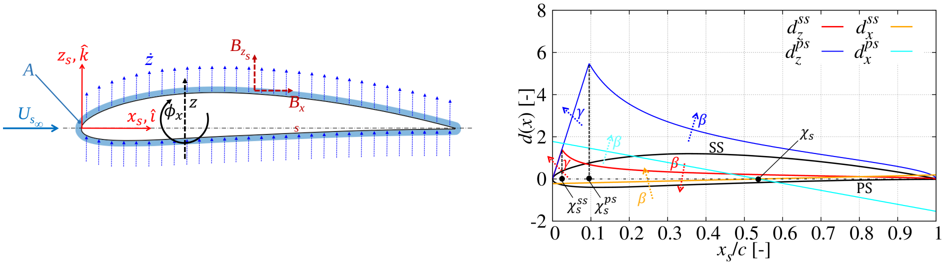

(b) *2D sketch of transpiration velocity and body-force*

(c) *Body-force chordwise distributions*

Figure 7.3: Description of the blade elastic effects modeling.

UNSTEADY FLAPPING EFFECTS AERODYNAMIC MODELING

The experimental unsteady blade flap deformation (averaged over the four blades) effects on the blade unsteady loading are modeled by prescribing a velocity wall boundary condition (i.e. transpiration velocity) equal to the time-derivative of the flap displacement (Eq. (7.1)):

$$\dot{z}(r,\Psi) = \sum_{i=1}^{3} \dot{q}_{z_i}(\Psi)\phi_{z_i}(r), \tag{7.10}$$

along the direction normal to the blade chord for $r/R > 0.35$ (see Fig. 7.3(b)). This approach follows from the idea that a small-amplitude plunge motion of the blade around its mean position can be modeled by applying a velocity wall boundary condition equal to the flap displacement that has an equivalent dynamic effect on the blade in terms of associated aerodynamic loading. Since Eq. (7.10) is applied through a built-in feature of the LBM code used in this work, namely the velocity wall boundary condition, its validation is not explicitly shown. Such a boundary condition is equivalent, for plunging/flapping motions, to the transpiration velocity concept traditionally used in CFD aeroelastic simulations through undeformed computational grids [217–219] or in boundary integral formulations derived under the assumption of rigid surfaces to include the effects of wall vibrations [220].

UNSTEADY TORSION EFFECTS AERODYNAMIC MODELING

The aerodynamic effects associated to the experimental unsteady torsion deformation (averaged over the four blades) are modeled by applying semi-empirical fluid body-forces within a volume surrounding the blade (for $r/R > 0.35$), which is generated as offset the blade surface with a thickness of 3 local voxels (i.e. mesh cells). These semi-empirical fluid body-force fields are described in terms of the blade torsion kinematics and, in a section coordinate system with origin on the leading-edge, x-axis (x_s) aligned with the chord and z-axis (z_s) normal to it (as depicted in Figs. 7.3(a) and 7.3(b)), read as:

$$\mathbf{B}(x_s, r, \Psi) = \underbrace{-\frac{d_{x_s}(x_s)\, b_{x_s}(r,\Psi)|_{\zeta_3\zeta_4}}{\rho A}}_{B_{x_s}} \hat{\mathbf{i}} \underbrace{-\frac{d_{z_s}(x_s)\, b_{z_s}(r,\Psi)|_{\zeta_1\zeta_2}}{\rho A}}_{B_{z_s}} \hat{\mathbf{k}}, \tag{7.11}$$

In Eq. 7.11, $\hat{\mathbf{i}}$ and $\hat{\mathbf{k}}$ are the chord-wise and chord-normal unit vectors, ρ is the fluid density, A is the cross-sectional area of fluid body-force application volume, d_{x_s} and d_{z_s} are the chordwise distributions of the body-forces along the x_s and z_s axes, namely:

$$d_{x_s}(x_s) = \begin{cases} d^{ss}_{x_s}(x_s) & = -(1-\beta)(-x_s/\chi_s + 1), \quad \text{on suction side} \\ d^{ps}_{x_s}(x_s) & = \ \ (1+\beta)(-x_s/\chi_s + 1), \quad \text{on pressure side} \end{cases} \tag{7.12}$$

and

$$d_{z_s}(x_s) = \begin{cases} d^{ss}_{z_s}(x_s), & \text{on suction side} \\ d^{ps}_{z_s}(x_s), & \text{on pressure side,} \end{cases} \tag{7.13}$$

with

$$d^{ss}_{z_s}(x_s) = \begin{cases} \gamma x_s, & \text{if } x_s < \chi^{ss}_s \\ (1-\beta)\sqrt{\frac{1-x_s}{x_s}}, & \text{if } x_s \geq \chi^{ss}_s \end{cases} \tag{7.14}$$

$$d^{ps}_{z_s}(x_s) = \begin{cases} \gamma x_s, & \text{if } x_s < \chi^{ps}_s \\ (1+\beta)\sqrt{\frac{1-x_s}{x_s}}, & \text{if } x_s \geq \chi^{ps}_s. \end{cases} \tag{7.15}$$

The minus sign in Eqs. Eq. (7.11) represents the action exerted by the fluid on the body, which is equal and opposite to that applied by the body on the fluid. Moreover, b_{x_s} and

b_{z_s} are the magnitude of the fluid body-force components (per unit span) along the x_s and z_s axes, respectively:

$$b_{x_s}(r,\Psi)|_{\zeta_3\zeta_4} = \rho\pi b^2\left(\frac{b}{2}\ddot{\tilde{\phi}}_x(r,\Psi)|_{\zeta_3\zeta_4} + U_{s_\infty}\dot{\tilde{\phi}}_x(r,\Psi)|_{\zeta_3\zeta_4}\right) \tag{7.16}$$

$$b_{z_s}(r,\Psi)|_{\zeta_1\zeta_2} = \rho\pi b^2\left(\frac{b}{2}\ddot{\tilde{\phi}}_x(r,\Psi)|_{\zeta_1\zeta_2} + U_{s_\infty}\dot{\tilde{\phi}}_x(r,\Psi)|_{\zeta_1\zeta_2}\right), \tag{7.17}$$

with $b = c/2$ and U_{s_∞} being the local airfoil semi-chord and free-stream velocity. In Eqs. (7.16) and (7.17), $\ddot{\tilde{\phi}}_x$ and $\dot{\tilde{\phi}}_x$ are the torsional acceleration and velocity, whose generalized coordinates (second and first time derivatives of Eq. (7.9)) are amplitude-modulated and phase-shifted with respect to those of the corresponding the torsion deformation input, namely:

$$\ddot{\tilde{\phi}}_x(r,\Psi)|_{\zeta_3\zeta_4} = \sum_{i=1}^{2}\ddot{\tilde{q}}_{x_i}(\Psi)|_{\zeta_3\zeta_4}\phi_{x_i}(r), \qquad \ddot{\tilde{\phi}}_x(r,\Psi)|_{\zeta_1\zeta_2} = \sum_{i=1}^{2}\ddot{\tilde{q}}_{x_i}(\Psi)|_{\zeta_1\zeta_2}\phi_{x_i}(r) \tag{7.18}$$

$$\dot{\tilde{\phi}}_x(r,\Psi)|_{\zeta_3\zeta_4} = \sum_{i=1}^{2}\dot{\tilde{q}}_{x_i}(\Psi)|_{\zeta_3\zeta_4}\phi_{x_i}(r), \qquad \dot{\tilde{\phi}}_x(r,\Psi)|_{\zeta_1\zeta_2} = \sum_{i=1}^{2}\dot{\tilde{q}}_{x_i}(\Psi)|_{\zeta_1\zeta_2}\phi_{x_i}(r), \tag{7.19}$$

with

$$\dot{\tilde{q}}_{x_i}(\Psi)|_{\zeta_3\zeta_4} = \sum_{k=1}^{6}[-a_{x_{ik}}\sin(k\Psi - 2\pi\zeta_4) + b_{x_{ik}}\cos(k\Psi - 2\pi\zeta_4)]k\Omega\zeta_3 \tag{7.20}$$

$$\dot{\tilde{q}}_{x_i}(\Psi)|_{\zeta_1\zeta_2} = \sum_{k=1}^{6}[-a_{x_{ik}}\sin(k\Psi - 2\pi\zeta_2) + b_{x_{ik}}\cos(k\Psi - 2\pi\zeta_2)]k\Omega\zeta_1 \tag{7.21}$$

$$\ddot{\tilde{q}}_{x_i}(\Psi)|_{\zeta_3\zeta_4} = \sum_{k=1}^{6}[-a_{x_{ik}}\cos(k\Psi - 2\pi\zeta_4) - b_{x_{ik}}\sin(k\Psi - 2\pi\zeta_4)](k\Omega)^2\zeta_3 \tag{7.22}$$

$$\ddot{\tilde{q}}_{x_i}(\Psi)|_{\zeta_1\zeta_2} = \sum_{k=1}^{6}[-a_{x_{ik}}\cos(k\Psi - 2\pi\zeta_2) - b_{x_{ik}}\sin(k\Psi - 2\pi\zeta_2)](k\Omega)^2\zeta_1. \tag{7.23}$$

According to Theodorsen's 2D unsteady aerodynamic theory [221], the forces being produced by the airfoil in an unsteady motion can be split into a *non-circulatory* contribution, related to the unsteady airfoil motion in absence of circulation, and a *circulatory* term, which is associated to the effect associated to *shed* vorticity in the airfoil wake[6]. The first contribution - which accounts for the effect associated to additional pressure forces that are needed to accelerate the fluid in the surrounding of an airfoil undergoing a non-stationary motion (i.e. the so-called *added mass* effect) - is that accounted by the proposed semi-empirical body-force model. Note that Eqs. (7.16) and (7.17) recall the non-circulatory lift contribution of the Theodorsen's theory, except for the plunge acceleration[7] and assuming the flapping displacement measured at the airfoil quarter-chord

---

[6] The vorticity of a three-dimensional blade/wing can be split into *shed* and *trailed* contributions. The former is emitted parallel to the trailing-edge and related to the motion of the body, while the latter is released perpendicularity to the trailing-edge in the direction of the relative wind and associated to the spanwise lift distribution.

[7] The aerodynamic effect associated to the flapping deflection (plunge in a 2D perspective) is already accounted in the computational setup by Eq. (7.10). Hence, the plunge acceleration is not included in Eqs. (7.16) and (7.16).

point. It should be pointed out that the circulatory part is not included in the fluid body-force modeling, since its effect is accounted by the CFD numerical solution through the wake blade shed vorticity induction, once the effect associated to the non-circulatory contribution has been modeled in the computational setup.

The fluid-body force normal to the chord (Eq. (7.17)) is distributed on the local airfoil chord similarly to the pressure coefficient distribution of a two-dimensional potential flow ($(1 \pm \beta)\sqrt{(1-x_s)/x_s}$), with a linear correction at the leading-edge (γx_s) to account for viscous effects (Eqs. (7.14)-(7.15)). The body-force component in the chord-wise direction (Eq. (7.16)), which is introduced to improve the correlation between the lift, drag and pitching moment generated by a real pitching airfoil and those produced by a steady airfoil subjected to the body force distribution, is distributed linearly along the local airfoil chord (Eqs. (7.12)). The parameter β, which appears with an opposite sign between suction and pressure side in Eqs. (7.12), (7.14) and (7.15), accounts for asymmetries of the pressure field between the two sides of the airfoil for non-symmetric profiles, and tends to zero for symmetric ones.

The parameters γ, β and χ_s in Eqs. (7.12)-(7.15), as well as the amplitude-modulating (ζ_1 and ζ_3) and phase-shifting parameters (ζ_2 and ζ_4) in Eqs. (7.20)-(7.23), depend on the local section reduced frequency $\hat{k} = k\Omega b/U_{s_\infty}$. These are tuning parameters required to adjust the magnitude, phase and chord-wise spatial distribution of the fluid body-forces in Eq. (7.11) in such a way that the lift, drag and pitching moment generated by a steady airfoil excited with fluid body-forces are close to those produced by the same blade section undergoing a physical unsteady torsional motion (i.e. a pitching motion from a 2D perspective). The functional dependency of the above mentioned parameters on the reduced frequency is determined by curve fitting of their optimal values obtained at different $\hat{k}$ by minimizing the error between the lift, drag and pitching moment generated by a real pitching airfoil and those produced by a steady airfoil subjected to the body-force distribution (Eq. (7.11)) as described in Appendix D. It should be pointed out that the above mentioned tuning process is required by the fact that the fluid body-force model emulates the effect associated to a non-circulatory surface force distribution through a volumetric fluid force distribution, prescribed in a finite volume surrounding the blade of arbitrary thickness of 3 local voxels in the surface normal direction.

7.4. NUMERICAL SETUP VALIDATION

As a sanity check of the employed computational setup and mesh, a preliminary grid convergence study is conducted without any modeling of the aerodynamic effects associated to the blade elastic deformation. Three resolution levels are considered, hereinafter referred to as *coarse*, *medium* and *fine*, corresponding to N=42, 60 and 85 voxels per blade chord ($\sqrt{2}$ refinement ratio between each grid) in the second finest VR, respectively. The whole computational mesh is refined accordingly using the same VR scheme for all simulations. A summary of the grid size and computational cost for the three meshes is reported in Tab. 7.2.

Simulations are performed using a 1000 cores cluster with Intel Xeon CPU E5-2690 2.90 GHz and require, for the finest case, about 2.5 hours per rotor revolution. For all the mesh resolutions, the main rotor is trimmed to the experimental thrust, rolling and pitching moments as described in Appendix C.

Res. level	N	# Voxels	# Surfels	CPUh/rev
Coarse	42	43.3	3.1	434
Medium	60	86.2	4.0	914
Fine	85	199.0	5.4	2472

Table 7.2: Grid size in million of elements and computational cost.

7.4.1. TRIM SETTINGS

Table 7.3 shows the comparison between the numerical collective and cyclic pitch commands for the three different mesh resolutions - obtained through the trimming procedure (outlined in Appendix C) - and the experimental ones. The lateral (θ_c) and longitudinal (θ_s) cyclics do not considerably change with the three different grids, while a relatively larger sensitivity to the mesh resolution is shown by the collective command (θ_0). However, a convergence trend for θ_0 can be identified. The worsening of the agreement between experimental and numerical data as the resolution increases, especially for what concerns the collective angle, is a consequence of considering a fully rigid rotor in the resolution study (i.e. without the inclusion of any effect associated to the blade elastic deformation). In the numerical simulations, the rotor blades experience a higher incidence during the rotation compared to the experimental case. As shown in Fig. 7.2(c), the outer part of the blade, which is that generating the largest amount of the total thrust, undergoes a negative (pitch down) torsion during the experiment for large part of the revolution. As a result, the local angle of attack experienced by the different blade sections in the simulations is higher than the experimental one for the same collective angle, thus requiring a lower θ_0 to generate the same mean rotor thrust. Moreover, as the mesh resolution increases, the pressure suction effect around the blade leading-edge is also increased, implying that the finest grid is able to generate a certain thrust with a lower θ_0 compared to the coarser meshes.

Case	θ_0 [deg]	θ_c [deg]	θ_s [deg]
Exp.	3.80	1.92	−1.34
Coarse	2.99	2.27	−1.88
Medium	2.75	2.30	−1.88
Fine	2.70	2.32	−1.89

Table 7.3: Trim settings variation with the mesh resolution. Experimental data from Ref. [222].

7.4.2. INSTANTANEOUS VORTICAL STRUCTURES

Figures 7.4(a) to 7.4(c) show instantaneous snapshots of the blade tip vortex system extracted according to the λ_2 criterion [153] for the three resolution levels. These images qualitatively illustrate that a higher mesh resolution results in a lower diffusion of the vortical structures, which preserve their coherent character over a larger number of wake spirals. This represents a crucial aspect for the accurate prediction of the BVI noise through CFD methods. Interestingly, a multitude of turbulent scales can be observed, in particular downstream the hub wake, and in the advancing side of the rotor, where vortices breakdown occurs because of the higher relative velocities and strain rates.

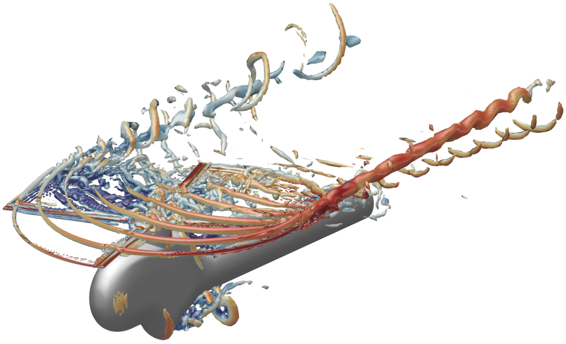

(a) *Coarse resolution*

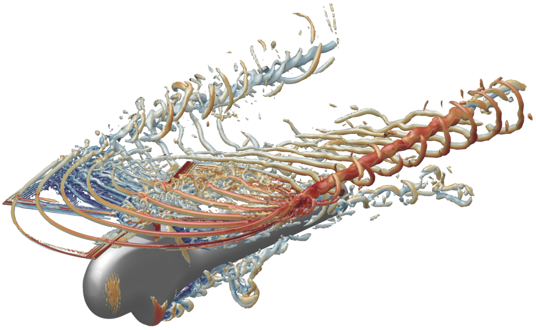

(b) *Medium resolution*

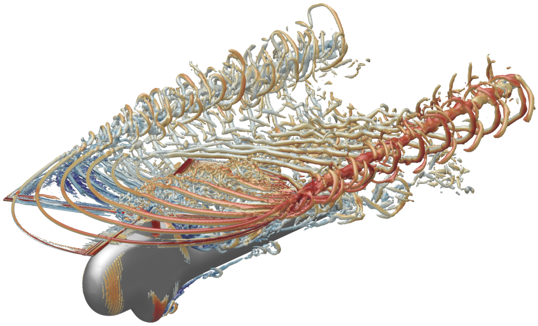

(c) *Fine resolution*

Figure 7.4: $\lambda_2 = -7500\ 1/s^2$ iso-surfaces of the instantaneous flow around the helicopter model colored by flow velocity magnitude; impact of the mesh resolution.

7.4.3. UNSTEADY LOADING

The sensitivity of the aerodynamic solution to the grid resolution is evaluated in terms of unsteady loading. For each resolution level, Fig. 7.5 shows the $c_n M^2$ coefficient time history (where c_n is the section normal force coefficient and M is the flow local Mach number) at the span-wise section located at $r/R = 0.87$. The $c_n M^2$ coefficient is computed by using surface pressure probes depicted in green Fig. 7.1(c) and following the experimental procedure reported in Ref. [223]. The $c_n M^2$ exhibits a weak grid dependence, and a convergence trend can be observed between the medium and fine resolutions. The discrepancies taking place roughly between 120° and 240°, among the three investigated resolution levels, could be ascribable to the different resolved suction pressure peak at the blade leading-edge, as well as to the different up-wash velocity field induced by the front part of the helicopter fuselage as a result of the grid refinement. Concerning the regions where BVI phenomenon occurs, the large spurious loading fluctuations occurring between 60° and 90° in the azimuth tend to decrease (and converge) as the mesh resolution is increased. The physical fluctuations of the $c_n M^2$ for $0° < \Psi < 60°$ also tend to converge between the medium and fine resolutions. However, such fluctuations are predicted with a certain phase delay compared to the experimental data for each resolution level. Conversely, the fluctuations associated to the BVI in the retreating side (i.e. between 270° and 330° in the azimuth) do not appear to be considerably affected by the mesh resolution. Note that the discrepancies taking place for $120° < \Psi < 240°$ and in the azimuthal sectors where BVI occurs between numerical results and experimental data are primarily due to the lack of simulation of the blade tip displacement.

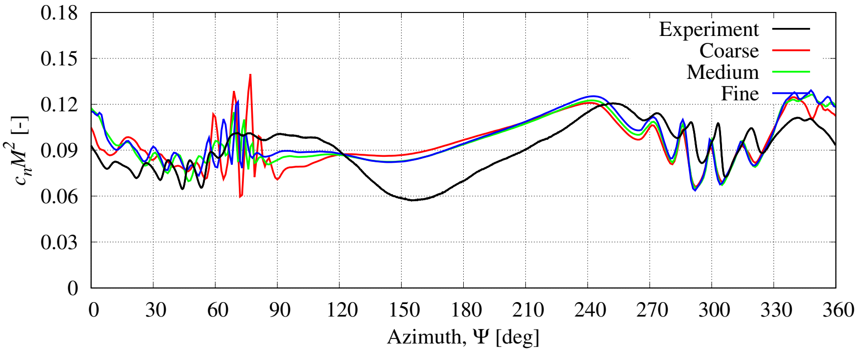

Figure 7.5: Time history of the $c_n M^2$ coefficient at $r/R = 0.87$; impact of the mesh resolution. Experimental data from Ref. [222].

7.4.4. NOISE RADIATION

The grid independence analysis is concluded by examining the sensitivity of the noise radiation to the mesh refinement. To this purpose, Fig. 7.6 shows the comparison between the experimental and numerical noise footprints evaluated on a carpet of microphones located 2.2 m below the rotor hub (shown in Fig. 7.1(c)). The noise contour maps are evaluated by integration of the FW-H equation on a porous surface encompassing the whole helicopter model (Fig. 7.1(c)). In order to highlight the BVI noise contribution, contour levels of the Overall Sound Pressure Level (OASPL) in the frequency range between the 6th and the 40th Blade-Passing Frequency (BPF) are plotted. The straight arrow indicates the direction of the free-stream velocity, while the circular one the direction of the rotor rotation. Hence, $y > 0$ m denotes the blade advancing side, while $y < 0$ m the retreating one.

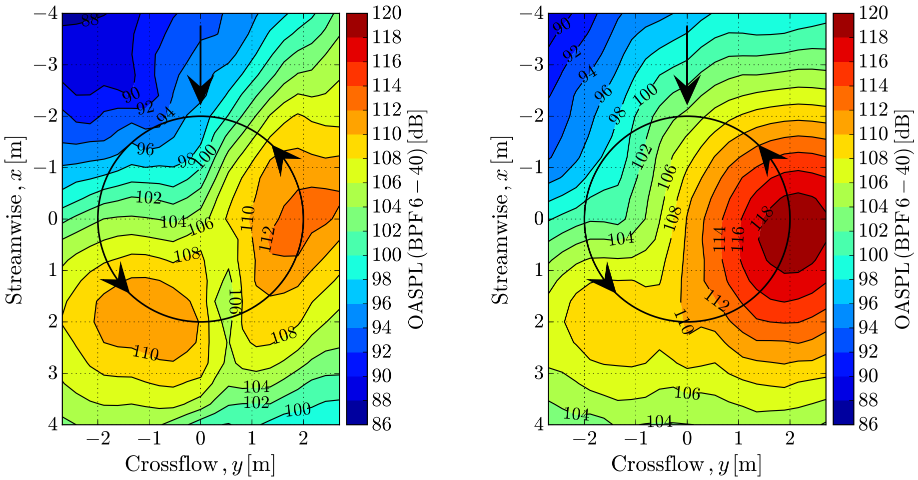

(a) *Experiment*

(b) *Coarse*

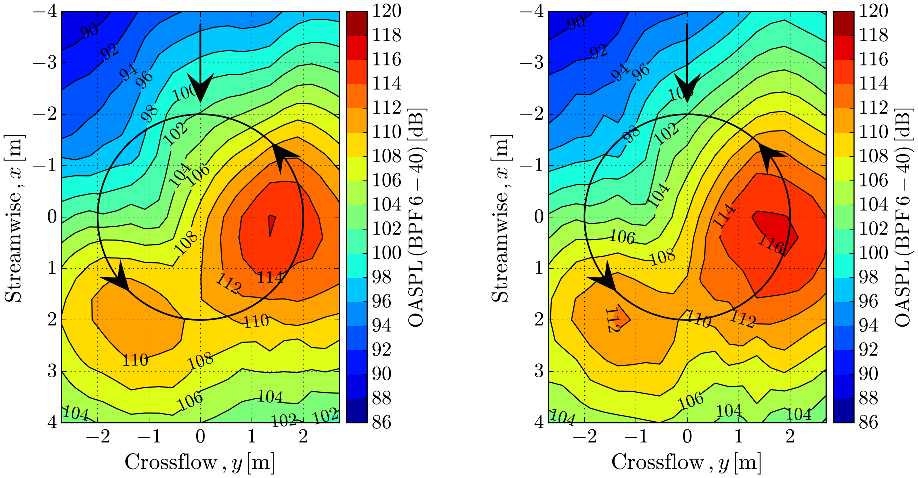

(c) *Medium*

(d) *Fine*

Figure 7.6: OASPL noise footprint contour levels (6th to 40th BPF); impact of the mesh resolution. Experimental data from Ref. [222].

The improvement of the aerodynamic solution associated with the computational grid refinement, which was particularly observed in the unsteady loading predictions (Fig. 7.5), reflects directly into the improvement of the far-noise radiation prediction. Indeed, the noise footprint for the coarse mesh shows an overestimation of 6 dB of the high-noise region in the advancing side and an underestimation of 2 dB of the noise levels in the retreating side. Conversely, the high-noise level lobe in the retreating side is accurately predicted for the two finest grids (besides a very small area of 2 dB OASPL over-prediction for the fine mesh), while the spot in the advancing side is over-predicted by 4 dB. The slightly higher far-field noise levels observed for the finest mesh compared to the medium one can be attributed to the slightly different occurrence of the blade-vortex interactions between the two cases (Fig. 7.5), as well as to the slightly lower numerical dissipation of the acoustic waves taking place for the finest grid.

In view of the above, it is possible to state that the fine mesh resolution provides a satisfactory levels of accuracy and grid convergence for the prediction of BVI-related phenomena. Therefore, it is used in the rest of this chapter to illustrate the effects on the numerical results of the modeling of the aerodynamic effects associated to the blade deformations.

7.5. ANALYSIS OF THE BLADE DEFORMATION EFFECTS AERODYNAMIC MODELING

This section describes the impact of different modeling assumptions of the aerodynamic effects associated to the blade deformations on the trim settings, unsteady airloads, vertical tip-vortex positions and far-field noise. To this aim, three different cases are considered:

- rigid rotor with underformed blade shape (*rigid* case);
- rigid rotor with blade shape deformed according to the experimental mean flap and torsion deformations (*semi-rigid* case);
- rigid rotor with blade shape deformed according to the experimental mean flap and torsion deformations, and unsteady aerodynamic effects of the blade deformation modeled through transpiration velocity and fluid body-forces as described in Sec. 7.3 (*elastic* case).

For all the cases, the main rotor is trimmed to the experimental thrust, rolling and pitching moments as described in Appendix C. It is worth to remark that, for all the three different cases mentioned above, only the rigid body kinematics of the blade is simulated. As mentioned in Sec. 7.3, this is imposed by a main limitation of the employed LBM code, which can reproduce rigid-body roto-translation motions, but not time-dependent deformations of the geometry. For the *rigid* case, the rotor moves according to the undeformed blade kinematics, whereas for the *semi-rigid* and *elastic* cases, the kinematics of the blade is that of the steady deformed blade. Hence, for the *elastic* case, the unsteady component of the blade deformation is not really simulated by the blade motion, but its aerodynamic effect is included in the computational setup through a combination of transpiration velocity and fluid body-forces. The three different configurations analyzed in this section are summarized in Fig. 7.7

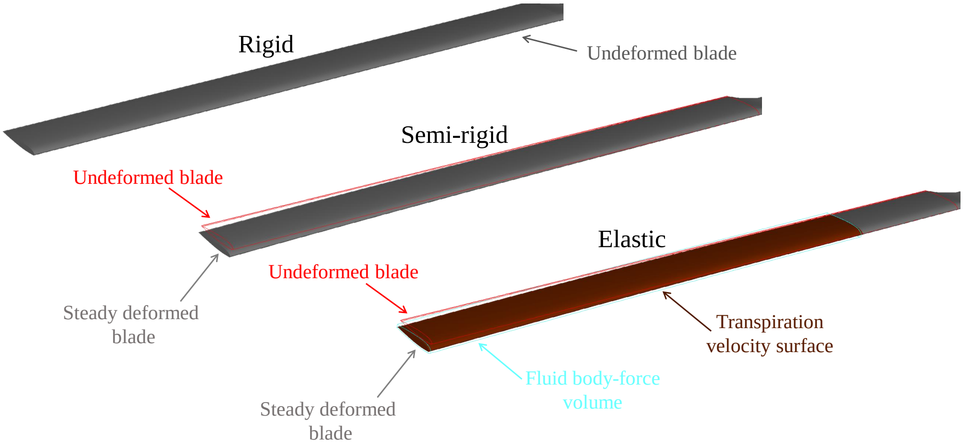

Figure 7.7: Summary of the three different configurations for the analysis of the blade deformation effects aerodynamic modeling.

7.5.1. TRIM SETTINGS

Table 7.4 shows the comparison between the experimental collective (θ_0), lateral (θ_c) and longitudinal (θ_s) cyclics, and those determined by applying the trim procedure to the *rigid*, *semi-rigid* and *elastic* cases, respectively. The inclusion of the steady deformation in the numerical simulation (*semi-rigid* case) leads to an improvement of the trim settings prediction compared to the *rigid* case, with the largest improvement observed for the collective angle. The steady deformed blade is indeed characterized by a negative torsion spanwise distribution (Fig. 7.2(c) and Fig. 7.7), which results in a reduction of the incidence experienced by the blade and the need for a higher collective angle to generate a given level of thrust, compared to the undeformed configuration (*rigid* case). The inclusion of unsteady aerodynamic effects associated to the flap and torsion deformations through the transpiration velocity and fluid body-forces yields to an even better prediction of the collective angle, as well as to a substantial improvement of the lateral and longitudinal cyclics.

Case	θ_0 [deg]	θ_c [deg]	θ_s [deg]
Exp.	3.80	1.92	−1.34
Rigid	2.70	2.32	−1.89
Semi-rigid	3.31	2.24	−1.78
Elastic	3.40	1.87	−1.68

Table 7.4: Trim settings variation with the modeling of the blade deformation aerodynamic effects. Experimental data from Ref. [222].

7.5.2. UNSTEADY LOADING

Figure 7.8(a) shows the impact of the modeling of the blade elastic deformation aerodynamic effects, on the $c_n M^2$ coefficient for the blade section at $r/R = 0.87$.

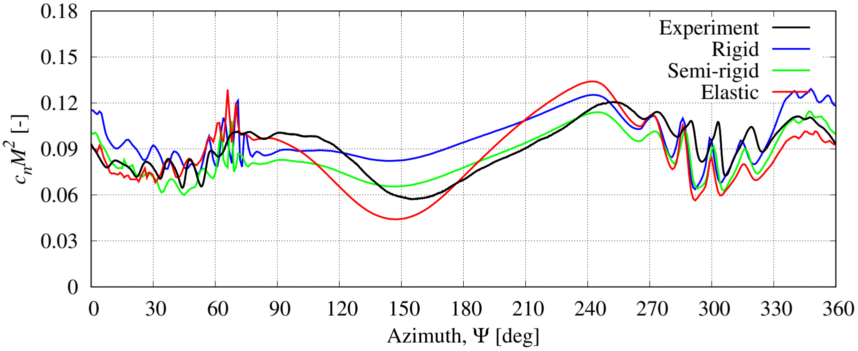

(a) *Total* $c_n M^2$

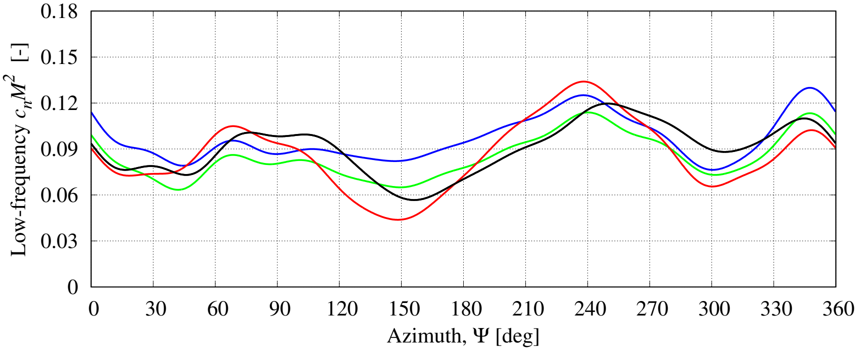

(b) *Low-frequency* $c_n M^2$ *content (up to* 10/*rev)*

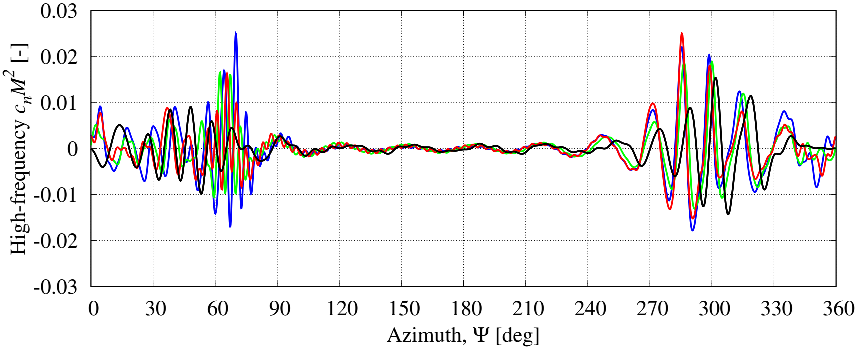

(c) *High-frequency* $c_n M^2$ *content (above* 10/*rev)*

Figure 7.8: Time histories of the total, low and high-frequency $c_n M^2$ coefficient at $r/R = 0.87$; impact of the modeling of the blade deformation aerodynamic effects. Experimental data from Ref. [222].

The total $c_n M^2$ coefficient is further decomposed into low- and high-frequency contents in Fig. 7.8(b) and Fig. 7.8(c) to better discern between aspects related to the blade kinematics and to the blade-vortex interaction, respectively. Indeed, the low-frequency $c_n M^2$ is mainly influenced by the rigid and elastic motion of the blade, and thus gives an indication on the goodness of the modeling of the aerodynamic effects induced by the blade elastic deformation; whereas the high-frequency $c_n M^2$ is mostly affected by BVI and hence can be used to examine the adequacy of three computational setups to predict BVI-related phenomena.

The inclusion of the steady deformation into the numerical setup (*semi-rigid* case) results in a lower normal force coefficient prediction at 87% of the span compared to the undeformed blade configuration, especially for azimuthal positions outside the regions of BVI occurrence ($90° < \Psi < 270°$). Moreover, the $c_n M^2$ fluctuations associated to BVI are better captured in the advancing side, in particular for what concerns the spurious fluctuations (for Ψ between 60° and 75°), whose magnitude is reduced for the *semi-rigid* configuration. Regarding the retreating side, the $c_n M^2$ fluctuations are predicted similarly to the undeformed case, with only minor variations in terms of phase and amplitude between the two cases. When also unsteady aerodynamic effects of the blade deformations are modeled through the transpiration velocity boundary condition and fluid body-forces (*elastic* case), a further improvement of the sectional loading along most of the rotor revolution can be observed: on the advancing side for locations where strong blade-vortex interactions occur (i.e. $0° < \Psi < 60°$), and for the azimuthal sector between 90° and 240°, with the low-frequency $c_n M^2$ variation (primarily due to unsteady elastic torsion, Fig. 7.2(c)) better reproduced by the *elastic* case. However, such a low-frequency variation, which was only slightly captured in the *rigid* and *semi-rigid* simulations, is still not perfectly reproduced by the *elastic* one, with discrepancies both in terms of phase (advanced) and amplitude (over-predicted) with respect to the experimental data. This might be related to 3D flow effects in the helicopter rotor simulation, as well as to Mach, Reynolds, and deformation amplitude effects, which were neglected in the 2D airfoil tuning process of the parameters of the semi-empirical fluid body-force model. For the *elastic* case, a further reduction of the spurious $c_n M^2$ fluctuations (for $60° < \Psi < 75°$) is also observed.

The above mentioned aspects are further quantitatively confirmed in terms of Pearson Correlation Coefficient (PCC) of the $c_n M^2$, representing a measure of the linear correlation between two sets of data (experimental and numerical data in the present case), which turns out to be 0.58 (moderate correlation) for the rigid case, and 0.77 (high correlation) for both the *semi-rigid* and *elastic* cases. However, it is worth mentioning once again that the main cause for the discrepancies between the numerical and experimental results is the lack of the simulation of the complete blade elastic deformation for the *rigid* case (mean and unsteady components) and of its unsteady part for the *semi-rigid* and *elastic* cases. This aspect will also concern the tip-vortex trace prediction shown in the following subsection and, in turn, the noise footprint results discussed in Sec. 7.5.4.

7.5.3. TIP-VORTEX TRACE

Figures 7.9(a) and 7.9(b) show the tip-vortices position (in dots), in the hub coordinate system, on two longitudinal planes placed in the advancing side ($y_h/R = 0.7$) and in the retreating side ($y_h/R = -0.7$), respectively. The tip-vortices location is determined by extracting the center of the vortex-core from vorticity magnitude contour plots. Following the vortex trajectory method applied to HART-II PIV data (Ref. [224]), advancing side traces for $x_h/R > 0$ are identified when one of the rotor blades is at $\Psi = 20°$, whereas those for $x_h/R < 0$ correspond to $\Psi = 70°$. Conversely, retreating side traces for $x_h/R > 0$ and $x_h/R < 0$ are extracted at $\Psi = 70°$ and $\Psi = 20°$, respectively. The trace of the blade position on the planes of examination is also reported for the experiment (in black), *rigid* case (in blue), and *semi-rigid* and *elastic* cases (in cyan) to provide a qualitative indication of the blade-vortex miss distance.

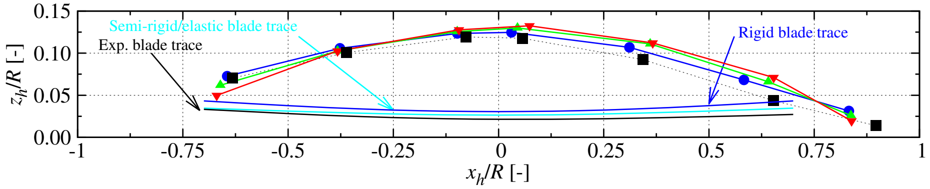

(a) *advancing side plane at* $y_h/R = 0.7$

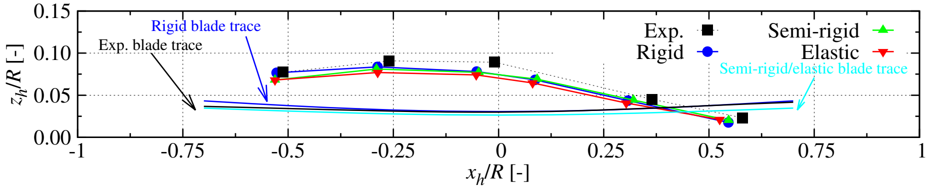

(b) *retreating side plane at* $y_h/R = -0.7$

Figure 7.9: Tip-vortex traces on two longitudinal planes at $y_h/R = 0.7$ and $y_h/R = -0.7$; impact of the modeling of the blade deformation aerodynamic effects. Experimental data from Ref. [222].

In the advancing side, the inclusion of the aerodynamic effects associated to the blade elastic deformations (*semi-rigid* and *elastic* cases) leads to a higher wake position prediction with respect to the *rigid* case for $x_h/R > 0$ and a slightly lower tip-vortex position for $x_h/R < -0.5$. This phenomenon is primarily due to the inclusion of the steady deformation in the numerical setup, which resulted in a modification of the tip-vortex circulation, point of release and convection. Moreover, it is further emphasized by the modeling of unsteady aerodynamic effects (*elastic* case) that are responsible for the modification of the unsteady blade loading experienced by the blade, which in turn affects the tip-vortex circulation and results in a slightly altered tip-vortex trajectory compared to the *semi-rigid* case. As previously mentioned, the accurate prediction of the blade-vortex miss distance has a strong influence on the pressure fluctuations induced by the tip-vortices on the blade and, thus, represents a crucial aspect in BVI noise prediction. In absolute terms, a partial worsening of the wake shape prediction in the advancing side for the *semi-rigid* and *elastic* cases can be observed. However, this does not result in a worsening of the prediction of the unsteady loading fluctuations in the advancing side for the *semi-rigid* and *elastic* cases (as shown in Fig. 7.8(c)), since the blade-vortex miss distance is not significantly changed between the *rigid* and *semi-rigid*/*elastic* cases, considering the the actual blade trajectory trace is higher for the latter compared to the former.

Concerning the retreating side, the numerical results show tip-vortex traces slightly below the experimental ones, as well as a less pronounced scatter of the tip-vortex positions among the three computational setups. This explains why the blade loading fluctuation due to BVI do not significantly differ between the *rigid*, *semi-rigid* and *elastic* cases for $270° < \Psi < 330°$. By simple geometrical considerations, it can be inferred that the approximate azimuthal positions at which the tip-vortices (whose traces are shown in Figs. 7.9(a) and 7.9(b)) are released by the rotor blade are $\Psi = 135°$ and $\Psi = 225°$ for the advancing and retreating sides, respectively. Hence, observing that larger flap and torsion elastic deformations (Figs. 7.2(a) and 7.2(c)) occur when the blade is at $\Psi = 135°$ compared to $\Psi = 225°$, one can understand the reason why the largest discrepancies between experimental and numerical results, as well as among the *rigid*, *semi-rigid* and *elastic* cases, take place on the blade advancing side.

7.5.4. NOISE RADIATION

To conclude the analysis on the blade deformation effects, Fig. 7.10 illustrates the effects of the blade elastic deformation on the predicted BVI noise footprint (OASPL between 6th to 40th BPF) on a horizontal plane located 2.2 m below the rotor hub. Coherently with the unsteady loading results presented in Fig. 7.8(a), the inclusion of the aerodynamic effects associated to the elastic deformation improves the accuracy of BVI noise prediction, with correlation coefficients between experimental and numerical the OASPL footprint of 0.94, 0.95 and 0.97 for the *rigid*, *semi-rigid* and *elastic* cases, respectively. The elastic rotor setup is able to accurately capture the overall noise directivity, as well as the high-noise lobes related to BVI in the advancing and retreating sides in a very satisfactory way. However, it should be recalled that the accurate prediction of the noise levels on the blade advancing side is not fully driven by the reproduction of the exact same physics observed in the experiment. Indeed, it is the result of the combination of two phenomena occurring in the simulation, namely: (i) the presence of some spurious loading fluctuations for $60° < \Psi < 75°$, that do not take place in the experiment; and (ii) the partially under-predicted force fluctuations between 0° and 60°, which tend to balance out and lead to very similar noise levels compared to the experiment. Such phenomena are both primarily associated to the inaccurate prediction of the blade-vortex miss distance, due to the lack of the proper simulation of the blade tip displacement in the numerical setup. Regarding the *rigid* and *semi-rigid* blade configurations, the retreating side is still quite accurately predicted, with only a small potion of the high-noise spot showing an over-prediction of 2 dB of the OASPL compared the measurements. This is in line with the previous $c_n M^2$ and tip-vortex position results, which do not show significant differences between the different computational setup employed in this study. On the advancing side, the *semi-rigid* case shows an over-prediction of 2 dB compared to the experimental data, due to the presence of larger spurious BVI-induced fluctuations for $60° < \Psi < 75°$, while for the undeformed blade configuration (*rigid* case) an even larger over-estimation of the noise levels as much as 4 dB can be observed for the same cause.

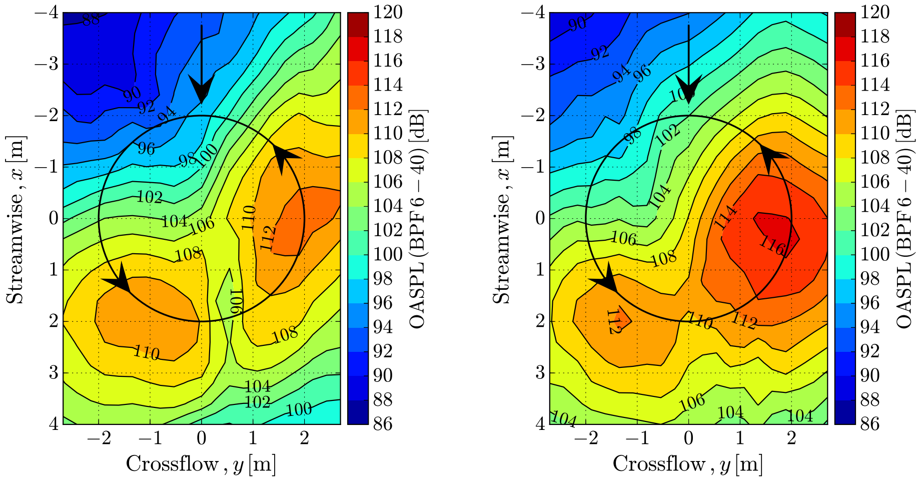

(a) *Experiment* (b) *Rigid*

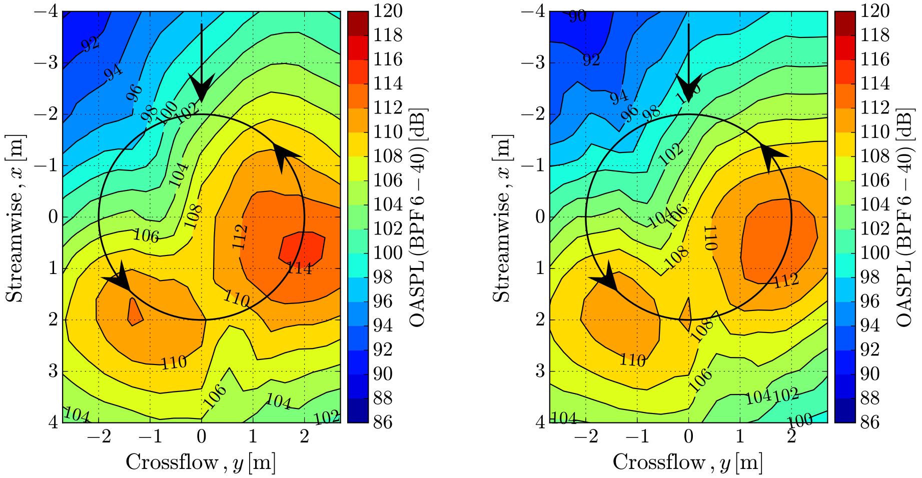

(c) *Semi-rigid* (d) *Elastic*

Figure 7.10: OASPL noise footprint contour levels (6th to 40th BPF); of the modeling of the blade deformation aerodynamic effects. Experimental data from Ref. [222].

7.6. CONCLUSIONS

In this chapter, the Lattice-Boltzmann/Very Large Eddy Simulation Method was used, for the first time to the author's knowledge, to predict the unsteady airloads, the rotor wake development and the noise radiation of helicopter rotors in BVI conditions. The considered benchmark was the baseline case of the HART-II experimental campaign. The numerical flow solution was obtained by solving the explicit, transient and compressible Lattice-Boltzmann equation implemented in the high-fidelity CFD/CAA solver SIMULIA PowerFLOW®. The acoustic far-field was computed by using the Ffowcs Williams & Hawkings' integral solution applied to a permeable surface encompassing the whole helicopter model.

First, a mesh resolution study was conducted considering trimmed *rigid* (undeformed) rotor blades, and it revealed an acceptable level of mesh convergence, with reasonably good results in terms of unsteady loading and noise footprint prediction obtained with a resolution of 85 voxels per blade chord in the second finest VR at a CPU cost of 2472 hours per rotor revolution (fine resolution case). Then, the impact of considering the steady deformed blade shape on the numerical results, as well as of the modeling of the aerodynamic effects associated to the unsteady blade flap and torsion deformations (through a combination of transpiration velocity and fluid body-force field) was analyzed. The modeling of the aerodynamic effects associated to the blade deformations led to a substantial improvement of trim settings, unsteady sectional airloads and BVI noise footprint predictions compared to the undeformed blade configuration.

The level of accuracy of the *rigid*, *semi-rigid* and *elastic* setups was overall higher than that obtained (at a quite lower computational cost) by comprehensive codes for the same benchmark as reported in Refs. [209, 210] - although BEM-based comprehensive approaches provided a level of accuracy similar to that of the LBM simulation at a lower computation cost [214] - and comparable to that obtained (at a similar computational cost) by CFD with prescribed blade elastic motion [225] and/or CFD/CSD coupled approaches [215]. However, it should be recalled that, in contrast with the above mentioned comprehensive codes and CFD/CSD methods, the current *elastic* and *semi-rigid* computations require blade elastic deformations as inputs in order to retrieve part of its aerodynamic effects, through the application of the transpiration velocity boundary condition/fluid body-force field, and/or the modification of the blade geometry into its steady deformed shape.

Although some intrinsic inaccuracies in the numerical results were observed, mainly due to the lack of a proper simulation of the rotor blade elastic deformations, the present study revealed the capability of the LBM to successfully simulate rotors in BVI conditions at engineering-level. The LBM may be therefore considered as an additional methodology for the prediction of rotorcraft BVI noise.

8

FAN BOUNDARY-LAYER INGESTION NOISE

Nothing has such power to broaden the mind
as the ability to investigate systematically
and truly all that comes under thy observation in life."

Marcus Aurelius

Chapter 7 presented the application and validation of the lattice-Boltzmann method to the prediction of tonal blade-vortex interaction noise for a main rotor/fuselage helicopter configuration. The present chapter is devoted to another source of rotor installation noise, namely fan boundary-layer ingestion noise, which can take place for eVTOLs characterized by distributed (electric) ducted fans, and blended wing body or tube-and-wing aircraft with semi-buried or rear-mounted turbofan engines. In particular, the aim of this chapter is to investigate the effects of the ingestion of the turbulent flow developing over an aircraft fuselage on the tonal and broadband noise emissions of a fan/OGV (Outlet Guide Vane) stage. The analysis is performed on a modified version of the Low-Noise NASA SDT fan-stage integrated into the ONERA NOVA fuselage. Installation effects due to the boundary-layer ingestion configuration are quantified by comparison with an isolated configuration of the modified Low-Noise SDT fan-stage at the same operating condition. It is found that the boundary-layer ingesting fan is characterized by strong azimuthal fan blade loading unsteadiness, less axisymmetric and coherent rotor wake tangential velocity variations and higher levels of in-plane velocity fluctuations compared to the isolated engine. This results in no distinct tonal components and higher broadband levels in the far-field noise spectra, as well as in an increment of the cumulative noise level up to 18 EPNdB.

Parts of this chapter have been published in the AESCTE journal (2020) [226].

8.1. INTRODUCTION

IN order to deal with the increasingly stringent aviation regulations for pollution and noise impact [25], the use of Ultra-High Bypass Ratio (UHBR) engines on next generation aircraft is receiving more attention due to their lower jet core flow velocity and noise emissions, and enhanced propulsive efficiency compared to low- and high-bypass turbofans. Such engines have a relatively larger fan diameter with consequent increase of the blade tip speed for constant cruise velocity. As a result of the jet noise reduction and increase of the blade size, fan noise becomes the primary source of noise for these configurations [36]. Moreover, their actual employment on future aircraft raises new integration challenges, requiring special designs to install such large and heavy engines minimizing their impact on aircraft performances.

In the last two decades, many researchers have put their efforts on developing novel aircraft configurations suited for UHBR engines integration [7, 227–229]. In this scenario, four different NOVA (Nextgen ONERA Versatile Aircraft) aircraft geometries have been designed by ONERA in last few years with a particular emphasis on engine integration: (i) a baseline architecture with wide lifting fuselage, under-wing engines, high wing aspect ratio and downward oriented winglets, (ii) a gull wing layout characterized by an increased dihedral angle in the wing inboard position to limit landing gears length, (iii) a podded configuration with engines mounted on the aft fuselage side, and (iv) a Boundary-Layer Ingestion (BLI) configuration with engines installed on the aft fuselage side and ingesting the boundary-layer convecting over the fuselage [7]. Starting from these studies, the present work, which takes place in the framework of the European Commission project ARTEM (Aircraft noise Reduction Technologies and related Environmental iMpact), focuses on this last configuration.

BLI propulsion systems aim at reducing the required propulsive power compared to conventional tube-and-wing configurations [7, 229–231]. Its theoretical propulsive benefit is based upon the possibility to reduce: (i) the overall aircraft mass and drag, due to the nacelle pylon removal and the lower wetted surface area; (ii) the power dissipation in the flow field, by reducing the exhaust jet wasted kinetic energy and filling-in the airframe wake velocity defect. Moreover, with BLI, the propulsion system is partially or completely shielded by the airframe, depending on the placement of the engine, thus yielding to a potential noise reduction due to acoustic shielding. However, many drawbacks should be addressed before quantifying the actual benefits associated to BLI, such as the inlet flow distortion on engine efficiency, operability, aeromechanics and aeroacoustics. The fuselage boundary-layer ingestion, as well as the possible presence of a s-duct inlet, lead to the partial loss of the fan inflow axial uniformity, thus causing a strong azimuthal variation of the fan blade loading with aerodynamic and aeroacoustic drawbacks. Therefore, this kind of engine integration deeply relies upon the possibility to alleviate the flow distortion and non-uniformity at the fan plane.

Although an extensive research has been conducted in order to investigate BLI propulsion systems in terms of performances and fuel efficiency [74, 230, 232–236], and inlet flow control analysis [237–239], the aeroacoustic assessment of BLI has not received much attention in the past and only few aeroacoustic studies are available in literature for such configurations.

Defoe *et al.* [240] have investigated the effects of BLI on the aeroacoustics of transonic fan rotors. They implemented a body-force formulation for the fan rotor description, extracted from a 3D Reynolds-Averaged Navier-Stokes (RANS) simulation, in an unsteady Euler calculation and evaluating the far-field noise via the Ffowcs Williams & Hawkings (FW-H) integral method using a permeable surface. They found out that the dominant mechanism for changes in far-field rotor shock noise, due to the boundary-layer ingestion at low free-stream Mach numbers, is the ingestion of stream-wise vorticity generated by the interaction of the upstream boundary-layer vorticity with the inlet lip.

A noise assessment at aircraft-level for the NASA D8 concept has been carried out by Clark *et al.* [76] by using the Aircraft NOise Prediction Program (ANOPP) comprehensive tool to predict the noise generated by each source component, with the BLI influence on fan noise empirically modeled based on experimental data. In that study, boundary-layer ingestion was predicted to have a detrimental impact on effective perceived noise levels in the order of 15 EPNdB.

Finally, Murray *et al.* [241] conducted aeroacoustic measurements for an unshrouded rotor partially immersed in a turbulent boundary-layer at low Mach number to investigate inflow distortion effects associated to airframe-integrated engines. They found out that, at low and moderate thrust conditions, the rotor produces broadband noise organized into haystacks generated by large eddies in the ingested turbulence being cut multiple times by neighboring rotor blades, contrarily to louder and more tonal acoustic signatures observed at high thrust conditions.

In view of the above, the existing research on fan BLI aeroacoustics is limited only to experimental/numerical studies at component level and to the analysis of BLI full-aircraft configuration by means of low-fidelity comprehensive codes. Since there are no detailed studies on the physics behind the noise generation for BLI embedded engines at full-aircraft level, the aim of this chapter is twofold: (i) to perform the first, to the author's knowledge, high-fidelity CFD/CAA simulation of a full-scale aircraft geometry comprehensive of a BLI fan/Outlet Guide Vane (OGV) stage; and (ii) to address BLI installation effects on fan noise for the NOVA BLI aircraft configuration by comparison between the same engine used in a conventional non-BLI and BLI layout. The analysis is carried out for an operating condition representative of a flyover with power cut-back to replicate one of the required conditions for noise certification [242].

In this chapter, SIMULIA PowerFLOW® time-explicit, compressible and transient solver based on the lattice-Boltzmann Method/Very Large Eddy Simulation (LBM/VLES) is used to simulate and analyze the flow and the acoustic near-field around the BLI fan-stage configuration. The aerodynamic noise generated by the fan and its interaction with the ingested turbulence, as well as the fan wake/OGV interaction is then estimated by using an acoustic analogy based on Farassat's formulation 1A of the FW-H equation applied on a permeable surface encompassing the engine and part of the fuselage. The same computational methodology has been successfully validated by Casalino *et al.* [243] and Gonzalez-Martino and Casalino [96] in the field on turbofan aeroacoustics. They predicted tonal and broadband noise of three fan/OGV configurations of the 22-in NASA Source Diagnostic Test (SDT) fan rig [244] with an accuracy in the order of the experimental uncertainty of 1 dB, at both subsonic and transonic tip-speed conditions.

The rest of the chapter is organized as follows. The test case and computational setup are described in Sec. 8.2. Numerical results are presented in Sec. 8.3, discussing boundary-layer ingestion installation effects in terms of velocity field, fan performances and far-field noise. Finally, the main conclusions of this work are summarized in Sec. 8.4.

8.2. TEST-CASES AND COMPUTATIONAL SETUP

8.2.1. GEOMETRIES AND OPERATING CONDITIONS

The geometry considered in this study is the NOVA lifting fuselage, wing and empennage (without engine and s-duct) - courtesy of ONERA - with a total length of 44 m and a semi-span of about 19 m. A modified version of the Low-Noise configuration of the NASA SDT, an existing scaled fan-stage configuration publicly available in the framework of the AIAA Fan Broadband Noise Prediction Workshop [244], was integrated into the fuselage to reproduce the NOVA BLI layout, as sketched in Fig. 8.1(a). In particular, the original Low-Noise SDT configuration, consisting of a 22-bladed fan and 26 stator swept vanes, was firstly scaled by a factor of 3.88 to match the NOVA fan radius ($R = 1.075$ m) and equipped with a redesigned nacelle, obtained by increasing the original inlet axial length in order to match the NOVA BLI engine intake-fan distance (2.35 m). A sketch of the modified Low-Noise SDT engine is depicted in Fig. 8.1(b). This redesigned engine geometry was then installed into the NOVA fuselage by considering a 40% buried intake, as in the original NOVA BLI layout, and tilt and toe angles of 1° and 2.5°, respectively. Finally, a s-shaped duct was designed to integrate the fan-stage into the NOVA fuselage geometry, as shown in Fig. 8.1(c). This s-duct configuration turned out to be the best one in terms of inlet flow separation among three other different s-duct geometries, all based on the above mentioned design parameters and characterized by having tangent surfaces to the fuselage and nacelle walls. Since the primary goal of this study is to address the BLI impact on fan noise for the NOVA BLI layout, two different configurations are investigated: (i) the isolated SDT fan/OGV stage with the modified nacelle (Fig. 8.1(b)) and (ii) the installed SDT fan/OGV stage into the original NOVA fuselage geometry (Fig. 8.1(c)).

The operating conditions considered in this study are representative of a take-off with power cut-back, which represents one of the required conditions for noise certification. The free-stream Mach number is $M_\infty = 0.25$ and the static pressure ($p_\infty = 97718$ Pa) and temperature ($T_\infty = 286.15$ K) are taken from the International Standard Atmosphere (ISA) at 1000 ft. Moreover, the aircraft angle of attack is $\alpha = 4°$, the pitch angle is $\varphi = 10°$ and the glide angle is $\gamma = 6°$ (note that the angle of attack is defined by the difference between the glide and pitch angles, i.e. $\alpha = \varphi - \gamma$). It should be pointed out that such angles, which define the engine incidence with respect to the free-stream together with the tilt and toe angles, are also considered for the isolated engine configuration. Finally, the fan angular velocity is $\Omega = 2603$ RPM, corresponding to the 80% of SDT fan nominal power and resulting into a tip Mach number and a Blade-Passing Frequency of $M_{tip} = 0.87$ and BPF= 954 Hz, respectively.

8.2.2. COMPUTATIONAL SETUP

Figure 8.2 depicts some details of the computational setup and grid adopted in this study. Identical setup and computational mesh, except for the presence of the fuselage geometry, are used for the isolated configuration. The rotor and the spinner are encom-

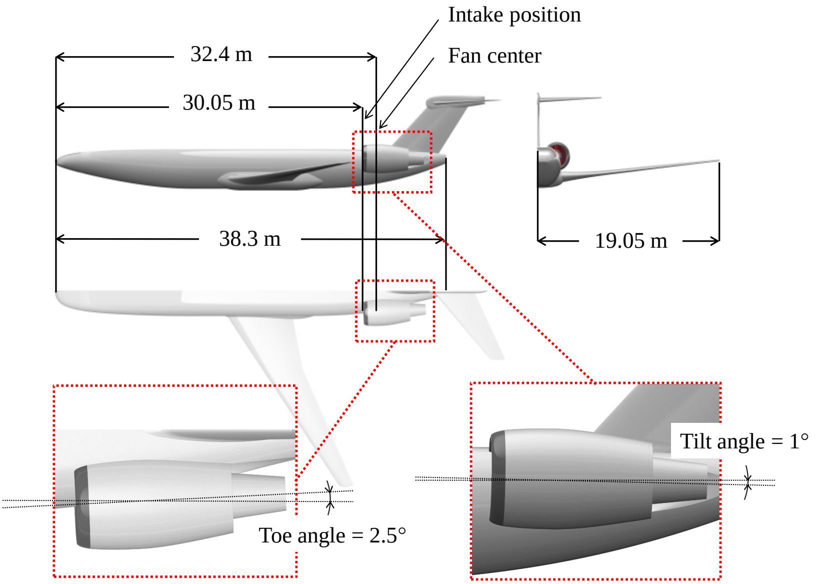

(a) *redesigned NOVA BLI aircraft configuration*

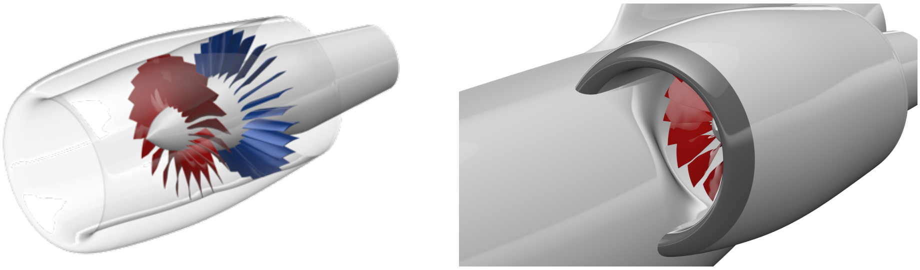

(b) *modified SDT fan-stage*

(c) *modified SDT fan-stage integration*

Figure 8.1: NOVA aircraft configuration equipped with the redesigned BLI engine nacelle.

passed by a volume of revolution that defines the LRF (Local Reference Frame), i.e. the rotating sliding mesh region used to reproduce the fan rotation. Since no primary jet is considered in this study, the center-body geometry is extended by employing an infinite solid cylinder downstream with slip boundary conditions to avoid flow recirculation behind it. For the BLI configuration, a zig-zag trip of 3.5 cm height, 5.8 cm wavelength and 6.4 cm amplitude was placed $3R$ upstream the engine inlet in order to trigger transition and develop a fully turbulent boundary-layer at the fan-stage location, while keeping the computational effort relatively low. The permeable FW-H integration surface (depicted in Fig. 8.2) used to compute the acoustic far-field consists of two regions: a spherical sector around the intake, and a conical surface in the exhaust region. The center part of the FW-H surface (cylinder) crosses through the solid walls of the nacelle: therefore, no flow data is extracted from there. The same applies for that portion of the FW-H surface passing through the aircraft fuselage for the BLI configuration. The downstream cap (end-cap) of the cone is not included, in order to avoid the spurious noise onset due to the hydrodynamic pressure fluctuations in the wake of the fan stage passing through it (see Sec. 3.3). However, the FW-H cone extends downstream enough to recover the bypass exhaust radiation for the directivity angles of interest (shown in Fig. 8.17).

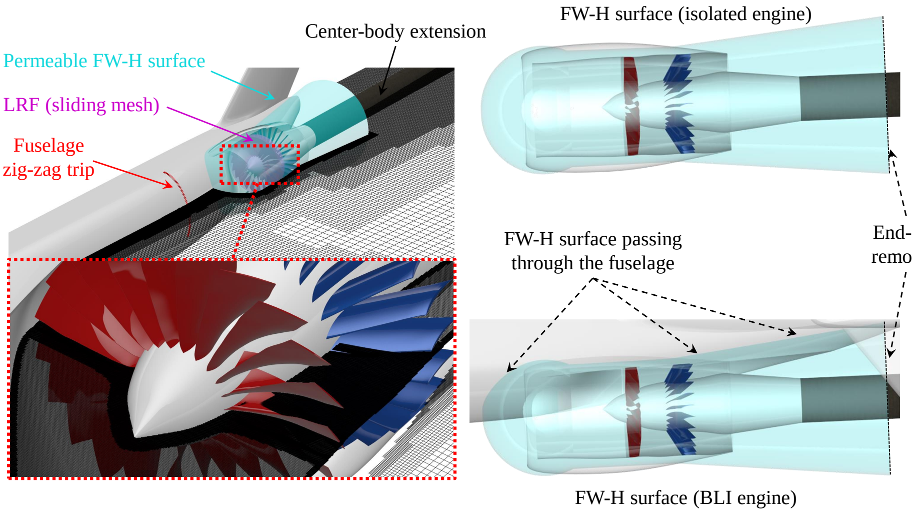

Figure 8.2: Details of the computational setup around the fan-stage: LRF, fuselage transition trip, center-body extension and FW-H surface.

A cubic simulation volume of edge length of 690R centered around the engine is used. Free-stream static pressure and velocity are prescribed on the outer boundary, and an acoustic sponge approach is used to damp the out-going acoustic waves and minimize the backward reflection from the outer boundary (Fig. 8.3). The acoustic sponge is defined by two concentric spheres of radius 40R and 150R, respectively, and centered around the engine geometry. Hence, the fluid kinematic viscosity is gradually increased starting from its real value within the inner sphere, up to an artificial value two orders of magnitude higher outside the outer one. A symmetry plane located at the fuselage centerline is used to reduce the computational cost.

A total of 16 Variable Resolution (VR) levels are employed to discretize the whole computational domain. The finest VR region covers the volume between the fan blade tip and the nacelle casing. The second finest VR level is used to discretize leading- and trailing-edges of both fan and OGV vanes. The third finest VR level is set as offset of the fan, the OGV and the nacelle bypass lip. The fourth finest VR level covers the whole bypass duct and the fuselage surface upstream of the intake (for the BLI case). The fifth finest VR level encloses the permeable surface used for FW-H computations. Finally, all the other VRs, characterized by fuselage and/or engine offsets and boxes, are used to model the remaining part of the computational domain up to its boundaries.

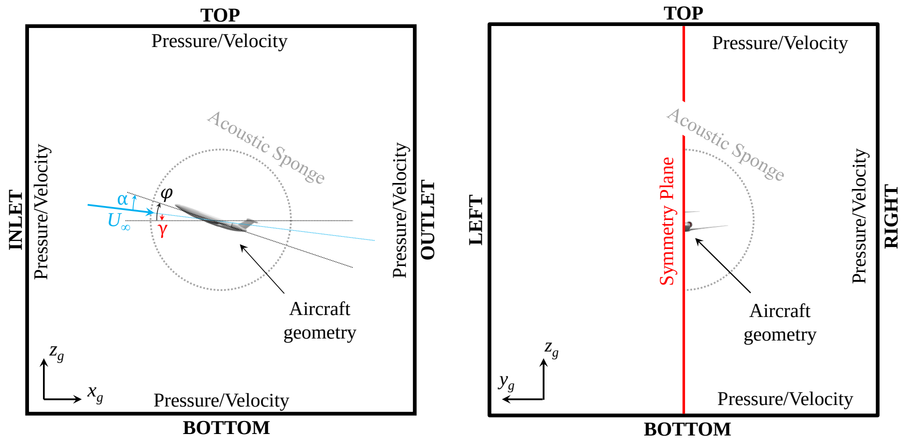

(a) *side view* (b) *front view*

Figure 8.3: Sketch of the computational domain (not drawn to scale): boundary conditions and acoustic sponge.

For the BLI configuration, a near-wall resolution which ensures a y^+ between 100 and 300 is prescribed on the fuselage surface in order to adequately capture the boundary-layer growth. Regarding the fan-stage region, the grid resolution employed in this study is based on the “fine” resolution successfully validated against the NASA SDT benchmark by Gonzalez-Martino and Casalino [96]. They demonstrated the capability of the solver to predict absolute broadband and tonal noise levels of the NASA SDT with an uncertainty of 1 dB, both at high-subsonic and transonic blade tip conditions. Such a resolution level results in a finest voxel size of 0.355 mm, roughly 6 voxels along the fan tip gap and 3.88 (i.e. the scaling factor) times coarser voxels for same VRs for the present computational setup. Due to this last aspect, the prediction of absolute broadband and tonal levels might be affected by an uncertainty larger than 1 dB. Nevertheless, the goal of the present study is to focus on BLI installation effects, and hence to highlight variations relative to the non-BLI configuration, rather than predicting absolute values.

The hybrid high-subsonic/transonic LBM solver implemented in SIMULIA PowerFLOW® 6-2020-R3 is used for computing the numerical flow solution (see Sec. 3.2). In particular, the transonic solver is used within the LRF (where high values of the Mach number are expected), while the high-subsonic solver is used elsewhere. Simulations are performed using a 1000 cores cluster with Intel Xeon CPU E5-2697 2.6 GHz and require approximately 6 hours per fan revolution for both isolated and BLI cases. A summary of the grid size and computational cost for both BLI and isolated cases are reported in Tab. 8.1. The whole fluid domain is firstly initialized with a uniform stream-wise velocity corresponding to the free-stream conditions for a coarser simulation ($\sqrt{2}$ times coarser than the finer one), which is in turn used to initialize a finer resolution case. Hence, after a settling time of 2 fan revolutions, corresponding to 0.0461 sec of physical time, sampling is started. Acoustic data are sampled at 180 kHz along 10 fan revolutions (0.2305 sec). Fourier transformed data are evaluated using a bandwidth of 25 Hz, 50% window overlap coefficient and Hanning weighting.

Case	# Voxels	# FEVoxels	# Surfels	# FESurfels	kCPUh (10 revs)
Isolated engine	541.1	69.6	51.9	17.8	61.5
BLI engine	545.9	70.1	57.5	18.1	62.1

Table 8.1: Grid size in millions of elements and computational cost.

8.3. NUMERICAL RESULTS

In this section, the numerical results for both BLI and isolated fan-stage configurations are presented. First, an assessment of the turbulent boundary-layer being ingested by the engine for the installed case is presented. Then, BLI installation effects for the NOVA BLI configuration during a take-off with power cut-back are outlined in terms of fan-stage velocity field, fan performances, fan blade sectional airloads, far-field noise directivity, noise power level and on-the-ground noise footprint.

8.3.1. FUSELAGE BOUNDARY-LAYER

As mentioned, a zig-zag transition trip is employed in this study to trigger the transition of the fuselage boundary-layer being ingested by the fan-stage. According to van der Velden *et al.* [245], who performed LBM-based Direct Numerical Simulations (DNS) of the flow past transition strips over flat plates, a canonical fully turbulent boundary-layer is experienced for a zig-zag trip after approximately 40 laminar boundary-layer thicknesses (evaluated at the location of the tripping device) downstream it. Following this study, and considering the actual laminar boundary-layer thickness evaluated at the transition trip location, a settling trip-engine distance of $1R$ would be required to ensure the ingestion of a fully turbulent boundary-layer into the fan-stage. Starting from these considerations, a larger and more conservative trip-engine distance of $3R$ was used.

An instantaneous view of iso-surfaces of λ_2 criterion [153] color-contoured by velocity magnitude is depicted in Fig. 8.4. This result qualitatively shows the presence of a turbulent boundary-layer convecting over the fuselage past the transition trip and being ingested by the fan-stage. Flow structures of coherence length of the order of the zig-zag trip wavelength are seen mixing and creating larger hairpins downstream it. Moreover, the stretch and re-orientation of the turbulent structures into stream-wise oriented filaments is observed as the flow approaches the engine intake, as a result of the large flow acceleration occurring in proximity of the engine intake due to the favorable pressure gradient induced by the fan downstream. Finally, the generation of horseshoe vortices is further observed at the junction between the fuselage and the engine nacelle.

To better assess the presence of a turbulent boundary-layer being ingested by the fan-stage, boundary-layer profiles are extracted on the fuselage at 10 different equispaced locations between the zig-zag strip and the engine intake, as depicted in Fig. 8.5. Such locations are referred to the engine coordinate system (denoted by x_e, y_e and z_e coordinates), whose origin coincides with the fan center location, while the x-axis is

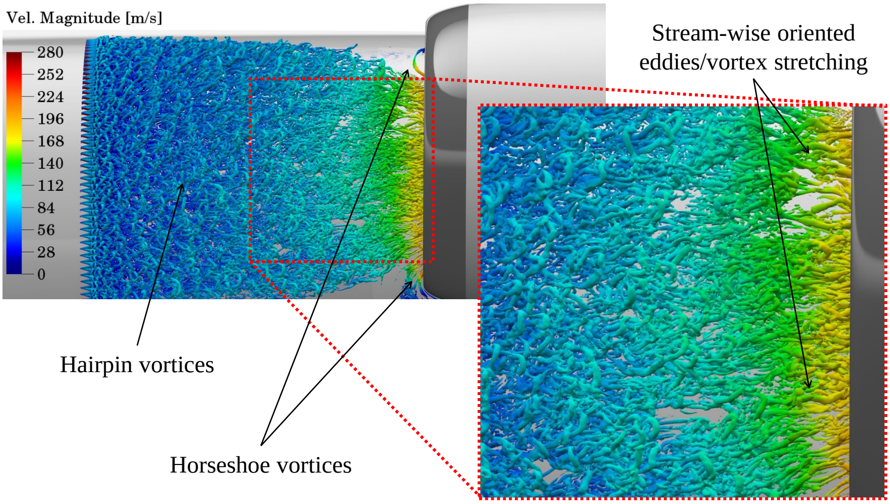

Figure 8.4: Iso-surfaces of λ_2 ($-75000\ 1/s^2$) color-contoured by velocity magnitude depicting the turbulent boundary-layer past the transition trip.

aligned with the engine axis and positive downstream, z-axis is normal to the fuselage and directed outwards and y-axis is defined by the right-hand rule. At each of these locations, time-averaged stream-wise velocity profiles $\overline{u}$ (Fig. 8.6(a)), and time-averaged Reynolds stress profiles $\overline{u'u'}$, $\overline{w'w'}$ and $\overline{u'w'}$ (Fig. 8.6(b), Fig. 8.6(c) and Fig. 8.6(d), respectively) are extracted from the unsteady flow solution, where u and w represent the wall-parallel and wall-normal velocity components, respectively. In Figs. 8.6(a) to 8.6(d), the velocity statistics and the wall-normal distance are respectively normalized by the free-stream velocity $U_\infty = 88.78$ m/s and the local boundary-layer thickness δ (which is summarized for each location in Tab. 8.2 along with the shape factor H).

x_e/R [-]	-4.61	-4.36	-4.11	-3.86	-3.61	-3.37	-3.12	-2.87	-2.62	-2.37
δ [m]	0.1338	0.1522	0.1627	0.1702	0.1883	0.1842	0.1834	0.1929	0.1963	0.1993
H [-]	1.94	1.67	1.52	1.43	1.36	1.31	1.25	1.19	1.13	1.09

Table 8.2: Boundary-layer thickness δ and shape factor H at several locations between the zig-zag strip and the engine intake.

Moving from the zig-zag trip to the engine intake, the mean streamwise velocity (Fig. 8.6(a)) shows an increment of the velocity gradient at the wall, with the transition from laminar-like to turbulent-like profiles already occurring for $x_e/R \leq -3.61$ (i.e. within roughly $1R$ distance from the tripping device). This is further confirmed by the shape factor H which goes below the threshold value of $1.3-1.4$ starting from $x_e/R \leq -3.61$, as expected for a turbulent boundary-layer [46]. Moreover, the outer parts of the different mean stream-wise velocity profiles tend to collapse on top of each other, with edge-velocity values slightly exceeding the free-stream one, for $x_e/R \leq -3.61$.

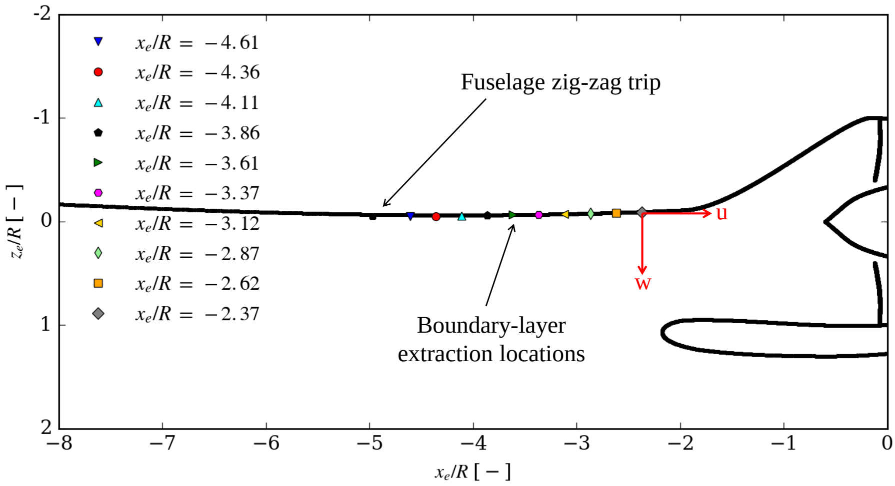

Figure 8.5: Locations of the fuselage boundary-layer extraction and coordinate system for measuring the wall-parallel (u) and wall-normal (w) velocity components.

Contrarily, the mean stream-wise velocity profiles show increasing edge-velocities at more downstream locations (up to approximately $1.75U_\infty$ for $x_e/R = -2.37$), as a consequence of the increasing favourable pressure gradient in the stream-wise direction. The stream-wise (Fig. 8.6(b)), wall-normal (Fig. 8.6(c)) and shear (Fig. 8.6(d)) Reynolds stresses show a rapid reduction of the peak value within the first 5 stream-wise stations ($-4.61 \leq x_e/R \leq -3.61$), i.e. within $1R$ from the zig-zag strip, where the settling of the turbulence enforced by the zig-zag strip is expected [245]. For more downstream positions, a weaker reduction of the turbulent levels is further observed for the $\overline{u'u'}$ and $\overline{u'w'}$ components. Contrarily, the wall-normal component shows no reduction of the turbulent levels with converging profiles for locations close to the engine intake. This might be related to the stretching and re-orientation of the boundary-layer vortices in the stream-wise direction, with a consequent re-distribution of the turbulent kinetic energy from the $\overline{u'u'}$ to the $\overline{w'w'}$ components in the overall Reynolds stresses energy budget. Finally, it is interesting to point out that the Reynolds stress levels, extracted in proximity of the engine intake ($x_e/R = -2.37$), are consistent with those of a canonical developed turbulent boundary layer, whose values at a wall-normal distance of 0.2δ are approximately $\overline{u'u'}/U_\infty^2 = 4.5 \cdot 10^{-3}$, $\overline{w'w'}/U_\infty^2 = 1.6 \cdot 10^{-3}$ and $-\overline{u'w'}/U_\infty^2 = 1.3 \cdot 10^{-3}$ according to Klebanoff [246].

8.3.2. FAN-STAGE VELOCITY FIELD

Figure 8.7 depicts a schematic description of a plane normal to the fuselage and passing through the engine axis, and different cross-flow planes along the inlet, interstage and bypass exhaust sections, which are used in the following to extract the fan-stage axial (i.e. aligned with engine axis) and in-plane (i.e. perpendicular to the engine axis) velocity fields along the engine. In this sketch, the x_e, y_e and z_e coordinates represent those of

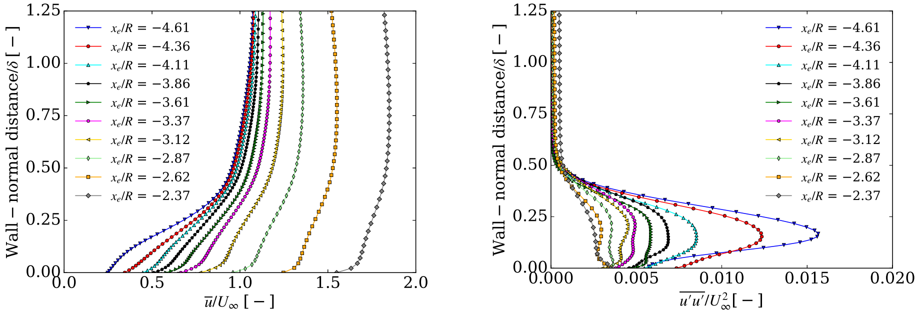

(a) $\overline{u}$ (b) $\overline{u'u'}$

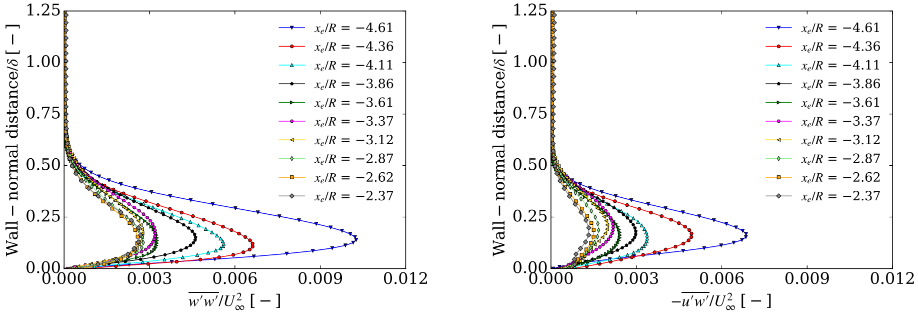

(c) $\overline{w'w'}$ (d) $\overline{u'w'}$

Figure 8.6: Time-average stream-wise velocity (a) and Reynolds stress (b), (c) and (d) profiles at several locations between the zig-zag strip and the engine intake.

the engine coordinate system previously defined.

Figure 8.8 shows the instantaneous axial velocity field for the BLI case extracted on a plane normal to the fuselage surface and passing through the engine axis at different time instants. The same quantity is depicted on the same plane for the isolated case in Fig. 8.9. The BLI configuration shows a flow acceleration at the intake section - due to the reduced inlet throat area of the installed configuration compared to the isolated one - and the presence of turbulence impinging the fan rotor. Such turbulent structures are connected to the fuselage turbulent boundary-layer being ingested by the fan-stage, as well as to the flow separation occurring at approximately 60% of the s-duct length, the latter induced by the adverse pressure gradient due to the rapid increase of the intake cross-sectional area. Conversely, the isolated configuration shows a rather uniform velocity field upstream the fan rotor, except for the first 25% of its extension, in which the flow tends to recover from its initial misalignment with respect to the axis engine due to the presence of non-zero angle of attack, tilt and toe angles. Upstream traveling waves are observed along the intake for the BLI engine, unlike the isolated one. The BLI configuration shows a thicker boundary-layer on the intake wall opposite to the fuse-

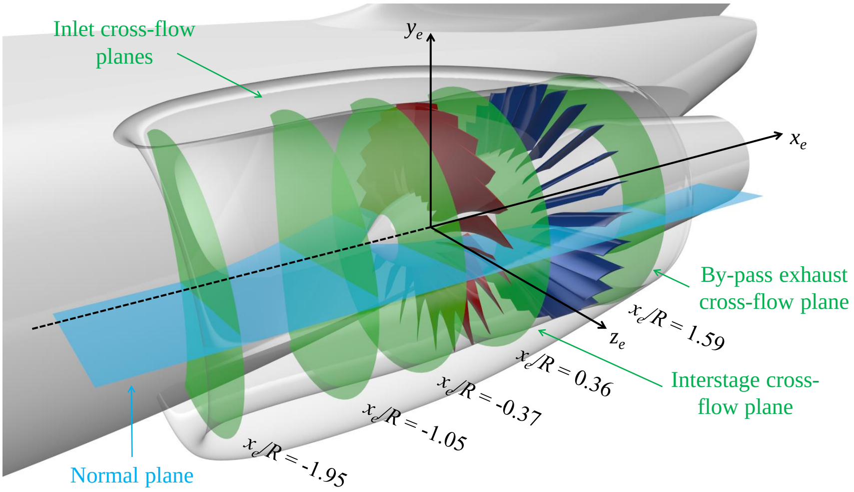

Figure 8.7: Sketch of the planes used to extract the fan-stage velocity fields across the engine.

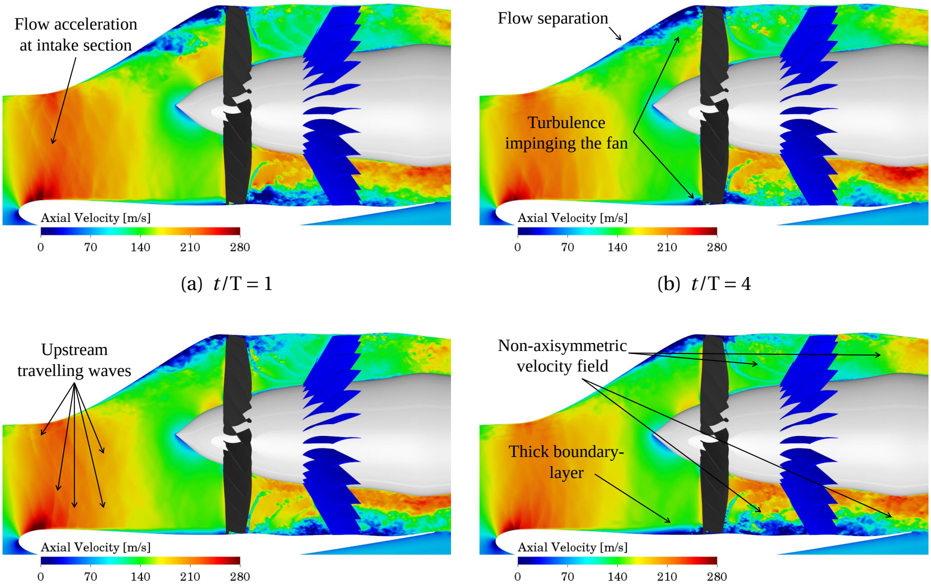

(a) $t/T = 1$ (b) $t/T = 4$

(c) $t/T = 7$ (d) $t/T = 10$

Figure 8.8: Instantaneous axial velocity field on a plane normal to the fuselage surface and passing through the engine axis at different time instants, BLI engine.

lage compared to the isolated case, which also tends to separate in proximity of the wall beneath the fan. The instantaneous axial velocity field further shows the occurrence of two different fan wake/OGV interaction mechanisms between the fuselage and the

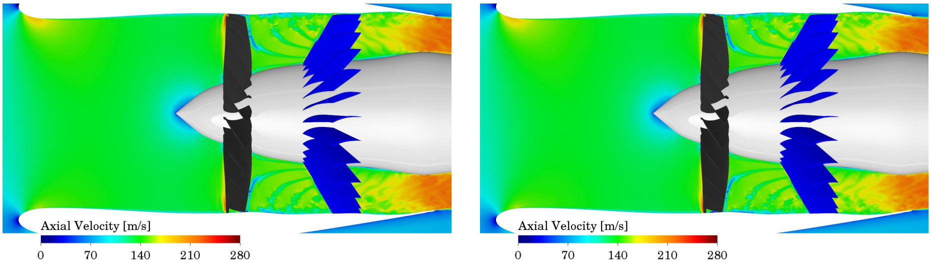

(a) $t/\mathrm{T} = 1$ (b) $t/\mathrm{T} = 4$

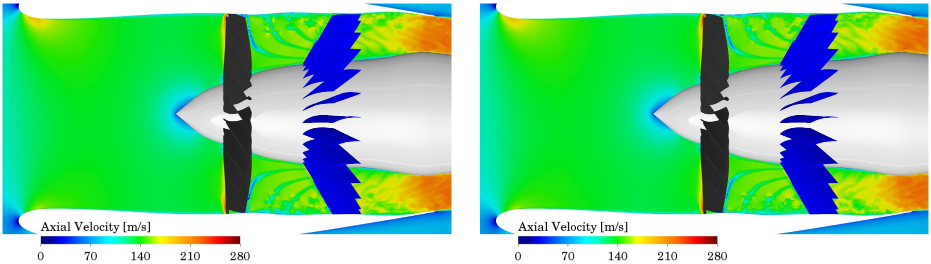

(c) $t/\mathrm{T} = 7$ (d) $t/\mathrm{T} = 10$

Figure 8.9: Instantaneous axial velocity field on a plane normal to the fuselage surface and passing through the engine axis at different time instants, isolated engine.

nacelle sides for the BLI case, whereas the isolated case shows the typical rotor-stator interaction mechanism with the fan viscous wakes impinging on each stator vanes at the blade-passing frequency. The BLI configuration shows a non-axisymmetric velocity field between the rotor and the stator, with much higher velocities observed in the region opposite to the fuselage side with respect to the isolated one. In this same region, the BLI case further shows stronger turbulent structures than those convecting on the fuselage side. Similar considerations can be made for the fluid regions downstream the stator as well.

INLET FLOW FIELD

Figures 8.10 and 8.11 show the time-averaged axial and in-plane velocity components on cross-flow disks upstream the fan plane for the BLI and isolated configurations, respectively. For the in-plane velocity plots, the in-plane velocity vectors are also shown. In these upstream-looking-downstream views, the fan blades rotate counter-clockwise as indicated by the circular arrow. Three different stream-wise locations (i.e. $x_e/R = -1.95$, $x_e/R = -1.05$ and $x_e/R = -0.37$), respectively corresponding to 15%, 55% and 85% of the inlet axial length, are considered. Moreover, the convention adopted to describe the fan blade azimuth angle is also reported. According to this convention, the fan blade sweeps the BLI area for azimuthal angles between 45° and 180° (Fig. 8.11).

The isolated case shows a moderate level of distortion across the engine intake, where the free-stream misalignment with respect to the engine axis (due to the non-zero

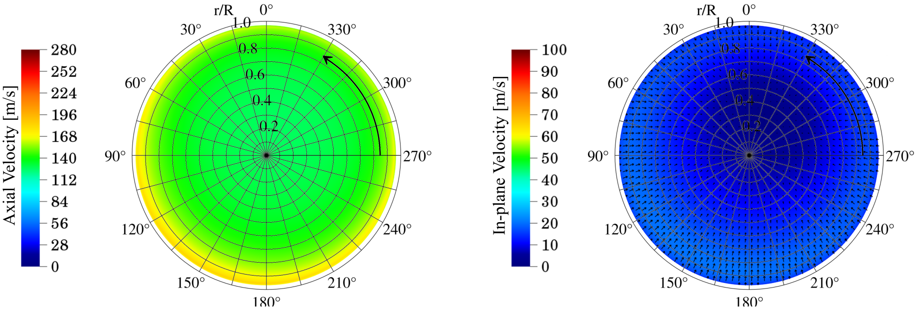

(a) *Axial component - x_e/R = -1.95* (b) *In-plane component - x_e/R = -1.95*

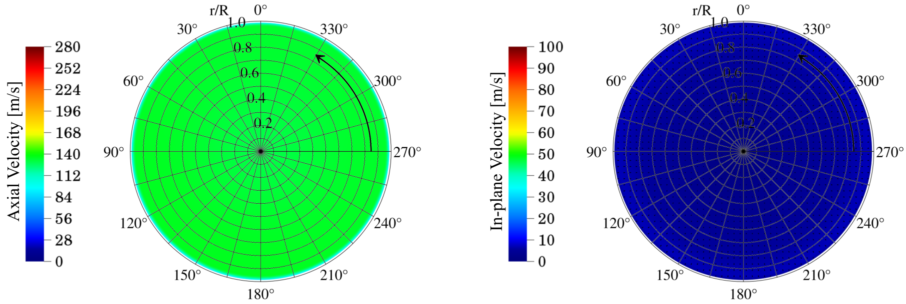

(c) *Axial component - x_e/R = -1.05* (d) *In-plane component - x_e/R = -1.05*

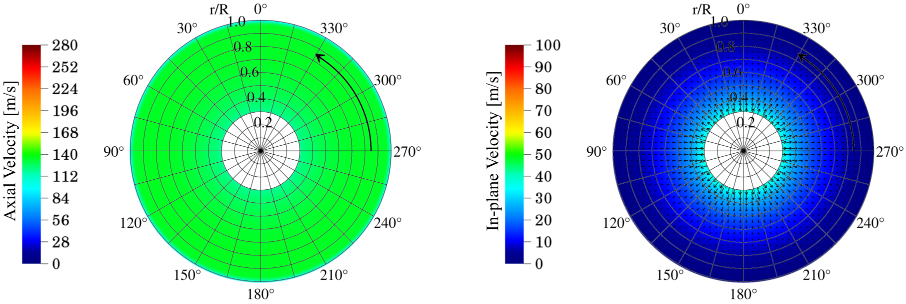

(e) *Axial component - x_e/R = -0.37* (f) *In-plane component - x_e/R = -0.37*

Figure 8.10: Time-averaged velocity field at different sections upstream the fan, isolated engine.

angle of attack, tilt and toe angles) is responsible of the non-symmetric acceleration of the flow around the intake lip (Fig. 8.10(a)) and the rise of an in-plane velocity component directed inboard (Fig. 8.10(b)). The velocity field uniformity is then completely re-established within the first half of the intake extension, where the flow approaching the fan section shows a quite constant mean axial velocity (Figs. 8.10(c) and 8.10(e)) and a moderate in-plane velocity directed outwards along the radial direction, as a conse-

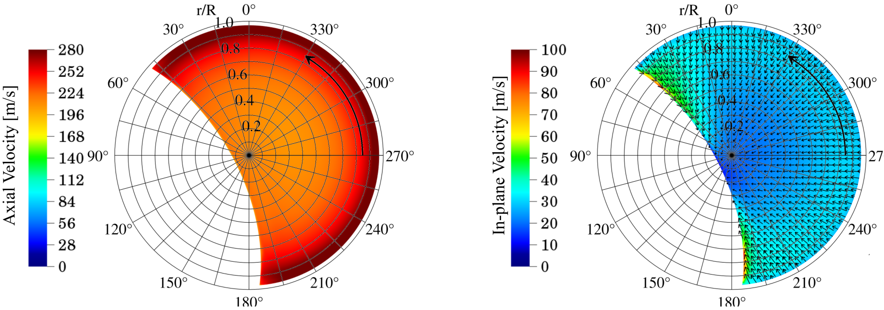

(a) *Axial component* - x_e/R = *-1.95* (b) *In-plane component* - x_e/R = *-1.95*

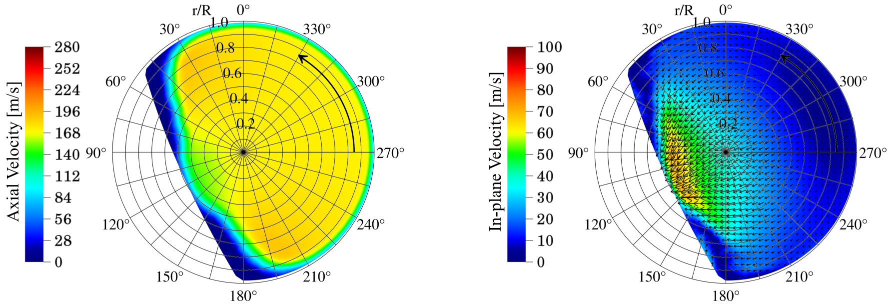

(c) *Axial component* - x_e/R = *-1.05* (d) *In-plane component* - x_e/R = *-1.05*

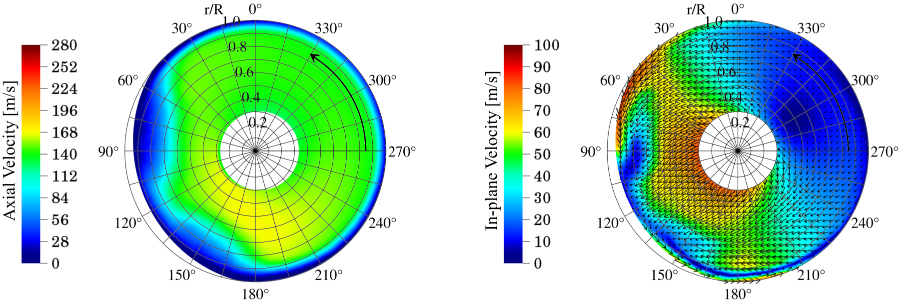

(e) *Axial component* - x_e/R = *-0.37* (f) *In-plane component* - x_e/R = *-0.37*

Figure 8.11: Time-averaged velocity field at different sections upstream the fan, BLI engine.

quence of the slightly divergent inlet geometry (Fig. 8.10(d)) and the presence of the downstream spinner (Fig. 8.10(f)).

Regarding the BLI configuration, the reduced engine intake frontal area yields to an increase of the axial (Fig. 8.11(a)) and in-plane inward directed (Fig. 8.11(b)) velocity components compared to the isolated case, the latter primarily showing a radial pattern with the highest magnitude values occurring around the junction between the fuselage and the engine nacelle. For further downstream sections, the mean flow exhibits high levels of non-uniformity and distortion in terms of both axial and in-plane velocities. More specifically, the axial component shows two nearly symmetric re-circulation/low-velocity regions on the fuselage side. Such flow separation areas are already visible at 55% of the inlet length (Fig. 8.11(c)) and extend further downstream (Fig. 8.11(e)) according to a nearly symmetrical pattern around the inlet plane of symmetry (around 120° in the fan blade azimuth). A nearly symmetrical pattern around 120° of the fan blade azimuth is also observable for the in-plane velocity at $x_e/R = -1.05$ (Fig. 8.11(d)), which shows the presence of a strong secondary flow directed from the engine nacelle side towards the fuselage one, as a consequence of the centrifugal pressure gradient due to the s-duct geometric curvature. This transverse secondary flow is also observed for the inlet section at $x_e/R = -0.37$, which further shows an entrainment motion imparted by the rotor blades on the low-velocity flow approaching the fan plane (Fig. 8.11(f)), i.e. for $r/R > 0.9$ and azimuthal angles within 45°-90° and 135°-210°, respectively.

It should be recalled that the current NOVA BLI configuration represents a rather idealized BLI-layout, due to the relative short s-duct length (2.35 m) and the large portion of intake embedded into the fuselage (40%). A more conservative sizing, e.g. based on a longer s-duct length and a lower percentage of buried intake, would help in reducing the amount of flow separation occurring on the s-duct, as well as of flow distortion at the fan plane. This at the cost of an additional mass and drag penalty, and inlet friction losses.

INTERSTAGE FLOW FIELD

Figures 8.12 and 8.13 show upstream-looking-downstream views of the velocity field for an interstage section between the rotor and the stator ($x_e/R = 0.36$) for the BLI and isolated configurations, respectively. More specifically, the velocity field is decomposed into phase-locked average of axial (Figs. 8.12(a) and 8.13(a)) and tangential (Figs. 8.12(b) and 8.13(b)) velocity components, and standard deviation of axial (Figs. 8.12(c) and 8.13(c)) and in-plane (Figs. 8.12(d) and 8.13(d)) velocity components. It is worth mentioning that the phase-locked average contour plots highlight the presence of periodic non-uniformities in the mean flow associated to the rotating fan blades (i.e. viscous blade wakes and tip-vortices), which generate tonal noise at BPF and its harmonics when they interact with the stator vanes. Instead, the phase-locked standard deviation contour plots can be used to examine the presence of random fluctuations in the flow (i.e. turbulence), which represent potential sources of broadband noise when they impinge on the stator surfaces (see Sec. 2.2.2).

Contrarily to the isolated configuration, where the two typical expected flow regions downstream the fan, i.e. the “viscous” region associated to both rotor blade wakes and tip-vortices and the “potential” flow region outside the viscous ones [247], are clearly defined throughout the radial coordinate (Figs. 8.13(a) and 8.13(b)), the same regions are visible only up to $r/R = 0.8$ of the span-wise coordinate for the BLI case (Figs. 8.12(a) and 8.12(b)). For the isolated configuration, the axial velocity in the potential flow regions is rather uniform along the span-wise direction (Fig. 8.13(a)), whereas the tangential ones tend to decrease for larger r/R (Fig. 8.13(b)). Moreover, for a given radial position, the axial velocity is lower in the viscous regions of the flow compared to the potential ones, whereas the tangential ones result to be higher. Similar trends can also be found for the BLI configuration, although some additional considerations need to be

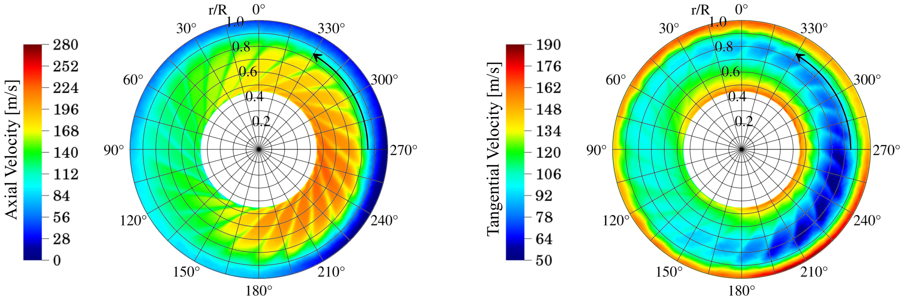

(a) *Axial component* - $x_e/R = 0.36$ (b) *Tangential component* - $x_e/R = 0.36$

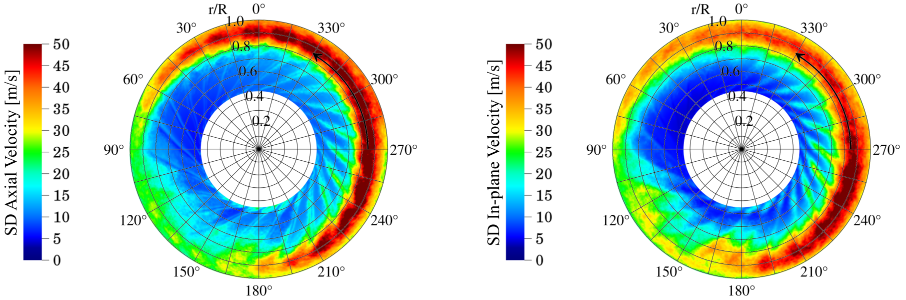

(c) *Axial component* - $x_e/R = 0.36$ (d) *In-plane component* - $x_e/R = 0.36$

Figure 8.12: Phase-locked average of axial (a) and tangential (b) velocity components and standard deviation (SD) of axial (c) and in-plane (d) velocity components on an interstage disk at $x_e/R = 0.36$, BLI engine.

outlined. First, the phase-locked average axial velocity shows a non-uniform distribution along the azimuthal coordinate, with higher values within 0°-45° and 135°-360° and lower values in the explementary circular sector compared to the isolated case. The same trend also occurs for the tangential component within the first 55% of the radial coordinate, whereas an opposite situation is observed for $0.55 < r/R < 0.9$. Finally, the BLI configuration shows lower axial velocities and higher tangential velocities above $r/R = 0.9$ compared to the isolated one. Regarding the turbulent fluctuations, the isolated case shows quite uniform standard deviation contours, with the largest velocity perturbations occurring within the viscous wake and at the tip for both axial (Fig. 8.13(c)) and in-plane (Fig. 8.13(d)) velocity components. The BLI configuration shows larger levels of fluctuations and flow non-uniformity for both components (Figs. 8.12(c) and 8.12(d), respectively). More specifically, velocity fluctuations roughly three times higher are observed within the outer 30% of the radial coordinate and for azimuthal position comprised between 0°-60° and 180°-360°, respectively. A secondary diffused region of high turbulence levels is also present between 50°-180°, i.e. in correspondence of the fuselage BLI area. Moreover, thicker viscous wakes are observed for the BLI configuration compared to the isolated one, especially for azimuthal angles between 180° and 360°.

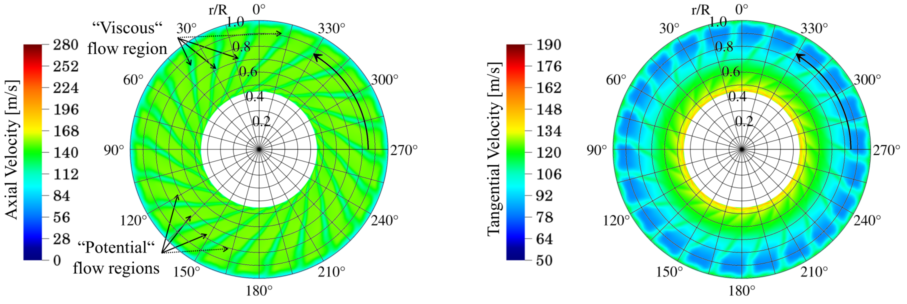

(a) *Axial component* - $x_e/R = 0.36$ (b) *Tangential component* - $x_e/R = 0.36$

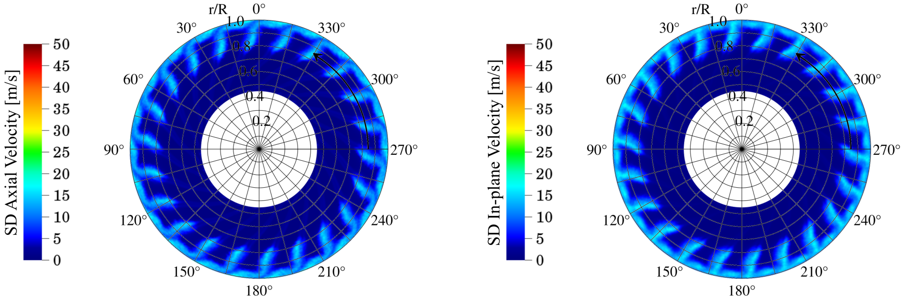

(c) *Axial component* - $x_e/R = 0.36$ (d) *In-plane component* - $x_e/R = 0.36$

Figure 8.13: Phase-locked average of axial (a) and tangential (b) velocity components and standard deviation (SD) of axial (c) and in-plane (d) velocity components on an interstage disk at $x_e/R = 0.36$, isolated engine.

Overall, the BLI interstage flow field is characterized by less axisymmetric and coherent tangential velocity variations and higher levels of in-plane velocity fluctuations. Such velocity components are thought to be more important in the generation of the rotor/stator interaction noise [247]. This type of noise is associated to the unsteady loading on the stator vanes, which is generated by fluctuations of the flow velocity component normal to the stator surface. In view of this, broadband noise is expected to dominate more the far-field noise spectrum for the BLI configuration compared to the isolated case. The detailed aeroacoustic analysis will be performed in Secs. 8.3.5 and 8.3.6 to prove the assumption.

Bypass exhaust flow field

To conclude the analysis of the fan-stage velocity field, Figs. 8.14 and 8.15 show upstream-looking-downstream views of the velocity field on a bypass exhaust transverse section ($x_e/R = 1.59$) for the BLI and isolated configurations, respectively. Again, the velocity field is presented in terms of phase-locked average of axial (Figs. 8.14(a) and 8.15(a)) and tangential (Figs. 8.14(b) and 8.15(b)) velocity components, and standard deviation of axial (Figs. 8.14(c) and 8.15(c)) and in-plane (Figs. 8.14(d) and 8.15(d)) velocity components.

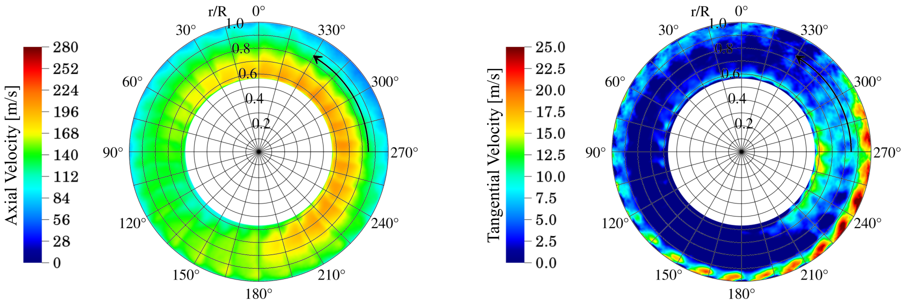

(a) *Axial component - x_e/R = 1.59* (b) *Tangential component - x_e/R = 1.59*

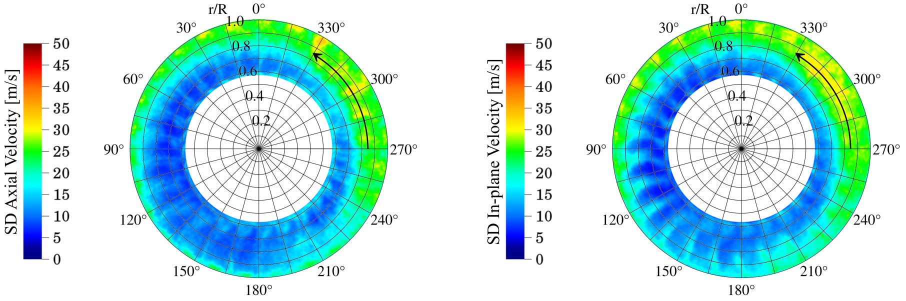

(c) *Axial component - x_e/R = 1.59* (d) *In-plane component - x_e/R = 1.59*

Figure 8.14: Phase-locked average of axial (a) and tangential (b) velocity components and standard deviation (SD) of axial (c) and in-plane (d) velocity components on a disk in the bypass exhaust at $x_e/R = 1.59$, BLI engine.

As already pointed out, the BLI case shows a non-axisymmetric phase-locked average axial velocity field along the azimuthal coordinate downstream the stator (Fig. 8.15(a)), with the highest and lowest values respectively taking place on the nacelle side up to $r/R = 0.7$ and above $r/R = 0.9$. Contrarily, the isolated configuration presents the expected axisymmetric axial velocity pattern characterized by the viscous wakes being convected from each stator vane (Fig. 8.15(a)). The BLI configuration further shows a non-uniform and lower flow swirl recovery downstream of the stator (Fig. 8.14(b)) compared to the isolated one (Fig. 8.15(b)), with high values of the tangential velocity still persisting along most of the outer part of the bypass exhaust ($r/R > 0.9$) and for the azimuthal sector between 225° and 315°. Concerning the turbulence levels in the bypass exhaust, the isolated case shows again quite axisymmetric standard deviation contours, with the largest velocity fluctuations occurring above 80% of the radial coordinate for both the axial (Fig. 8.15(c)) and in-plane (Fig. 8.15(d)) velocity components. Finally, similarly to what observed for the interstage velocity field, the BLI configuration manifests large values of velocity fluctuations for both the axial and in-plane components (Figs. 8.14(c) and 8.14(d), respectively), with levels approximately three times higher than those of the isolated case for $r/R > 0.7$ and for the azimuthal sectors within 0°-60°

and 180°-360°.

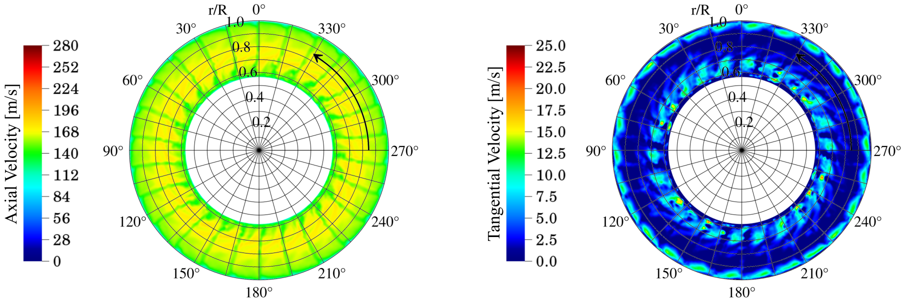

(a) *Axial component - x_e/R = 1.59* (b) *Tangential component - x_e/R = 1.59*

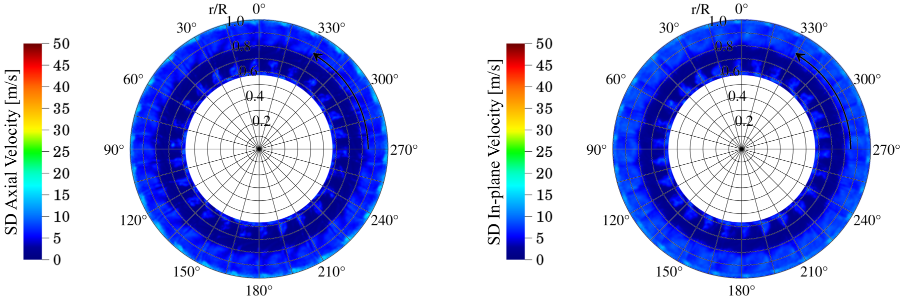

(c) *Axial component - x_e/R = 1.59* (d) *In-plane component - x_e/R = 1.59*

Figure 8.15: Phase-locked average of axial (a) and tangential (b) velocity components and standard deviation (SD) of axial (c) and in-plane (d) velocity components on a disk in the bypass exhaust at $x_e/R = 1.59$, isolated engine.

8.3.3. FAN BLADE SECTION AIRLOADS

Figure 8.16 depicts the sectional thrust coefficient time-history $c_T\tilde{V}^2$ at 6 different spanwise sections uniformly distributed between 45% and 95% of the blade span. For each section and fan blade azimuthal position, the $c_T\tilde{V}^2$ coefficient is computed by integration of the airfoil pressure distribution p over the airfoil contour Σ using the following formula:

$$c_T\tilde{V}^2 = -\frac{\oint_{\Sigma} p\mathbf{n}\cdot\mathbf{i}_{x_e}\mathrm{d}\Sigma}{\frac{1}{2}\rho_\infty V^2\ell_c}\tilde{V}^2 = -\frac{2}{\rho_\infty a_\infty^2\ell_c}\oint_{\Sigma} p\mathbf{n}\cdot\mathbf{i}_{x_e}\mathrm{d}\Sigma \qquad (8.1)$$

where $\mathbf{n}$ is the outward-pointing normal to the airfoil contour, $\mathbf{i}_{x_e}$ is the engine axis unit vector (positive when directed downstream) and $\mathrm{d}\Sigma$ is the infinitesimal airfoil contour element. Moreover, $\tilde{V} = V/a_\infty$ is the velocity perceived by the fan blade section at the radial coordinate r normalized by the free-stream speed of sound a_∞, ρ_∞ is the free-stream density and ℓ_c is the airfoil chord. Note that the line integral in Eq. (8.1) is computed clockwise with respect to the airfoil contour Σ.

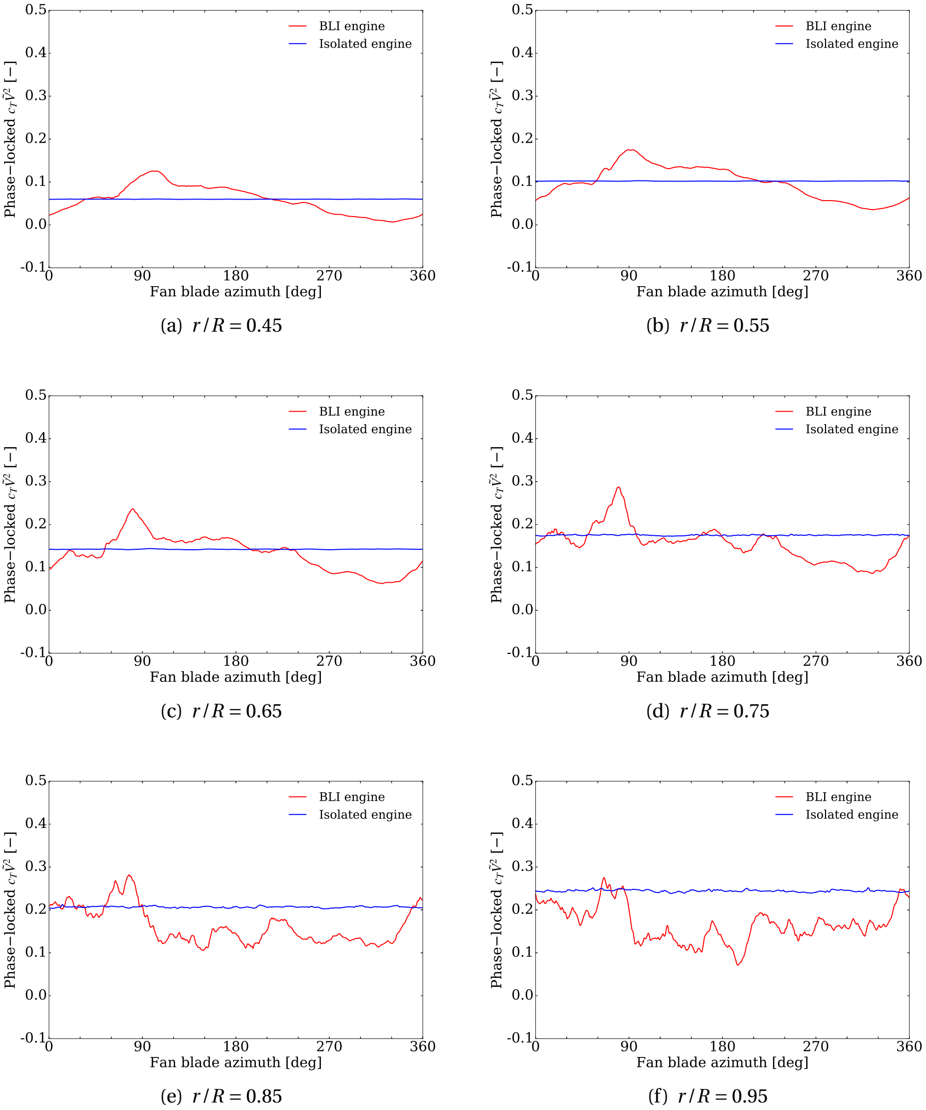

(a) $r/R = 0.45$

(b) $r/R = 0.55$

(c) $r/R = 0.65$

(d) $r/R = 0.75$

(e) $r/R = 0.85$

(f) $r/R = 0.95$

Figure 8.16: Phase-locked fan blade sectional thrust coefficient time-histories at different span-wise locations.

As expected, the isolated configuration shows almost constant time-histories of the sectional thrust for each span-wise location, with a mean value increment moving from inboard (Fig. 8.16(a)) to outboard (Fig. 8.16(f)) sections of the fan blade. Only the outer section at $r/R = 0.95$ shows some weak unsteadiness due to the interaction between the blade tip and the boundary-layer developing along the inlet wall. Contrarily, the BLI configuration shows a low-frequency thrust unsteadiness (predominantly 1/rev) for inboard blade sections (Figs. 8.16(a) to 8.16(c)), as a consequence of the strong mean flow distortion. For these sections, an increment of the sectional thrust is observed approximately between 60° and 180° (i.e. in correspondence of the BLI area) compared to the isolated case, whereas lower values of the $c_T\tilde{V}^2$ coefficient are observed elsewhere. As the radial coordinate increases, more intense and impulsive unsteadiness, as well as lower mean values of the sectional thrust are observed (Figs. 8.16(d) to 8.16(f)) compared to the isolated case, due to the ingestion of turbulence associated to the flow separation occurring on the nacelle and fuselage sides, respectively. All the aforementioned thrust fluctuations represent an additional source of noise. Among them, those occurring on the outer part of the blade are expected to contribute more to the far-field noise, due to the higher levels of unsteadiness and Mach numbers compared to those in blade inboard regions.

8.3.4. FAN PERFORMANCES

Table 8.3 shows BLI installation effects on the fan performances in terms of fan pressure ratio FPR and isentropic efficiency η_f. As a consequence of the highly distorted flow and the ingestion of turbulence, a reduction the FPR by 2.5% and of the isentropic efficiency by 9.2% is observed when the same fan is operated at same RPM in the BLI layout with respect to the conventional non-BLI case.

Parameter	Isolated engine	BLI engine	Relative difference
FPR [-]	1.27	1.24	-2.5%
η_f [-]	0.917	0.836	-9.2%

Table 8.3: Fan pressure ratio, fan isentropic efficiency and relative difference between isolated and BLI engines.

8.3.5. FAR-FIELD NOISE DIRECTIVITY

Figure 8.17 depicts the microphone array used in this study for far-field noise computations. It is composed by 7 even meridian arcs of 10 m radius, centered around the fan center and covering a semi-spherical surface. Each arc is characterized by 15 microphones distributed every 10°, with directivity angles ranging from 20° upstream the engine to 160° downstream it.

As mentioned in Sec. 8.2.2, the far-field noise is computed by integration of the FW-H equation on a permeable surface encompassing the engine. Since the FW-H formulation adopted in this work does not include the volume integral, spurious signals might arise when the permeable surface is intersected by turbulence (i.e. the fuselage turbulent boundary-layer) [122]. The presence of such spurious effects has been assessed (for the BLI case) by comparing far-field noise predictions from the whole permeable FW-H surface (to be intended already without end-cap, as shown in Fig. 8.2) to those obtained by removing that portion of the surface intersected by the fuselage boundary-layer. It turned out that the two different approaches provided almost identical results within the directivity angles of interest (shown in Fig. 8.17), thus allowing the use of the whole FW-H permeable surface (even for the BLI configuration) for the far-field noise computations. This aspect is not in contrast with the aforementioned choice of removing the cone end-cap of the permeable FW-H surface. Indeed, the hydrodynamic pressure fluctuations within the bypass exhaust jet and potentially passing through the end-cap are significantly more intense and would affect a larger portion of the integration surface compared to the fuselage turbulent boundary-layer fluctuations that cross the spherical sector of the FW-H surface around the intake.

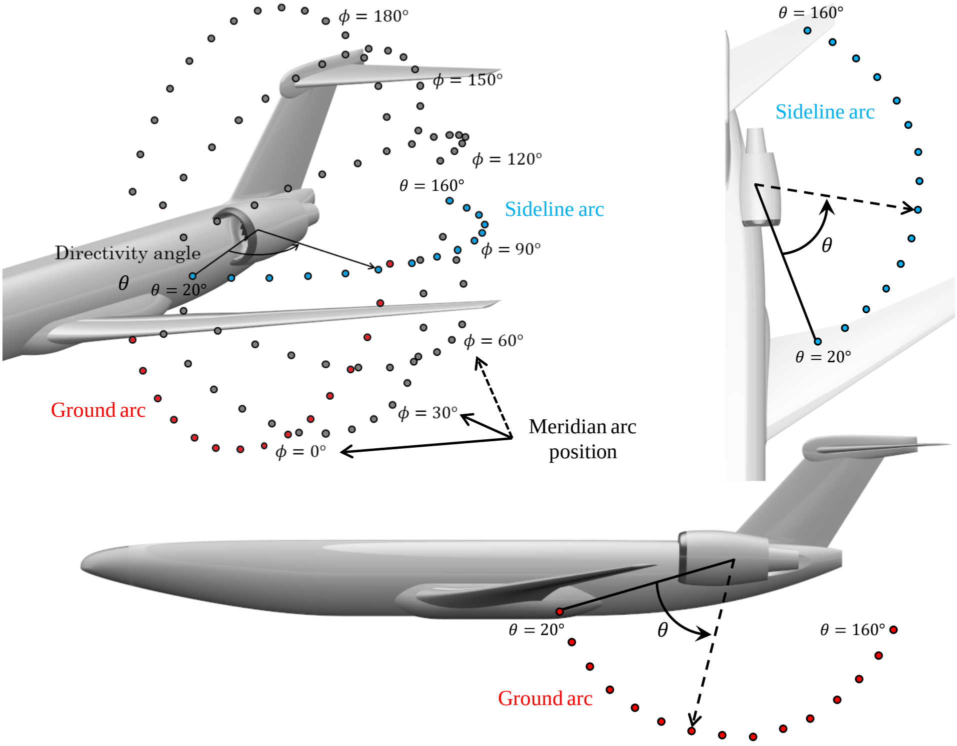

Figure 8.17: Sketch of the microphone array used for far-field noise computations. The angle ϕ denotes the position of each meridian arc, while θ is the directivity angle along each meridian arc.

A spectral representation (Power Spectral Density, PSD) of the far-field noise directivity normalized by the BPF is shown in Fig. 8.18 and Fig. 8.19 for the BLI and isolated cases, respectively. In addition, far-field noise differences between such configurations are depicted in Fig. 8.20. For the sake of conciseness, only the results for the arcs at $\phi = 0°$ (ground arc) and $\phi = 90°$ (sideline arc) are shown in following. For both the BLI and isolated configurations, the noise is radiated most efficiently downstream the engine. However, besides such a similarity, the two examined configurations show quite different results. The isolated engine presents both broadband and tonal noise contributions, with the latter showing distinct peaks at multiples of the blade-passing frequency downstream the engine (up to BPF-3). Conversely, tones at harmonics of the BPF do not emerge with respect to broadband levels for the BLI case. Haystacked peaks are found around BPF-1 for downstream directivity angles, as better highlighted in Fig. 8.21 for the ground arc at 140° and 150° observer angles. Such peaks are believed to be generated by the correlated unsteady airloads on neighboring blades, and associated to both the stream-wise elongated vortices coming from the fuselage turbulent boundary-layer and the large eddies being shed from the s-duct wall, which might be cut multiple times by successive blades (a similar phenomenon has been already experimentally observed by Murray *et al.* [241] and Alexander *et al.* [248] for a rotor case ingesting a planar boundary-layer, see also Sec. 2.1.5). For the BLI case, broadband levels turn out to be from 10 to 20 dB overall higher than those related to the isolated configuration, for most of the frequencies and directivity angles considered. Moreover, the BLI layout appears to be as noisy as the isolated one on the sideline arc for directivity angles around 90° and frequencies higher than BPF-2 (Fig. 8.20(b)), or quieter by 5-10 dB on the ground arc (Fig. 8.20(a)). This last aspect might be related to some noise shielding effects introduced by the partial placement of the engine into the fuselage.

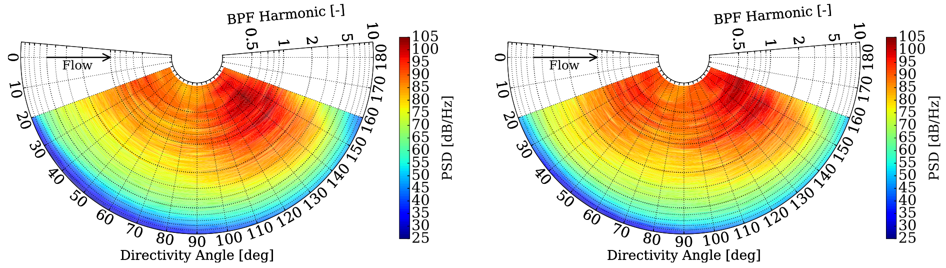

(a) *Ground arc* - $\phi = 0°$ (b) *Sideline arc* - $\phi = 90°$

Figure 8.18: Far-field noise directivity on ground (a) and sideline (b) arcs of 10 m radius and centered around the fan, BLI engine.

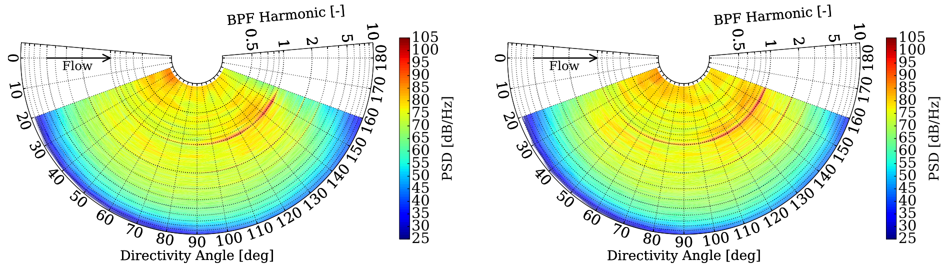

(a) *Ground arc* - $\phi = 0°$ (b) *Sideline arc* - $\phi = 90°$

Figure 8.19: Far-field noise directivity on ground (a) and sideline (b) arcs of 10 m radius and centered around the fan, isolated engine.

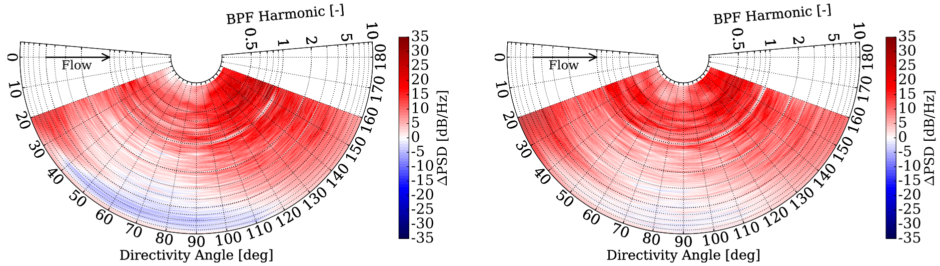

(a) *Ground arc* - $\phi = 0°$ (b) *Sideline arc* - $\phi = 90°$

Figure 8.20: Far-field noise directivity on ground (a) and sideline (b) arcs of 10 m radius and centered around the fan, difference between BLI and isolated engines.

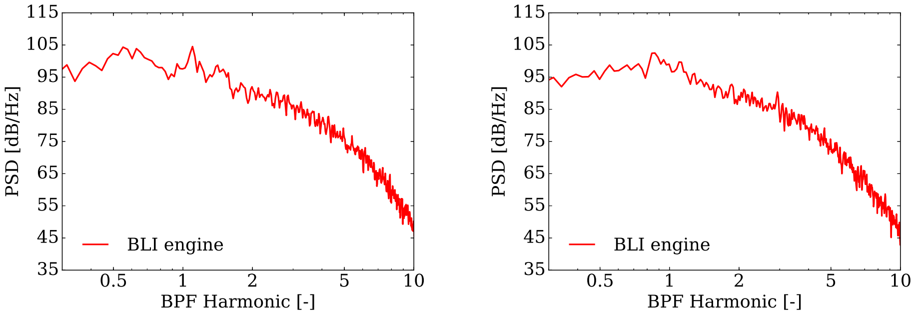

(a) *Directivity angle* $\theta = 140°$ (b) *Directivity angle* $\theta = 150°$

Figure 8.21: Far-field noise spectra on ground arc at downstream directivity angles: 140° (a) and 150° (b), BLI engine.

8.3.6. NOISE POWER LEVEL

In Fig. 8.22 one-side narrow-band source Power Level (PWL) is presented for both the BLI and isolated configurations (Fig. 8.22(a)). For convenience, the difference between the power levels of the two cases is also shown in Fig. 8.22(b). In this study, the PWL is computed by integration of the PSDs over the semi-spherical surface portion corresponding to the aforementioned microphone array, using the following formula:

$$\mathrm{PWL}(f) = \int_{\theta_{min}}^{\theta_{max}} \int_{\phi_{min}}^{\phi_{max}} R_s^2 \sin(\theta) \frac{[1 + M_\infty \cos(\theta)]^2 \mathrm{PSD}(f,\theta)}{2\rho_\infty a_\infty} \mathrm{d}\phi \mathrm{d}\theta \qquad (8.2)$$

where f is the frequency, R_s is the hemisphere radius, ϕ is the meridian arc angular position (defined as in Fig. 8.17) and varying from $\phi_{min} = 0°$ to $\phi_{max} = 180°$, whereas θ is the directivity angle varying from $\theta_{min} = 20°$ to $\theta_{max} = 160°$. Moreover, M_∞ is the free-stream Mach number, and ρ_∞ and a_∞ are the ambient density and speed of sound, respectively.

As previously observed, broadband component dominates the power level spectrum for the BLI configuration, as a consequence of the less axisymmetric rotor wakes and higher levels of turbulence impinging on the stator vanes. No tones at harmonics of the BPF are observed, and only a weak haystacked peak around BPF 1 is found. As mentioned before, such a broadened peak might be connected to blade-to-blade unsteady airloads correlation associated to the simultaneous impingement of large vortical structures with multiple neighboring fan blades. Finally, regarding the isolated engine, the PWL presents distinct tones at the first 3 blade-passing frequencies, and lower broadband source power levels, from 4-5 dB at high frequencies up to 15-18 dB at low ones, with respect to the BLI configuration.

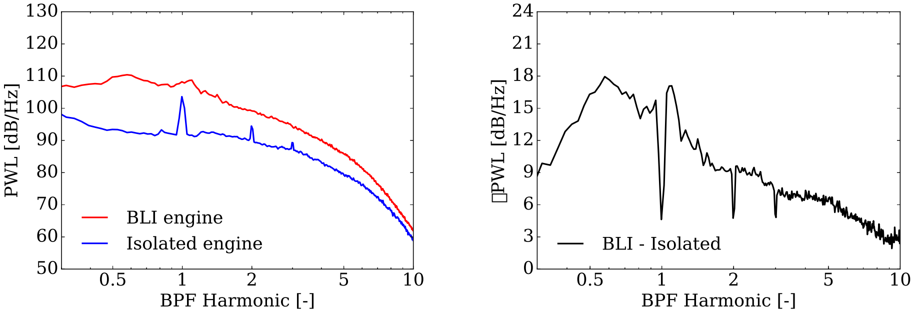

(a) *BLI and isolated engines*

(b) *BLI - isolated*

Figure 8.22: Source Power Level: BLI and isolated engines (a) and their difference (b).

8.3.7. EFFECTIVE PERCEIVED NOISE LEVEL

The analysis of BLI installation effects on fan noise is concluded by investigating the Effective Perceived Noise Level (EPNL) footprint during a take-off flight path with power cut-back. The EPNL is computed according to the FAR procedure [242] using the *Opty∂B*-FOOTPRINT code from Dassault Systèmes. Mathematical details on the EPNL tool and its validation can be found in Casalino *et al.* [249]. For the sake of conciseness, only a brief overview of the procedure is outlined in the following. First, the permeable FW-H approach is used to compute the far-field noise signals and, in turn, Narrow-Band Noise (NBN) spectra (in the frequency range 50Hz–10kHz) on 300 microphones distributed over a hemisphere of 60 m radius. Such a hemisphere is centered around the aircraft reference frame (denoted by x_a, y_a and z_a) and is rigidly connected to it, as sketched in Fig. 8.23. Then, for each microphone k on a ground carpet, and for every flight subsegment i of 0.5 sec duration, the emission position $(x_g, y_g, z_g)_k^i$ of the aircraft is determined (with x_g, y_g and z_g being the ground-fixed, i.e. inertial, reference frame coordinates). A ray is traced between the microphone k and the vehicle emission position, and its intersection S_k^i with the rotated hemisphere determines the point where the NBN spectra are interpolated from the closest microphones on the hemisphere. Similarly, the intersection $\tilde{S}_k^i$ between the reflected ray and the hemisphere is also determined, and the NBN spectra are interpolated at this point to account for ground reflection. Finally, the interpolated NBN spectra are projected on the ground carpet by applying spherical spreading, atmospheric absorption, Doppler effects and ground reflection.

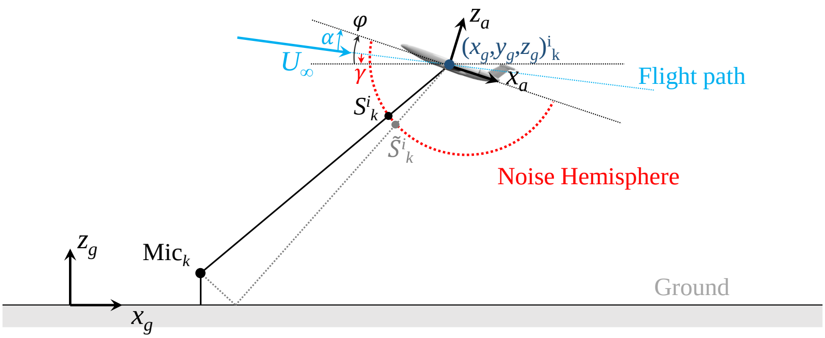

Figure 8.23: Sketch of the on-the-ground EPNL footprint calculation procedure. α, γ and φ denote the aircraft angle of attack, glide angle and pitch angle, respectively.

For the EPNL calculation, a rectilinear flight path of 2 km length (from $x_g = -1000$ m to $x_g = 1000$ m), 210 m altitude difference (from $z_g = 200$ m to $z_g = 410$ m) and 23.7 sec duration is considered. The free-stream conditions applied are those presented in Sec. 8.2 and an atmospheric relative humidity of 70% is considered. Figures 8.24(a) and 8.24(b) show the EPNL on a plane 1.2 m above the ground over an area of 2.5x2.5 km^2 for the BLI and isolated cases, respectively, whereas the EPNL difference between the two configurations is shown in Fig. 8.24(c). Since in this study simulations are performed by employing a symmetry plane located at the centerline of the aircraft, the EPNL footprint is computed by mirroring the source of noise (i.e. the noise hemisphere) with respect to the same plane (located at $y_g = 0$ m) prior to the projection of the NBN spectra on the ground microphone carpet. The two contributions of the mirrored hemispheres are added incoherently. As expected, due to the take-off flight path considered, both the EPNL contours show that the highest noise levels take place at the beginning of the flight trajectory, i.e. when the distance between the source of noise and the ground is the minimum. Then, for both cases, the on-the-ground noise levels gradually decreases along the flight direction as the noise source altitude increases. Nevertheless, the two configurations show quite different EPNL levels and directivity patterns. First, the EPNL map is characterized by a peak value of 108 EPNdB for the BLI case, which is roughly 10 EPNdB larger than that of the isolated one (98 EPNdB). Secondarily, the BLI configuration shows that the noise on the ground, during the take-off maneuver, is mainly radiated along the sideline and downstream directions, contrarily to the isolated case whose take-off noise radiation is predominantly directed upstream. Overall, the BLI case turns out to be from 4 EPNdB (front side) to 18 EPNdB (aft side) nosier than the isolated one for the operating condition hereof considered.

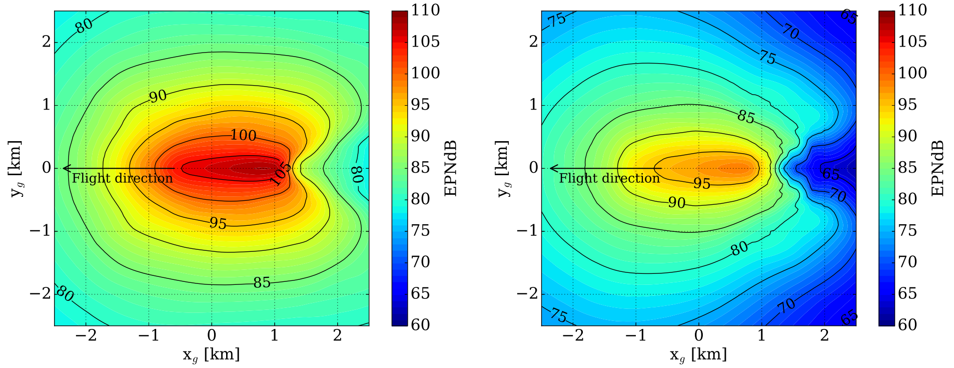

(a) *BLI engine* (b) *Isolated engine*

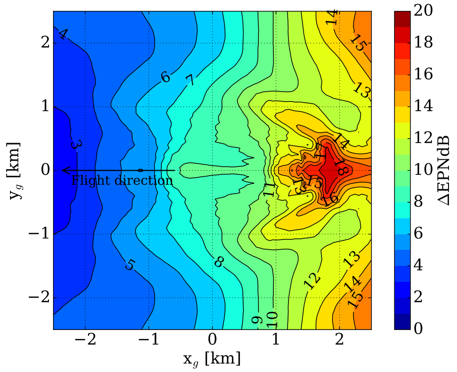

(c) *BLI - isolated*

Figure 8.24: EPNL on a plane 1.2 m above the ground during a take-off flight path with power cut-back: BLI engine (a), isolated engine (b) and their difference (c).

8.4. CONCLUSIONS

For the first time, a high-fidelity CFD/CAA simulation of a full-scale aircraft geometry comprehensive of a BLI fan/OGV stage was performed. A modified version of the Low-Noise configuration of the NASA SDT fan-stage was embedded into the ONERA NOVA fuselage in order to reproduce the NOVA BLI aircraft configuration. The numerical flow solution was obtained by solving the explicit, transient and compressible lattice-Boltzmann equation implemented in the high-fidelity CFD/CAA solver SIMULIA PowerFLOW®. The acoustic far-field was computed by using the Ffowcs Williams & Hawkings' integral solution applied to a permeable surface encompassing the fan-stage. Installation effects of the BLI configuration, which is not optimal, were investigated by comparison with an isolated setup of the modified Low-Noise SDT fan-stage geometry in terms of fan-stage velocity field, fan performances, fan blade unsteady airloads, far-field noise and on-the-ground noise footprint. All simulations were performed for an operating condition representative of a take-off with power cut-back.

The analysis of the fan-stage velocity field showed that, for the considered operating condition and geometry, the embedded BLI fan-stage caused high levels of mean flow distortion and flow separation at approximately 60% of the s-duct length and in proximity of the fan plane on the nacelle side. The mean flow distortion was found to be responsible of a low-frequency periodic variation of the fan blade sectional thrust for inboard blade sections. The ingestion of turbulence, associated to the flow separation on the s-duct and inlet walls, led to high levels of unsteadiness, as well as to a deficit in thrust generation in outboard blade regions. A reduction of the FPR by 2.5% and of the fan isentropic efficiency by 9.2% was observed for the BLI configuration compared to the isolated one. In addition, the BLI engine interstage flow field was characterized by less axisymmetric and coherent tangential velocity variations associated to the rotor wake, and higher levels of in-plane velocity fluctuations, compared to the isolated one. Finally, the BLI configuration showed a non-uniform and lower swirl recovery downstream of the stator compared to the isolated engine, as well as higher levels of turbulent fluctuations.

Far-field noise directivity predictions revealed that the noise is radiated most efficiently downstream the engine for the BLI layout, as also observed for the isolated engine. However, while the latter manifested both broadband and tonal noise contributions, no tones clearly emerged with respect to broadband levels for the BLI case. A Weak haystacked peak was found around BPF 1 for downstream observer angles. Such a peak might be connected to blade-to-blade unsteady airloads correlation associated to the simultaneous impingement of large vortical structures within the fuselage turbulent boundary-layer and separating from the s-duct wall with multiple neighboring fan blades. Overall, the BLI configuration showed from 10 to 20 dB higher broadband levels in the far-field compared those related to the isolated configuration, for most of the frequencies and directivity angles considered. The BLI layout resulted to be by 5-10 dB quieter than the isolated one on the ground arc, for directions nearly perpendicular to the engine axis and for frequencies higher than BPF 2, as a result of some airframe shielding related to the partial placement of the engine inside the fuselage. Finally, the BLI configuration is found to have a detrimental impact on cumulative noise levels during a take-off flight with power cut-back up to 18 EPNdB .

It should be recalled that the fan stage considered in this study was designed for isolated engines, thus it is not suitable for a operate in highly distorted flows such as in BLI configurations. Moreover, the current NOVA BLI configuration represents a rather idealized BLI-layout, due to the relative short s-duct length and the large portion of intake area embedded into the fuselage. A more conservative sizing, e.g. based on a longer s-duct length and a lower percentage of buried intake, would have reduced the amount of flow separation and distortion at the fan section, with expected benefits on fan-stage operability and noise emissions, however at the additional cost of higher nacelle mass, drag and inlet friction losses.

9

CONCLUSIONS AND RECOMMENDATIONS

No book can ever be finished.
While working on it,
we learn just enough
to find it immature
the moment we turn away from it.

Karl Popper

There is no real ending.
It's just the place,
where you stop the story.

Frank Herbert

This conclusive chapter summarizes the work presented in thesis along with its main findings. Recommendations, suggestions for improvements and future outlook are finally drawn.

9.1. INTRODUCTION

IN this work, numerical models based on the Lattice-Boltzmann/Very-Large Eddy Simulation (LB/VLES) method, coupled with the Ffowcs Williams & Hawkings' (FW-H) acoustic analogy (Chapter 3), have been applied for the identification, characterization and prediction of the primary sources of aerodynamic noise in open rotors/propellers and ducted-fans in non-conventional aircraft configurations (Chapter 2). In particular, the first objective of this thesis was the development and validation of a LB/VLES numerical model to predict free-transition turbulent boundary-layer trailing-edge noise at airfoil level, and investigate the impact of the serration flap angle upon the add-ons noise reduction effectiveness (Chapter 4). Then, the second objective concerned the development and validation of a LB/VLES computational approach based on a zig-zag transition trip to predict the performances and the tonal/broadband noise radiation of a propeller operating at low-Reynolds numbers (Chapter 5). The same computational approach was then exploited to address the impact of a non-axial inflow (i.e. yaw angle effects) on the tonal and broadband noise radiated by propellers operating at low blade-tip speed conditions (Chapter 6), which represented the third objective of this work. The fourth objective dealt with the assessment of the numerical method to predict rotor blade-vortex interaction noise, with and without the inclusion of the aerodynamic effects associated to the blade elastic deformations (Chapter 7). Finally, the fifth objective of this thesis was the analysis, characterization and quantification of the noise generation mechanisms and radiation in boundary-layer ingestion turbofan systems (Chapter 8). The story-line of this thesis is illustrated once again in Fig. 9.1, while the main findings of this work, as well as recommendations and future outlook, are summarized in the following subsections.

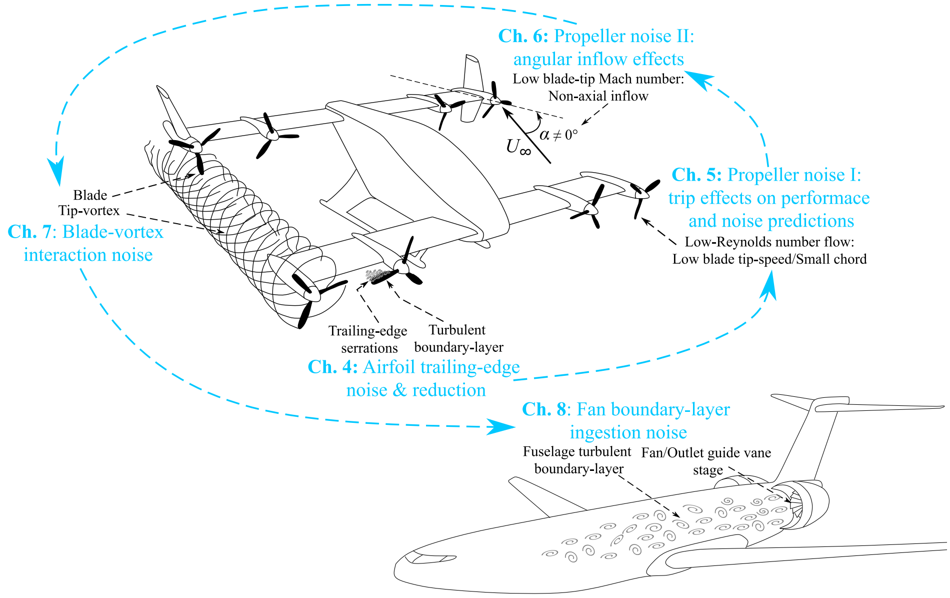

Figure 9.1: Story-line of this thesis.

9.2. SUMMARY AND MAIN RESULTS

AIRFOIL BLADE TRAILING-EDGE NOISE & REDUCTION

In Chapter 4, turbulent boundary-layer trailing-edge noise and its reduction by means of sawtooth serrations were investigated for a cambered and lifting airfoil (representing a propeller blade segment) undergoing natural boundary-layer transition at moderated Reynolds numbers ($Re = 1.43 \cdot 10^6$). The impact of the serration flap angle on the noise mitigation effectiveness was analyzed for two different airfoil angles of attack.

The LB/VLES numerical results were first compared against experimental data for a straight trailing-edge, revealing a good prediction of the natural boundary-layer transition process, as well as of the airfoil pressure distribution, boundary-layer profiles, far-field noise radiation and spanwise coherence length. However, a large over-prediction of the wall-pressure spectrum in proximity of the straight trailing-edge was observed. A further comparison against semi-empirical wall-pressure spectra, as well as a cross-comparison between numerical results, experiments, and semi-analytical far-field noise predictions (fed with experimental wall-pressure spectra) suggested that the observed discrepancies were not simply due to artifacts in the numerical simulations, but could be related to a combination of inaccuracies in both simulations and experiments.

Then, the influence of the serration flap angle on their noise reduction effectiveness was investigated by retrofitting the airfoil section with sawtooth serrations according to three different flap angle configurations (such that the serration was aligned with the chord, with the chamber line or was positioned in between these two layouts). For the positive and shallow negative airfoil angles of attack considered, the intermediate flap angle was found to have a minimal impact on the airfoil pressure distribution and to generate only a low pressure gradient across the serration, implying that this configuration should not considerably affect the performances and the steady loading noise when retrofitted to a rotor/propeller blade trailing-edge. Moreover, it manifested the overall best noise suppression behavior, except at very low frequencies, while the chord- and camber-aligned serrations showed opposite noise reduction behaviors depending on the specific airfoil angle of attack. The analysis of the serration scattering showed that no (or only minimal) destructive interference among noise sources distributed along the serrated edge is promoted when a serration is at incidence, compared to zero incidence cases.

Finally, the serration flap angle was found to influence the far-field noise emission primarily through a modification of: the effective angle at which the turbulent structures are convected over the serrated edge; the convection velocity and spanwise coherence length along the serration; the intensity of the hydrodynamic wall-pressure fluctuations that are scattered along the serrated edge. The first and last mechanisms were found to play the most significant role upon the far-field noise reduction, while the combined variation of the convection velocity and spanwise coherence length was found to influence the noise mitigation mainly at low frequency.

PROPELLER NOISE I: TRIP EFFECTS ON PERFORMANCE AND NOISE PREDICTIONS

In Chapter 5, the focus was extended to a complete propeller geometry operating at low-Reynolds numbers. A computational approach based the use of a zig-zag transition trip was employed to predict the performances and noise signature associated to a two-bladed propeller operated at low Reynolds numbers at industrial level. The transition trip was adopted to drive the numerical scheme switching from modeled to scale-resolving turbulence mode, and to trigger the formation of vortical structures with scales able to emulate the complexity of the low-Reynolds number boundary-layer on the blade (for the sake of turbulent boundary-layer trailing-edge noise radiation). Two different tripping strategies were considered by positioning the trip along the quarter-chord and the expected turbulent boundary-layer transition lines, respectively.

First, the numerical predictions were compared against loads and noise measurements carried out at TU-Delft. Thrust and torque predictions showed a satisfactory agreement with the experiments, although some discrepancies were observed for the former at low and middle advance ratios, and at intermediate ones for the latter. The trip position marginally affected the prediction of the thrust, and to a slightly larger extent that of the torque. The numerical tonal and broadband noise compared favorably against the experimental data, especially for intermediate advance ratios. A certain over-prediction of the broadband noise levels was found for the hover case, due to excessively high levels of turbulence generated by the trip under high blade loading conditions. Contrarily, at the highest advance ratio, the numerical results did not show the high-frequency broadband hump due to laminar boundary-layer instability noise, with the two trip approaches both underestimating the broadband noise. Tonal noise was not significantly influenced by the presence and position of the trip, whereas the broadband noise levels were found to be affected to a slightly larger extent by the chordwise position of the trip. Clean-SC beamforming noise maps calculations further showed that the trip self-noise did not contribute in a tangible way to the broadband noise levels.

The satisfactory agreement between the numerical thrust, torque and tonal/broadband noise and the experimental ones validated the proposed approach for the prediction of performances and noise radiation associated to low-Reynolds number propellers at engineering level. Moreover, the robustness of the proposed method for industrial studies was demonstrated by the low sensitivity of the trip chordwise location and height.

PROPELLER NOISE II: ANGULAR INFLOW EFFECTS

In Chapter 6, the previous approach based on the usage of a zig-zag transition trip was used to evaluate the impact of a non-axial inflow (i.e. non zero yaw angle or propeller angle of attack) on the aeroacoustics of propellers operating at low blade-tip speed conditions. The numerical results were first compared against forces and noise measurements carried out at TU-Delft, in order to assess the capability of the employed computational setup to predict loads, tonal and broadband noise modifications due to a non-zero propeller yaw angle.

Both absolute values and variations (due to the propeller yaw angle change) of the time-averaged thrust and torque were reasonably captured by the computational setup, although to a lower extent compared to those observed in the experimental data. The sectional angle of attack azimuthal variation was found to take place with a phase shift of 30° in advance with respect to that of the tangential velocity, causing the unsteady aerodynamic loadings to reach the highest and lowest values slightly after 90° and 270° in the azimuth, respectively. Moreover, the larger sectional thrust and torque increments observed on the blade advancing side, compared to the reductions occurring on the retreating one, were found to be the cause for the higher mean thrust and torque coefficients obtained in both numerical and experimental data for the propeller at incidence.

The computed tonal noise at BPF 1 and broadband noise above BPF 30 agreed well with the experimental data. Specifically, the numerical setup was able to capture the large tonal noise variation, as well as the moderate high-frequency broadband changes, at different observer locations due the variation of the propeller yaw angle. The effect of the propeller yaw angle on the far-field noise resulted in a large increment of the noise radiated along the propeller axis, and in an increase of the sound pressure level in the region from which the propeller was tilted away and a decrease in the opposite one. These aspects were consistent with previous studies on propellers operating at high blade-tip Mach numbers.

However, contrarily to the latter, the noise directivity change was found to be related only to the generation of deterministic unsteady loadings on the blade due to the periodic variation of the incidence and velocity experienced by the blade. This was proved by FW-H computations without the cross-flow velocity component, which provided almost identical results to those in which the in-plane convective effects were considered. This implied that the kinematic/acoustic modulation effect of the sources strength could be neglected for low-speed propellers at incidence. Finally, thickness and broadband noise did not show a significant directivity variation due to the propeller yaw angle, as a consequence of the moderate variation of the sectional angle of attack and velocity, which resulted in a negligible unsteady flow displacement and turbulent boundary-layer properties changes at the blade trailing-edge.

ROTOR BLADE-VORTEX INTERACTION NOISE

Chapter 7 addressed the noise associated to a more complex type of inflow non uniformity, which is that related to the velocity field induced by a blade tip-vortex, when a rotor rotor/propeller blade interacts or passes in close proximity to it. Simulations were performed by first considering a rigid blade motion ("fully-rigid" case). Then, a computational approach based on the application of a transpiration velocity boundary condition, a fluid body-force field and the steady deformed blade shape, was developed to account for the steady and unsteady aerodynamic effects associated to the blade elastic deformations ("semi-rigid" and "elastic" cases). The numerical results were compared against the experimental data from the HART-II benchmark.

It was shown that the modeling of the aerodynamic effects related to the elastic deformation of the rotor led to a substantial improvement of the trim settings, unsteady sectional airloads and BVI noise footprint predictions compared to the undeformed blade configuration. The level of accuracy of the "fully-rigid", "semi-rigid" and "elastic" setups was overall higher than that obtained (at a quite lower computational cost) by comprehensive codes for the same benchmark - although boundary element method-based comprehensive approaches provided a level of accuracy similar to that of the LBM simulation at a lower computation cost - and comparable to those obtained (at a similar computational cost) by CFD with prescribed blade elastic motion and/or CFD/CSD coupled approaches. However, contrarily to these methods, the proposed "semi-rigid" and "elastic" approaches required the blade deformations as inputs, in order to retrieve part of the aerodynamic effects associated to the blade elastic deformations, through the application of the transpiration velocity boundary condition/fluid body-force field, and/or the modification of the blade geometry into its steady deformed shape.

This study represented the first application, to the author's knowledge, of the lattice-Boltzmann method to the prediction of the unsteady airloads, the rotor wake development and the noise radiation of helicopter rotors in strong BVI conditions. Although some intrinsic inaccuracies in the numerical results were observed, mainly due to the lack of a proper simulation of the rotor blade elastic deformations, this study demonstrated the capability of the LB/VLES approach to successfully simulate rotors in BVI conditions at industrial level, enabling it as an additional method for the prediction of rotorcraft blade-vortex interaction noise.

FAN BOUNDARY-LAYER INGESTION NOISE

Finally, Chapter 8 was devoted to the study of another source of rotor installation noise, namely fan boundary-layer ingestion (BLI) noise, which can take place in eVTOLs characterized by distributed (electric) ducted fans, blended wing body or tube-and-wing aircraft with semi-buried or rear-mounted turbofan engines. Specifically, a modified version of the Low-Noise configuration of the NASA SDT fan-stage was embedded into the ONERA NOVA fuselage in order to reproduce the NOVA BLI aircraft configuration. Installation effects of the BLI configuration were investigated by comparison with an isolated engine setup of the modified Low-Noise SDT fan-stage geometry for an operating condition representative of a take-off with power cut-back ($M_\infty = 0.25$ and $M_{tip} = 0.87$). This study represented, to the author's knowledge, the first high-fidelity CFD/CAA simulation performed for a full-scale aircraft geometry comprehensive of a BLI fan/Outlet Guide Vane (OGV) stage.

The analysis of the fan-stage velocity field showed that, for the considered operating condition and geometry, the embedded BLI fan-stage caused high levels of mean flow distortion and flow separation at approximately 60% of the s-duct length and in proximity of the fan plane on the nacelle side. The mean flow distortion was found to be responsible of a low-frequency periodic variation of the fan blade sectional thrust for inboard blade sections, while the ingestion of turbulence, associated to the flow separation on the s-duct and inlet walls, led to high levels of unsteadiness, as well as to a deficit in thrust generation in outboard blade regions. In addition, the BLI engine interstage flow field (i.e. between the rotor and the stator) was characterized by less axisymmetric and coherent tangential velocity variations associated to the rotor wake, and higher levels of in-plane velocity fluctuations, compared to the isolated one.

For both the BLI and isolated configurations, the far-field noise was radiated mostly downstream the engine. However, the latter showed both broadband and tonal noise contributions, whereas no clear tones emerged from broadband levels for the BLI case and a weak wide-band peak was found around BPF 1 for downstream observer angles. Such a peak a was expected to be due to some blade-to-blade unsteady loadings correlation associated to the simultaneous impingement of large vortical structures within the fuselage turbulent boundary-layer and separating from the s-duct wall with multiple neighboring fan blades. Overall, the BLI configuration showed from 10 to 20 dB higher broadband levels in the far-field compared those related to the isolated configuration, for most of the frequencies and directivity angles considered. The BLI layout resulted to be by 5-10 dB quieter than the isolated one on a ground facing arc, for directions almost perpendicular to the engine axis and for frequencies higher than BPF 2, as a consequence of some airframe shielding due to the partial integration of the engine inside the fuselage. Moreover, the BLI configuration was found to increase the cumulative noise levels during a take-off flight with power cut-back up to 18 EPNdB compared to the same isolated fan-stage.

9.3. RECOMMENDATIONS AND FUTURE OUTLOOK

This subsection outlines some recommendations and suggestions for improvement for future studies:

- **Airfoil blade trailing-edge noise & reduction**. The comparison of the numerical wall-pressure spectra against the experimental ones, for the straight trailing-edge case (Chapter 4), showed a large over-prediction of the former compared to the latter, which could explain the moderate far-field noise levels over-estimation. On the other hand, semi-empirical wall-pressure spectrum computations agreed more favorably with the numerical data. Moreover, the semi-analytical trailing-edge noise predictions (fed with the experimental wall-pressure spectra) provided lower far-field noise spectra compared to the experimental ones. As previously mentioned, this could suggest that the discrepancies in the wall-pressure spectra and far-field noise results could be due to a combination of factors in both simulations and experiments. Therefore, future studies based on wall-resolved LES or DNS computations, as well as independent measurements for similar flow configurations, might shed more light on the case of the such differences.

  The analysis of the impact of the flap angle on the serration noise reduction effectiveness could be extended from a blade segment in rectilinear motion to a complete propeller operating at low blade-tip Mach numbers, for which the effects related to the presence of a spanwise velocity component might be important and alter the performances of a serration at a given flap angle, compared to the 2.5D case. Since a certain serration flap angle modifies the local airfoil circulation and lift, the serrated propeller simulation should be performed at iso-thrust conditions, to fairly compare the broadband trailing-edge noise reduction along with potential steady loading noise variations. Finally, the analysis of a low-speed propeller with a serrated trailing-edge in hover could also help to assess the benefit on the broadband self-noise reduction together with a potential modification of the broadband blade-turbulent wake interaction noise, due to a different turbulent wake organization and convection promoted by a given serration incidence.

- **Low-speed propeller noise**. The computational approach based on the use of a zig-zag transition trip was successfully validated in Chapter 5 for the prediction at industrial level of the performances and tonal/broadband noise of a propeller operating at low-Reynolds numbers. However, some discrepancies in both thrust and torque predictions, as well as broadband noise in hover and at high advance ratio, were observed. For cases in hover conditions or at very low advance ratios, the force and broadband noise predictions could be improved by considering a spanwise varying trip thickness, defined through the critical roughness height-based Reynolds number at the trip location, and a local mesh refinement around the trip geometry. This should yield to a less intrusive trip, with benefits especially in terms of thrust prediction and mitigation of the over-tripping conditions. In order to capture the laminar separation bubble and the associated aerodynamic and aeroacoustic effects, PowerFLOW® simulations with an improved VLES modeling will be attempted. In this new VLES model, the prediction of transitional phenomena is enhanced by taking into account local flow swirl effects for three dimensional flows. This extension is expected to improve the simulation of turbulent flows at moderate to low Reynolds numbers and low y^+ values. Ongoing simulations at high advance ratios[1] are showing promising results, with the improved VLES model being able to capture the laminar separation bubble, as well as the associated broadband hump in the far-field noise spectrum.

The trip approach based on the critical roughness height-based Reynolds number, as well as the extended PowerFLOW® VLES model, could be further used to explore angle of attack/yaw angle effects on the broadband noise of a propeller operating at low blade-tip speed, for advance ratios lower and higher than the intermediate one considered in Chapter 6 ($J = 0.4$). Moreover, the extended VLES model, which seems promising in capturing the laminar separation bubble, could be further exploited to investigate laminar boundary-layer instability noise reduction solutions through the elimination of the aeroacoustic feedback loop by means of serrated trailing-edges

- **Rotor blade-vortex interaction noise**. In Chapter 7, intrinsic inaccuracies in the prediction of blade-vortex interaction related phenomena were observed due to the lack of a proper simulation of the blade elastic deformations. For slender and highly flexible blades, such as those of a conventional helicopter main rotor, the prediction of these phenomena could only be further improved by reproducing the real elastic deformation motion of the blade in the aerodynamic simulation. This feature is not currently supported by the LBM solver employed in this work. Nevertheless, the prediction of both trim settings and low-frequency unsteady loadings induced by the blade torsional deformations could be further improved by developing an extended fluid body-force model, which includes higher harmonics of the reduced frequency, as well as the effects related to the torsional deformation amplitude, Mach number, and Reynolds number in the model coefficients[2]. The aerodynamic loadings obtained through the LBM simulation with improved fluid body-force model could be loose-coupled to a structural dynamics solver for the prediction of the blade deformation, in order to remove the limitation of the proposed blade deformation effects modeling, which required the knowledge of the kinematics of the blade deformation as input.

---

[1] Where, based on experimental evidences, the laminar separation bubble is expected to considerably influence the performance and the broadband noise radiation for the examined propeller and operating conditions.

[2] Currently, only the fundamental reduced frequency harmonic is considered, whereas the model coefficients have been assumed to change only with the reduced frequency (Appendix D).

It is worth to mention that for rotors and propellers equipped on novel eVTOL multi-rotor configurations, the rotor blades are expected to experience more moderate deflections compared to conventional helicopters, as a consequence of the smaller diameters and lower loading conditions. Moreover, blade-vortex interactions are expected to occur not only inter-rotors, but also intra-rotors. Hence, the modeling of the blade deformation effects is expected to be less important compared to conventional rotorcraft.

- **Fan boundary-layer ingestion noise**. In Chapter 8, it was shown that the boundary-layer ingesting fan was characterized by strong azimuthal fan blade loading unsteadiness, less axisymmetric and coherent rotor wake tangential velocity variations and higher levels of in-plane velocity fluctuations compared to the isolated engine, which resulted in higher broadband levels in the far-field noise spectra up to 20 dB and an increment of the cumulative noise levels up to 18 EPNdB. However, it should be recalled that the fan blades considered in this study were designed for operating in a conventional engine, thus they might not be suited for operating in highly distorted flows such as in a BLI configuration. Moreover, the current NOVA BLI configuration represented a rather idealized BLI-layout, due to the relative short s-duct length and the large portion of intake area embedded into the fuselage. A more conservative sizing, e.g. based on a longer s-duct length and a lower percentage of buried intake, would have reduced the amount of flow separation and distortion at the fan section, with expected benefits on fan-stage operability and noise emissions, however at the additional cost of higher nacelle mass, drag and inlet friction losses. As future outlook, simulations by employing flow-control techniques could be performed for the same BLI configuration in order to mitigate the flow separation over the s-duct wall and to assess related benefits in terms of noise emissions.

  A more realistic comparison between the isolated engine and the BLI configuration could be done by reducing the intake length for the former, since the extended intake for the isolated nacelle was not really representative of a classical UHBR engine with a short inlet. On the one hand, this is expected to change the cut-off/on behavior of the intake, thus reducing its capability to suppress the propagation of the acoustic modes excited by the fan and stator. On the other hand, the reduced intake length would make the fan stage more exposed to distorted inflows. The comparison between the non-BLI and BLI engines could be further improved by simulating the former in a classical under wing layout, thus also accounting for the potential noise reflection by the wing in the far-field noise radiation. These aspects are expected to lead to an increment of the noise radiated towards the ground by the canonical engine configuration, thus making the installation noise effects due to BLI less detrimental compared to the results shown in Chapter 8.

REFERENCES

[1] A. Gittens, S. Hocquard, A. de Juniac, F. Liu, and E. Fanning. Aviation Benefit Report 2019. *ICAO Technical report*, (2019). URL⟵.

[2] ICAO Eds. ICAO Long-Term Traffic Forecasts. *ICAO Technical report*, (2018). URL⟵.

[3] J. E. Penner, D. H. Lister, D. J. Griggs, D. J. Dokken, and M. McFarland (Eds.). Aviation and the Global Atmosphere: A Special Report of the Intergovernmental Panel on Climate Change. *Cambridge University Press*, (1999). DOI⟵.

[4] D. S. Lee, D. W. Fahey, P. M. Forster, P. J. Newton, R. C. N. Wit, L. L. Lim, B. Owen, and R. Sausen. Aviation and Global Climate Change in the 21st Century. *Atmospheric Environment*, **43**(22-23):3520–3537, (2009). DOI⟵.

[5] IATA Eds. Aircraft Technology Roadmap to 2050. *IATA Technical Report*, (2020). URL⟵.

[6] P. Schmollgruber, O. Atinault, I. Cafarelli, C. Döll, C. François, J. Hermetz, R. Liaboeuf, B. Paluch, and M. Ridel. Multidisciplinary Exploration of DRAGON: an ONERA Hybrid Electric Distributed Propulsion Concept. In *Proceedings of the AIAA Scitech 2019 Forum*, paper 1585, (2019). DOI⟵.

[7] L. Wiart, O. Atinault, R. Grenon, B. Paluch, and D. Hue. Development of NOVA Aircraft Configurations for Large Engine Integration Studies. In *Proceedings of the 33rd AIAA Applied Aerodynamics Conference*, paper 2254, (2015). DOI⟵.

[8] NASA Armstrong Fact Sheet: NASA X-57 Maxwell. URL⟵.

[9] J. F. Brouckaert, F. Mirville, K. Phuah, and P. Taferner. Clean Sky Research and Demonstration Programmes for Next-Generation Aircraft Engines. *The Aeronautical Journal*, **122**(1254):1163–1175, (2018). DOI⟵.

[10] J. Holden and N. Goel. Fast-Forwarding to a Future of On-demand Urban Air Transportation. *Uber Elevate White Paper*, (2016).

[11] S. Rizzi, D. L. Huff, B. S. Henderson, P. Bent, K. A. Pascioni, D. C. Sargent, D. L. Josephson, M. Marsan, H. He, and R. Snider. Urban Air Mobility Noise: Current Practice, Gaps, and Recommendations. *NASA/TP–2020-50074337*, (2020). URL⟵.

[12] Electric VTOL News^{TM}, Airbus CityAirbus. URL⟵.

[13] Electric VTOL News^{TM}, Volocopter VoloCity. URL⟵.

[14] Electric VTOL News^{TM}, Lift HEXA. URL←.

[15] Electric VTOL News^{TM}, Lilium Jet. URL←.

[16] Electric VTOL News^{TM}, Airbus A^3 Vahana. URL←.

[17] Electric VTOL News^{TM}, Bell Nexus 6HX. URL←.

[18] Electric VTOL News^{TM}, Uber eCRM-003. URL←.

[19] Electric VTOL News^{TM}, Aurora Pegasus PAV. URL←.

[20] B. Berglund, T. Lindvall, D. H. Schwela, World Health Organization, et al. Guidelines for Community Noise. *WHO Technical Report*, (1999). URL←.

[21] J. P. Clarke. The Role of Advanced Air Traffic Management in Reducing the Impact of Aircraft Noise and Enabling Aviation Growth. *Journal of Air Transport Management*, **9**(3):161–165, (2003). DOI←.

[22] FAA Eds. Aviation Noise Abatement Policy 2000. *Federal Register*, **65**(136):43802–43824, (2000). URL←.

[23] ICAO Eds. ICAO Annex 16: Environmental Protection, Volume I–Aircraft Noise. (2014). URL←.

[24] ICAO Eds. ICAO Annex 16: Environmental Protection, Volume II–Aircraft Engine Emissions. (2017). URL←.

[25] S. Kallas, M. Geoghegan-Quinn, M. Darecki, C. Edelstenne, T. Enders, E. Fernandez, and P. Hartman. Flightpath 2050 Europe's Vision for Aviation: Report of the High Level Group on Aviation Research. *European Commission Technical Report*, (2011). DOI←.

[26] H. H. Hubbard. *Aeroacoustics of Flight Vehicles: Theory and Practice. Volume 1: Noise Sources.* (1991). URL←.

[27] R. G. Rackl, G. Miller, Y. Guo, and K. Yamamoto. Airframe Noise Studies: Review and Future Direction. *NASA/CR-2005-213767*, (2005). URL←.

[28] H. H. Hubbard. *Aeroacoustics of Flight Vehicles: Theory and Practice. Volume 2: Noise Control.* (1991). URL←.

[29] C. Wagner, T. Hüttl, and P. Sagaut. *Large-Eddy Simulation for Acoustics*. Cambridge University Press, (2007). URL←.

[30] H. Chen, S. Chen, and W. Matthaeus. Recovery of the Navier-Stokes Equations Using a Lattice-Gas Boltzmann Method. *Physical Review A*, **45**(8):5339–5342, (1992). DOI←.

[31] H. Chen, C. Teixeira, and K. Molvig. Realization of Fluid Boundary Conditions via Discrete Boltzmann Dynamics. *International Journal of Modern Physics C*, **9**(8):1281–1292, (1998). DOI←.

[32] H. Chen, S. Kandasamy, S. A. Orszag, S. Succi, and V. Yakhot. Extended Boltzmann Kinetic Equation for Turbulent Flows. *Science*, **301**(5633):633–636, (2003). DOI⟵.

[33] H. Chen, S. Orszag, I. Staroselsky, and S. Succi. Expanded Analogy Between Boltzmann Kinetic Theory of Fluid and Turbulence. *Journal of Fluid Mechanics*, **519**:301–314, (2004). DOI⟵.

[34] J. E. Ffowcs Williams and D. L. Hawkings. Sound Generated by Turbulence and Surfaces in Arbitrary Motion. *Philosophical Transactions of the Royal Society of London, Series A*, **A264**(1151):321–342, (1969). DOI⟵.

[35] S. Glegg and W. Devenport. *Aeroacoustics of Low Mach number Flows: Fundamentals, Analysis, and Measurement.* Academic Press, (2017). URL⟵.

[36] C. E. Hughes. NASA Collaborative Research on the Ultra High Bypass Engine Cycle and Potential Benefits for Noise, Performance, and Emissions. *NASA/TM-2013-216345*, (2013). URL⟵.

[37] T. Brooks, D. Pope, and M. Marcolini. Airfoil Self-Noise and Prediction. *NASA Reference Publication 1218*, (1989). URL⟵.

[38] E. J. G. Arcondoulis, C. J. Doolan, A. C. Zander, and L. A. Brooks. A Review of Trailing Edge Noise Generated by Airfoils at Low to Moderate Reynolds Number. *Acoustics Australia*, **38**(3), (2010). URL⟵.

[39] R. E. Longhouse. Vortex Shedding Noise of Low Tip Speed, Axial Flow Fans. *Journal of Sound and Vibration*, **53**(1):25–46, (1977). DOI⟵.

[40] H. Arbey and J. Bataille. Noise Generated by Airfoil Profiles Placed in a Uniform Laminar Flow. *Journal of Fluid Mechanics*, **134**:33–47, (1983). DOI⟵.

[41] C. K. W. Tam. Discrete Tones of Isolated Airfoils. *The Journal of the Acoustical Society of America*, **55**(6):1173–1177, (1974). DOI⟵.

[42] G. Desquesnes, M. Terracol, and P. Sagaut. Numerical Investigation of the Tone Noise Mechanism over Laminar Airfoils. *Journal of Fluid Mechanics*, **591**:155, (2007). DOI⟵.

[43] S. Pröbsting and S. Yarusevych. Laminar Separation Bubble Development on an Airfoil Emitting Tonal Noise. *Journal of Fluid Mechanics*, **780**:167, (2015). DOI⟵.

[44] E. Arcondoulis, C. J. Doolan, A. C. Zander, L. A. Brooks, and Y. Liu. An Investigation of Airfoil Dual Acoustic Feedback Mechanisms at Low-to-Moderate Reynolds Number. *Journal of Sound and Vibration*, **460**:114887, (2019). DOI⟵.

[45] M. S. H. Boutilier and S. Yarusevych. Parametric Study of Separation and Transition Characteristics over an Airfoil at Low Reynolds Numbers. *Experiments in fluids*, **52**(6):1491–1506, (2012). DOI⟵.

[46] H. Schlichting and K. Gersten. *Boundary-Layer Theory.* Springer, (2016). DOI⟵.

[47] G. Yakhina, M. Roger, S. Moreau, L. Nguyen, and V. Golubev. Experimental and Analytical Investigation of the Tonal Trailing-Edge Noise Radiated by Low Reynolds Number Aerofoils. *Acoustics*, **2**(2):293–329, (2020). DOI←.

[48] A. Leslie, K. Wong, and D. Auld. Broadband Noise Reduction from a Mini-UAV Propeller Through Boundary Layer Tripping. In *Proceedings of the 14th AIAA/CEAS Aeroacoustics Conference (29th AIAA Aeroacoustics Conference)*, paper 3069, (2008). DOI←.

[49] D. Casalino, E. Grande, G. Romani, D. Ragni, and F. Avallone. Definition of a Benchmark for Low Reynolds Number Propeller Aeroacoustics. *Aerospace Science and Technology*, **113**:106707, (2021). DOI←.

[50] M. Roger and S. Moreau. Back-Scattering Correction and Further Extensions of Amiet's Trailing Edge Noise Model, Part 1: Theory. *Journal of Sound and Vibration*, **286**(3):477–506, (2005). DOI←.

[51] J. E. Ffowcs Williams and L. H. Hall. Aerodynamic Sound Generation by Turbulent Flow in the Vicinity of a Scattering Half-Plane. *Journal of Fluid Mechanics*, **40**:657–670, (1970). DOI←.

[52] S. Lee, L. Ayton, F. Bertagnolio, S. Moreau, T. P. Chong, and P. Joseph. Turbulent Boundary Layer Trailing-Edge Noise: Theory, Computation, Experiment, and Application. *Progress in Aerospace Sciences*, **126**:100737, (2021). DOI←.

[53] M. J. Lighthill. On Sound Generated Aerodynamically: I. General Theory. *Proceeding of The Royal Society of London A*, **A211**(1107):564–578, (1952). DOI←.

[54] W. C. P. van der Velden. Computational Aeroacoustic Approaches for Wind Turbine Blade Noise Prediction. *PhD thesis, Delft University of Technology*, (2017). URL←.

[55] S. Pröbsting. Airfoil Self-Noise: Investigation With Particle Image Velocimetry. *PhD thesis, Delft University of Technology*, (2015). URL←.

[56] S. Oerlemans. Reduction of Wind Turbine Noise Using Blade Trailing Edge Devices. In *Proceedings of the 22nd AIAA/CEAS Aeroacoustics Conference*, paper 3018, (2016). DOI←.

[57] Z. Ning, R. W. Wlezien, and H. Hu. An Experimental Study on Small UAV Propellers with Serrated Trailing Edges. In *Proceedings of the 47th AIAA Fluid Dynamics Conference*, paper 3813, (2017). DOI←.

[58] A. Halimi, B. G. Marinus, and S. Larbi. Analytical Prediction of Broadband Noise from Mini-RPA Propellers with Serrated Edges. *International Journal of Aeroacoustics*, **18**(4-5):517–535, (2019). DOI←.

[59] W. K. Blake. *Mechanics of Flow-Induced Sound and Vibration*. Academic Press, (1986). URL←.

[60] M. Roger and S. Moreau. Tonal-Noise Assessment of Quadrotor-Type UAV Using Source-Mode Expansions. *Acoustics*, **2**(3):674–690, (2020). DOI⟵.

[61] M. Roger. Computational Aeroacoustics: On the Noise from Open Rotors. *Von Karman Institute Lecture Notes*, (2006). URL⟵.

[62] C. Tung, Y. Yu, and S. Low. Aerodynamic Aspects of Blade-Vortex Interaction (BVI). In *Proceedings of the AIAA Fluid Dynamics Conference*, paper 2010, (1996). DOI⟵.

[63] H. Y. Yung. Rotor Blade–Vortex Interaction Noise. *Progress in Aerospace Sciences*, **36**(2):97–115, (2000). DOI⟵.

[64] S. Glegg, W. J. Devenport, K. S. Wittmer, and D. S. Pope. Broadband Helicopter Noise Generated by Blade Wake Interactions. *Journal of the American Helicopter Society*, **44**(4):293–301, (1999). DOI⟵.

[65] M. L. Wilbur and W. K. Wilkie. Active-Twist Rotor Control Applications for UAVs. In *Transformational Science And Technology For The Current And Future Force*, pages 185–192. World Scientific, (2006). DOI⟵.

[66] A. Anobile, G. Bernardini, M. Gennaretti, and C. Testa. Synthesis of Active Twist Controller for Rotor Blade–Vortex Interaction Noise Alleviation. *Journal of Aircraft*, **53**(6):1865–1874, (2016). DOI⟵.

[67] D. Casalino, W. C. P. van der Velden, and G. Romani. Community Noise of Urban Air Transportation Vehicles. In *Proceedings of the AIAA Scitech 2019 Forum*, paper 1834, (2019). DOI⟵.

[68] M. Roger. Computational Aeroacoustics: Duct Acoustics and Turbomachinery Noise. *Von Karman Institute Lecture Notes*, (2006). URL⟵.

[69] S. Moreau. Turbomachinery Noise Predictions: Present and Future. *Acoustics*, **1**(1):92–116, (2019). DOI⟵.

[70] M. Roger. Fundamentals of In-Duct Propagation. *ADOPSYS Lecture Notes*, (2017).

[71] S. W. Rienstra. Fundamentals of Duct Acoustics. *Von Karman Institute Lecture Notes*, (2015). URL⟵.

[72] E. Envia. Fan Noise Reduction: an Overview. *International Journal of Aeroacoustics*, **1**(1):43–64, (2002). DOI⟵.

[73] E. Envia. Intake Noise Issues: Measurements, Modelling & Prediction, and Mitigation. *Von Karman Institute Lecture Series*, (2011). URL⟵.

[74] A. Uranga, M. Drela, E. M. Greitzer, D. K. Hall, N. A. Titchener, M. K. Lieu, N. M. Siu, C. Casses, A. C. Huang, G. M. Gatlin, et al. Boundary Layer Ingestion Benefit of the D8 Transport Aircraft. *AIAA Journal*, **55**(11):3693–3708, (2017). DOI⟵.

[75] F. Petrosino, M. Barbarino, and M. Staggat. Aeroacoustics Assessment of an Hybrid Aircraft Configuration with Rear-Mounted Boundary Layer Ingested Engine. *Applied Sciences*, **11**(7):2936, (2021). DOI⟵.

[76] I. Clark, R. H. Thomas, and Y. Guo. Aircraft System Noise Assessment of the NASA D8 Subsonic Transport Concept. In *Proceedings of the 2018 AIAA/CEAS Aeroacoustics Conference*, paper 3124, (2018). DOI⟵.

[77] D. Hawkings. Multiple Tone Generation by Transonic Compressors. *Journal of Sound and Vibration*, **17**(2):241–250, (1971). DOI⟵.

[78] K. S. Brentner and F. Farassat. Analytical Comparison of the Acoustic Analogy and Kirchhoff Formulation for Moving Surfaces. *AIAA Journal*, **36**(8):1379–1386, (1998). DOI⟵.

[79] R. Ewert and W. Schröder. Acoustic Perturbation Equations Based on Flow Decomposition via Source Filtering. *Journal of Computational Physics*, **188**(2):365–398, (2003). DOI⟵.

[80] C. Mockett, W. Haase, and D. Schwamborn. *Go4Hybrid: Grey Area Mitigation for Hybrid RANS-LES Methods*, volume 134. Springer, (2018). DOI⟵.

[81] T. Krüger, H. Kusumaatmaja, A. Kuzmin, O. Shardt, G. Silva, and E. M. Viggen. The Lattice Boltzmann Method. *Springer International Publishing*, **10**(978-3):4–15, (2017). URL⟵.

[82] W. Bechara, C. Bailly, P. Lafon, and S. M. Candel. Stochastic Approach to Noise Modeling for Free Turbulent Flows. *AIAA Journal*, **32**(3):455–463, (1994). DOI⟵.

[83] D. Casalino, S. Moreau, and M. Roger. One, No One and One Hundred Thousand Methods for Low-Speed Fan Noise Prediction. *International Journal of Aeroacoustics*, **9**(3):307–327, (2010). DOI⟵.

[84] T. Colonius and S. K. Lele. Computational Aeroacoustics: Progress on Nonlinear Problems of Sound Generation. *Progress in Aerospace sciences*, **40**(6):345–416, (2004). DOI⟵.

[85] M. Wang, J. B. Freund, and S. K. Lele. Computational Prediction of Flow-Generated Sound. *Annu. Rev. Fluid Mech.*, **38**:483–512, (2006). DOI⟵.

[86] P. G. Tucker. *Computational Aeroacoustics*, pages 271–324. Springer Netherlands, (2014). DOI⟵.

[87] C. Bailly and D. Juve. Numerical Solution of Acoustic Propagation Problems Using Linearized Euler Equations. *AIAA Journal*, **38**(1):22–29, (2000). DOI⟵.

[88] J.-H. Seo and Y. J. Moon. Perturbed Compressible Equations for Aeroacoustic Noise Prediction at Low Mach Numbers. *AIAA Journal*, **43**(8):1716–1724, (2005). DOI⟵.

[89] D. Casalino. An Advanced Time Approach for Acoustic Analogy Predictions. *Journal of Sound and Vibration*, **261**(4):583–612, (2003). DOI←.

[90] D. Casalino, A. F. P. Ribeiro, E. Fares, and S. Nölting. Lattice-Boltzmann Aeroacoustic Analysis of the LAGOON Landing Gear Configuration. *AIAA Journal*, **52**(6):1232–1248, (2014). DOI←.

[91] D. Casalino, A. F. P. Ribeiro, and E. Fares. Facing Rim Cavities Fluctuation Modes. *Journal of Sound and Vibration*, **333**(13):2812–2830, (2014). DOI←.

[92] M. Khorrami, E. Fares, and D. Casalino. Towards Full Aircraft Airframe Noise Prediction: Lattice Boltzmann Simulations. In *Proceedings of the 20th AIAA/CEAS Aeroacoustics Conference*, paper 2481, (2014). DOI←.

[93] E. Fares, D. Casalino, and M. Khorrami. Evaluation of Airframe Noise Reduction Concepts via Simulations Using a Lattice Boltzmann Approach. In *Proceedings of the 21st AIAA/CEAS Aeroacoustics Conference*, paper 2988, (2015). DOI←.

[94] W. C. P. van der Velden, D. Casalino, P. Gopalakrishnan, A. Jammalamadaka, Y. Li, R. Zhang, and H. Chen. Validation of Jet Noise Simulations and Resulting Insights of Acoustic Near Field. *AIAA Journal*, **12**(57):5156–5167, (2019). DOI←.

[95] D. Casalino, A. Hazir, and A. Mann. Turbofan Broadband Noise Prediction using the Lattice Boltzmann Method. In *Proceedings of the 22nd AIAA/CEAS Aeroacoustics Conference*, paper 2945, (2016). DOI←.

[96] I. Gonzalez-Martino and D. Casalino. Fan Tonal and Broadband Noise Simulations at Transonic Operating Conditions Using Lattice-Boltzmann Methods. In *Proceedings of the 2018 AIAA/CEAS Aeroacoustics Conference*, paper 3919, (2018). DOI←.

[97] S. Succi. *The Lattice Boltzmann Equation: for Fluid Dynamics and Beyond*. Oxford university press, (2001). DOI←.

[98] X. Shan, X.-F. Yuan, and H. Chen. Kinetic Theory Representation of Hydrodynamics: a Way Beyond the Navier-Stokes Equation. *Journal of Fluid Mechanics*, **550**:413, (2006). DOI←.

[99] T. Astoul. Towards Improved Lattice Boltzmann Aeroacoustic Simulations with Non-Uniform Grids: Application to Landing Gears Noise Prediction. *PhD Thesis, Aix-Marseille University*, (2021). DOI←.

[100] H. Chen, R. Zhang, and P. Gopalakrishnan. Filtered Lattice Boltzmann Collision Formulation Enforcing Isotropy and Galilean Invariance. *Physica Scripta*, **95**(3):034003, (2020). URL←.

[101] P. L. Bhatnagar, E. P. Gross, and M. Krook. A Model for Collision Processes in Gases. I. Small Amplitude Processes in Charged and Neutral One-Component Systems. *Physical Review*, **94**(3):511–525, (1954). DOI←.

[102] S. Chapman and T. G. Cowling. *The Mathematical Theory of Non-Uniform Gases: an Account of the Kinetic Theory of Viscosity, Thermal Conduction and Diffusion in Gases.* Cambridge University Press, (1990). URL↩.

[103] X. Nie, X. Shan, and H. Chen. A Lattice-Boltzmann/Finite-Difference Hybrid Simulation of Transonic Flow. In *Proceedings of the 47th AIAA Aerospace Sciences Meeting including The New Horizons Forum and Aerospace Exposition*, paper 0139, (2009). DOI↩.

[104] E. Fares, M. Wessels, R. Zhang, C. Sun, N. Gopalaswamy, P. Roberts, J. Hoch, and H. Chen. Validation of a Lattice-Boltzmann Approach for Transonic and Supersonic Flow Simulations. In *Proceedings of the 52nd AIAA Aerospace Sciences Meeting*, paper 952, (2014). DOI↩.

[105] X. Shan and H. Chen. Lattice Boltzmann Model for Simulating Flows with Multiple Phases and Components. *Physical Review E*, **47**(3):1815, (1993). DOI↩.

[106] M. Sbragaglia, R. Benzi, L. Biferale, H. Chen, X. Shan, and S. Succi. Lattice Boltzmann Method with Self-Consistent Thermo-Hydrodynamic Equilibria. *Journal of Fluid Mechanics*, **628**:299–309, (2009). DOI↩.

[107] R. Zhang, C. Sun, Y. Li, R. Satti, R. Shock, J. Hoch, and H. Chen. Lattice Boltzmann Approach for Local Reference Frames. *Communications in Computational Physics*, **9**(5):1193–1205, (2011). DOI↩.

[108] J. P. Boris, F. F. Grinstein, E. S. Oran, and R. L. Kolbe. New Insights into Large Eddy Simulation. *Fluid Dynamics Research*, **10**(4-6):199, (1992). DOI↩.

[109] V. Yakhot and S. A. Orszag. Renormalization Group Analysis of Turbulence. I. Basic Theory. *Journal of Scientific Computing*, **1**(1):3–51, (1986). DOI↩.

[110] V. Yakhot, S. A. Orszag, S. Thangam, T. B. Gatski, and C. G. Speziale. Development of Turbulence Models for Shear Flows by a Double Expansion Technique. *Physics of Fluids A*, **4**(7):1510–1520, (1992). DOI↩.

[111] C. M. Teixeira. Incorporating Turbulence Models into the Lattice-Boltzmann Method. *International Journal of Modern Physics C*, 9:1159–1175, (1998). DOI↩.

[112] C. G. Alexander, H. Chen, S. Kandasamy, R. Shock, and S. R. Govindappa. Simulations of Engineering Thermal Turbulent Flows Using a Lattice Boltzmann Based Algorithm. *ASME-PUBLICATIONS-PVP*, **424**:115–126, (2001). URL↩.

[113] R. B. Kotapati, R. Shock, and H. Chen. Lattice-Boltzmann Simulations of Flows Over Backward-Facing Inclined Steps. *International Journal of Modern Physics C*, **25**(01):1340021, (2014). DOI↩.

[114] B. E. Launder and D. B. Spalding. The Numerical Computation of Turbulent Flows. *Computer Methods in Applied Mechanics and Engineering*, **3**:269–269, (1974). DOI↩.

[115] G. A. Brès, F. Pèrot, and D. M. Freed. Properties of the Lattice-Boltzmann Method for Acoustics. In *Proceedings of the 15th AIAA/CEAS Aeroacoustics Conference (30th AIAA Aeroacoustics Conference)*, paper 3395, (2009). DOI↩.

[116] F. Farassat and G. P. Succi. The Prediction of Helicopter Discrete Frequency Noise. *Vertica*, **7**(4):309–320, (1983). DOI↩.

[117] K. S. Brentner and F. Farassat. Modeling Aerodynamically Generated Sound of Helicopter Rotors. *Progress in Aerospace Sciences*, **39**(2-3):83–120, (2003). DOI↩.

[118] G. A. Brès, K. S. Brentner, G. Perez, and H. E. Jones. Maneuvering Rotorcraft Noise Prediction. *Journal of Sound and Vibration*, **275**(3-5):719–738, (2004). DOI↩.

[119] B. Goldman and K. S. Brentner. New Algorithms for Reduced Memory and Real-Time Noise Prediction. In *Proceedings of the 18th AIAA/CEAS Aeroacoustics Conference*, paper 2237, (2012). DOI↩.

[120] P. Di Francescantonio. A New Boundary Integral Formulation for the Prediction of Sound Radiation. *Journal of Sound and Vibration*, **202**(4):491–509, (1997). DOI↩.

[121] C. Testa, F. Porcacchia, S. Zaghi, and M. Gennaretti. Study of a FWH-based Permeable-Surface Formulation for Propeller Hydroacoustics. *Ocean Engineering*, **240**:109828, (2021). DOI↩.

[122] L. V. Lopes, D. D. Boyd, D. M. Nark, and K. E. Wiedemann. Identification of Spurious Signals from Permeable Ffowcs Williams and Hawkings Surfaces. In *Proceedings of the 73rd American Helicopter Society Annual Forum (FORUM 73)*, (2017). URL↩.

[123] P. R. Spalart, K. V. Belyaev, M. L. Shur, M. K. Strelets, and A. K. Travin. On the Differences in Noise Predictions Based on Solid and Permeable Surface Ffowcs Williams–Hawkings Integral Solutions. *International Journal of Aeroacoustics*, **18**(6-7):621–646, (2019). DOI↩.

[124] S. Mendez, M. Shoeybi, S. K. Lele, and P. Moin. On the use of the Ffowcs Williams-Hawkings Equation to Predict Far-Field Jet Noise from Large-Eddy Simulations. *International Journal of Aeroacoustics*, **12**(1/2):1–20, (2013). DOI↩.

[125] D. Lockard and J. Casper. Permeable Surface Corrections for Ffowcs Williams and Hawkings Integrals. In *Proceedings of the 11th AIAA/CEAS Aeroacoustics Conference*, paper 2995, (2015). DOI↩.

[126] G. Rahier, M. Huet, and J. Prieur. Additional Terms for the Use of Ffowcs Williams and Hawkings Surface Integrals in Turbulent Flows. *Computers & Fluids*, **120**:158–172, (2015). DOI↩.

[127] T. Ikeda, S. Enomoto, K. Yamamoto, and K. Amemiya. Quadrupole Corrections for the Permeable-Surface Ffowcs Williams–Hawkings Equation. *AIAA Journal*, **55**(7):2307–2320, (2017). DOI↩.

[128] G. Romani, D. Casalino, and W. C. P. van der Velden. Numerical Analysis of Airfoil Trailing-Edge Noise for Straight and Serrated Edges at Incidence. *AIAA Journal*, **59**(7):2558–2577, (2021). DOI⟵.

[129] R. H. Schlinker and R. K. Amiet. Helicopter Trailing Edge Noise. In *Proceedings of the 7th AIAA Aeroacoustics Conference*, (1981). DOI⟵.

[130] Y. N. Kim and A. R. George. Trailing-Edge Noise from Hovering Rotors. *AIAA Journal*, **20**(9):1167–1174, (1982). DOI⟵.

[131] Y. Rozenberg, M. Roger, and S. Moreau. Rotating Blade Trailing-Edge Noise: Experimental Validation of Analytical Model. *AIAA Journal*, **48**(5):951–962, (2010). DOI⟵.

[132] S. Oerlemans, P. Sijtsma, and B. M. López. Location and Quantification of Noise Sources on a Wind Turbine. *Journal of sound and vibration*, **299**(4-5):869–883, (2007). DOI⟵.

[133] S. Wagner, R. Bareiss, and G. Guidati. *Wind Turbine Noise*. Springer Science & Business Media, (2012). DOI⟵.

[134] M. S Howe. Aerodynamic Noise of a Serrated Trailing Edge. *Journal of Fluids and Structures*, **5**(1):33–45, (1991). DOI⟵.

[135] M. S. Howe. Noise Produced by a Sawtooth Trailing Edge. *The Journal of the Acoustical Society of America*, **90**(1):482–487, (1991). DOI⟵.

[136] M. Herr and W. Dobrzynski. Experimental Investigations in Low-Noise Trailing Edge Design. *AIAA Journal*, **43**(6):1167–1175, (2005). DOI⟵.

[137] D. J. Moreau and C. J. Doolan. Noise-Reduction Mechanism of a Flat-Plate Serrated Trailing Edge. *AIAA Journal*, 51(**10**):2513–2522, (2013). DOI⟵.

[138] M. Azarpeyvand, M. Gruber, and P. F. Joseph. An Analytical Investigation of Trailing Edge Noise Reduction Using Novel Serrations. In *Proceedings of the 19th AIAA/CEAS Aeroacoustics Conference*, paper 2009, (2013). DOI⟵.

[139] M. Gruber, P. F. Joseph, and M. Azarpeyvand. An Experimental Investigation of Novel Trailing Edge Geometries on Airfoil Trailing Edge Noise Reduction. paper 2011, (2013). DOI⟵.

[140] T. P. Chong and A. Vathylakis. On the Aeroacoustic and Flow Structures Developed on a Flat Plate with a Serrated Sawtooth Trailing Edge. *Journal of Sound and Vibration*, **354**:65–90, (2015). DOI⟵.

[141] C. Arce-León, F. Avallone, S. Pröbsting, and D. Ragni. PIV Investigation of the Flow Past Solid and Slitted Sawtooth Serrated Trailing Edges. In *Proceedings of the 54th AIAA Aerospace Sciences Meeting*, paper 1014, (2016). DOI⟵.

[142] C. Arce-León, D. Ragni, S. Pröbsting, F. Scarano, and J. Madsen. Flow Topology and Acoustic Emissions of Trailing Edge Serrations at Incidence. *Experiments in Fluids*, **57**(5):91, (2016). DOI⟻.

[143] W. C. P. van der Velden, A. van Zuijlen, and D. Ragni. Flow Topology and Noise Emission Around Straight, Serrated and Slitted Trailing Edges using the Lattice Boltzmann Methodology. In *Proceedings of the 22nd AIAA/CEAS Aeroacoustics Conference*, paper 3021, (2016). DOI⟻.

[144] F. Avallone, S. Pröbsting, and D. Ragni. Three-Dimensional Flow Field Over a Trailing-Edge Serration and Implications on Broadband Noise. *Physics of Fluids*, **28**(11):117101, (2016). DOI⟻.

[145] F. Avallone, W. C. P. Van der Velden, D. Ragni, and D. Casalino. Noise Reduction Mechanisms of Sawtooth and Combed-Sawtooth Trailing-Edge Serrations. *Journal of Fluid Mechanics*, **848**:560–591, (2018). DOI⟻.

[146] A. Vathylakis, C. C. Paruchuri, T. P. Chong, and P. Joseph. Sensitivity of Aerofoil Self-Noise Reductions to Serration Flap Angles. In *Proceedings of the 22nd AIAA/CEAS Aeroacoustics Conference*, paper 2837, (2016). DOI⟻.

[147] C. Arce-León, R. Merino-Martínez, D. Ragni, F. Avallone, F. Scarano, S. Pröbsting, M. Snellen, D. G. Simons, and J. Madsen. Effect of Trailing Edge Serration-flow Misalignment on Airfoil Noise Emissions. *Journal of Sound and Vibration*, **405**:19–33, (2017). DOI⟻.

[148] M. Gruber, P. Joseph, and T. P. Chong. Experimental Investigation of Airfoil Self Noise and Turbulent Wake Reduction by the Use of Trailing Edge Serrations. In *Proceedings of the 16th AIAA/CEAS Aeroacoustics Conference*, paper 3803, (2010). DOI⟻.

[149] A. Fischer. Experimental Characterization of Airfoil Boundary Layers for Improvement of Aeroacoustic and Aerodynamic Modeling. *PhD Thesis, Technical University of Denmark*, (2011). URL⟻.

[150] M. Drela. XFOIL: An Analysis and Design System for Low Reynolds Number Airfoils. In *Low Reynolds Number Aerodynamics*, pages 1–12. Springer, (1989). DOI⟻.

[151] D. Ragni, F. Avallone, W. C. P. van der Velden, and D. Casalino. Measurements of Near-Wall Pressure Fluctuations for Trailing-Edge Serrations and Slits. *Experiments in Fluids*, **60**(1):6, (2019). DOI⟻.

[152] J. C. Bhatia, F. Durst, and J. Jovanovic. Corrections of Hot-Wire Anemometer Measurements Near Walls. *Journal of Fluid Mechanics*, **122**:411–431, (1982). DOI⟻.

[153] J. Jeong and F. Hussain. On the Identification of a Vortex. *Journal of Fluid Mechanics*, **285**:69–94, (1995). DOI⟻.

[154] Y. Rozenberg, G. Robert, and S. Moreau. Wall-Pressure Spectral Model Including the Adverse Pressure Gradient Effects. *AIAA Journal*, **50**(10):2168–2179, (2012). DOI⟵.

[155] M. Kamruzzaman, D. Bekiropoulos, T. Lutz, W. Würz, and E. Krämer. A Semi-Empirical Surface Pressure Spectrum Model for Airfoil Trailing-Edge Noise Prediction. *International Journal of Aeroacoustics*, **14**(5-6):833–882, (2015). DOI⟵.

[156] S. Lee. Empirical Wall-Pressure Spectral Modeling for Zero and Adverse Pressure Gradient Flows. *AIAA Journal*, **56**(5):1818–1829, (2018). DOI⟵.

[157] G. M. Corcos. The Structure of a Turbulent Pressure Field in Boundary-Layer Flows. *Journal of Fluid Mechanics*, **18**:353–378, (1964). DOI⟵.

[158] Y. Rozenberg, S. Moreau, M. Henner, and S. Morris. Fan Trailing-Edge Noise Prediction Using RANS Simulations. In *Proceedings of the 16th AIAA/CEAS Aeroacoustics Conference*, paper 3720, (2010). DOI⟵.

[159] S. Lee and J. G. Shum. Prediction of Airfoil Trailing-Edge Noise Using Empirical Wall-Pressure Spectrum Models. *AIAA Journal*, **57**(3):888–897, (2019). DOI⟵.

[160] M. S. Howe. A Review of the Theory of Trailing-Edge Noise. *Journal of Sound and Vibration*, 61(**3**):437–465, (1978). DOI⟵.

[161] W. R. Wolf and S. K. Lele. Trailing-Edge Noise predictions Using Compressible Large-Eddy Simulation and Acoustic Analogy. *AIAA Journal*, **50**(11):2423–2434, (2012). DOI⟵.

[162] J. Christophe, J. Anthoine, and B. Leduc. Application of Hybrid Methods to High Frequency Aeroacoustics. *PhD Thesis, Von Karman Institute/Université Libre de Bruxelles*, (2011). URL⟵.

[163] D. Palumbo. Determining Correlation and Coherence Lengths in Turbulent Boundary Layer Flight Data. *Journal of Sound and Vibration*, **331**(16):3721–3737, (2012). DOI⟵.

[164] S. Pröbsting, F. Scarano, M. Bernardini, and S. Pirozzoli. On the Estimation of Wall Pressure Coherence Using Time-Resolved Tomographic PIV. *Experiments in fluids*, **54**(7):1567, (2013). DOI⟵.

[165] B. Lyu, M. Azarpeyvand, and S. Sinayoko. Prediction of Noise from Serrated Trailing Edges. *Journal of Fluid Mechanics*, **793**:556–588, (2016). DOI⟵.

[166] R. K. Amiet. Noise Due to Turbulent Flow Past a Trailing Edge. *Journal of Sound and Vibration*, **47**(3):387–393, (1976). DOI⟵.

[167] G. P. Romano. Analysis of Two-Point Velocity Measurements in Near-Wall Flows. *Experiments in fluids*, **20**(2):68–83, (1995). DOI⟵.

[168] L. E. Jones and R. D. Sandberg. Acoustic and Hydrodynamic Analysis of the Flow Around an Aerofoil with Trailing-Edge Serrations. *Journal of Fluid Mechanics*, **706**:295–322, (2012). DOI⟵.

[169] G. Romani, E. Grande, F. Avallone, D. Ragni, and D. Casalino. Performance and Noise Prediction of Low-Reynolds Number Propellers using the Lattice-Boltzmann Method. *Aerospace Science and Technology*, In Press:107086, (2021). DOI⟵.

[170] G. Sinibaldi and L. Marino. Experimental Analysis on the Noise of Propellers for Small UAV. *Applied Acoustics*, **74**(1):79–88, (2013). DOI⟵.

[171] N. S. Zawodny, D. D. Boyd, and C. L. Burley. Acoustic Characterization and Prediction of Representative, Small-Scale Rotary-Wing Unmanned Aircraft System Components. In *Proceedings of the 72nd Annual Forum of the American Helicopter Society*, (2016). URL⟵.

[172] Y. Yang, Y. Liu, Y. Li, E. Arcondoulis, and Y. Wang. Aerodynamic and Aeroacoustic Performance of an Isolated Multicopter Rotor During Forward Flight. *AIAA Journal*, **58**(3):1171–1181, (2020). DOI⟵.

[173] C. Thurman, N. S. Zawodny, N. A. Pettingill, L. V. Lopes, and J. D. Baeder. Physics-informed Broadband Noise Source Identification and Prediction of an Ideally Twisted Rotor. In *Proceedings of the AIAA Scitech 2021 Forum*, paper 1925, (2021). DOI⟵.

[174] R. R. Mankbadi, S. O. Afari, and V. V. Golubev. High-Fidelity Simulations of Noise Generation in a Propeller-Driven Unmanned Aerial Vehicle. *AIAA Journal*, **59**(3):1020–1039, (2021). DOI⟵.

[175] J. Brandt and M. Selig. Propeller Performance Data at Low Reynolds Numbers. In *Proceedings of the 49th AIAA Aerospace Sciences Meeting including the New Horizons Forum and Aerospace Exposition*, paper 1255, (2011). DOI⟵.

[176] J. Winslow, H. Otsuka, B. Govindarajan, and I. Chopra. Basic Understanding of Airfoil Characteristics at Low Reynolds Numbers ($10^4 - 10^5$). *Journal of Aircraft*, **55**(3):1050–1061, (2018). DOI⟵.

[177] D. Casalino, M. Barbarino, and A. Visingardi. Simulation of Helicopter Community Noise in Complex Urban Geometry. *AIAA Journal*, **49**(8):1614–1624, (2011). DOI⟵.

[178] F. Menter, J. Schutze, K. Kurbatskii, R. Lechner, M. Gritskevich, and A. Garbaruk. Scale-Resolving Simulation Techniques in Industrial CFD. In *Proceedings of the 6th AIAA Theoretical Fluid Mechanics Conference*, paper 3474, (2011). DOI⟵.

[179] E. Grande, G. Romani, D. Ragni, F. Avallone, and D. Casalino. Aeroacoustic Investigation of a Propeller Operating at Low-Reynolds Number. *AIAA Journal*, Article in Advance, (2021). DOI⟵.

[180] G. E. Elsinga and J. Westerweel. Tomographic-PIV Measurement of the Flow Around a Zigzag Boundary Layer Trip. *Experiments in fluids*, **52**(4):865–876, (2012). DOI↩.

[181] A. L. Braslow. Simplified Method for Determination of Critical Height of Distributed Roughness for Boundary-layer Transition at Mach Numbers from 0 to 5. *NACA-TN-4363*, (1958). URL↩.

[182] W. Zhang, R. Hain, and C. J. Kähler. Scanning PIV Investigation of the Laminar Separation Bubble on a SD7003 Airfoil. *Experiments in Fluids*, **45**(4):725–743, (2008). DOI↩.

[183] P. Sijtsma. CLEAN Based on Spatial Source Coherence. *International Journal of Aeroacoustics*, **6**(4):357–374, (2007). DOI↩.

[184] E. Reshotko. Transition Issues for Atmospheric Entry. *Journal of Spacecraft and Rockets*, **45**(2):161–164, (2008). DOI↩.

[185] R. P. J. O. M. Van Rooij and W. A. Timmer. Roughness Sensitivity Considerations for Thick Rotor Blade Airfoils. *J. Sol. Energy Eng.*, **125**(4):468–478, (2003). DOI↩.

[186] G. Romani, E. Grande, F. Avallone, D. Ragni, and D. Casalino. Computational Study of Flow Incidence Effects on the Aeroacoustics of Low blade-tip Mach Number Propellers. *Aerospace Science and Technology*, **120**:107275, (2022). DOI↩.

[187] Electric VTOL News^{TM}, VoloDrone. URL↩.

[188] Electric VTOL News^{TM}, eHang 216. URL↩.

[189] Electric VTOL News^{TM}, eHang 116. URL↩.

[190] M. M. Connors. Factors that Influence Community's Acceptance of Noise: An Introduction for Urban Air Mobility. *NASA/TM-2019-220325*, (2019). URL↩.

[191] P. Block. The Effects of Installation on Single- and Counter-Rotation Propeller Noise. In *Proceedings of the 9th AIAA Aeroacoustics Conference*, paper 2263, (1984). DOI↩.

[192] P. Block. Experimental Study of the Effects of Installation on Single and Counter-Rotation Propeller Noise. *NASA TP-2541*, (1986). URL↩.

[193] R. Woodward. Measured Noise of a Scale Model High Speed Propeller at Simulated Takeoff/Approach Conditions. In *Proceedings of the 25th AIAA Aerospace Sciences Meeting*, paper 526, (1987). DOI↩.

[194] R. Mani. The Radiation of Sound from a Propeller at Angle of Attack. *Proceedings of the Royal Society of London. Series A: Mathematical and Physical Sciences*, **431**(1882):203–218, (1990). DOI↩.

[195] M. Carley. The Structure of Wobbling Sound Fields. *Journal of Sound and Vibration*, **244**(1):1–19, (2001). DOI↩.

[196] E. Krejsa. Prediction of the Noise from a Propeller at Angle of Attack. *NASA Technical Memorandum 103627*, (1990). URL⟵.

[197] E. Envia. Prediction of Noise Field of a Propfan at Angle of Attack. In *Unsteady Aerodynamics, Aeroacoustics, and Aeroelasticity of Turbomachines and Propellers*, pages 685–703. Springer, (1993). DOI⟵.

[198] D. B. Hanson. Sound from a Propeller at Angle of Attack: a New Theoretical Viewpoint. *Proceedings of the Royal Society of London. Series A: Mathematical and Physical Sciences*, **449**(1936):315–328, (1995). DOI⟵.

[199] J. Frota, P. Lempereur, and M. Roger. Computation of the Noise of a Subsonic Propeller at an Angle of Attack. In *Proceedings of the 4th AIAA/CEAS Aeroacoustics Conference*, paper 2282, (1998). DOI⟵.

[200] H. Rahimi, M. Hartvelt, J. Peinke, and J. G. Schepers. Investigation of the Current Yaw Engineering Models for Simulation of Wind Turbines in BEM and Comparison with CFD and Experiment. *Journal of Physics: Conference Series*, **753**(2):022016, (2016). DOI⟵.

[201] H. Rahimi, J.G. Schepers, W. Z. Shen, N. R.. García, M. S. Schneider, D. Micallef, C. J. S. Ferreira, E. Jost, L. Klein, and I. Herráez. Evaluation of Different Methods for Determining the Angle of Attack on Wind Turbine Blades with CFD Results Under Axial Inflow Conditions. *Renewable Energy*, **125**:866–876, (2018). DOI⟵.

[202] G. Romani and D. Casalino. Rotorcraft Blade-vortex Interaction Noise Prediction using the Lattice-Boltzmann Method. *Aerospace Science and Technology*, **88**:147–157, (2019). DOI⟵.

[203] G. Romani and D. Casalino. Powerflow Simulations of Helicopters in Blade-Vortex Interaction Conditions. In *Proceedings of the 75th Annual Vertical Flight Society Forum and Technology Display (FORUM 75)*, paper 185, (2019). DOI⟵.

[204] Y. H. Yu, C. Tung, B. G. van der Wall, H.-J. Pausder, C. Burley, T. Brooks, P. Beaumier, Y. Delrieux, E. Mercker, and K. Pengel. The HART-II test: Rotor Wakes and Aeroacoustics with Higher-Harmonic Pitch Control (hhc) Inputs-The Joint German/French/Dutch/Us Project. In *Proceedings of the 58th Annual Forum of the American Helicopter Society*, (2002). URL⟵.

[205] B. G. van der Wall, B. Junker, C. Burley, T. Brooks, Y. H. Yu, C. Tung, M. Raffel, H. Richard, W. Wagner, E. Mercker, et al. The HART II Test in the LLF of the DNW-a Major Step Towards Rotor Wake Understanding. In *Proceedings of the 28th European Rotorcraft Forum*, pages 273–284, (2002). DOI⟵.

[206] J. W. Lim, C. Tung, Y. H. Yu, C. L. Burley, T. Brooks, D. Boyd, B. G. Van Der Wall, O. Schneider, H. Richard, and M. Raffel. HART-II: Prediction of Blade-Vortex Interaction Loading. In *Proceedings of the 20th European Rotorcraft Forum*, (2003). DOI⟵.

[207] B. G. van der Wall. 2nd HHC Aeroacoustic Rotor Test (HART II)-Part I: Test Documentation. *Institute Report, IB-111-2003/31*, (2003). URL←.

[208] B. G. van der Wall and C. L. Burley. 2nd HHC Aeroacoustic Rotor Test (HART II)-Part II: Representative Results. *Institute Report, IB-111-2005/34*, (2005). URL←.

[209] B. G. van der Wall, J. W. Lim, M. J. Smith, S. N. Jung, J. Bailly, J. D. Baeder, and D. D. Boyd. An Assessment of Comprehensive Code Prediction State-Of-The-Art Using the HART II International Workshop Data. In *Proceedings of the 68th Annual Forum of the American Helicopter Society*, (2012). URL←.

[210] B. G. van der Wall, J. W. Lim, M. J. Smith, S. N. Jung, J. Bailly, J. D. Baeder, and D. D. Boyd. The HART II International Workshop: an Assessment of the State-of-the-art in Comprehensive Code Prediction. *CEAS Aeronautical Journal*, **4**(3):223–252, (2013). DOI←.

[211] M. J. Smith, J. W. Lim, B. G. van der Wall, J. D. Baeder, R. T. Biedron, D. D. Boyd, B. Jayaraman, S. N. Jung, and B.-Y. Min. An Assessment of CFD/CSD Prediction State-of-the-art Using the HART II International Workshop Data. In *Proceedings of the 68th Annual Forum of the American Helicopter Society*, (2012). URL←.

[212] M. J. Smith, J. W. Lim, B. G. van der Wall, J. D. Baeder, R. T. Biedron, D. D. Boyd, B. Jayaraman, S. N. Jung, and B.-Y. Min. The HART II International Workshop: an Assessment of the State of the Art in CFD/CSD Prediction. *CEAS Aeronautical Journal*, **4**(4):345–372, (2013). DOI←.

[213] G. Bernardini, J. Serafini, S. Ianniello, and M. Gennaretti. Assessment of Computational Models for the Effect of Aeroelasticity on BVI Noise Prediction. *International Journal of Aeroacoustics*, **6**(3):199–222, (2007). DOI←.

[214] M. Gennaretti, G. Bernardini, J. Serafini, and G. Romani. Rotorcraft Comprehensive Code Assessment for Blade–Vortex Interaction Conditions. *Aerospace Science and Technology*, **80**:232–246, (2018). DOI←.

[215] D. D. Boyd. HART-II Acoustic Predictions Using a Coupled CFD/CSD Method. In *Proceedings of the 65th Annual Forum of the American Helicopter Society*, (2009). URL←.

[216] B. G. van der Wall. Mode Identification and Data Synthesis of HART II Blade Deflection Data. *Institute Report, IB-111-2007/28*, (2007). URL←.

[217] L. Sankar, S. Ruo, and J. Malone. Application of Surface Transpiration in Computational Aerodynamics. In *Proceedings of the 24th AIAA Aerospace Sciences Meeting*, paper 511, (1986). DOI←.

[218] C. Stephens, A. Arena, and K. Gupta. Application of the Transpiration Method for Aeroservoelastic Prediction using CFD. In *Proceedings of the 39th AIAA/ASME/ASCE/AHS/ASC Structures, Structural Dynamics, and Materials Conference and Exhibit*, 2071, (1998). DOI←.

[219] G. Romanelli, E. Serioli, and P. Mantegazza. A" Free" Approach to Computational Aeroelasticity. In *Proceedings of the 48th AIAA Aerospace Sciences Meeting Including the New Horizons Forum and Aerospace Exposition*, paper 176, (2010). DOI←.

[220] M. Gennaretti and C. Testa. A Boundary Integral Formulation for Sound Scattered by Elastic Moving Bodies. *Journal of Sound and Vibration*, **314**(3-5):712–737, (2008). DOI←.

[221] T. Theodorsen and W. H. Mutchler. General theory of Aerodynamic Instability and the Mechanism of Flutter. *NACA Report No. 496*, (1935). URL←.

[222] The Data Base of the HART II International Workshop, URL←.

[223] O. Schneider and B. G. van der Wall. Conditionally Averaging of Pressure Data from HART II. *Institute Report, IB 111-2006/08*, (2006). URL←.

[224] F. Hoffmann and B. G. van der Wall. The Vortex Trajectory Method Applied to HART II PIV Data. *Institute Report, IB-111-2005/34*, (2005). URL←.

[225] G. Gopalan, J. Sitaraman, J. D. Baeder, and F. H. Schmitz. Aerodynamic and Aeroacoustic Prediction Methodologies with Application to the HART II Model Rotor. In *Proceedings of the 62nd Annual Forum of the American Helicopter Society*, (2006). URL←.

[226] G. Romani, Q. Ye, F. Avallone, D. Ragni, and D. Casalino. Numerical Analysis of Fan Noise for the NOVA Boundary-Layer Ingestion Configuration. *Aerospace Science and Technology*, **96**:105532, (2020). DOI←.

[227] E. M. Greitzer, P. A. Bonnefoy, E. De la Rosa Blanco, C. S. Dorbian, M. Drela, D. K. Hall, R. J. Hansman, J. I. Hileman, R. H. Liebeck, J. Levegren, et al. N+3 Aircraft Concept Designs and Trade Studies. Volume 1. *NASA CR-2010-216794/Vol 2*, (2010). URL←.

[228] C. Heykena, L. Savoni, J. Friedrichs, and R. Rudnik. Engine Airframe Integration Sensitivities For a STOL Commercial Aircraft Concept with over-the-wing Mounted UHBR-Turbofans. In *Proceedings of Montreal 2018 Global Power and Propulsion Forum*, (2018). URL←.

[229] L. Wiart, O. Atinault, J.-C. Boniface, and R. Barrier. Aeropropulsive Performance Analysis of the NOVA Configurations. In *30th Congress of the International Council of the Aerodynamical Sciences*, (2016). URL←.

[230] A. Plas, D. Crichton, M. Sargeant, T. Hynes, E. Greitzer, C. Hall, and V. Madani. Performance of a Boundary Layer Ingesting (BLI) Propulsion System. In *Proceedings of the 45th AIAA Aerospace Sciences Meeting and Exhibit*, paper 450, (2007). DOI←.

[231] M. Drela. Power Balance in Aerodynamic Flows. *AIAA Journal*, **47**(7):1761–1771, (2009). DOI←.

[232] L. Hardin, G. Tillman, O. Sharma, J. Berton, and D. Arend. Aircraft System Study of Boundary Layer Ingesting Propulsion. In *Proceedings of the 48th AIAA/ASME/SAE/ASEE Joint Propulsion Conference & Exhibit*, paper 3993, (2012). DOI⟵.

[233] G. Carrier, O. Atinault, R. Grenon, and C. Verbecke. Numerical and Experimental Aerodynamic Investigations of Boundary Layer Ingestion for Improving Propulsion Efficiency of Future Air Transport. In *Proceedings of the 31st AIAA Applied Aerodynamics Conference*, paper 2406, (2013). DOI⟵.

[234] K. M. Sabo and M. Drela. Benefits of Boundary Layer Ingestion Propulsion. In *Proceedings of the 53rd AIAA Aerospace Sciences Meeting*, paper 1667, (2015). DOI⟵.

[235] P. Lv, D. Ragni, T. Hartuc, L. Veldhuis, and A. G. Rao. Experimental Investigation of the Flow Mechanisms Associated with a Wake-ingesting Propulsor. *AIAA Journal*, **55**(4):1332–1342, (2016). DOI⟵.

[236] P. Lv, A. G. Rao, D. Ragni, and L. Veldhuis. Performance Analysis of Wake and Boundary-Layer Ingestion for Aircraft Design. *Journal of Aircraft*, **53**(5):1517–1526, (2016). DOI⟵.

[237] A. Anabtawi, R. Blackwelder, P. Lissaman, and R. Liebeck. An Experimental Investigation of Boundary Layer Ingestion in a Diffusing S-Duct with and without Passive Flow Control. In *Proceedings of the 37th AIAA Aerospace Sciences Meeting and Exhibit*, paper 739, (1999). DOI⟵.

[238] S. Gorton, L. Owens, L. Jenkins, B. Allan, and E. Schuster. Active Flow Control on a Boundary-Layer-Ingesting Inlet. In *Proceedings of the 42nd AIAA Aerospace Sciences Meeting and Exhibit*, paper 1203, (2004). DOI⟵.

[239] L. R. Owens, B. G. Allan, and S. A. Gorton. Boundary-layer-ingesting Inlet Flow Control. *Journal of Aircraft*, **45**(4):1431–1440, (2008). DOI⟵.

[240] J. J. Defoe and Z. S. Spakovszky. Effects of Boundary-Layer Ingestion on the Aero-Acoustics of Transonic Fan Rotors. *Journal of Turbomachinery*, **135**(5):051013, (2013). DOI⟵.

[241] H. H. Murray, W. J. Devenport, W. N. Alexander, S. Glegg, and D. Wisda. Aeroacoustics of a Rotor Ingesting a Planar Boundary Layer at High Thrust. *Journal of Fluid Mechanics*, **850**:212–245, (2018). DOI⟵.

[242] Federal Aviation Administration (FAA) U.S. Departement of Transportation (DOT). Code of Federal Regulation (CFR) - Title 14: Aeronautics and Space - Part 36. Noise Standards: Aircraft Type and Airworthiness Certification - Subpart B: Noise Levels for Transport Category and Jet Airplanes. (1969). URL⟵.

[243] D. Casalino, A. Hazir, and A. Mann. Turbofan Broadband Noise Prediction Using the Lattice Boltzmann Method. *AIAA Journal*, **56**(2):609–628, (2017). DOI⟵.

[244] E. Envia. Fan Noise Source Diagnostic Test-Vane Unsteady Pressure Results. In *Proceedings of the 8th AIAA/CEAS Aeroacoustics Conference & Exhibit*, paper 2430, (2002). DOI←.

[245] W. C. P. van der Velden, A. H. van Zuijlen, A. T. de Jong, and D. Ragni. Flow and Self-noise Around Bypass Transition Strips. *Noise Control Engineering Journal*, **65**(5):434–445, (2017). DOI←.

[246] P. S. Klebanoff. Characteristics of Turbulence in a Boundary layer with Zero Pressure Gradient. *NACA-TR-1247*, (1955). URL←.

[247] G. Podboy, M. Krupar, S. Helland, and C. Hughes. Steady and Unsteady Flow Field Measurements within a NASA 22 Inch Fan Model. In *Proceedings of the 40th AIAA Aerospace Sciences Meeting & Exhibit*, paper 1033, (2002). DOI←.

[248] W. N. Alexander, W. J. Devenport, and S. Glegg. Noise from a Rotor Ingesting a Thick Boundary Layer and Relation to Measurements of Ingested Turbulence. *Journal of Sound and Vibration*, **409**:227–240, (2017). DOI←.

[249] D. Casalino, S. Noelting, E. Fares, T. Van de Ven, F. Perot, and G. A. Brès. Towards Numerical Aircraft Noise Certification: Analysis of a Full-Scale Landing Gear in Fly-Over Configuration. In *Proceedings of the 18th AIAA/CEAS Aeroacoustics Conference (33rd AIAA Aeroacoustics Conference)*, paper 2235, (2012). DOI←.

[250] M. Goody. Empirical Spectral Model of Surface Pressure Fluctuations. *AIAA Journal*, **42**(9):1788–1794, (2004). DOI←.

[251] R. L. Simpson, M. Ghodbane, and B. E. McGrath. Surface Pressure Fluctuations in a Separating Turbulent Boundary Layer. *Journal of Fluid Mechanics*, **177**:167–186, (1987). DOI←.

[252] M. V. Zagarola and A. J. Smits. Mean-Flow Scaling of Turbulent Pipe Flow. *Journal of Fluid Mechanics*, **373**:33–79, (1998). DOI←.

[253] F. H. Clauser. Turbulent Boundary Layers in Adverse Pressure Gradients. *Journal of the Aeronautical Sciences*, **21**(2):91–108, (1954). DOI←.

[254] J. F. Nash. Turbulent-Boundary-Layer Behaviour and the Auxiliary Equation. *ARC CP 835*, (1966). URL←.

[255] D. Casalino and M. Barbarino. Stochastic Method for Airfoil Self-Noise Computation in Frequency Domain. *AIAA Journal*, **49**(11):2453–2469, (2011). DOI←.

APPENDIX

A

SEMI-EMPIRICAL WALL-PRESSURE SPECTRUM MODELS

This appendix describes the four semi-empirical wall-pressure spectrum models that are employed in Chapter 4 to compute the wall-pressure spectrum beneath a turbulent boundary-layer at the airfoil trailing-edge, from inner and/or outer boundary-layer variables extracted from the XFOIL simulation. These are the Schlinker & Amiet's [129], Rozenberg's [154], Kamruzzaman's [155], and Lee's [156] models, and are presented in the following.

SCHLINKER & AMIET'S MODEL

Schlinker and Amiet derived the following wall-pressure spectrum model by fitting flat plate experimental wall-pressure spectra for zero pressure gradient cases [129]:

$$\frac{\Phi_{pp}(\tilde{\omega})}{(1/2)\rho^2\delta^* U_e^3} = 2\cdot 10^{-5}\left[1+\tilde{\omega}+0.217\tilde{\omega}^2+0.00562\tilde{\omega}^4\right]^{-1}, \tag{A.1}$$

where Φ_{pp} represents the wall-pressure power spectral density and is a function of $\tilde{\omega} = \omega\delta^*/U_e$, ω is the angular frequency, δ^* is the boundary-layer displacement thickness, U_e is the boundary-layer edge velocity and ρ is the fluid density. The previous model can be corrected through a semi-empirical function $DIFF(\tilde{\omega})$[1] to account for the modification between airfoil and flat plate surface pressure spectra [129].

ROZENBERG'S MODEL

The wall-pressure spectrum model proposed by Rozenberg is an extension of the Goody's ones [250] (which incorporates Reynolds number effects, but is limited to zero-pressure gradient cases) to include adverse pressure-gradient effects [154]. The model has been derived considering the wall-pressure spectra from several experimental and

---

[1] Representing the difference between the wall pressure spectra for an airfoil and a flat plate.

numerical test cases on pipe-flow and loaded airfoils turbulent boundary-layers. Rozenberg's model reads as:

$$\frac{\Phi_{pp}(\tilde{\omega})U_e}{\tau_{max}^2\delta^*} = \frac{\left[2.82\Delta^2\left(6.13\Delta^{-0.75}+F_1\right)^{A_1}\right]\left[4.2\left(\frac{\Pi}{\Delta}\right)+1\right]\tilde{\omega}^2}{\left[4.76\tilde{\omega}^{0.75}+F_1\right]^{A_1}+\left[C_3'\tilde{\omega}\right]^{A_2}}, \tag{A.2}$$

where τ_{max} is the maximum shear stress along the normal that can be taken as the wall-shear stress τ_w [251], Δ is the ratio between the boundary-layer thickness and displacement thickness (Zagarola-Smith's parameter [252]) and:

$$A_1 = 3.7+1.5\beta_c, \quad A_2 = \min\left[3, 19/\sqrt{R_T}\right]+7, \quad F_1 = 4.76\left(\frac{1.4}{\Delta}\right)^{0.75}[0.375A_1-1],$$

$$\Pi = 0.8(\beta_c+0.5)^{3/4}, \quad C_3' = 8.8R_T^{-0.57}, \tag{A.3}$$

where $\beta_c = (\Theta/\tau_w)(\mathrm{d}p/\mathrm{d}x)$ is the Clauser's parameter [253] (where Θ is the boundary-layer momentum thickness and $\mathrm{d}p/\mathrm{d}x$ is the streamwise pressure gradient), while $R_T = (\delta/U_e)/(\nu/u_\tau^2) = (u_\tau\delta/\nu)\sqrt{C_f/2}$ is the ratio between inner and outer boundary-layer pressure time scales (with ν being the fluid kinematic viscosity, u_τ the friction velocity and C_f the skin friction coefficient).

Kamruzzaman's model

The model developed by Kamruzzaman [155] is a simpler extension of Goody's [250] and Rozenberg's [154] wall-pressure spectrum models that accounts for Reynolds number, boundary-layer loading and pressure gradient effects:

$$\frac{\Phi_{pp}(\tilde{\omega})U_e}{\tau_w^2\delta^*} = \frac{B_2\tilde{\omega}^2}{\left[\tilde{\omega}^p+B_1\right]^q\left[B_3\tilde{\omega}\right]^7}, \tag{A.4}$$

where the quantities:

$$B_2 = 0.45\left[1.75\left(\Pi^2\beta_c^2\right)^m+15\right] \quad \text{with} \quad m = 0.5\left(\frac{\delta^*/\Theta}{1.31}\right)^{0.3},$$

$$p = 1.637, \quad q = 2.47, \quad B_1 = 0.27, \quad B_3 = (1.15R_T)^{-r} \quad \text{with} \quad r = 2/7 \tag{A.5}$$

have been determined by best fit wall-pressure spectrum measurements for different airfoils at different Reynolds numbers and angles of attack. Note that in Kamruzzaman's model the Clauser's parameter β_c is computed through a curve-fit approach [254], while the R_T parameter is computed using δ^* thickness in place of δ.

Lee's model

Lee's model [156] is an extension and generalization of the Rozenberg's [154] one to deal with zero and adverse pressure gradient flows. Both flat plate and airfoil wall pressure spectrum data are employed for tuning the model parameters. Lee's model read as:

$$\frac{\Phi_{pp}(\tilde{\omega})U_e}{\tau_w^2\delta^*} = \frac{\max[A, (0.25\beta_c-0.52)A]\tilde{\omega}^2}{\left[4.76\tilde{\omega}^{0.75}+F_1^*\right]^{A_1}+\left[C_3'\tilde{\omega}\right]^{A_2^*}}, \tag{A.6}$$

where

$$A = \left[2.82\Delta^2\left(6.13\Delta^{-0.75} + F_1\right)^{A_1}\right]\left[4.2\left(\frac{\Pi}{\Delta}\right) + 1\right] \tag{A.7}$$

while the parameters $F1^*$ and $A2^*$ are respectively defined as:

$$F_1^* = \max[1.0, 1.5F_1] \quad \text{if} \quad \beta_c < 0.5 \quad \text{else} \quad F_1^* = F_1, \tag{A.8}$$

and

$$A_2^* = \min[3, (0.139 + 3.1043\beta_c)] + 7. \tag{A.9}$$

Specifically, the A_2 parameter in Rozenberg's model is replaced by a new A_2^* parameter to improve the wall-pressure spectrum prediction at high frequency for different pressure gradient conditions [156]. A new F_1 parameter (namely F_1^*) is used to improve the prediction at low and middle frequencies for zero and low pressure gradient conditions [156]. Finally, the modification of the numerator at the right-hand side of Eq. (A.2) is further introduced to solve the typical under-prediction of the wall-pressure spectrum amplitude of the Rozenberg's model for high values of β_c [156].

B

SEMI-ANALYTICAL TRAILING-EDGE MODEL

This appendix describes the semi-analytical model proposed by Roger and Moreau [50] to compute airfoil trailing-edge noise from the knowledge of the aerodynamic wall-pressure statistics in proximity to the trailing-edge. This model represents an extension of the Amiet's semi-analytical trailing-edge model [166] to 3D incident gusts, with an inclusion of the a leading-edge back-scattering[1]. Such a correction is relevant at low reduced frequency for airfoils with a relatively small chord when the airfoil itself is acoustically compact [50].

Considering a blade segment of chord c, span L, and a coordinate system x, y, z centered at the trailing-edge mid-point (with x and z axes aligned with the free-stream velocity and trailing-edge (Fig. B.1), respectively), the far-field noise power spectral density of Roger and Moreau's model reads as:

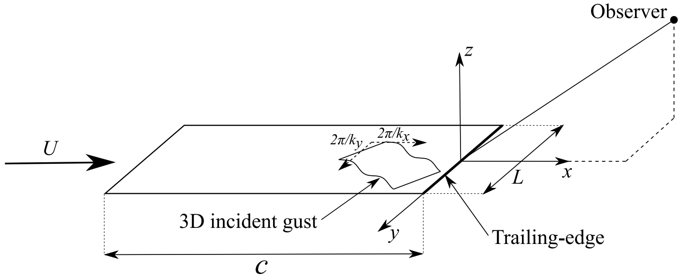

Figure B.1: Airfoil and trailing-edge coordinate system.

---

[1] Acoustic waves generated at the blade trailing-edge when pass the leading-edge "sees" another discontinuity and scatter again. This mechanism is called back-scattering and can be a relevant contributor to the overall noise radiation for airfoils of small chord at low reduced frequencies.

$$\Phi_{aa}(x,y,z,\omega) = \left(\frac{\bar{k}z}{4\pi\sigma^2}\right)^2 2\pi L \left| I\left(\frac{\bar{k}}{u_c}, \bar{k}_y\right)\right|^2 \Pi_0\left(\frac{\omega}{u_c}, k_y\right), \tag{B.1}$$

where $\bar{k} = \omega c/(2c_0)$ is the non dimensional acoustic wavenumber (with ω being the angular frequency and c_0 the undisturbed speed of sound), $\sigma = \sqrt{x^2 + \beta^2(y^2+z^2)}$ is the observer distance with Prandtl-Glauert correction (where $\beta^2 = 1 - M^2$ and $M = u_e/c_0$ is the asymptotic boundary-layer Mach number, with u_e being the edge velocity), Π_0 is the streamwise-integrated wavenumber-frequency spectral density of the wall-pressure, $\bar{k}_y = k_y c/2$ is the non-dimensional spanwise wavenumber, while I is the radiation integral (i.e. the acoustic transfer function that represents the scatter response to an incident pressure disturbance). The radiation integral is the sum of two contributions, I_1 and I_2, respectively representing the first-order direct-scattering (i.e. trailing-edge solution under the semi-infinite flat plate and high-frequency approximations) and the second-order back-scattering (i.e the finite chord correction) [255]:

$$I_1 = \frac{ie^{2iC}}{C}\left[(1+i)e^{-2iC}\left(\frac{B}{B-C}E^*(2B-2C) - (1+i)E^*(2B) + 1\right)^{1/2}\right], \tag{B.2}$$

$$I_2 = H\left\{e^{4i\bar{\kappa}}\left[1-(1+i)E^*(4\bar{\kappa})\right]\right\}^{\epsilon} + H\left[-e^{2i\Theta^-} + i\left(\Theta^- + \bar{k}_x + M\bar{\mu} - \bar{k}\right)G\right], \tag{B.3}$$

where $\bar{k}_x = k_x c/2$ is the streamwise non-dimensional wavenumber, $\bar{\mu} = \omega c/(2c_0\beta^2)$, E^* is the Fresnel integral:

$$E^*(\xi) = \int_0^{\xi} e^{-it}/\sqrt{2\pi t}\,\mathrm{d}t,$$

while the subscript ϵ implies that the imaginary part within the curly brackets has to be multiplied by the factor $\epsilon = 1/\sqrt{1+1/(4\bar{\kappa})}$. Moreover,

$$\begin{aligned}
&B = \bar{K}_x - M\bar{\mu} + \bar{\kappa}, \quad C = \bar{K}_x - \bar{\mu}(x/\sigma - M),\\
&H = \frac{(1+i)e^{-4i\bar{\kappa}}(1-\Theta^2)}{2\sqrt{\pi}(\alpha-1)\bar{k}_x\sqrt{B}}, \quad \Theta^- = \bar{\kappa} - \bar{\mu}x/\sigma,\\
&G = (1+\epsilon)e^{i(2\bar{\kappa}+\Theta^-)}\frac{\sin(\Theta^- - 2\bar{\kappa})}{(\Theta^- - 2\bar{\kappa})} + (1-\epsilon)e^{i(-2\bar{\kappa}+\Theta^-)}\frac{\sin(\Theta^- + 2\bar{\kappa})}{(\Theta^- + 2\bar{\kappa})}\\
&\quad + \frac{(1+\epsilon)(1-i)}{2(\Theta^- - 2\bar{\kappa})}e^{4i\bar{\kappa}}E^*(4\bar{\kappa}) - \frac{(1-\epsilon)(1+i)}{2(\Theta^- + 2\bar{\kappa})}e^{-4i\bar{\kappa}}E^*(4\bar{\kappa})\\
&\quad + \frac{e^{2i\Theta^-}}{2}\sqrt{\frac{2\bar{\kappa}}{\Theta^-}}E^*(2\Theta^-)\left[\frac{(1-\epsilon)(1+i)}{\Theta^- + 2\bar{\kappa}} - \frac{(1+\epsilon)(1-i)}{\Theta^- - 2\bar{\kappa}}\right],
\end{aligned} \tag{B.4}$$

where $\bar{K}_x = \omega c/(2u_c)$, $\bar{\kappa}^2 = \bar{\mu}^2 - \bar{k}_y^2/\beta^2$, $\alpha = u_e/u_c$ and u_c is the eddy convection velocity. The wavenumber-frequency power spectral density in Eq. (B.1) can be expressed as [50]:

$$\Pi_0\left(\frac{\omega}{u_c}, k_y\right) = \frac{1}{\pi}\Phi_{pp}(\omega)\ell_y(\omega, k_y), \tag{B.5}$$

where Φ_{pp} is the wall-pressure power spectral density at the trailing-edge, while ℓ_y is the spanwise coherence length defined as:

$$\ell_y(\omega, k_y) = \int_0^{\infty} \sqrt{\gamma^2(\eta_2, \omega)}\cos(k_y\eta_2)\mathrm{d}\eta_2. \tag{B.6}$$

where γ^2 is the wall-pressure spanwise squared coherence function between two points separated by the distance η_2 along the span at the trailing-edge.

In order to compute the overall far-field noise, Eq. (B.1) along with Eq. (B.5) has to be applied to both the suction and pressure sides of the airfoil. Note that, in Chapter 4, the spanwise coherence length in Eq. (B.6) has been replaced by the Corcos' model [157]:

$$l_z(\omega) = \frac{b_c u_c}{\omega}, \tag{B.7}$$

where b_c is a constant, typically chosen between 1.2 and 1.7 [158].

C

HELICOPTER MAIN ROTOR TRIM PROCEDURE

This appendix describes the automated trim procedure (adopted in Chapter 7) to trim the main rotor thrust, rolling and pitching moments to the experimental values and ensure that the computational setup is simulated at an operating condition consistent with the experiment. More specifically, starting from the experimental collective (θ_0), lateral (θ_c) and longitudinal cyclic (θ_s) pitch commands as initial guesses, a Newton-Raphson iterative method is used to trim the main rotor to the experimental thrust, $T = 3300$ N, and hub rolling and pitching moment, $M_x = 20$ Nm and $M_y = -20$ Nm, respectively. θ_0, θ_c and θ_s are such that the blade pitch angle θ (positive nose-up) with respect to the blade pre-twist is defined as:

$$\theta(\Psi) = \theta_0 + \theta_c \cos(\Psi) + \theta_s \sin(\Psi), \tag{C.1}$$

where Ψ is the azimuthal angle (or azimuth) denoting the blade angular position with respect to the tail of the helicopter and taken positive in the direction of rotation of the blade.

The following set of three equations, representing the steady main rotor hub loads equilibrium (thrust, and rolling and pitching moments only), is considered:

$$f_1 = T - \hat{T}(\theta_0, \theta_c, \theta_s) = 0 \tag{C.2}$$

$$f_2 = M_x - \hat{M}_x(\theta_0, \theta_c, \theta_s) = 0 \tag{C.3}$$

$$f_3 = M_y - \hat{M}_y(\theta_0, \theta_c, \theta_s) = 0 \tag{C.4}$$

where $\hat{T}$, $\hat{M}_x$ and $\hat{M}_y$ are the aerodynamic hub loads integrated over the main rotor blades, and θ_0, θ_c and θ_s are the unknowns of the problem (i.e. the new trim settings to be defined). It should be noted that no inertial contributions appear in Eqs. C.2-C.4 due to the steady flight condition considered in this study. As mentioned, the solution to the former set of equations is determined by using a Newton-Raphson scheme with a constant Jacobian matrix, applying the following iterative procedure at the end of every main rotor revolution until convergence is reached (with n indicating the iteration step number):

$$\Theta_n = \Theta_{n-1} - \rho \mathbf{J}_0^{-1} \Delta\mathbf{f}_{n-1} \tag{C.5}$$

where $\Theta_n = [\theta_0, \theta_c, \theta_s]_n^T$, $\mathbf{J}_0 = \partial(f_1, f_2, f_3)/\partial(\theta_0, \theta_c, \theta_s)|_0$ is the Jacobian matrix evaluated at $n = 0$, $\Delta\mathbf{f}_{n-1} = [f_1, f_2, f_3]_{n-1}^T$ and ρ is a relaxation factor for improving the convergence of the iterative scheme. The approximation of the fixed Jacobian matrix in Eq. C.5 allows to evaluate the Jacobian matrix only once, thus avoiding the computationally expensive requirement of calculating it at every iteration of the algorithm.

An overview of the trim procedure workflow is given in Fig. C.1. In the coarse run, which is also used to generate a statistically converged flow to initialize the finer simulation initial solution, the Jacobian matrix is determined by applying perturbations of 0.5° on the trim parameters. The coarse simulation is run for 14 revolutions of the main rotor: 4 for the initial settling of the flow solutions, 2 for computing the reference conditions (i.e. the operating condition around which Eqs. (C.2)-(C.4) are linearized), 2 for every trim setting parameter perturbation and 2 final revolutions for restoring the reference condition and generating the seeding file for the finer simulation. Hence, the finer simulation is started and the mean thrust, hub rolling and pitching moments values are computed after each rotor revolution in order to adjust the trim settings according to Eq. (C.5). Convergence is reached when either the thrust and moment relative errors are below 1% or if the collective/cyclic pitch angles variations are smaller than 0.25% (generally after 3-4 main rotor revolutions of the fine simulation).

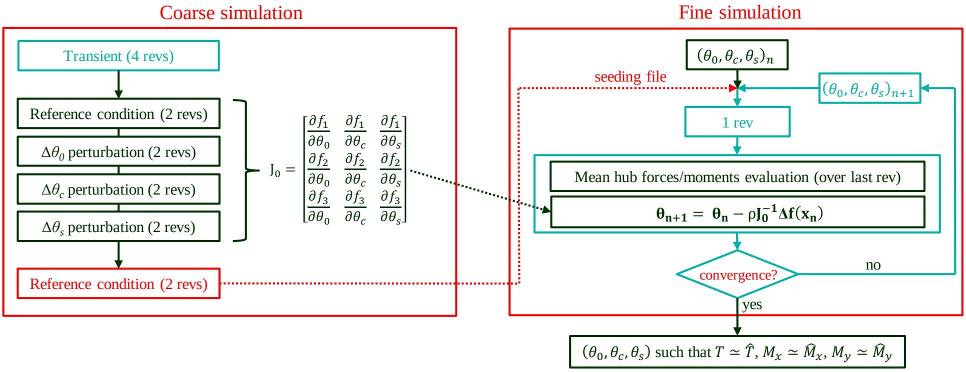

Figure C.1: Sketch of the coarse-to-fine simulation approach implementing the trim procedure workflow.

D

2D FLUID BODY-FORCE ASSESSMENT

This appendix presents the 2D assessment of the fluid body-force model outlined in Chapter 7, which is used to include the aerodynamic effects associated to the blade torsional deformations without actually deforming the blade geometry in the numerical simulation. In order to tune and validate the body-force model, two different bidimensional non-symmetric NACA 23012 cases are considered:

- a physically airfoil oscillating about a zero static angle of attack by:

  $$\tilde{\phi}_x(t) = \phi_A \sin(\hat{k}\hat{\tau}), \tag{D.1}$$

  representative, from a 2D perspective, of a local blade section undergoing a torsional deformation equal to $\tilde{\phi}_x$. In Eq. (D.1), ϕ_A is the pitch amplitude, $\hat{k} = \omega b / U_{s_\infty}$ is the reduced frequency (with ω being the pitch angular frequency, b the airfoil semi-chord and U_{s_∞} the free-stream velocity) and $\hat{\tau} = U_{s_\infty} t / b$ is the non-dimensional time;

- an airfoil at zero static angle of attack excited by a fluid body-forces field applied in the fluid volume region surrounding it (Fig. 7.3(b)) according to Eq. (7.11), with Eqs. (7.18) and (7.19) respectively replaced by:

  $$\ddot{\tilde{\phi}}_x(t)|_{\zeta_3\zeta_4} = -\phi_A \frac{\hat{k}^2 U_{s_\infty}^2}{b^2} \zeta_3 \sin(\hat{k}\hat{\tau} - 2\pi\zeta_4) \tag{D.2}$$

  $$\ddot{\tilde{\phi}}_x(t)|_{\zeta_1\zeta_2} = -\phi_A \frac{\hat{k}^2 U_{s_\infty}^2}{b^2} \zeta_1 \sin(\hat{k}\hat{\tau} - 2\pi\zeta_2) \tag{D.3}$$

  and

  $$\dot{\tilde{\phi}}_x(t)|_{\zeta_3\zeta_4} = \phi_A \frac{\hat{k} U_{s_\infty}}{b} \zeta_3 \cos(\hat{k}\hat{\tau} - 2\pi\zeta_4) \tag{D.4}$$

  $$\dot{\tilde{\phi}}_x(t)|_{\zeta_1\zeta_2} = \phi_A \frac{\hat{k} U_{s_\infty}}{b} \zeta_1 \cos(\hat{k}\hat{\tau} - 2\pi\zeta_2). \tag{D.5}$$

A 3x3 test matrix is considered to tune and assess the body-forces model behavior at different reduced frequencies ($\hat{k} = 0.03, 0.16, 0.30$) and amplitudes ($\phi_A = 0.25°, 1.38°, 2.50°$) of the pitching motion, which cover the amplitude-frequency domain of the torsion deformation for the baseline case of the HART-II experiment [216]. The Reynolds and Mach numbers considered are those relative to the blade section at the 70% of the blade span of the HART-II main rotor blade, respectively equal to $1.3 \cdot 10^6$ and 0.5. For each reduced frequency, the optimal values of ζ_1, ζ_2, ζ_3, ζ_4, γ, β and χ_s are determined by the minimization (through a genetic algorithm optimization) of the sum of the mean squared relative errors between the lift (C_L), drag (C_D) and pitching moment[1] (C_M) coefficients time histories generated by a steady airfoil undergoing the fluid body-force field (BF) and those produced by the a physically pitching airfoil (P) along one period of oscillation, namely:

$$\min\left[\frac{1}{N_s}\sum_{i=1}^{N_s}\left(\frac{C_L^{BF}-C_L^{P}}{C_L^{P}}\right)_i^2+\frac{1}{N_s}\sum_{i=1}^{N_s}\left(\frac{C_D^{BF}-C_D^{P}}{C_D^{P}}\right)_i^2+\frac{1}{N_s}\sum_{i=1}^{N_s}\left(\frac{C_M^{BF}-C_M^{P}}{C_M^{P}}\right)_i^2\right] \tag{D.6}$$

where N_s represents the number of samples of the C_L, C_D and C_M time histories. These optimal values are fit into power or exponential functions to derive formulae describing their dependency from the reduced frequency and to be used for the 3D helicopter main rotor case as described in Chapter 7. It is assumed that the previous parameters are only function of the reduced frequency and not of the amplitude of the pitching motion/torsional deformation ϕ_A. This assumption is confirmed by the observation that the optimal values of ζ_1, ζ_2, ζ_3, ζ_4, γ, β and χ_s are weakly dependent by ϕ_A and more considerably influenced by the variations of $\hat{k}$. The results of the optimization and the corresponding fitting function are shown in Tab. D.1 for $\phi_A = 1.38°$.

Param.	$\hat{k} = 0.03$	$\hat{k} = 0.16$	$\hat{k} = 0.30$	Fitting functions
ζ_1	2.419	0.298	0.143	$0.03083955\hat{k}^{-1.243994}$
ζ_2	-0.233	-0.207	-0.187	$-0.1403119 - 0.100626e^{-2.571309\hat{k}}$
ζ_3	0.020	0.024	0.029	$16.02422 - 16.00545/2^{\hat{k}/338.1517}$
ζ_4	-0.440	-0.476	-0.512	$-1.08886 + 0.6576319/2^{\hat{k}/1.586511}$
γ	152.952	131.644	102.246	$232.1835 - 74.99451/2^{\hat{k}/-0.3783304}$
β	0.615	0.495	0.350	$-1114.364 + 1115.012e^{-0.000882627\hat{k}}$
χ_s	0.543	0.451	0.446	$0.4455562 + 0.1899998/2^{\hat{k}/0.03106636}$

Table D.1: Optimal values of the fluid body-force model and fitting functions for $\phi_A = 1.38°$.

The comparison, along one oscillation period T, between the lift, drag and pitching moment coefficients time histories generated by the real pitching airfoil and the static one excited by the fluid body-forces field is shown in Figs. D.1 to D.3 for $\hat{k} = 0.03$, 0.16 and 0.30, respectively. Each plot shows the results for the three pitching amplitudes considered, $\phi_A = 0.25°$ in black, $\phi_A = 1.38°$ in blue and $\phi_A = 2.50°$ in red, with the real pitching

---

[1] Computed at the airfoil quarter-chord point.

airfoil results reported as solid line and the body-force ones as dots. A very good agreement is obtained for each reduced frequency and for the two lowest pitch amplitudes (ϕ_A = 0.25° and 1.38°) for the lift and pitching moment coefficients. A certain under-prediction of the maximum and minimum values of C_L and C_M can be observed for $\phi_A = 2.50°$, due to the fact that, at relatively large pitch amplitudes (i.e. torsional deformations from the 3D helicopter case perspective), the body-forces field is no longer able to rearrange the flow surrounding the airfoil in such a way that aerodynamic loadings identical to those of the real moving airfoil are generated.

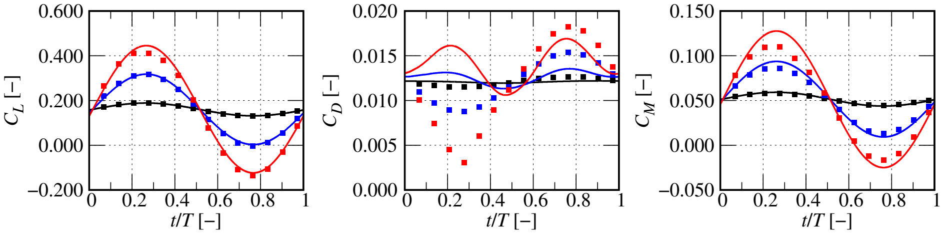

Figure D.1: Non-dimensional lift, drag and pitching moment coefficients time histories between a real pitching airfoil (solid line) and a simulated pitching airfoil by means of the body-force approach (dots) for $\hat{k}$ = 0.03; ϕ_A = 0.25° (black), ϕ_A = 1.38° (blue) and ϕ_A = 2.50° (red).

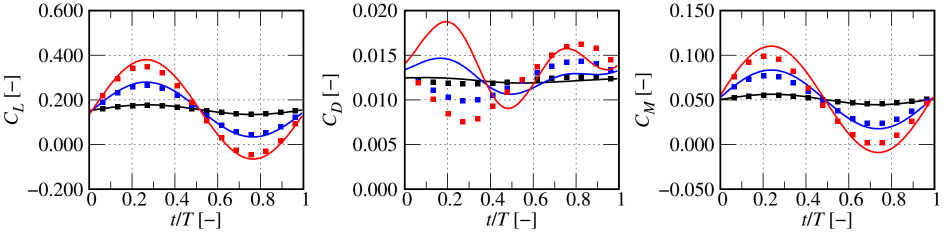

Figure D.2: Non-dimensional lift, drag and pitching moment coefficients time histories between a real pitching airfoil (solid line) and a simulated pitching airfoil by means of the body-force approach (dots) for $\hat{k}$ = 0.16; ϕ_A = 0.25° (black), ϕ_A = 1.38° (blue) and ϕ_A = 2.50° (red).

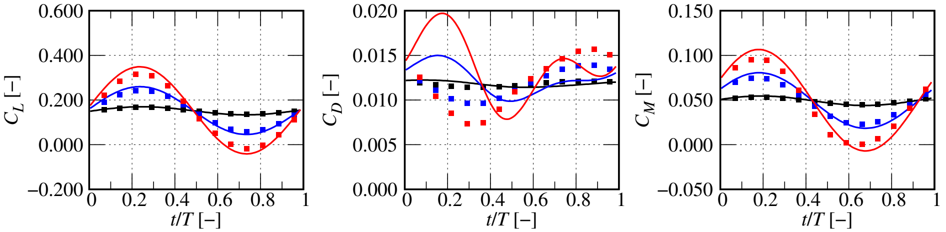

Figure D.3: Non-dimensional lift, drag and pitching moment coefficients time histories between a real pitching airfoil (solid line) and a simulated pitching airfoil by means of the body-force approach (dots) for $\hat{k}$ = 0.30; ϕ_A = 0.25° (black), ϕ_A = 1.38° (blue) and ϕ_A = 2.50° (red).

Concerning the drag coefficient, much larger discrepancies are observed for all the values of $\hat{k}$ and ϕ_A considered. In particular, during the first half of the airfoil pitching oscillation ($t/T < 0.5$), the drag generated by the airfoil excited by the body-force field shows an opposite phase compared to the that of the real pitching airfoil. As shown in Figs. D.1 to D.3, an airfoil periodically pitching at a frequency $1/T$ leads to the generation of a periodic drag coefficient time history characterized by a dominant harmonic of frequency $2/T$. Since the proposed fluid body-force model is fed with the same harmonic content of the input pitching motion, it cannot reproduce the effects induced by the pitching motion at harmonic highers than those characterizing the airfoil motion itself.

The modeling of these effects could be generally accounted by the proposed fluid body-force model through the inclusion of harmonics of frequency $2/T_k$, with $1/T_k$ ($k = 1,..,n$) representing the generic harmonic content of the input pitching motion/torsion kinematics, however at a higher computational cost. Moreover, it should be pointed out that the drag coefficient, and its variation due to a local blade section torsional deformation (or pitching motion from a 2D point or view), plays a secondary role concerning the aeroelastic behavior of the rotor blades compared to the lift and pitching moment. This is consequence of the fact that the drag force is more than one order of magnitude smaller than the lift, and that it primarily acts along the chord-wise direction where the rotor blades are generally one order of magnitude stiffer than in the chord-normal direction.

Hence, it can be concluded that, once the optimal values for ζ_1, ζ_2, ζ_3, ζ_4, γ, β and χ_s are determined for a specific reduced frequency, the proposed body-force model is able to reproduce with a satisfactory accuracy the most relevant part of the aerodynamic response (i.e. lift and pitching moment) of a 2D airfoil undergoing a torsional deformation/pitching motion, especially for small-to-moderate values of the amplitude of the oscillation.

ACKNOWLEDGEMENTS

After four and a half years of hard and devoted work, I have finally reached the end of this journey. Leaving my home country, family and friends to start working in Stuttgart as engineer and pursuing a PhD at TU-Delft has been the most challenging, yet rewarding, experience of my life so far. During these years, I met many interesting people and faced several challenges that helped me to grow as a professional and human being. I always describe myself as a person of few words, who neither loves to make empty nor rhetorical speeches. However, I now feel the need to add a few further lines to this thesis to show my gratitude to all those people, who took part to this journey - directly or indirectly - along with me.

First of all, I am deeply grateful to my PhD promotor and manager at Dassault Systèmes, Prof. Damiano Casalino, for the trust you have placed in me by first hiring me at Exa Corporation, and then for giving me the chance to pursue a PhD at TU-Delft under your guidance. Thank you for your support, advice and patience towards me. I feel privileged to have worked and continue working with such a smart and inspiring person like you.

Then, I am so thankful to you, Wouter, the most Italian Dutch guy I ever met. I owe you much more than what you could ever think. We became colleagues as soon as you earned your PhD from TU-Delft. Pursuing a PhD so far away from Delft made it difficult for me to share thoughts and concerns with fellow peers on a daily basis. However, your experience, suggestions and advice helped me to go through the hurdles of the PhD life. I always pleasantly remember the time spent talking about everything in front of a pizza at "Marcellino" or a beer (actually more than one!) at "Maulwurf". Stuttgart is a much more boring place since you came back to the Netherlands.

Next, thank you Deepali. You haven't just been a colleague for me, but actually my first friend in Stuttgart. Sharing my thoughts, stories and, sometimes, PhD-related frustration with you really helped me to go beyond the difficult moments of a PhD or when I was simply feeling so far away from home.

I would also like to thank my former colleagues at Dassault Systèmes, Davide and Umberto. I really enjoyed the thousands of coffee breaks, our Italian dinners and the time spent together hanging out in Stuttgart and surroundings. You brought a lot of Italy here in Germany.

I would like to share my gratitude to Francesco Avallone and Daniele Ragni from TU-Delft as well. Although you have not officially been part of my supervisory team, your feedback, collaboration and supervision have been essential to improve the quality of the work related to this thesis, as well as to shape my attitude in conducting research. Still from TU-Delft, I also had great pleasure of working with Edoardo. I really enjoyed collaborating with you on the propeller stuff. The three of you, guys, made me feel closer to TU-Delft and bridged the 650 km gap that separates Stuttgart from Delft.

Now it is the turn of my "BFF", Violetta. After our Masters graduation, we shared the same path and both reluctantly left Roma Tre University to pursue a PhD abroad: you in the United Kingdom and I in the Netherlands. During these years, we shared so many moments of deep frustration, but also of joy and rewarding success. Although the fate has physically separated us, we continue to be there for each other. Thanks for always being there when it matters.

I should also thank my friends in my hometown: Francesco, Luca, Marco and Vanessa. It is always nice to come back home, talk about the unexpected development of our lives, and spend time with you guys in front of one or more beers, just like old times. Such moments, lately unfortunately rare, helped me relax and re-energize from the PhD life.

Many thanks to Stefano and Klemi for the relaxing outdoor trips and the several evenings spent eating delicious food and chilling out after a long and stressful week of work. You can now call me "Doctor" appropriately!

I cannot mention my amazing friends and neighbors: Gennaro, Vanessa and the little Aurora. I was writing down the first lines of this dissertation when we started living next to each other. Your support, the coffee breaks, the dinners together and all the cakes and sweets you brought to me, boosted me towards the final lines of this thesis.

I want to spend some time to thank my mother and father. Thank you for the education you gave me and for all what you have done since the first day of school to let me study in peace and without worries. See? I have finally got out of school! I also have to thank my brother, Fabio, and my sister-in-law, Roberta, for being there for me. The long-distance actually brought us closer.

Thanks should also go to my girlfriend's family, which soon became my second family: Carmela, Salvatore, Francesca, Fabio and "nonna" Francesca. Thanks for always finding the way to help me out, no matters the unexpected events and difficulties of life.

Last but not least, I wish to thank my amazing girlfriend and partner in life, Maria. We met only in the middle of this adventure, but your presence quickly became essential for me to overcome the hurdles of the PhD life and push me towards the finish line. You are the furthest person from all that is science, but I could not have wished for a better person to stand by my side during this journey. Thank you for your endless love and every day support. The best is yet to come.

CURRICULUM VITÆ

Gianluca ROMANI

16-03-1991	Born in Aprilia, Italy.

EXPERIENCE

2021–present	**R&D Software Developer** Fluids Science and Technology Dassault Systemes Deutschland GmbH, Stuttgart, Germany
2020–2021	**Fluids Industry Process Expert Specialist** Disciplines Enablement Acoustics Dassault Systemes Deutschland GmbH, Stuttgart, Germany
2019–2020	**Solution Consultant** Aerospace & Defence Dassault Systemes Deutschland GmbH, Stuttgart, Germany
2016–2018	**Application Engineer** Aerospace & Defence Exa GmbH, Stuttgart, Germany

EDUCATION

2017–2021	**Doctor of Philosophy (PhD) in Aerospace Engineering** Delft University of Technology, Delft, the Netherlands
Thesis:	Computational Aeroacoustics of Rotor Noise in Novel Aircraft Configurations: a Lattice-Boltzmann Method-Based Study
Promotor:	Prof.dr.ing. D. Casalino
2013–2016	**Master of Science (MSc) in Aeronautical Engineering** Roma Tre University, Rome, Italy
Thesis:	Development of a Solution Technique for the Aero-acusto-elastic Analysis of Helicopter Rotors in Forward Flight
Promotor:	Prof.dr.ing. M. Gennaretti
2010–2013	**Bachelor of Science (BSc) in Mechanical Engineering** Roma Tre University, Rome, Italy
Thesis:	2-D Numerical Analysis of the Acoustic Field Generated by the Flow Around Circular Cylinders
Promotor:	Prof.dr.ing. R. Camussi
2005–2010	**High School Education** Liceo Scientifico Antonio Meucci, Aprilia, Italy

LIST OF PUBLICATIONS

JOURNAL ARTICLES

10. **G. Romani**, E. Grande, F. Avallone, D. Ragni, D. Casalino, *Computational Study of Flow Incidence Effects on the Aeroacoustics of Low Blade-tip Mach Number Propellers*, Aerospace Science and Technology, **120**, 107275 (2022).
9. **G. Romani**, E. Grande, F. Avallone, D. Ragni, D. Casalino, *Performance and Noise Prediction of Low-Reynolds Number Propellers using the Lattice-Boltzmann Method*, Aerospace Science and Technology, 107086 (2021).
8. E. Grande, **G. Romani**, D. Ragni, F. Avallone, D. Casalino, *Aeroacoustic Investigation of a Propeller Operating at Low-Reynolds number*, AIAA Journal (Article in Advance) (2021).
7. W. C. P. van der Velden, **G. Romani**, D. Casalino, *Validation and Insight of a Full-Scale S-76 Helicopter Rotor using the Lattice-Boltzmann Method*, Aerospace Science and Technology **118**, 107007 (2021).
6. D. Casalino, E. Grande, **G. Romani**, D. Ragni, F. Avallone, *Definition of a Benchmark for Low Reynolds Number Propeller Aeroacoustics*, Aerospace Science and Technology **113**, 106707 (2021).
5. **G. Romani**, W. C. P. van der Velden, D. Casalino, *Numerical Analysis of Airfoil Trailing-Edge Noise for Straight and Serrated Edges at Incidence*, AIAA Journal **59**:7, 2558–2577 (2021).
4. D. Casalino, E. Grande, **G. Romani**, D. Ragni, F. Avallone, *Towards the Definition of a Benchmark for Low Reynolds Number Propeller Aeroacoustics*, J. Phys.: Conf. Ser. **1909** 012013 (2021).
3. **G. Romani**, Q. Ye, F. Avallone, D. Ragni, D. Casalino, *Numerical Analysis of Fan Noise for the NOVA Boundary-Layer Ingestion Configuration*, Aerospace Science and Technology **96**, 105532 (2020).
2. **G. Romani**, D. Casalino, *Rotorcraft Blade-Vortex Interaction Noise Prediction using the Lattice-Boltzmann Method*, Aerospace Science and Technology **88**, 147–157 (2019).
1. M. Gennaretti, G. Bernardini, J. Serafini, **G. Romani**, *Rotorcraft Comprehensive Code Assessment for Blade–Vortex Interaction Conditions*, Aerospace Science and Technology **80**, 232–246 (2018).

CONFERENCE PAPERS

10. E. Grande, **G. Romani**, D. Ragni, F. Avallone, D. Casalino, *Experimental Aeroacoustics Investigation of a Propeller Operating at Low-Reynolds Number*, 1st Delft International Conference on Urban-Air-Mobility, Delft, the Netherlands (2021).

9. **G. Romani**, E. Grande, F. Avallone, D. Ragni, D. Casalino, *Low-Reynolds Number Propeller Noise Prediction Using the Lattice-Boltzmann/Very Large Eddy Simulation Method*, 1st Delft International Conference on Urban-Air-Mobility, Delft, the Netherlands (2021).

8. D. Casalino, W. C. P. van der Velden, **G. Romani**, *Aeroacoustic Analysis of Urban Air Operations using the LB/VLES Method*, 25th AIAA/CEAS Aeroacoustics Conference, Delft, the Netherlands, paper 2662 (2019).

7. **G. Romani**, Q. Ye, F. Avallone, D. Ragni, D. Casalino, *Fan Noise Boundary-Layer Ingestion Installation Effects for NOVA Aircraft Configuration*, 25th AIAA/CEAS Aeroacoustics Conference, Delft, the Netherlands, paper 2429 (2019).

6. **G. Romani**, D. Casalino, *PowerFLOW Simulations of Helicopters in Blade-Vortex Interaction Conditions*, Vertical Flight Society 75th Annual Forum & Technology Display, Philadelphia, Pennsylvania, 185 (2019).

5. D. Casalino, W. C. P. van der Velden, **G. Romani**, *Community Noise of Urban Air Transportation Vehicles*, 2019 AIAA Aerospace Sciences Meeting, San Diego, California, paper 1834 (2019).

4. I. Gonzalez-Martino, **G. Romani**, J. Wang, D. Casalino, *Rotor Noise Generation in a Turbulent Wake using Lattice-Boltzmann Methods*, 24th AIAA/CEAS Aeroacoustic Conference, Atlanta, Georgia, paper 3447 (2018).

3. **G. Romani**, W. C. P. van der Velden, D. Casalino, *Deterministic and Statistical Analysis of Trailing-Edge Noise Mechanisms with and without Serrations*, 24th AIAA/CEAS Aeroacoustic Conference, Atlanta, Georgia, paper 3129 (2018).

2. **G. Romani**, D. Casalino, *Application of Lattice-Boltzmann Method to Rotorcraft Aerodynamics and Aeroacoustics*, 43rd European Rotorcraft Forum, Milan, Italy (2017).

1. M. Gennaretti, G. Bernardini, J. Serafini, **G. Romani**, *Assessment of a Comprehensive Aero-Acousto-Elastic Solver for Rotors in BVI Conditions*, 43rd European Rotorcraft Forum, Milan, Italy (2017).